UNIVERSITÉ LILLE 1 – SCIENCES ET TECHNOLOGIES

**Doctoral School*: Material sciences, Radiation and Environment*

Discipline: *Optics and Lasers, Physical Chemistry, Atmosphere*

Dissertation

PULSED LASER DEPOSITION AND CHARACTERIZATION OF CHALCOGENIDE THIN FILMS

by

Gloria Oana POMPILIAN

*Reviewers***:**	**Virginie NAZABAL**	**Chargée de Recherche CNRS à l'Université de Rennes 1**
	Cristian Petrica LUNGU	**Senior Researcher, National Institute for Laser, Plasma and Radiation Physics, Bucharest, Romania**
Examiners:	**Mohamed BOUAZAOUI**	**Professeur, Université Lille 1 Sciences et Technologies**
	Petr NEMEC	**Associate Professor, University of Pardubice, Czech Republic**
	Silviu GURLUI	**Associate Professor, Université "Alexandru Ioan Cuza" Iasi, Romania**
*Supervisor***:**	**Cristian FOCSA**	**Professeur, Université Lille 1 Sciences et Technologies**

11 July 2013

Table of contents

Chapter I

Introduction

I.1 Context

This thesis was performed in the research group ANATRAC at the Laboratoire de Physique des Lasers, Atomes et Molécules (UMR 8523 CNRS – Université Lille 1). The main goal of these studies was to grow and characterize chalcogenide thin films in various deposition conditions (using the Pulsed Laser Deposition technique). The deposition and some characterizations (Raman, optical microscopy, spectrophotometry, optical emission spectroscopy (OES) of the plasma plume) were performed in our laboratory, while for the other characterization techniques we benefited from a collaborative network, either with laboratories from our University (UCCS for Time-of-Flight Secondary Ions Mass Spectrometry, IEMN for stylus profilometry) or with external research groups, at University of Pardubice (Czech Republic) for X-ray diffraction and ellipsometry, Université de Rennes 1 (France) and Technical University of Iasi (Romania) for the scanning electron microscopy and energy-dispersive X-ray spectroscopy, Université Paris XI (Orsay, France) for stylus profilometry. This large collaborative network allowed me to be in contact with numerous characterization techniques. On the other hand, synchronizing the deposition runs and the characterization campaigns on the various instruments became sometimes a complex task, leading to some shortage in the complete systematic study initially envisaged. We note nevertheless that this work contributed to the amplification of the existing relations, as it was confirmed by the recent attribution of two international PHC (Partenariats Hubert Curien) projects, one with Romania (Brancusi) and the other one with Czech Republic (Barrande).

Two families of chalcogenide glasses were studied in this thesis:

1. Ge-Sb-Te (GST), with five different compositions, which can be written in the compact form $(GeTe)_x(Sb_2Te_3)_{1-x}$, where $x = 0, 1/3, 1/2, 2/3$, and 1;
2. Ga-La-S (GLS), pure or doped with Er and Pr rare earths.

Some elements on the importance of these compounds will be presented in the next section. Further in this chapter, some (theoretical) considerations on the PLD technique (used for the first time in our group during this thesis) will be introduced.

Chapter II will detail the practical implementation of the PLD and OES techniques and will give an overview of the characterization methods. The results obtained for the GST family will be presented in Chapter III, while those for GLS in Chapter IV. These two chapters have a quite repetitive structure, as we choose to organize the presentation of the results following the material deposited, and not following the characterization technique. However, we will try to draw some conclusions/comparisons at several intermediate points. Chapter V is dedicated to the study (by space- and time-resolved optical emission spectroscopy) of the transient plasma plume generated by laser ablation during the PLD process. Finally, conclusions and perspectives of this work will be presented.

I.2 Chalcogenide glasses

Chalcogenide glasses are materials based on the group VI elements Sulfur (S), Selenium (Se) and Tellurium (Te) and their addition to at least one electropositive element like Germanium (Ge), Antimony (Sb), Gallium (Ga), Arsenic (As) etc. Due to their atomic bonding structure, chalcogenide materials are considered to be more rigid than polymers but with a higher flexibility than oxides, thus their transition temperatures and elastic properties being between those found for the two mentioned types of materials [Singh 2010]. Although chalcogenide glasses present low mechanical hardness and thermal stability, other characteristics such as high thermal expansion and refractive index, optical non-linearity and larger range of infrared transparency make them suitable for various applications (see Figure I.1) from civil to medical and military areas [Singh 2010, Zakery and Elliott 2007].

Chalcogenide glasses are low-phonon energy materials (200-500 cm^{-1} – depending on the composition [Frumar et al. 2006]), thus they present an increased potential for active devices related to photoluminescence [Anne et al. 2009].
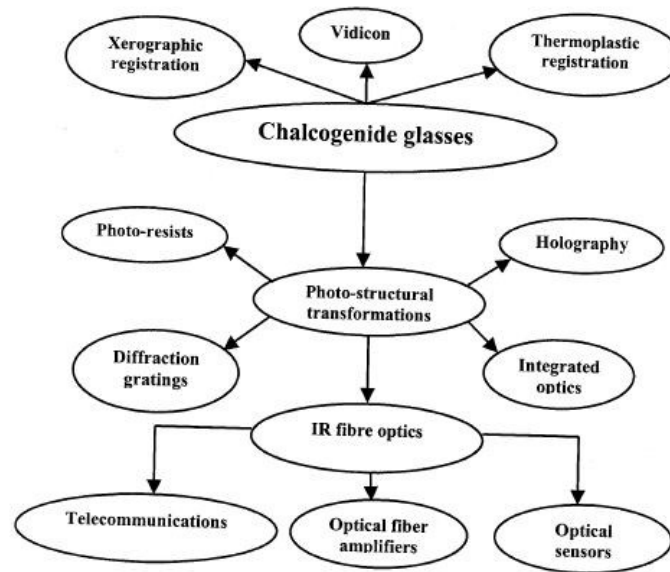
Figure I.1.   Application fields of chalcogenide glasses [Mehta 2006].

Considering the large variety of elements that can form the chalcogenide glasses, several characteristics (e.g. refractive index, optical band gap energy) can be modified to fit one's application (see Figure I.2).
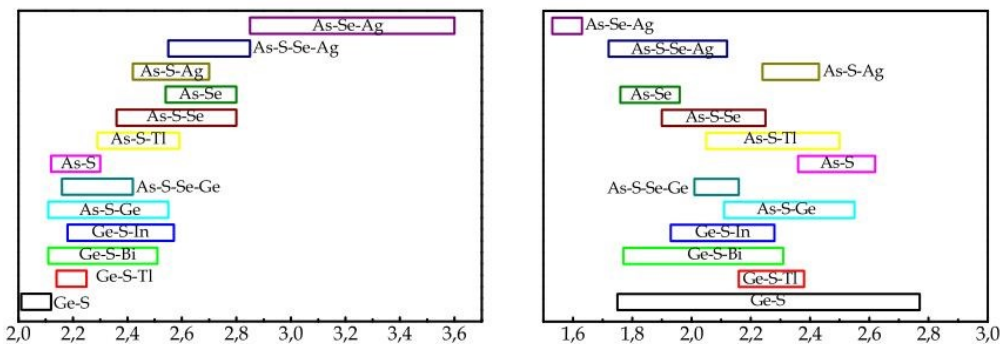
Figure I.2.   Refractive indices (left) and optical band gaps (right, in eV) of several chalcogenide glasses [Todorov et al. 2012].

For the formation of photonic crystals with applications that include resonant cavities, waveguide crossing and nonlinear devices, the main objective is to induce changes in electrochemical and optical parameters simply by exposing the material to light or to electric fields and X-ray beams [Andriesh et al. 2002, Rode at al. 2002]. Chalcogenide films based on As-Se, As-S-Se and As-S-Se-Ge compounds can present changes in refractive index of 7 %, 4 % and 5.8 % respectively when light irradiated [Todorov et al. 2012, Robinson et al 2003].

A large interest is also given to the photoinduced processes in chalcogenide materials. Both photodarkening and metal-photodissolution effect have been used to fabricate transmissive gratings with significant applications in monochromators, laser-tuning devices, shapers, optical-fiber couplers etc. For instance, gratings have been written holographically in sputtered $Ge_{10}As_{40}S_{25}Se_{25}$ films using the 514.5 nm radiation from an Ar-ion laser [Ramachandran and Bishop 1999]. This process also enhances the photosensitivity and the magnitude of photoinduced index changes ($\Delta n \sim 5\%$). Robinson et al. have achieved holographic recording of Bragg gratings in amorphous As_2Se_3 thin films with Δn as large as 0.037 (1.4%) at a wavelength of 1550 nm. The pure phase gratings were found to be permanent and their strength 2 orders of magnitude greater than those demonstrated in As_2S_3 [Robinson et al. 2003]. The effect of laser irradiation on refractive index observed by Todorov et al. [2012] is presented in Figure I.3.
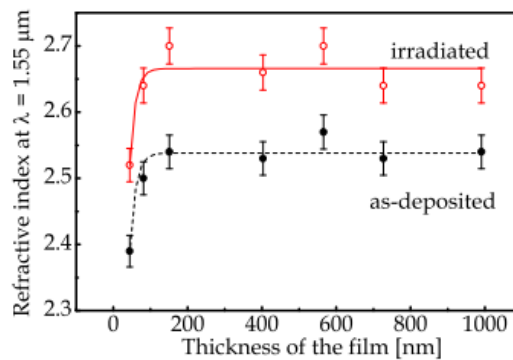
Figure I.3 Thickness dependence of refractive index (at λ=1.55 µm) for the as-deposited and irradiated films of AsSe [Todorov et al. 2012].

As one can observe significant variation of refractive index can be obtained not only by irradiation but by increasing the samples thickness from 50 to 200 nm. For higher thickness values, the deposited films present approximately the same optical characteristics.

Radiation sensors can be obtained using the radiation sensitivity of chalcogenide glasses (ChG) and radiation induced ion diffusion. These sensors are microelectronic devices that react to radiation by producing easily measured change in electrical resistance. A schematic representation of this type of device is presented in Figure I.4. The active region consisting of a chalcogenide glass is placed between two-terminal micro devices.
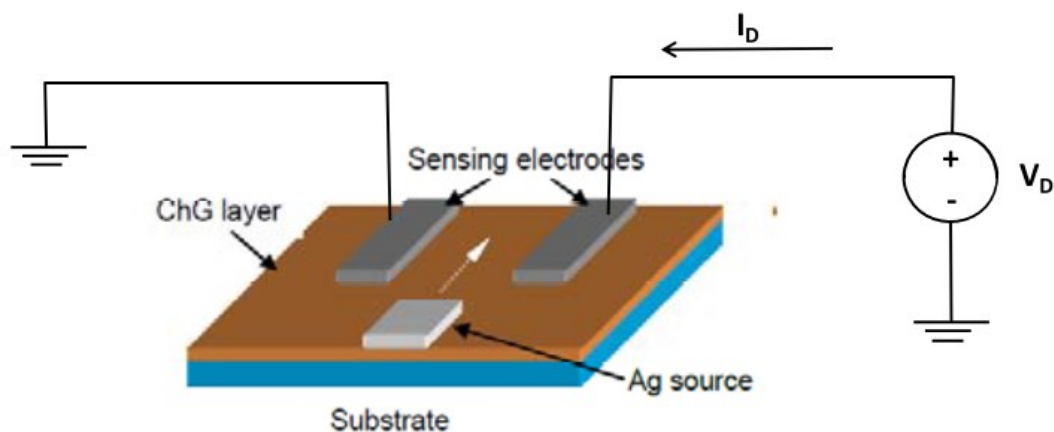
Figure I.4. Schematic representation of a chalcogenide based radiation sensor
[Ailavajhala et al. 2012].

The exposure to ionizing radiation induces radiation effects in the chalcogenide layer and determines a silver diffusion and incorporation in the active region, thus reducing the material's resistivity. Since these devices are based on amorphous films, they can be fabricated on flexible and non-planar substrates, thus increasing their range of application. Since the family of the chalcogenide glasses includes a large number of materials, there are many possibilities of tailoring the sensitivity of the sensor.

A notable advantage when using chalcogenide materials is the wide transmission window (1-20μm, depending on composition, see Figure I.5) which enables their use in applications such as: laser power delivery [Kosolapov et al. 2011], chemical and bio-sensing [Anne et al. 2009, Todorov et al. 2012], temperature measurements [Santos et al.1998], thermal imaging [Zhang and Lucas 2003, Cha et al. 2012], fibers [Seddon et al. 2010] and telecommunication systems [Pelusi et al. 2009, Aggarwal and Sanghera 2002]. The first commercial application of chalcogenide based materials concerned optical components for IR transmission [Zhang and Lucas 2003, Zhang et al. 2003].

In the 1980's, an increased attention was accorded to the fabrication of ultra-low loss chalcogenide fibers in order to replace the silica optical fibers. The fiber optic based sensors present numerous advantages: small size, absence of electrical interference, unnecessary reference electrode, remote sensing etc.
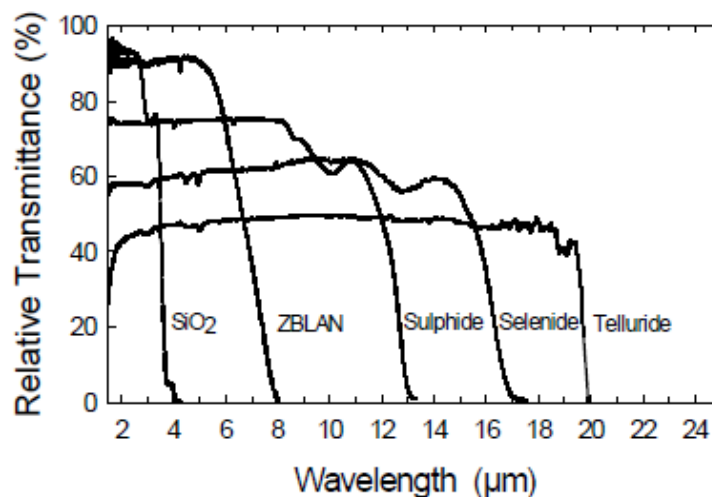
Figure I.5. Transmittance spectra of several types of chalcogenides with thicknesses of 2-3mm [Aggarwal and Sanghera 2002].

The doping of chalcogenide glasses with rare-earth elements has allowed the possibility of using these materials in active applications such as amplifiers and lasers. Mori et al. [1997] investigated the optical amplification at 1.083µm of rare earth doped Ge–As–Ga–Sb–S fiber. They obtained a 6.8dB internal gain for a pump power of 180mW. The optic-fiber applications are not limited only to telecommunication systems. Chalcogenide fibers can be successfully utilized in medical areas. Yoo et al. [2009] fabricated an IR optical fiber based sensor which can monitor the respiration of a patient.

Like silica fibers, chalcogenide fibers can be drawn from a pre-form but in this case the drawing temperature is close to the crystallization temperature. Crystallization weakens a fiber and alters several properties. Another problem when manufacturing chalcogenide fibers is the glass contamination. Although chalcogenide materials present the right properties for many applications, a difficult task is to obtain fibers with characteristics that match the theoretical ones.

Bio-molecules have complex vibrational spectra with distinct features in the region between 5 and 12 µm. These characteristics allow a selective identification of the biomolecules if the spectra can be recorded with a high enough quality. Thus, the chalcogenide glasses can be successfully used in bio-sensors [Anne et al. 2009]. Most bio-molecules and microorganisms present a net surface charge that can be utilized to force their displacement by simply applying an electric field.

6
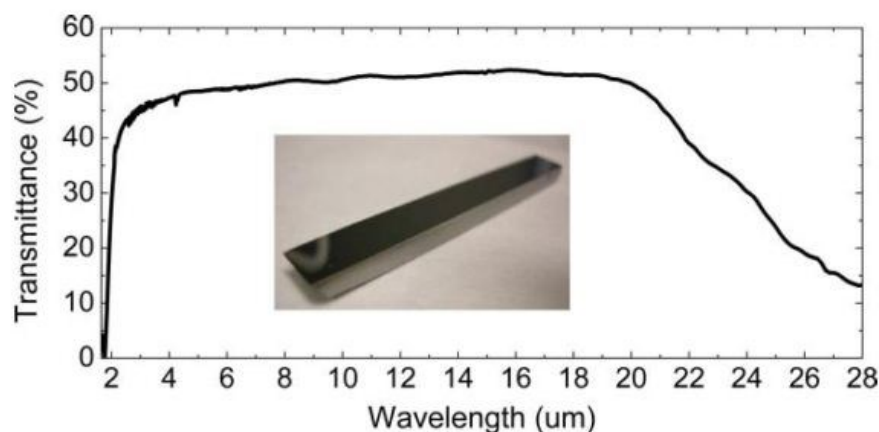
Figure I.6   Transmittance spectra of a 2 mm polished disk of $Ge_{10}As_{15}Te_{75}$ glass together with a photograph of the Attenuated Total Reflection [Yang et al. 2010].

Yang et al. [2010] developed and characterized a sensor based on $Ge_{10}As_{15}Te_{75}$ chalcogenide glass that can be used as both an infrared optical element and as an electrode for electrophoretic collection and detection of biological molecules. Their study evidenced the potential application of this type of material using an Attenuated Total Reflection (ATR) configuration (Figure I.6). The high conductivity ($7.8 \cdot 10^{-5} \Omega^{-1} \cdot cm^{-1}$) together with a wide transparency window in the infrared region (see Figure I.6) makes the $Ge_{10}As_{15}Te_{75}$ material a well suited candidate for bio-sensing as well as online monitoring of water safety.

The first systematic research on chalcogenide materials started in 1950's when Frerichs [1953] reported studies on As_2S_3 glasses with transmittance in mid-IR (up to 12μm). These results encouraged its use in IR optical components systems, As_2S_3 becoming the first chalcogenide commercially developed. In the next decades, progress was made with S- and Se-based chalcogenides, as well as binary Se-Te systems for far-IR optical devices [Zakery and Elliott 2007, Mehta 2006].

Depending on the composition, chalcogenide glasses present optical band gaps in the range 1-3 eV and can be considered as semiconductors [Mehta 2006]. This band gap decreases in the sequence S→Se→Te, thus in glass containing large amounts of Te the metallic character is enhanced. Moreover, in Ag–As(Ge)–S chalcogenides, the electric conductivity is governed by ionic conduction of Ag ions [Zakery and Elliott 2007].

Starting with Ovshinsky's paper published in 1968 [Ovshinsky 1968] many research groups focused their study on phase change (PC) materials as recording

media in storage devices. PC memories are based on changes in optical and conductive properties of chalcogenide materials upon a rapid amorphous to crystalline phase transition and vice – versa. These two states must present a high enough contrast in resistivity or other optical parameters in order to be identified. The rapid changes from amorphous (high resistivity) to crystalline structure (low resistivity) is induced by Joule effect using an electric current pulse. Depending on the intensity and duration of the pulses, the PC memory cells can be written or erased. Figure I.7 presents the intensity-time dependence for three current pulses used to write, erase or read the memory cell. I_m and I_x are the intensities needed to melt and crystallize the material, respectively. A low resistive state is achieved by setting the PC memory cell in crystalline phase using a medium electric current pulse, thus heating the material up to a temperature between the crystallization temperature and the melting temperature. To reset the cell into an amorphous phase, a large electric current pulse is applied for a short period in order to melt the crystallized area and then rapidly quench the material.
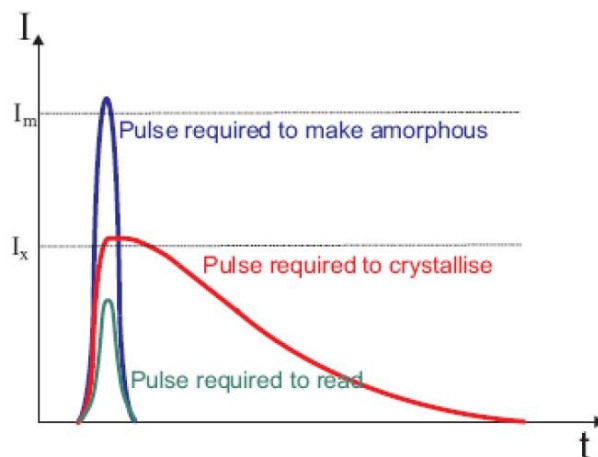
Figure I.7. Representation of crystallization pulse (red), amorphising pulse (blue) and read pulse (green) [Hewak et al. 2010]

Any material can present an amorphous and crystalline phase, but only a few of them are adequate for PC memory devices. Although the concept of information storage based on phase switching is known from 1960s, a considerable attention to this technology was given after the development of new chalcogenide alloys with interesting properties.

Nowadays, only a few chalcogenide alloys can be considered as promising materials for PC memory applications. These include: Se based compounds (which

have the lowest phase transition temperature), Sb-Te alloys doped with other metals (Ag, In) and Ge-Sb-Te based systems. The last two mentioned materials are already used in the manufacturing of DVD-RW and DVD-RAMS and are considered to be the next alternative for electric-pulse-controlled PC memory cells for non-volatile information storage devices [Kozyukhin et al. 2011]. Figure I.8 presents the cross section of a conventional CD-RW.
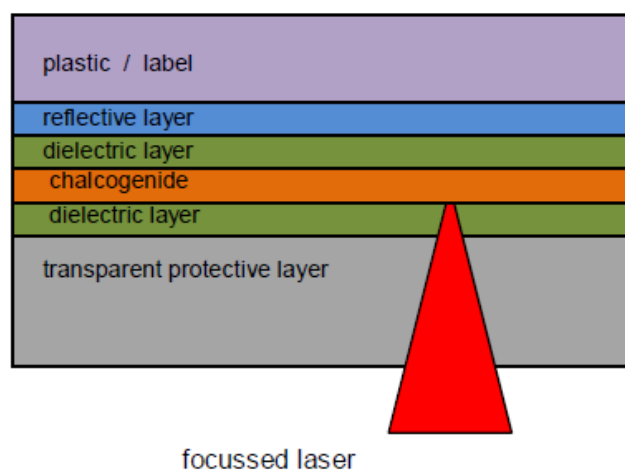
Figure I.8. Cross section of an optical disk based on Ge-Sb-Te alloy [Hewak et al.2010].

In optical phase change devices, the writing and reading is achieved using the same laser as the reading process, but for each step, a different laser power is used. For reading, the incident laser radiation is reflected from the surface and depending on the intensity of the reflected beam information on the phase of the film is achieved.

The above detailed applications prove that chalcogenide glasses are interesting and promising materials that can be used in various areas. Many of the mentioned devices imply a thin film deposition and a quick literature survey suggest that an appropriate method for their manufacturing is the pulsed laser deposition (PLD) technique. A complex study on chalcogenide thin films deposited by PLD is reported in [Frumar et al. 2006]. Besides the advantages and drawbacks of PLD, this review also presents the general characteristics of several chalcogenide glasses.

I.3 Pulsed Laser Deposition for thin film growth

Among the various techniques available for the growth of amorphous chalcogenide thin films (vacuum thermal evaporation, sputtering, spin-coating,

chemical vapor deposition – CVD etc.), the Pulsed Laser Deposition is one of the most promising, mainly by its capability to ensure the stoichiometric transfer from target to substrate, but also to synthesize thin films of less usual composition [Eason 2007]. Since its invention, this technique triggered considerable interest, due to the relatively simple experimental arrangement and to the possibility of preparing a large variety of thin films: superconductor materials [Kwok et al. 1991 ; Witanachchi et al. 1988 ; Singh et al. 1989], DLC (diamond-like carbon) [Krishnaswamy et al. 1989 ; Voevodin and Donley 1996], oxides [Fogarassy et al. 1990], carbides [Balooch et al. 1990], nitrides [Biunno et al. 1989], ferroelectrics [Kidoh et al. 1991] etc.

A typical PLD experimental set-up is shown in Figure I.9. A laser beam of wavelength λ and pulse width τ is directed into a vacuum chamber and focused onto the target surface. For sufficiently high beam energies, a plasma of target material is ejected from the surface and deposited onto the substrate opposite the target. If the laser beam energy is too low, below the threshold for ablation, the laser radiation will serve only to heat the target and cause thermal evaporation. The substrate and target are often rotated to enhance deposition and ablation uniformity, and a background gas may be used to enhance gas phase chemistry or thermalize the high energies of ablated species. For some specific materials, the substrate can be also heated in order to achieve desired structural properties of the deposited material.
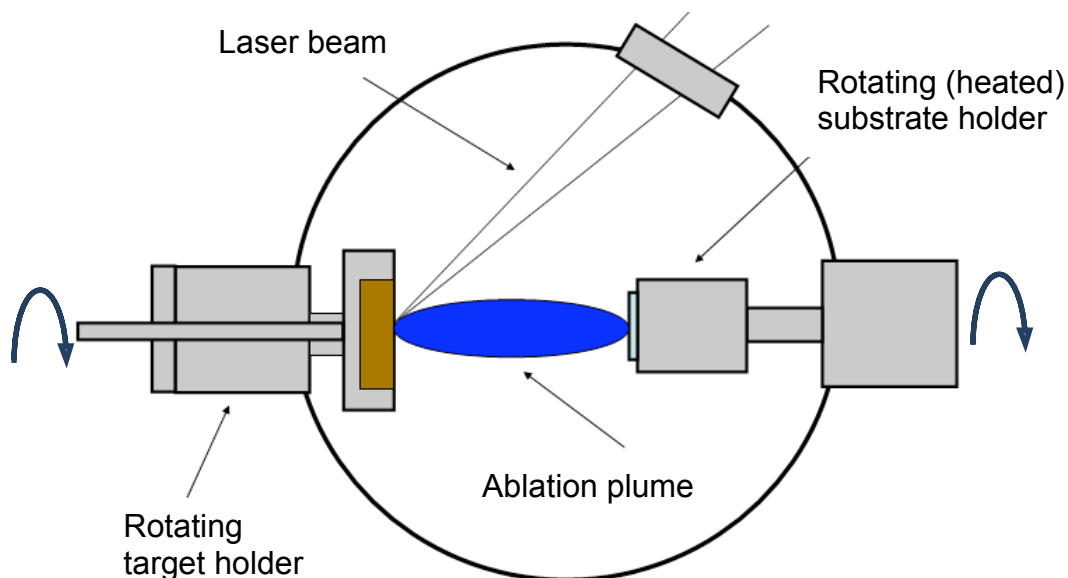
Figure I.9. Schematic view of a typical PLD experimental set-up.

Aside the "stoichiometry control" mentioned above, the PLD technique offers also some other advantages [Schou 2009]:

- the laser-target interaction initiating the ablation process is completely decoupled from other process parameters, as background pressure, type of background gas, type and temperature of the substrate;

- the atoms and ions in the plume have kinetic and internal excitation energies that initially may exceed thermal energy by two orders of magnitude. At the arrival on the substrate these non-thermal particles have an appropriate excess energy which increases the sticking and nucleation rate as well as the surface mobility;

- PLD is a pulsed process, by which the number of particles arriving at the substrate can be precisely controlled with the number of pulses and fluence. This means that layer-by-layer growth can be achieved by adjusting the number of arriving atoms in a monolayer, and thus highly perfect surfaces and interfaces in sandwich-systems can be produced.

I.3.1   Laser ablation and plume expansion

Despite this simple technological picture, even the first stages of the PLD process (interaction of matter with pulsed laser of high intensity leading to generation of the plasma plume) are far from being completed understood, as they involve various physics domains, from the thermodynamic and optical properties of the solid target, to phase transitions, expansion of the gas phase and its interaction with the laser, electrical interactions between the components of the plasma created etc. The term "laser ablation" that we will use in the following can be defined as "the laser induced ejection of a significant fraction of an atomic monolayer of the irradiated material" [Miller and Haglund 1998]. The studies performed in this thesis involved laser pulses in the nanosecond, picosecond and femtosecond regimes, with fluences of the order of 1 J/cm^2, which lead to intensities higher than 1 GW/cm^2. At this level, the energy coupled into the solid is so high that, beyond the ejection of an important quantity of material (much more that the monolayer mentioned above), a significant degree of ionization of the ejected entities can arise, leading to the creation of a plasma which then propagates into vacuum or background gas. A simplified view of these processes would involve the following steps :

1. Absorption (total or partial) of the laser beam energy into the material induces temperature increase and heat diffusion. This heating (which depends also on the temporal regime of the laser employed) can lead to a phase transition or a chemical degrading of the system (depending on the wavelength used, photochemical processes can also occur, especially in the UV spectral range). In general (in the nanosecond regime), the irradiated material is considered as being in local thermodynamic equilibrium (LTE), as the relaxation time is shorter than the pulse duration [Bäuerle 2000]. For ps and (especially) fs regime, the picture is more complicated, as the thermal relaxation time (usually tens of ps) is greater than the pulse duration. In this case, the energy absorbed by the electrons (inverse bremsstrahlung processes) is not transferred to the ions, leading to an "electrostatic" ablation [Reif 2010], i.e. the electrons will leave the target in the first stage of the laser-matter interaction, leaving behind regions positively charged. The surface becomes electrically unstable and will emit positively charged particles, which will be further accelerated by the electromagnetic field. The absence of the solid-liquid phase change can lead to stoichiometric ablation of nanoparticles.

2. Ejection of matter in form of atoms, molecules, clusters, nanoparticles or micron-sized droplets occurs if the temperature is high enough. Rapid expansion of matter (with velocities usually in the range 1-10 km/s) can lead to the creation of a shock wave.

3. In nanosecond regime, the ejected matter can interact with the laser pulse by diffusion, absorption (direct photo-excitation, inverse bremsstrahlung) etc. A plasma can develop above the surface.

4. After the end of the laser pulse, the material cools down and ionized species recombine. Part of the ejected material can re-condense on the target surface.

At the theoretical level, numerous analytical and numerical models have been proposed in order to unveil this complexity [Bityurin et al. 1998, Arnold et al. 1998, Lunney and Jordan 1998, Boardman et al. 1996, Anisimov et al. 1999, Tosto 2002, Rosen et al. 1982]. However, the great disparity of time scales involved makes that the simultaneous simulation (in the frame of the same model) of ablation and plasma expansion is not very practical. For instance, a typical calculation would need an adequate description of the laser energy deposition (at time scales ranging from tens of fs to tens of ns, and sub-millimeter space scales) and, simultaneously, of the plasma

evolution which in the final phase of expansion can take place on tens of μs and at cm-range distances with respect to the initial event. Consequently, an often adopted solution is to use several models, each one adapted to a particular stage, and to subsequently link them through intermediate times. The plasma plume evolution itself involves two important parts: the initial uni-dimensional expansion (the laser diameter being much larger than the penetration depth in the material) and the final tri-dimensional expansion [Bogaerts et al. 2003, Murakami et al. 2005, Mora 2003, Anisimov et al. 1996]. The initial uni-dimensional stage involves the laser energy deposition, followed by the very first instants of the expansion. The longitudinal dimension of the heated material is still very low compared to the transversal dimension defined by the laser spot diameter. The laser-material interaction and the energy and matter transport are the main processes to be considered during this stage. After some time, the plasma cloud becomes tri-dimensional, but the physics involved is somehow simplified, in the sense that the plume evolution is described by classical hydrodynamics and is sensitive only to integral parameters of the laser pulse. Various approaches have been proposed to describe this expansion, by hydrodynamic models [Peterlongo et al. 1994, Balazs et al. 1991, Amoruso 1999, Bulgakov and Bulgakova 1995], Monte Carlo simulations [Sibold and Urbassek 1993, Garrelie et al. 1999], or by a combination of both [Itina et al. 2003]. Recently, even a fractal model has been proposed [Gurlui et al. 2008, Nica et al. 2009].

From a practical point of view, the properties of the deposited materials depend on the characteristics of the plasma propagating between the target and the substrate. This expansion (either uni-dimensional or tri-dimensional) is accompanied by a strong luminescence from excited atoms and ions. The study of this transient plasma dynamics through plume imaging and optical emission spectroscopy (as we did in Chapter 5) can give precious information for defining the optimal working conditions [Amoruso et al. 2010] and for the control of various properties of the deposited thin films, like composition (with respect to the target composition), growth rate, amorphous or crystalline structure etc. This dynamics is different in vacuum (the ablated atoms will eventually flow with constant velocity) and in background gas (the plume can be slowed down or even stopped to a confined structure). Finally, (some of) the plume atoms will be collected on the substrate and grow as a film in different modes, depending on the energetics of the atoms and aggregates on the surface, as well as on the arrival energy [Warrender and Azziz 2007].

I.3.2   Thin film growth

Thin films are formed on the substrate by nucleation and growth processes. The nucleation is the occurrence on the substrate of condensation centers (nuclei), which will further become growth germs. Nucleation in films grown by PLD is different from other deposition techniques because of the relatively high peak deposition rate and high energy of the plume when it reaches the substrate [Horwitz and Sprague 1994, Willmott 2004]. Nucleation is dependent upon the substrate and film materials, and parameters such as plume properties, background gas pressure and substrate temperature. The processes involved in film nucleation are summarized in Figure I.10 [Horwitz and Sprague 1994, Venables 1994].
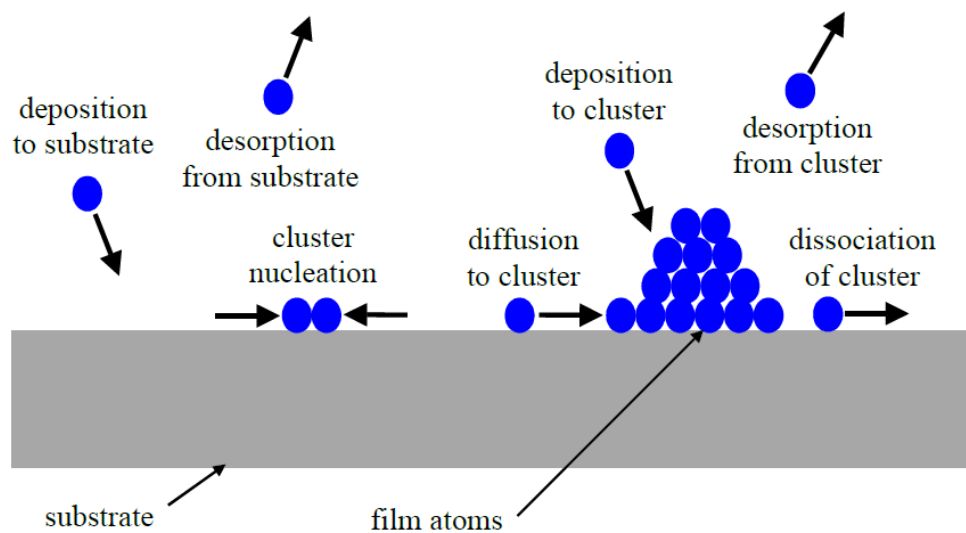
Figure I.10. Processes involved in thin film nucleation [Horwitz and Sprague 1994].

Three different modes of film growth can arise under different conditions of free energy on the substrate surface:

- Three-dimensional island growth (Volmer-Weber): three-dimensional islands are formed because the film components are more bound to each other than to the substrate [Ohring 1992]. In this case, on average, cluster free energy decreases as more atoms join, making the clusters stable.

- Two-dimensional full monolayer growth (Frank-van der Merwe): the film grows in a two-dimensional planar layer-by-layer way because the film components are more bound to the substrate than to each other [Ohring

1992]. In this case, on average, cluster free energy increases as more atoms join, making the clusters unstable and leading to layer-by-layer growth.

- Monolayers and islands (Stranski-Krastinov); the film grows in monolayers initially and islands start to occur as the surface conditions change as the film grows because of strain/stresses in the film [Venables 1994]. In this case the free energy dynamics change as the film is deposited, causing a switch from layer-by-layer growth to three-dimensional island growth.

Atoms from a laser ablation plume typically possess sufficient kinetic energy to diffuse some distance on the surface, until stable, energetically favorable bonds with other film atoms or substrate atoms have been established. A necessary condition for stoichiometry in the film is that atoms of all components are available in the desirable ratio at the growth points. While atoms of all components may not arrive in the original stoichiometric ratio, the surface diffusion may introduce another deviation on an even longer timescale, since heavy atoms will diffuse more slowly than light ones on the film. The primary processes which take place on a microscopic scale are: (i) atom/ion reflection on the surface, (ii) sputtering of film atoms by the ablation products, and (iii) implantation of arriving atoms.

Most of the (few) measurements performed to characterize the (i) reflection of atoms were done on metals or light ions (e.g. H^+, D^+ and He^+ [Eckstein et al. 1984]). Kondoh et al. [1993] found that the reflection coefficient of Cu atoms and Ni atoms with energies below 200 eV on graphite was less than 0.1. For the same atoms on gold the reflection coefficient peaked at about 50 eV with a maximum value of 0.4, but was significantly decreasing for higher energies. In contrast, sputtering (ii) of a growing film by the ablated particles has been recognized as an issue, in particular for PLD at fluences exceeding 4 J/cm^2 [Gonzalo et al. 2007, Jordan et al. 1995, Fähler et al. 1999]. The last authors [Fähler et al. 1999] showed that there is a sputtering rate of 0.55 for silver at 4.5 J/cm^2, i.e. that only about one-half of the arriving Ag atoms remain on the silver film. The underlying reason is that the kinetic energy of the ablated atoms in vacuum increases with fluence, and that a substantial fraction of the particles have a kinetic energy that exceeds 50 eV for fluences already about 2 J/cm^2 [Hansen et al. 1998]. At these energies the sputtering yield increases considerably with energy [Andersen et al. 1981, Behrisch and Eckstein 2007].

A clear effect of sputtering of a multicomponent film during a PLD run was found by van de Riet et al. [1993]. These authors demonstrated that for a FeSiGaRu thin film, gallium was preferentially lost. This agrees with the expectation that the most volatile component (cohesive energy = 2.8 eV for Ga-atoms in a gallium solid compared with much larger values for the other components) will be depleted. This effect turned out to be large at the highest fluence 6.5 J/cm^2, at which the ablated particles have a larger energy, and therefore, the sputtering is more efficient. Also O'Mahony et al. [2007] have pointed out that preferential sputtering of a film is an issue.

Implantation (iii) of ablated ions has been observed for PLD in few cases [Barnes et al. 2003, Suarez-Garcia et al. 2003, Fähler et al. 2000]. As the light ions penetrate deeper under the surface of the growing film, the surface will be enriched with the heavy component, and the stoichiometry will not be maintained. In summary, the bombardment of the surface by ablated ions can radically change the stoichiometry, in particular if the mass difference among the components is large and if the incident ion energy exceeds 50-100 eV. A strategy to avoid deviations from stoichiometry has been proposed by Schou [2009]: it is advised to avoid too low laser fluence (to be in the ablation regime rather than in an evaporative one), but also too high fluence (to reduce (re)sputtering of the film); moreover, use of a background gas as a moderator for the fast ablated particles (again to avoid (re)sputtering) is recommended, but at not too high pressure (which would lead to "preferential" diffusion of light atoms in the gas). The background gas should also compensate for lack of stoichiometry when working with volatile compounds (e.g. use oxygen for oxides, sulphur (if possible !) for sulphides etc;). The substrate should be placed not too close, but not too far from the target, in order to limit the preferential diffusion and the sputtering of the film. As one can see, this "recipe" is far from being "exact science", this explaining the fact that after almost three decades of intense use of PLD in thin films growth, the control and optimization of the deposition parameters are still generally done in an empirical manner.

Another major drawback of the PLD technique affecting the film quality is the deposition of microscopic particles (droplets) on the substrate / film surface [Singh et al. 1998]. These undesired particulates can have several origins: dislodging of existing or laser-produced protruding surface features, subsurface superheating, splashing of the molten surface layer, or condensation from vapor species due to supersaturation

[Chen 1994]. While the particles formed from the solid target tend to be irregular in shape, those formed in the liquid and the vapor phase state tend to be spherical. The size of the deposited droplets depends on the phase and may have submicron to micron size scale in the case of the solid and liquid phases to nanometer size for droplets formed in the vapor phase. To avoid deposition of droplets onto the growing film, several techniques are used depending on the geometry of the experimental PLD set-up, the laser type, the material properties and the background gas. Particulates that arise from target damage can be avoided by polishing the target at periodic intervals so that the target surface never gets damaged enough to make the occurrence of particulates increase significantly [Chang et al. 1990].

Generally, to reduce the particulate number density the simplest technique is to decrease the laser fluence [Watanabe et al. 1995a,b]. However, as said above, lowering the fluence too much will change the stoichiometry of the films. One interesting technique uses velocity filtration of the plasma by placing a rotating vane particle filter in the plume. This method is based on the fact that the particulates are slower than the atomic and molecular species in the plasma plume. Using velocity filtration, Pechen et al. [1995] and Nino et al. [2001] were able to reduce the particle density on the films by a factor of 10. Another method used to reduce the particles is to use off-axis geometry for the growing film [Siegert et al. 1999, Němec and Frumar 2003, Frumar et al. 2006]. This method works to decrease the number of particles because the macro-particles are constrained to travel along their initial trajectory direction, while the atomic and molecular species are scattered in the plume. Of course, one of the disadvantages to this method is that the deposition rate is reduced. Secondary lasers have also been used to reduce the occurrence of particulates by heating the plume and breaking them up [Gyorgy et al. 2002]. The use of two crossing plumes in the crossed-beam pulsed laser deposition technique (CBPLD) has also been successful in reducing the effect of particulates [Gorbunov et al. 1996, Willmott et al. 2002].

I.4 Work plan

The "simplified" picture sketched above shows how complicate the definition of variables for the production of optimized thin films can be. This complexity comes

also from the correlations between these variables, as changing one parameter often changes the ideal settings for others. The effects of changing a single variable can be identified by keeping all other variables constant, and variables such as target composition, laser characteristics (other than fluence) and background gas species are generally kept constant for simplicity. A nice global view of the parameters and processes involved in the optimization of the film quality has been proposed by May-Smith [2005] and is reproduced in Figure I.11.
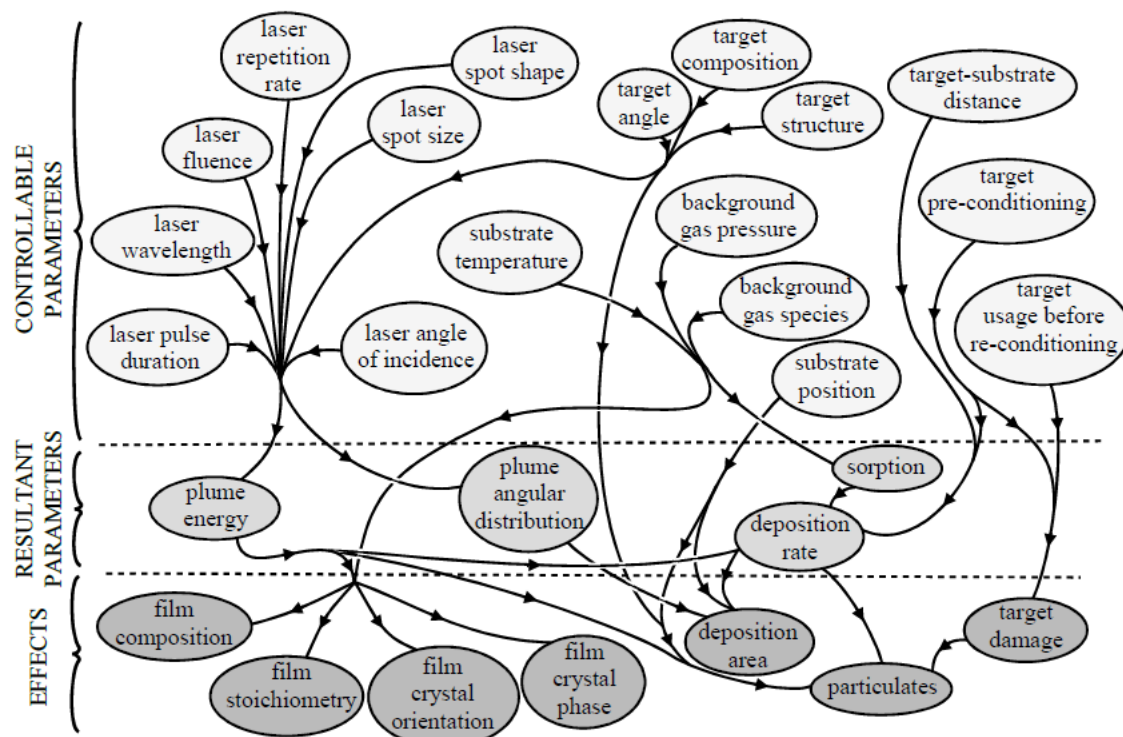
Figure I.11. A schematic representation of the parameters involved in PLD thin film growth [May-Smith 2005].

A complete systematic study of the influence of all the controllable parameters displayed in Figure I.11 is unreachable in the limited time of a PhD thesis. This is why we focused our attention in a first step on the laser wavelength and pulse duration influence, for various target compositions in the two chalcogenide families mentioned above. Some other parameters (as laser fluence, target-substrate distance, background pressure) have been secondarily changed in order to see possible effects. Additional theoretical considerations on the influence of some of these parameters in the PLD process are presented below.

Pulse length. Both wavelength and pulse length (ns, ps and fs) may affect the laser-induced plasma parameters like plasma potential, temperatures, number densities, but also may influence the entire space-time dynamics of the ablation process. Generally, if the pulse duration is shortened, the laser has less time to transfer energy to the surrounding material before being ejected and consequently, the laser energy is more rapidly deposited into the material leading to a more rapid material ejection. From the theoretical models point of view, the hydrodynamic motion of the matter under the laser irradiation can be ignored using short duration laser pulses and consequently no fluid dynamics is considered in the frame time of the laser-matter irradiation. One of the advantages of fs ablation compared to longer pulse length is that it offers a plasma with high temperature and density because the laser energy is delivered before significant thermal conduction occurs. The second advantage is that there is no interaction between the laser beam and the ablated plume, thus somehow simplifying the theoretical treatment of the whole process [Liu et al. 1997].

Wavelength. The laser wavelength is a very important parameter for the ablation process because it has a significant effect on the yield of the ablated particles. Generally, the ablation rate increases with decreasing the laser wavelength because a shorter wavelength offers a higher photon energy which may be more suitable for an efficient vaporization and ionization of the target. Also, the penetration depth of the laser in the material (defined as the inverse of the absorption coefficient) is shorter in the UV, which can reduce the thermal effects (subsurface heating, leading to droplets ejection) in nanosecond regime. Moreover, the reflection coefficient of the target surface is highly dependent on the laser wavelength, and consequently, since UV light has a lower reflectivity for many materials in comparison with the visible-infrared light, a shorter wavelength may increase the ablation rate through a better coupling of the energy into the target material [Stapleton et al. 2005, von Allmen and Blatter 1995].

Laser fluence. The fluence of a laser pulse has to be larger than a certain threshold to induce ablation. As said above, the generation of particulates during the PLD process is an important factor affecting the smoothness of the resulting film. In order to reduce the number of particulates on the deposited film, the fluence must be consequently decreased. Moreover, high fluence will induce high kinetic energy for plume species due to the so called Coulomb explosion that is detrimental for PLD thin

film growth because of the high-energy ion plasma plume bombardment causing the sputtering of the growing thin film. This phenomenon plays an important role in the ability to control not only of the morphology and the quality of the deposited thin films, but also the deposition rate.

Target-substrate distance. The target–substrate distance is a very important parameter because it influences the thickness and the physical properties (refractive index, resisitivity, porosity etc.) of the deposited thin films [Aruta et al. 2012]. Some previous results show that the refractive index decreases with distance due mainly to the appearance of some voids at longer distance. [Galca et al. 2011]. On the other hand, the increase of the target–substrate distance may improve the surface morphology as well as the reflectivity of the thin films [Mostako and Khare 2012]; the substrate-target distance influences the amount of the material reaching the substrate and consequently the balance between nucleation rate and grains growth.

Background gas. The ambient gas environment is commonly used as a moderator for the energetic plume species during the expansion time from target to substrate. It plays a critical role in the microstructure and quality of the thin films because it can thermalize the plume. This may strongly influence on the spatial distribution, deposition rate, kinetic energy, etc. Thus, the kinetic energy of the deposited particles may be easily controlled using laser ablation plasma expansion in inert or reactive gas atmosphere (where chemical reactions may occur). Consequently, some hydrodynamic models and experiments upon the expanding laser ablation plasma into vacuum or in background gas evidence the behavior of the heating, melting and vaporization, maximum evaporation rate and the evaporation depth of the target at various ambient pressures [Chen et al. 2006, Singh and Kumar 1998].

The expansion plasma plume at low pressure (mostly used in our studies) is adiabatic and relatively well described by the models. The interaction of the plume with higher pressure ambient gas is a far more complex dynamic process that involves deceleration and thermalization of the ablated species, as well as the formation of shock waves [Harilal et al. 2006, Stapleton et al. 2005, Anisimov et al. 1996]. In this regime, Rayleigh-Taylor instabilities may also occur, as result of the turbulent mixing phenomena between the expanding ablation plasma and the ambient gas [Anisimov et al. 1996]. Moreover, the plume lengths are quite different and a spatial confinement and slowing down of the expanding plume are observed: the larger the ambient

pressure, the shorter the plume length; the plume propagation in background gas can lead to the stopping of the ablated materials. In some cases, the materials can even move backward and several reflected shocks within the plume are evidenced [Harilal et al. 2006]; the plume expansion into radial direction becomes important with different ambient pressures. Thus, both the maximum vapor density and the maximum electron density seem to decrease more slowly at higher ambient pressures than at lower ambient pressures.

The pressure of the ambient gas in PLD substantially influences the characteristics of deposed thin films, especially upon the lattice parameters [Anisimov et al. 1996]. High relatively ambient pressure produces smaller lattice parameter and lower plasma temperature of ejected plasma compounds. Contrarily, the low ambient pressure produces both larger lattice parameters, high plasma temperature of ejected plasma compounds but also high vacancy concentration on the film may be obtained because of the bombardment of energetic species ejected by the laser beam.

The very ambitious work plan initially established aimed to a complete systematic study on the influence of all these parameters on the chalcogenide thin films growth by PLD. However, this "ideal" plan has been revised during the thesis because of "practical" considerations. For instance, the limited availability of some lasers (ps, fs), and also of most of the characterization instruments precluded the completeness of this study in some parts. Therefore, this work should be seen as a preliminary step in a comprehensive approach for the optimization of the PLD process related to the deposition of amorphous chalcogenide thin films. It opens nevertheless the way to future complementary studies based on a statistical (including parameter correlations) experimental design methodology.

22

Chapter II

Experimental methods

This chapter is intended to provide a complete overview of the apparatuses and experimental techniques employed in this work, as they have been used in the following Chapters III, IV and V.

II.1 Pulsed Laser Deposition set-up

II.1.1 Vacuum chamber

The depositions were performed in a cylindrical stainless steel vacuum chamber (~10 l volume, 30 cm height, 20 cm diameter) shown in Figure II.1.The chamber is evacuated to a base pressure of ~10^{-6} Torr by a 550 l/s turbomolecular pump (Agilent Technologies TV-551) placed in vertical position at the bottom of the chamber, coupled to a 12.6 m^3/h dry fore pump (Agilent Technologies TS-300). The turbomolecular pump can be isolated from the chamber by a manual gate valve (VAT). The pressure is measured by a full-range gauge (Pfeiffer, position F in Figure II.1). For some experiments, a buffer gas (Ar, N$_2$) was introduced into the chamber through a needle valve (position E in Figure II.1). Pressures in the range $1.2x10^{-6} – 7x10^{-2}$ Torr have been used in our studies.

The targets are placed on a micrometric precision XYZ stage and can be rotated with a motorized vacuum feedthrough (Caburn MDC). The targets are usually placed on a metallic target holder, which is electrically isolated from the rest of the experiment by a ceramic (alumina) block; in some experiments the substrate holder was biased by a dc source (see Chapter III).The substrate is placed parallel to the target; the target-substrate

distance can be adjusted in the range 0-10 cm. For some experiments the substrate was also rotated. A resistive heater (up to 600 °C) is available on the substrate holder, but it was not used in our experiments, as we were trying to deposit amorphous thin films of chalcogenides with low crystallization temperatures.

The ablation laser beam was usually incident at 45° on the target surface, entering the chamber through the window D in Figure II.1, with the substrate holder placed on port C. For some experiments, the laser beam entered through port C, also at 45° angle of incidence, but in this case the (rotating) substrate holder was placed on port D, and the target was placed on a home-made 45° holder, i.e. the target and substrate surfaces were always kept parallel. In this case the target was not rotated but moved in the XY plane with the micrometric stage. Finally, incidence at 0° was also used for some other experiments. More details on the exact deposition configurations used will be given in section II.1.4.
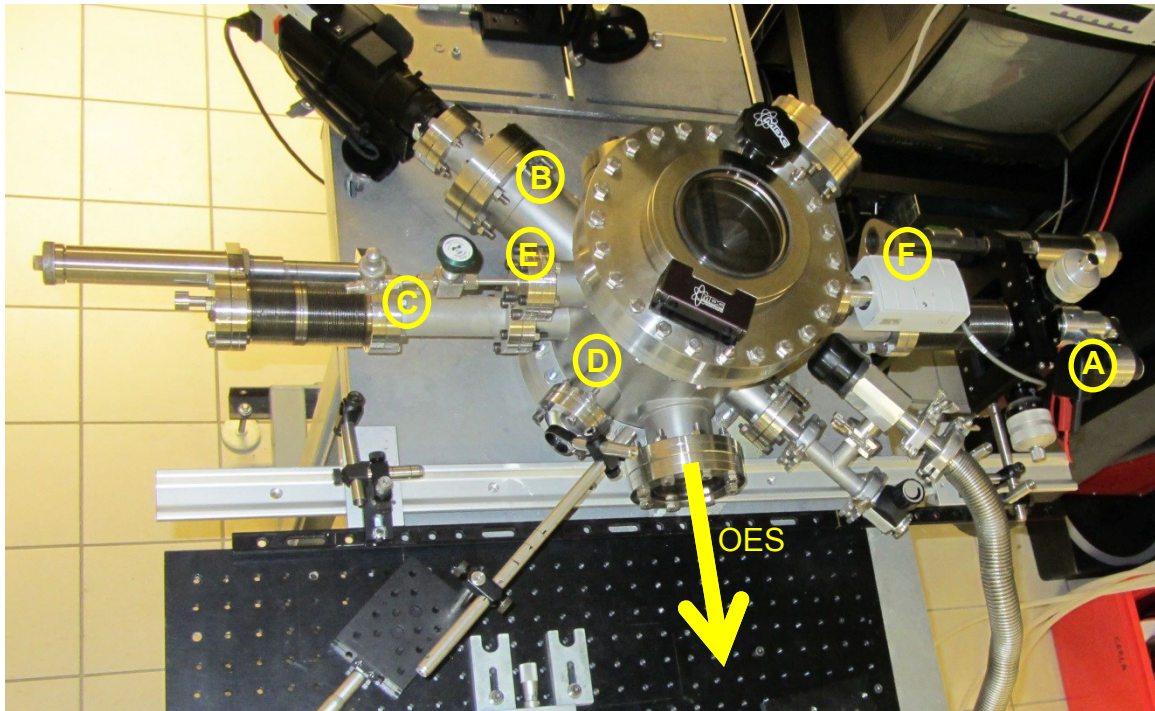
Figure II.1. Vacuum chamber used for PLD and OES experiments.

II.1.2 Targets and substrates

The targets were synthesized by P. Nemec at University of Pardubice (Czech Republic), using the classical melt-quenching method [Nemec et al. 2000] and high purity (5N) elements in evacuated and sealed silica ampoules. The materials used in these studies were GaLaS (GLS), GaLaS doped with Er^{3+} and Pr^{3+}, GeTe, Sb_2Te_3, $GeSb_2Te_4$ (GST124), $GeSb_4Te_7$ and $Ge_2Sb_2Te_5$ (GST225). The GST family can be unitary written as $(GeTe)_{1-x}(Sb2Te3)_x$, with x = 0, 1/3, 1/2, 2/3, and 1. The GST targets were polycrystalline, with a pronounced metallic character (due to Tellurium), while the GLS targets were glassy (some pictures are presented in Figure II.2). All the samples were polished prior to deposition.

Figure II.2. Pictures of typical targets used in the PLD process: GST (left) and GLS (right).

The nominal composition of the GST targets can be easily calculated using the chemical formula. For GLS glasses this is slightly more complicated as some amount of oxide (La_2O_3, between 0 and 3 mol%) must be added to the mixture in order to prevent crystallization. Consequently, for pure GLS targets the composition varied between 70 mol% (Ga_2S_3) + 30 mol% (La_2S_3) and 65 mol% (Ga_2S_3) + 32 mol% (La_2S_3) + 3 mol% (La_2O_3). In normalized atomic percentages this means: Ga between 26.5 and 28 at%, La between 12 and 14.2 at%, and S between 59.3 and 60 at%. The Er^{3+}-doped GLS targets were synthesized using 2 mol% Er_2S_3, leading to the nominal composition: Ga: 27.44 at%; La: 11.76 at%; S: 60 at%; Er: 0.8 at%. For the Pr^{3+}-doped GLS targets, two concentrations of dopant have been used: 0.2 wt% and 2 mol% of Pr_2S_3, leading to

nominal compositions: Ga: 27.96 at%; La: 11.98 at%; S: 60 at%; Pr: 0.06 at% and Ga: 27.44 at%; La: 11.76 at%; S: 60 at%; Pr: 0.8 at%, respectively.

Most of the depositions were made on crystalline Si substrates (MTI, p-type (B-doped), (100) orientation, 10x10x0.6 mm^3 dimensions, one-side polished, surface roughness < 5 Å). Circular masks (diameter 6-10 mm) have been used to define the deposition zone on the substrate (rectangular masks were also used for some depositions of larger dimensions, ~2-4 cm). For some (fewer) other experiments, the deposition was made on microscope slides (SiO$_2$ glass). Prior to deposition, the substrates were ultrasonically cleaned in acetone and isopropanol baths for 20 minutes.

II.1.3 Lasers

Two different lasers have been used in this study: a nanosecond Q-switched Nd:YAG (Continuum Surelite III-10) and a femto/picosecond mode-locked Ti:Sa (Spectra Physics). The nanosecond laser is able to generate four distinct wavelengths (harmonics) at 1064, 532, 355 and 266 nm, with maximum energy/pulse of 900, 430, 170 and 110 mJ, respectively, at a repetition rate of 10 Hz. The pulse duration is in the range 3-6 ns (depending on the harmonics employed), and the beam diameter is ~9 mm (for a divergence of 0.5mrad). The optical layout of this laser is shown in Figure II.3. A customized external optical arrangement allows attenuation of the beam energy of each harmonics and their propagation on the same output axis.
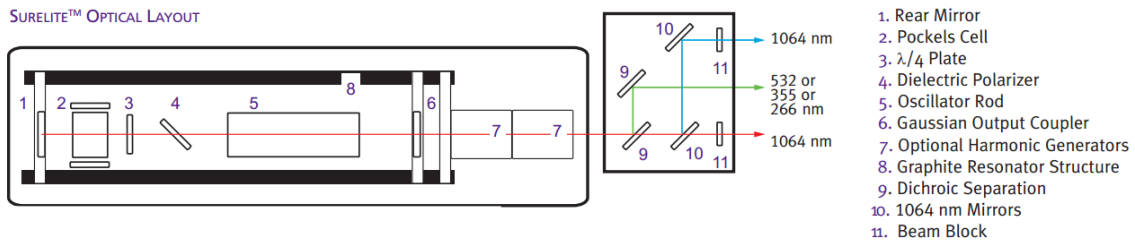
Figure II.3. Optical layout of the Nd: YAG nslaser (Continuum Surelite III-10).

For the ps and fs regimes, we used the Ti:Sa mode-locked amplified chain available (in shared access) in our laboratory. This type of laser uses the chirped pulse

amplification (CPA) technique introduced in the mid-80's [Strickland and Mourou 1985] in order to amplify the ultrashort laser pulse up to the petawatt level. The energy of a beam generated by a crystal Ti: Sa is of the order of the nJ, although the peak intensity is very high due to the short duration of the order of 25-30 fs. These pulses cannot be amplified because they cause non-linear effects in the gain medium and also damage the optical components. One must then reduce the peak intensity while keeping the same energy, this is achieved by stretching the pulse temporally using diffraction. Pulses spread to hundreds of ps and are then amplified (by up to nine orders of magnitude) by a regenerative amplifier. Following amplification, the pulse is compressed again thanks to the negative dispersion introduced by a second pair of diffraction gratings (see Figure II.4).
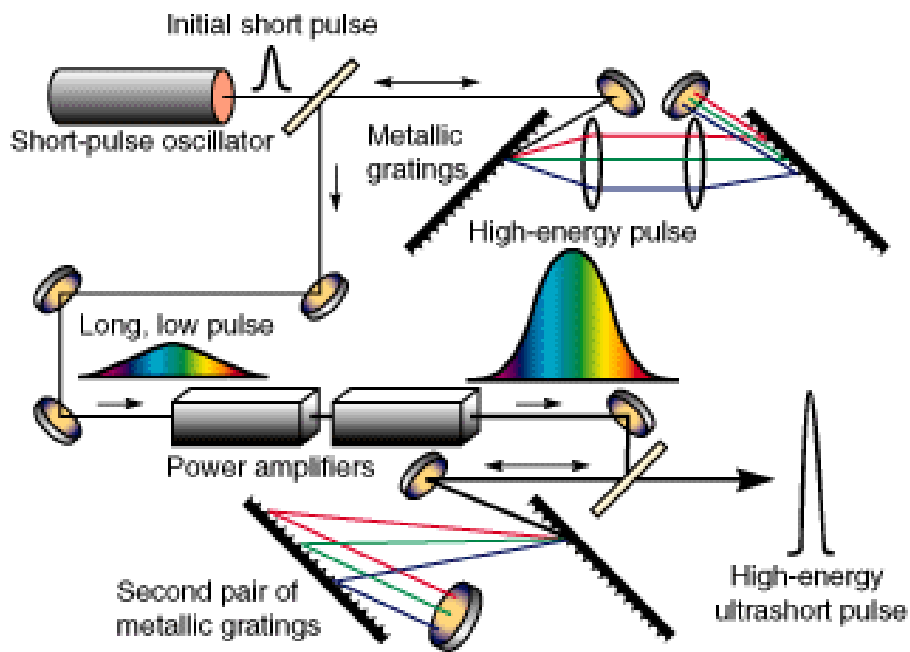
Figure II.4. Principle of the Chirped Pulse Amplification on the Spectra Physics fs/ps laser used in our laboratory.

The Spectra Physics chain available in our laboratory can work in three different temporal regimes, with pulse durations of 40 fs, 120 fs and 2 ps, with repetition rates up to 1 kHz. Among these, we used only the two last regimes (120 fs and 2 ps). The maximum energy per pulse available was ~2 mJ (for both regimes), for a beam diameter

of ~8 mm. The spectral bandwidths were ~10 nm (120 fs) and ~1 nm (2 ps), around the central emission wavelength of 800 nm.

The laser beams were focused on the target at 0° or 45° incidence by a CaF_2 plano-convex lens placed outside the vacuum chamber and entered this through a quartz window. Two different lenses have been used, with focal lengths of 25 cm and 15 cm, depending on the desired fluence. The dimensions of the irradiation spot on the target were varied by changing the distance between the lens and the target surface. The ablation fluence, which is the ratio between the pulse energy and the irradiated area, was varied by changing one of these two parameters or both. The laser energy/pulse was continuously monitored by pyroelectric joulemeters (Coherent or Ophir).

Fluence calculations

Calculating a precise fluence is quite easy for excimer lasers (which have a top-hat beam profile), but it is somehow more complicated for the lasers used in our studies, as they have a Gaussian-type profile (for instance, the matching of the Gaussian profile is 70% in near field and 95% in far field for the Continuum ns laser). This means that the effective fluence will be higher in the center of the focused beam than on its wings. Consequently, without using a beam profiler, one can calculate only an average fluence. In order to do this, we measured the impact spots on three different materials: on the target itself, on photosensitive paper and on aluminum targets (see some examples in Figure II.5). The impact spots were circular (for normal incidence) or elliptic with the ratio of the two diameters roughly equal to $\sqrt{2}$ (for 45° angle of incidence).

However, even this method is not completely justified, as the mark left by the beam on the photosensitive paper, or the crater drilled in the solid targets, correspond actually to the specific response of each material to the beam fluence. For instance if the material A has a higher "response" (ablation, marking) threshold than material B (see Figure II.6), then the measured "impact" area will be lower for A than for B, leading (with the same pulse energy) to higher fluence for A compared to B. Defining the "average" impact area is not easy in these conditions, especially for the photosensitive paper, as one can see from Figure II.5 (left side picture: the red ellipse defines the zone

where the paper is "burnt", while the blue ellipse defines the zone where the paper is "marked"). Depending on what impact area is considered, the calculated fluence can vary by more than 50% for a given laser energy/pulse. We thus warn that the fluences displayed in the following chapters are rather "indicative estimations" than precise values.
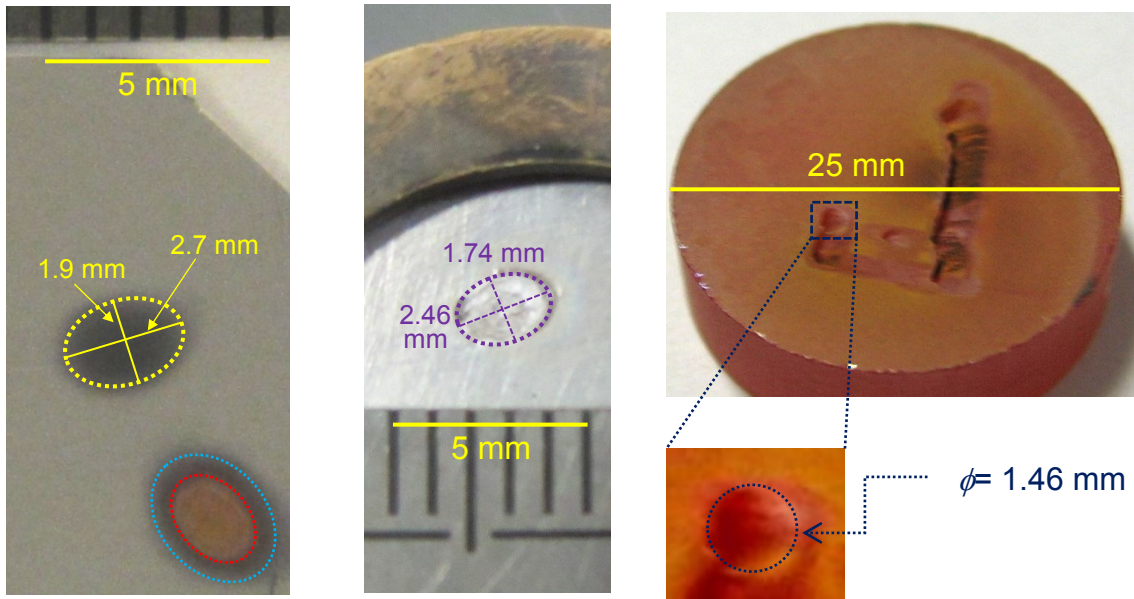
Figure II.5. Laser impact spots on photosensitive paper (left, AOI = 45°), aluminum (center, AOI = 45°), and GaLaS chalcogenide (right, AOI = 0°).
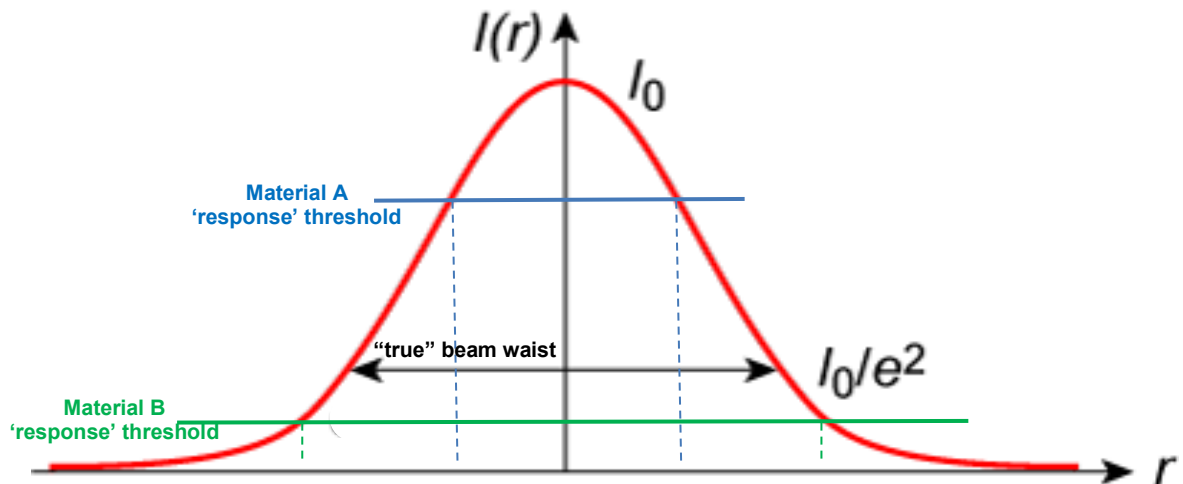
Figure II.6. Measuring the impact spot on two different materials for a laser beam with Gaussian intensity profile.

II.1.4 Deposition configurations

Three geometrically different configurations (summarized in Figure II.7) have been used. In configuration 1 (Figure II.7a), the substrate was placed (on port C in Figure II.1) in front of the target, parallel to it and on the same axis (i.e. the center of the substrate was on the normal to the target raised in the ablation point). The laser entered the chamber through port D (Fig. II.1) and was incident on the target at 45°. In order to ablate (as much as possible) from fresh target areas, this was continuously rotated and also translated from time to time along the X axis. Consequently, the laser ablated on circular tracks of various radii (see insets in Figure II.7a). The substrate was kept fixed in this configuration.

In configuration 2 (Fig. II.7b), the laser entered the vacuum chamber through port C, but was still incident as 45°, as the target was placed on a home-made holder inclined at 45°. The substrate holder was placed on port D. Consequently, the target and substrate surfaces were again parallel. The laser ablation point and the substrate center were on the same normal common to both surfaces. In this configuration, the target was not rotated, but moved in the XY plane to ablate fresh areas. In some experiments the substrate was kept fixed, while in others it was rotated.

Finally, in configuration 3 (Figure II.7c) we performed off-axis deposition (this was used only for the fs and ps regimes).This time the laser was incident at 0° (entering through port C) on the target rotated and translated along the X axis.The substrate (kept fixed) was placed on the 45° holder through port D, i.e. the target and substrate surfaces were parallel. However, the normal to the substrate in its center and the normal to the target in the ablation point were this time distant of 12 mm. Considering the target-substrate distances used in this configuration (20, 30 and 40 mm) leads to off-axis angles of about 31°, 22° and 17°, respectively.

Using these various configurations, a total of 120 samples were deposited on Si substrate (102 samples) and on SiO_2 glass (18 samples). From these, 46 were deposited in nanosecond regime, 9 in picosecond and 65 in femtosecond. Complete details on the deposition parameters will be given in each corresponding section.
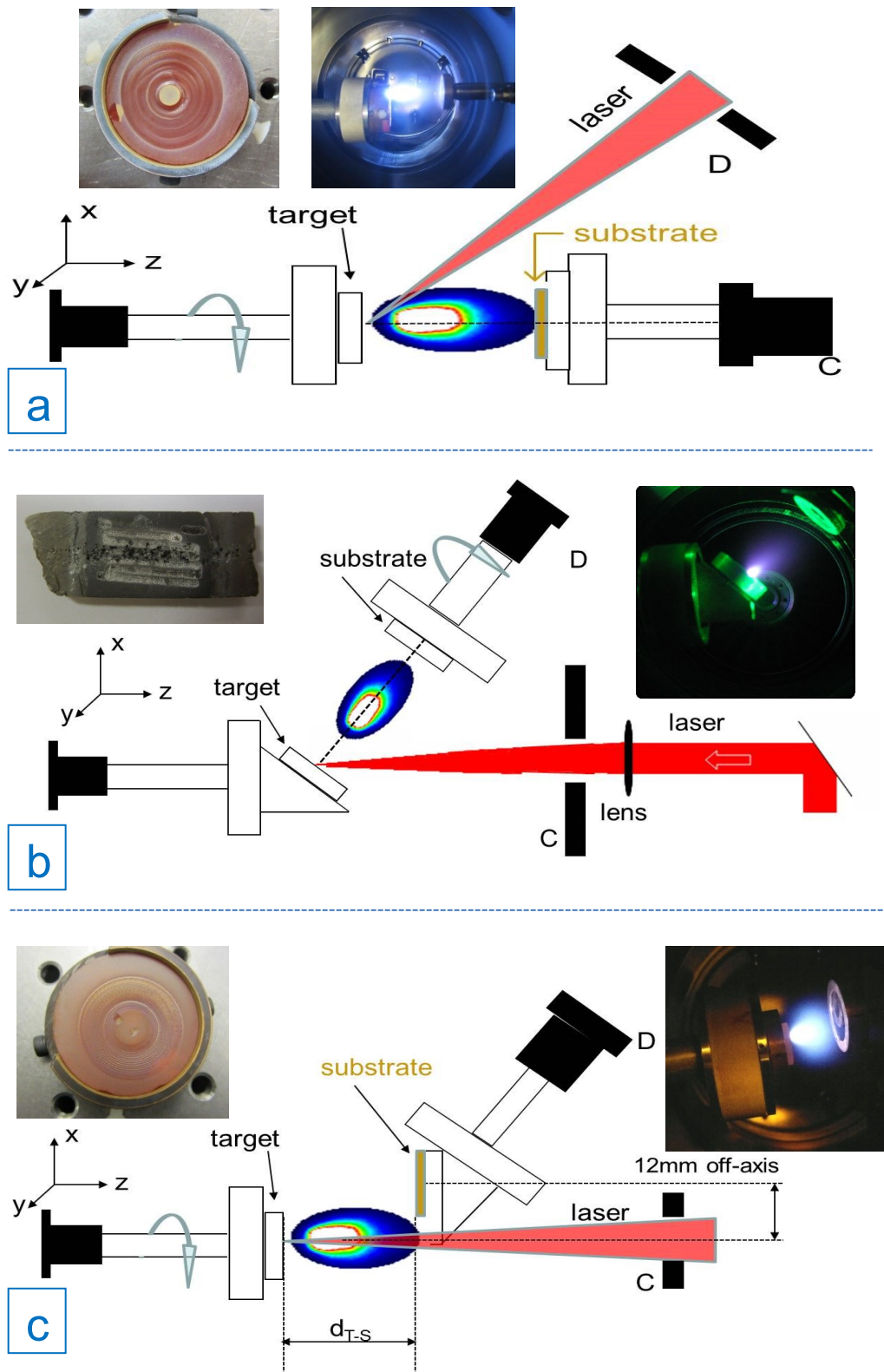
Figure II.7. Experimental set-up for a) configuration 1; b) configuration 2; c) configuration 3 (see text). Insets: typical pictures of ablated targets and deposition plasma in each configuration.

II.2 Optical characterization of the laser ablation plasma plume

For a better understanding of the processes connected with the PLD technique, in view of their optimization for amorphous chalcogenide thin film deposition, studying the dynamics of the plasma plume formed during laser ablation was appealing. We took advantage of the existence in our laboratory of an experimental set-up (see Figure II.8) connected to the PLD deposition chamber, which has been used previously for similar studies on other various materials [Nica et al. 2012, 2010, 2009, Ursu et al. 2010, 2009, Focsa et al. 2009, 2008, Gurlui et al. 2008].

The dynamics of the plasma plume has been studied by means of a high-resolution monochromator (Acton SP2500i, 500 mm focal length) and an intensified charge-coupled device (ICCD) camera (Roper Scientific PI MAX2-1003-UNIGEN2, 1024×1024 pixels, minimum gating time 2ns). The monochromator is fitted with one mirror and two diffraction gratings (300 l/mm, blazed at 300 nm, and 2400 l/mm, blazed at 240nm) mounted on the same three-position turret, which allows an easy switching between imaging, low-resolution, and high-resolution spectroscopy experiments (see below). The monochromator has an alternative exit port fitted with a photomultiplier (PM, Hamamatsu, 0.5 ns rise time) in order to record fast temporal profiles of a given spectral line. The PM output is sent to a fast digital oscilloscope (2 GHz, LeCroy). Figure II.8 also shows the presence of electrical devices for biasing the target and the substrate and for recording the induced transient currents. Moreover, Langmuir probes (connected to the fast oscilloscope) can be used for recording of these currents. However, electrical characterization of the plasma plume has not been performed in this thesis.

In order to obtain preliminary insight on the dynamics of the laser ablation plasma plume, ICCD sequential pictures of the spectrally unresolved plasma optical emission were recorded at various delays (typically between 20 and 1300 ns) with respect to the laser pulse. For these experiments, a Nikon objective was used to form the image of the whole plasma plume on the ICCD array through the kinematic entrance slit (12 mm x 12 mm opening) of the spectrometer and with the turret fixed in the mirror position. The ICCD camera was triggered on the TTL output of the ablation lasers, and an internal routine was used to increment the delay between the laser pulse and the gate opening. For

this configuration, gate widths of 5 ns were usually employed, in order to catch as much as possible sharp temporal snapshots in the space-time evolution of the plume. Averaging on 20 snapshots for each delay has been performed.
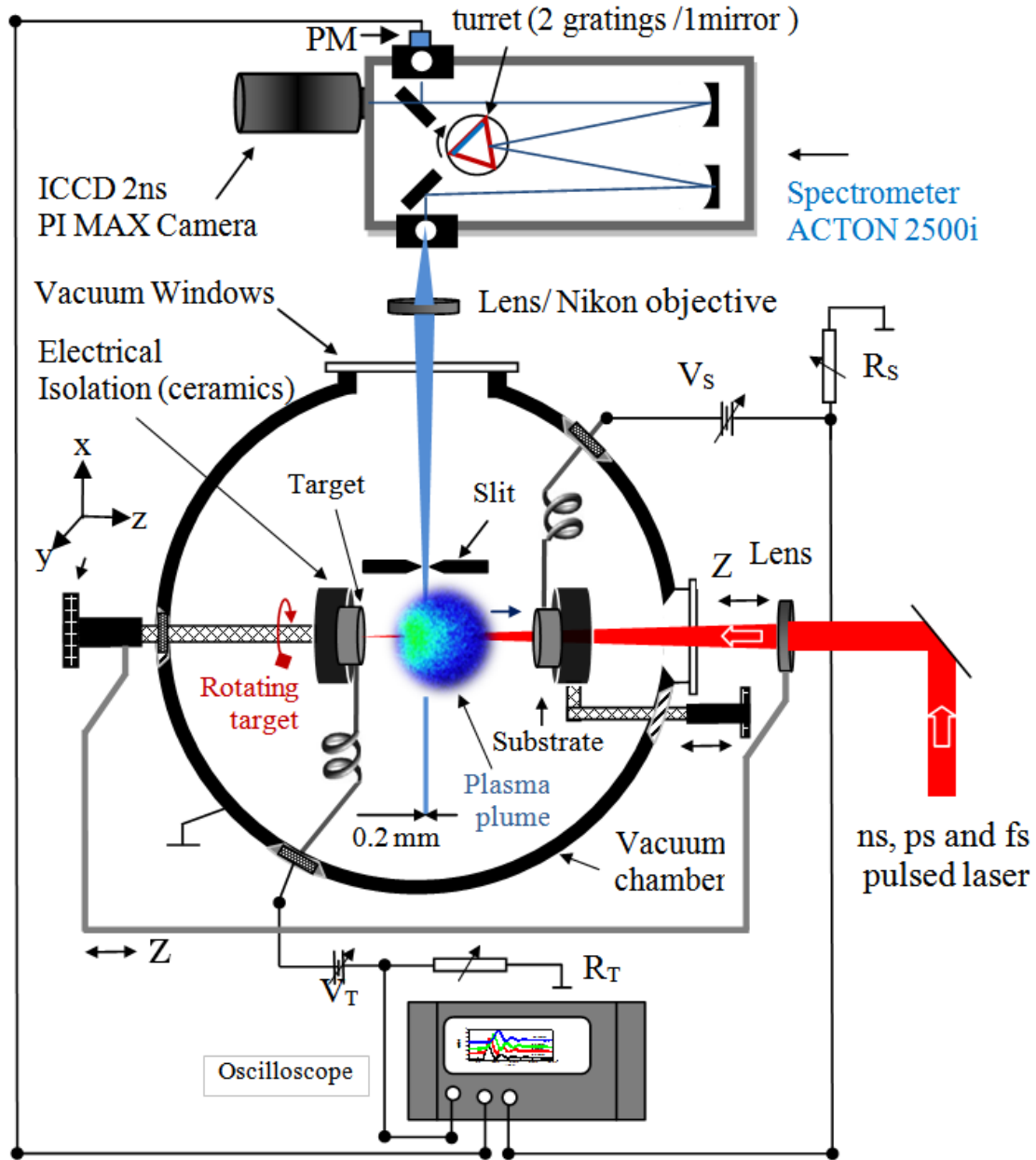
Figure II.8. Schematic view of the experimental set-up used for optical characterization of laser ablation plasma plume.

For spectrally resolved studies, the plasma plume emission was focused on the monochromator entrance slit by an f = 40 mm cylindrical lens (see Figure II.8). Low-resolution spectra were recorded using the 300 l/mm grating and a monochromator entrance slit width of 50 μm in order to identify the spectral regions of interest. In this configuration, ~80 nm broad spectra were recorded for a given position of the grating, with a spectral resolution of ~0.5 nm. Finally, the high-resolution spectra were recorded with the 2400 l/mm grating and a slit width of 50 μm, resulting in a spectral resolution of ~0.06 nm on ~8 nm broad spectra for a given grating position. The complete spectrum was obtained by using the "step-and-glue" procedure of the monochromator/camera software, which automatically increments the grating position once a given (80 nm or 8 nm wide) spectrum was recorded.

For space-resolved optical emission spectroscopy studies, a 1 mm × 5 mm slit was placed in the vacuum chamber, at 40 mm from the normal to the target (see Figure II. 8). This slit defined 1-mm width plasma plume "slices" parallel to the target surface, which were further imaged (~1:10 magnification) by the cylindrical lens on the monochromator entrance slit. The slit was maintained fixed and, for spatial scanning, we translated the target and the laser focusing lens as a whole (i.e. without modifying the distance between them), as they were both attached to the same XYZ micrometric translation stage. For all optical characterization experiments, the laser was focused by a f = 25 cm lens at normal incidence to the target, through a hole manufactured in the substrate holder (see above). This arrangement ensures the same ablation spot diameter on the target, i.e. the same fluence, for all the experiments performed. With this system, good spatial resolution (0.2 mm along the normal to the target, for a monochromator entrance slit of 20 μm) and S/N ratio (usually >100) have been achieved.

II.3 Characterization methods

The physical and chemical properties of the as-deposited thin films were investigated by various techniques. Preliminary information on the surface morphology of the samples was obtained using optical microscopy, stylus profilometry and scanning electron microscopy techniques. The chemical distribution of the constituent elements

was monitored by Energy Dispersive X-ray Spectroscopy and Time of Flight – Secondary Ion Mass Spectrometry. Moreover, Raman spectroscopy and X-Ray diffraction measurements were used to describe the structural arrangement of the elements in the deposited material. Very important characteristics of chalcogenide materials are related to optical parameters. With this aim, ellipsometry measurements were done to obtain information on the energy dependence of refractive index, extinction coefficient and optical band gap values. With the same goal, a few optical transmission measurements were also performed by using a spectrophotometer. This subchapter includes a brief description of all these techniques.

II.3.1 Preliminary investigations of the deposited films surface

II.3.1.1 Optical microscopy

A starting point in thin film investigation is to obtain information on the surface morphology of the deposited samples. A simple way to do that is by optical microscopy. This technique allows the user to obtain 2D images at different scales and can give an overall preview of the analyzed material. For the study of the thin films discussed here, we used a confocal optical microscope (Olympus) coupled to the Raman spectroscopy set-up (Renishaw) available in our laboratory (see below).

A simple representation of the confocal microscopy set-up is presented in Figure II.9. Using a lens or objective, the light source is focused on the sample. The image spot is then focused on the detector. The pinhole aperture placed between the microscope objective and the image plane rejects the residual scattered rays originated from any out-of-focus points on the sample and functions as a spatial filter, therefore the contrast of the image is substantially enhanced. Our images were obtained using the 50x objective (N.A. = 0.5, working distance 10.6 mm), which gives a lateral resolution of ~1 μm.
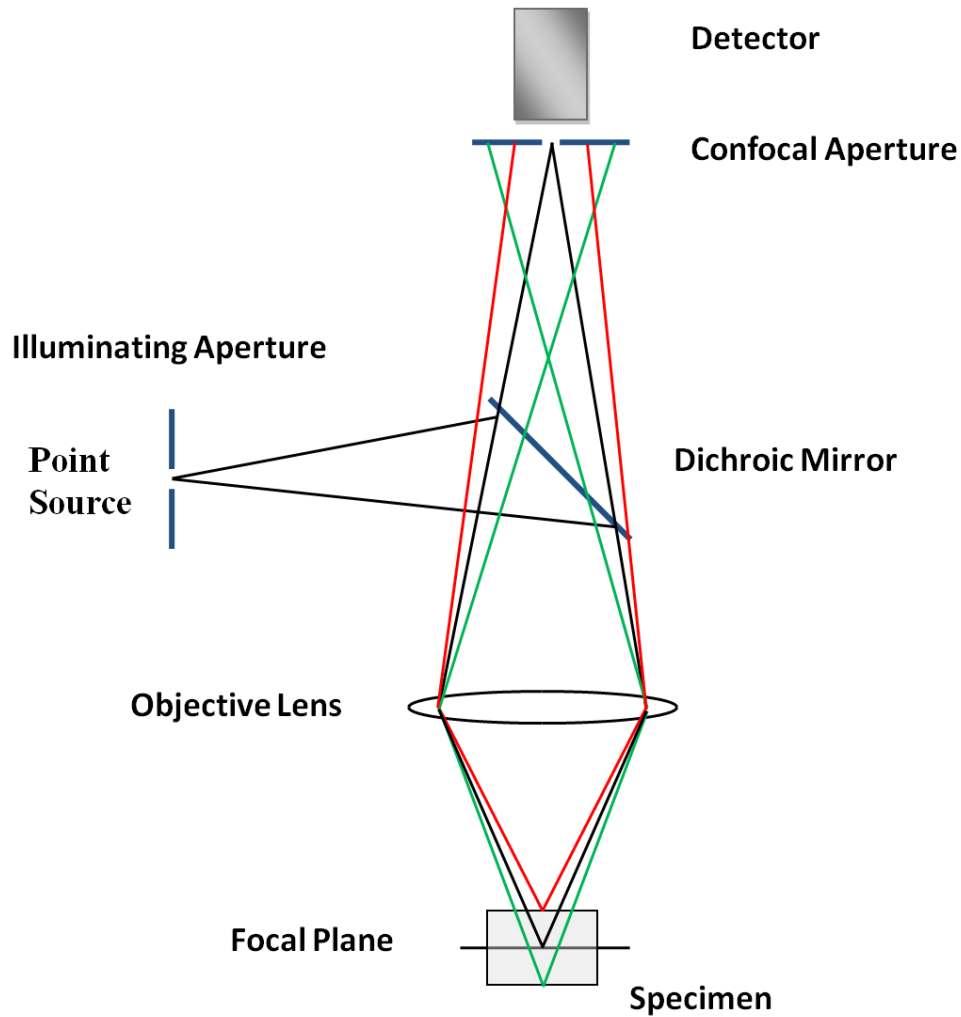
Figure II.9.   Confocal microscopy optical set-up (http://www.tcd.ie/Physics/ photonics/research/plasmon.php).

II.3.1.2   *Stylus profilometry*

An in-situ method to monitor the thickness of the deposited thin films such as the one using a quartz crystal micro-balance [Elam 2002] cannot be applied for PLD thin films due to the strong directionality of the plume generated at the interaction between the laser radiation and the bulk source material. In this case, stylus profilometry measurements can be performed ex-situ in order to investigate the roughness and thickness of the samples after deposition. This technique is based on monitoring the vertical displacement of a cantilever while it scans the sample surface (substrate and thin

film). For signal detection, optic or electric methods can be used. For the first case, a laser beam is focused on a highly reflecting region on the back of the cantilever. The cantilever motion will modify the reflection angle and thus the detector will register another spot position. This type of detection is also used in Atomic Force Microscopy set-ups. Another detection method in profilometry is based on the direct recording of electric signals upon cantilever motion. A block diagram together with annotated picture of the set-up is presented in Figure II.10.
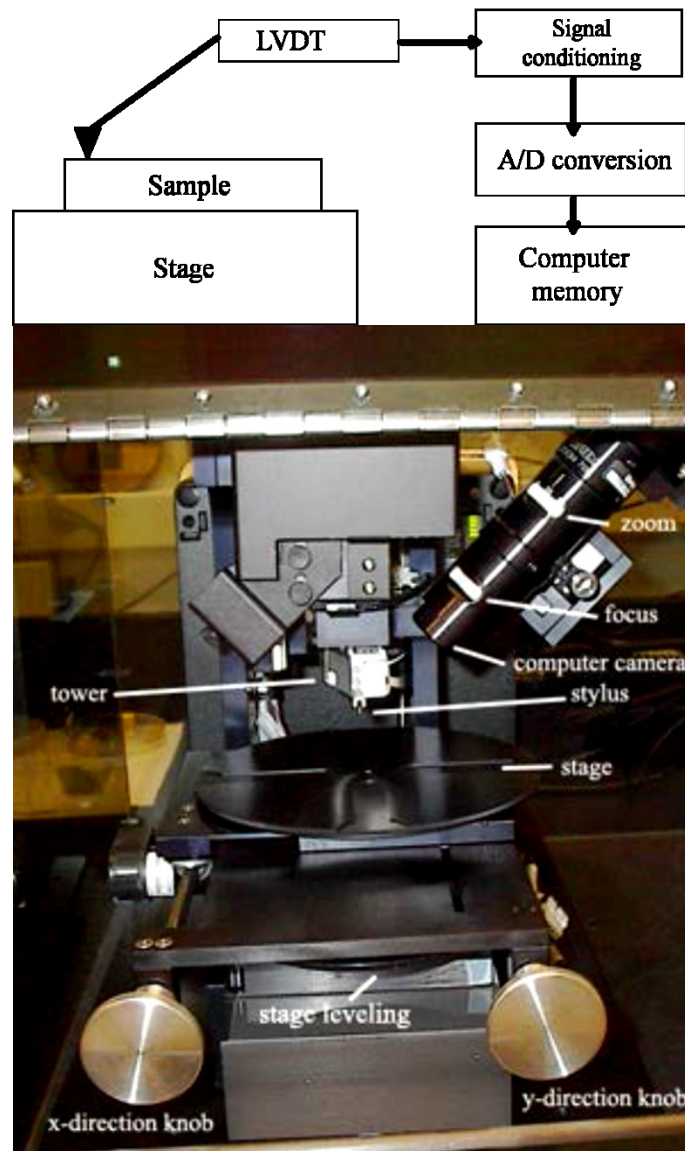
Figure II.10. Block diagram and annotated picture of the stylus profilometer Dektak 6M set-up.

In this configuration the measurements are done by moving the sample beneath a diamond-tipped stylus. The scan length, speed and stylus force during this displacement are controlled by a programmed high-precision stage. Upon a vertical translation of the stylus, the position of the linear variable differential transformer (LVDT) changes and proportional electric signals are induced in the detection circuit.

Three different instruments were used in this thesis: Bruker Veeco Dektak 3 (IEMN, Villneuve D'Ascq), Dektak 6M (LPGP, Orsay) and KLA Tencor Alpha-Step IQ (UMET, Villeneuve d'Ascq). For these three instruments, we used stylus forces of 5 mg, 3 mg and 38 mg, respectively. The stylus radii were 12.5 μm for the Bruker instruments, and 5 μm for KLA Tencor. Linear scans of ~ 10 mm length were performed over thin films diameters, with horizontal steps in the range 0.1 – 1.25 μm, depending on the instrument and the analyzed sample. Vertical resolution varied from 0.2 Å (KLA Tencor) to 10 Å (Bruker).

II.3.1.3   *Scanning Electron Microscopy*

A more detailed analysis of a surface can be done using Scanning Electron Microscopy. SEM provides a very wide, easily adjustable magnifications range and for most materials, minimal or no sample preparation is required. A comparison between the images obtained by SEM and an optical micrograph is presented in Figure II.11. A wide range of magnifications is possible, from about 10 times (about equivalent to that of a powerful hand-lens) to more than 500,000 time (about 250 times the magnification limit of the best light microscopes). These show the net advantage of SEM technique. Beside sample topography, other information can be obtained.
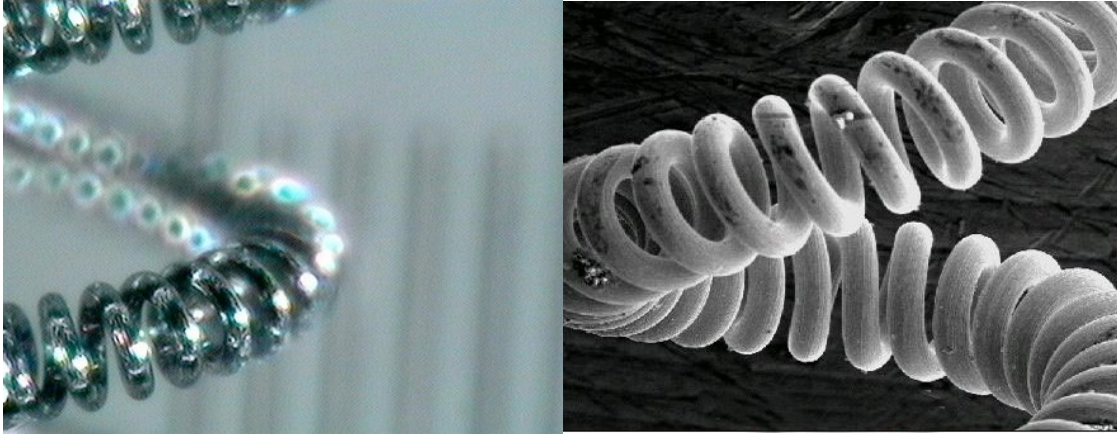
Figure II.11. Optical micrograph (left) and SEM image (right) of a tungsten filament (http://ion.asu.edu/descript_depth.htm).

For this measurement the analyzed material is placed in a vacuum chamber, where a beam of electrons is focused on its surface. As a result of the electron penetration into the outer layers of the surface, other electrons or photons are generated. Part of the emitted electrons is collected by a detector and then processed by a cathode ray tube. The incident electron beam is rastered over the sample surface to obtain a 2D image of the topography features. The x-y displacement of the cathode is synchronized with the voltages applied to the deflection coils that control the electron beam. A schematic description of a SEM set-up is presented in Figure II. 12. Depending on the nature of the elements collected, three types of images can be obtained: secondary electron images, backscattered electron images and elemental X-ray maps. The first two are separated according to the energy of the collected electrons. At the interaction between the initial electron beam and the sample atoms, inelastic or elastic scattering processes occur. The emitted electrons with energies less than 50eV are considered to be secondary electrons and are generated through inelastic scattering with an electron from the sample [Brundle et al. 1992]. Higher energy electrons are primary electrons and they are scatters elastically by the nucleus of an atom. Another possible interaction in SEM is the one when the primary electrons eject a core electron from an atom in the solid, through collisions. When the excited atoms decay to the ground state they will emit characteristic X-ray photons, which are then captured and analyzed to obtain additional information. These processes will be detailed in the next section.

The thin layer analysis using the scanning electrons microscope depends a lot on the electric conductivity of both chalcogenide material and substrate type. The samples must be conductive or coated with thin conductive layer compatible with the vacuum environment.
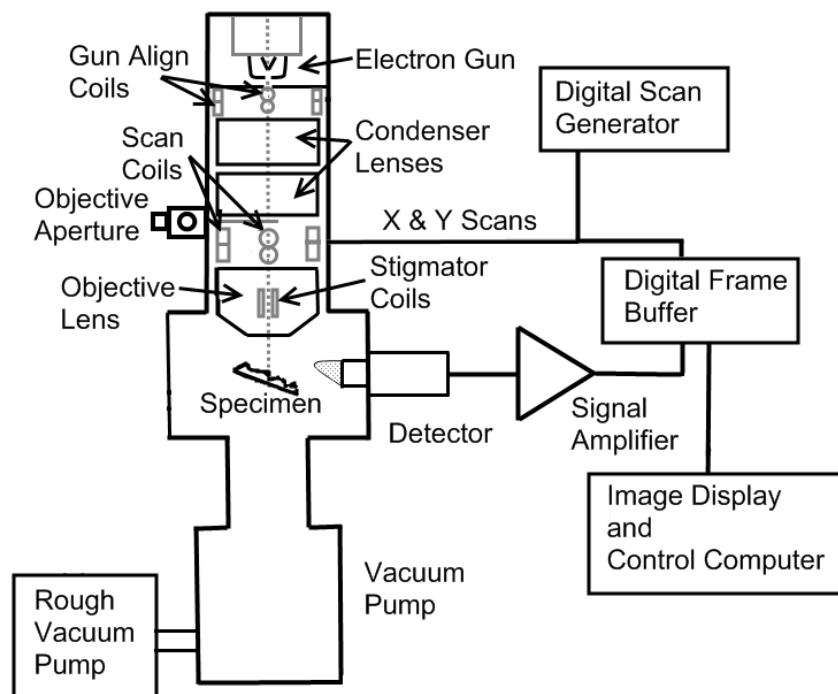
Figure II.12. Typical Scanning Electron Microscopy set-up.

As well as the EDS measurements, two scanning electrons microscope instruments were used in our studies: a) the SEM-Vega Tescan LMH II of Materials Science and Engineering Faculty, Gh. Asachi Technical University of Iasi, Romania [Cimpoesu et al. 2010a,b] and b) the SEM-JEOL JSM 6400 of Université de Rennes (Equipe Verres et Ceramiques, Institut des Sciences Chimiques de Rennes), France [Nemec et al. 2011a,b]. Specifications for both these instruments can be found in Table II.1. For the samples analyzed using the first mentioned instrument, conductivity connections were required. This was realized using a double carbon tape.

Table II.1 Specifications of the two instruments used for SEM/EDX analysis.

Specifications	Tescan Vega II LMH	JEOL JSM 6400
Resolution	3.0 nm at 30 kV	10 nm
Working vacuum	$< 10^{-2}$ Pa	
Magnification	4x to 1,000,000x	10x to 300,000x
Accelerating voltage	0.2kV to 30 kV	0.2kV to 40 kV
Scanning speed	From 160 ns to 10 ms per pixel	
Electron gun	Tungsten heated cathode	tungsten hair pin filament

In this thesis, 2D SEM images of the deposited thin films were obtained at various magnifications and accelerating voltages. Due to the large number of deposited samples and to various analyzing conditions, more details will be given in the respective sections.

II.3.2 Elemental composition

II.3.2.1   Energy dispersive X-Ray spectroscopy (EDX / EDS)

Chemical analysis in the scanning electron microscope is performed by measuring the energy and intensity distribution of x-ray signals generated at the interaction between a focused electron beam and the analyzed sample. The processes through which the X-ray production is realized were mentioned in the previous section. Here we will focus on the methods used to detect these radiations and how to obtain quantitative analysis on the concentration of each element present in the samples material.

The key component in an EDS instrument is a diode made from a silicon crystal with lithium atoms diffused, or drifted from one end into the matrix. Lithium is an n-type dopant which is used to compensate the relatively low concentration of grown-in impurity atoms by neutralizing them. The as-obtained n-p junction is an intrinsic semiconductor that can be enlarged by applying a biased field. A schematic description of the EDS set-up is presented in Figure II.13. The X-ray photons generated from the sample pass through a thin window that isolates the detector from the rest of the chamber and arrive to a cooled, reversed-biased p-i-n (p-type, intrinsic, n-type) Si(Li) crystal. Their absorption by the detector material leads to the ejection of photoelectrons which dissipate their energy in interactions that promote valence-band electrons to the conduction band, leaving holes in the once-filled valence-band. The charge carriers are

swept away by the bias field to form a charged pulse which is then converted to a voltage signal by using a preamplifier [Goldstein et al. 2003]. The response is than processed by a computer X-ray analyzer where a histogram of intensity by voltage is plotted. One should consider that the recorded signal is proportional to the energy of the incoming X-Ray photon. Apart from electron-hole pair generation, the energy deposited by the incident X-rays can be also dissipated by heat generation processes that induce leakage currents. To minimize this thermally induced background, the detectors are operated at low temperatures using liquid nitrogen cooling system.
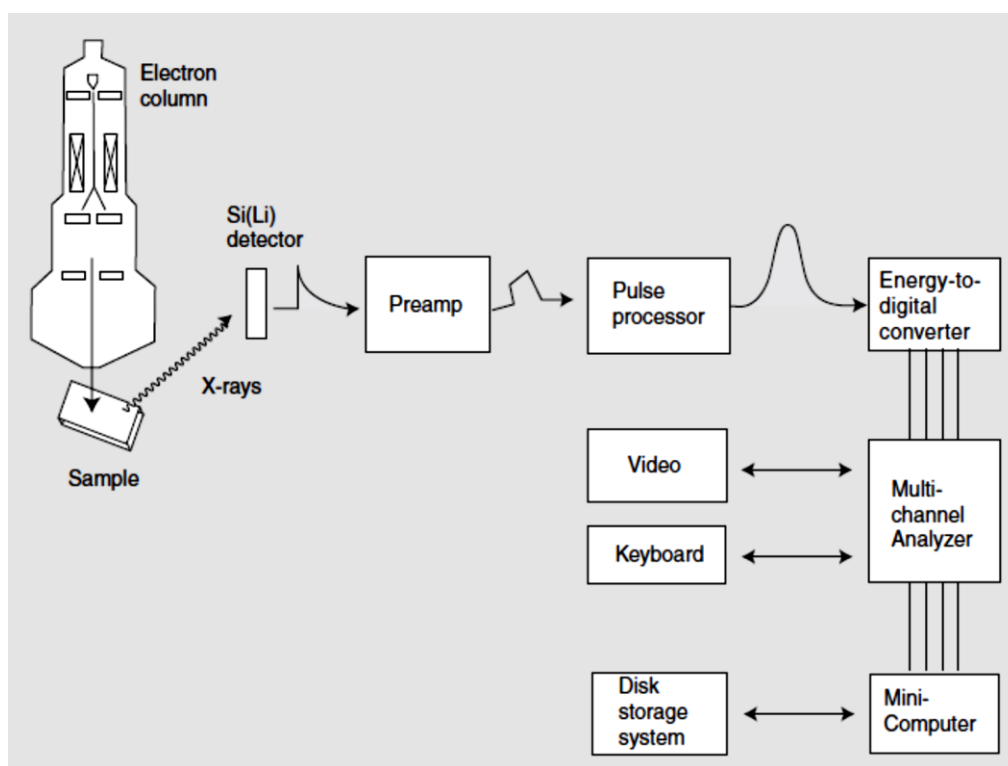
Figure II.13. Description of an EDS system [Vaughan 1999].

With modern detectors, EDS systems can detect X rays from all the elements in the periodic table above beryllium, if present in sufficient quantity. For elements with Z higher than 11 the minimum detection limit is as low as 0.02wt%, but only when the peaks are isolated and the spectra has at least $2.5 \cdot 10^5$ total counts. In general, however this limit is about 0.1wt%and could increase up to 1-2wt%if there is a severe peak overlapping. A high enough percentage is also observed for elements with Z lower than

10 when under the best conditions, this minimum detection limit is about 1-2wt% [Brundle et al. 1992].

For our EDS measurements, two instruments were used: JEOL JSM 6400 (Université de Rennes, France) and Tescan Vega II LMH (Technical University of Iasi, Romania). The accelerating voltages used during acquisition were 10kV and 30kV, respectively. Different analyzing conditions such as investigated surface size and de-excitation line series were used to obtain information on the chemical properties of the deposited chalcogenide thin films. These details will be given at each EDS result presentation.

The equipment has the possibility of three extra analyze modes for better conclusions on chemical sample aspects. In Point Mode a very small area is analyze based on the selected point using a 90x90 nm^2 investigation area for experimental results. Using the Line Mode user has the ability to follow the selected chemical elements variation on different lines from 500 nm to 5 mm longs. The Mapping Mode realize a distribution of selected chemical elements, based on them intensity and depth, on an individual selected area. The software presents the opportunity of combining the results in order to conclude the chemical nature of compounds or existing chemical bonds.

II.3.2.2   *Time of Flight – Secondary Ion Mass Spectroscopy*

Secondary Ion Mass Spectrometry (SIMS) is a technique that can detect very low concentrations of dopants and impurities and provides an interesting combination of extremely high sensitivity for all elements from Hydrogen to Uranium and above and high lateral resolution imaging. SIMS is based on the interaction of primary ions with energy in the keV range with a solid sample to generate secondary ions from the outer layers of the analyzed material (~10 Å). The resulting secondary ions are accelerated into a mass spectrometer, where they are analyzed by measuring their time-of-flight from the sample surface to the detector.

There are three different modes of analysis in TOF-SIMS:

 - mass spectra are acquired to determine the elemental and molecular species on a surface;

 - images are acquired to visualize the distribution of individual species on the surface

- depth profiles are used to determine the distribution of different chemical species as a function of depth from the surface (from a few Å to tens of microns).

When an energetic primary ion interacts with the sample, it penetrates into the lattice and hits many atoms on its trajectory. In a first approximation, inelastic collisions take place and the resulting "collision cascade" slows down the primary projectile until it is finally implanted in the lattice. The momentum transfer to the sample atoms destroys the original molecular arrangement of the elements. As the collision cascade propagates inside the sample, some of the elements from the outer layers receive an impulse. Once the transferred energy becomes greater than the binding energy, particles from the surface are removed. Most of these particles are neutral, but ions are ejected as well. The unbalance between the incoming and outgoing charges inevitably alters the surface potential of non-conductive samples and the proper functioning of the instrument is affected. Thus a neutralization of the sample surface is necessary, neutralization that can be done by using an electron flux [Straub et al. 2010]. Figure II.14 presents the basic working principle of a ToF-SIMS apparatus. When a high primary ion current density is used, the outer sample layer is rapidly consumed and secondary ions are generated from underlying layers, where intensive atom relocation has taken place.

In ToF-SIMS the detection is realized by separating the ions that are generated at the same moment from the sample surface, according to the m/z ratio. To obtain the maximal mass resolution, all ions must be generated from the same point in the acceleration field. The introduction of an ion reflector (at half of the drift tube) allows the difference in flight time for ions with the same m/z (started at the same time) but with different energies to be compensated at the point of detection [Bexell 2003, Grehl 2003]. Ions with higher energy penetrate deeper into the reflective field and thus spend more time on a longer path than the ions with less energy. In this way, the peak width is reduced and mass resolution is increased [Vickerman and Briggs 2001].
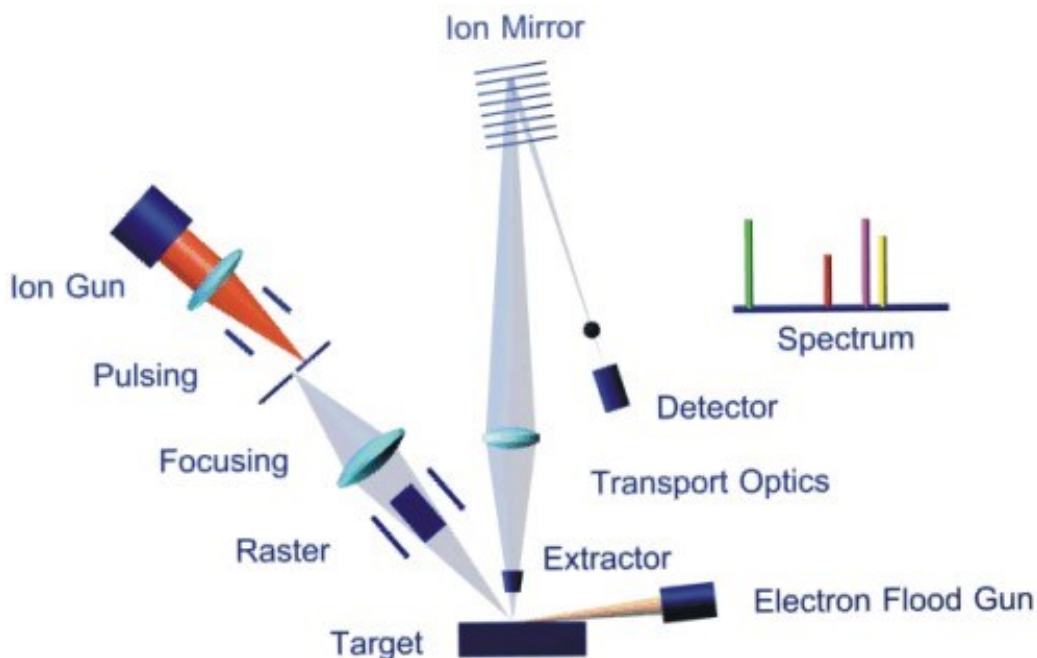
Figure II.14.   Schematic representation of the TOF-SIMS technique [© ION-TOF
                      GmbH].

        The principal impediment in a quantitative analysis is the fast variation of the
ionization efficiency that depends on many parameters. But relative quantitative
information can be obtained by comparing the spectra or by analyzing the intensity ratios.

        The thin films discussed in this thesis were analyzed using an ION-TOF 5 SIMS
instrument (Unite de Catalyse et Chimie du Solide, Université Lille 1) with a mass
resolution (m/Δm) of 10^4 and a depth resolution of ~1nm. The field of view can be varied
from μm² to cm² range with a lateral resolution <100nm. For depth profile recording, two
types of ion beams can be used (Cs and O_2) and the sputtering speed can be increased up
to 10μm/h. For analysis a Bi primary gun is used (Bi^+ or Bi_3^+ ions).

        The ToF-SIMS images were acquired by analyzing a 500x500 μm area in positive
or negative polarity (for some samples a 300x300 μm area was analyzed). For depth
profiling, either the O_2 (for positive polarity analysis), or the Cs (for negative polarity
analysis) ion beams (typical parameters 1 kV, ~100 nA) were used to "dig" a crater in the

film (usually 300x300 µm square section) and during the process an inner (centered) surface (usually ~100x100 µm) was analyzed with the Bi ion beam (typically 25 kV, ~1 pA).

II.3.3   Structural characterization

II.3.3.1   Raman spectroscopy

Raman spectroscopy is a non-destructive technique which can be used to identify the chemical bonds present in the analyzed material and can provide information on the amorphous or crystalline nature of the samples. In different conditions, a quantitative analysis can be achieved. IR spectroscopy and Raman spectroscopy are techniques based on the investigation of vibrational modes of the molecules in a crystal but they rely on different processes in which the energy of the incident photon is transferred to the chemical bond. The IR spectroscopy considers the transitions between two vibrational energy levels as a result of IR radiation absorption. In Raman spectroscopy, a much wider wavelength range can be used for analysis as this technique is based on the frequency displacement between the incident and the scattered radiation [Larkin 2011]. The main process is the inelastic scattering of an incident photon which loses part of its energy by transferring it to the molecule vibrations. The remaining energy is scattered as a phonon with lower frequency. To observe the Raman spectrum, it is necessary to separate the collected Raman scattered light. In dispersive Raman instruments, this is accomplished by focusing the Raman scattered light onto a diffraction grating, which splits the beam into its constituent wavelengths. These are directed onto a silicon charge-coupled device (CCD) detector. Figure II.15 gives a schematic representation of the Raman spectroscopy set-up. Dispersive Raman spectroscopy uses excitation radiations in the UV-visible spectral range and has a (best) spatial resolution of ~1µm, thus being able to detect even sample contamination. The recorded Raman signal is proportional to $1/\lambda^4$, hence lower excitation wavelengths can give better results, but in these conditions, fluorescence processes are most likely to occur.

Contrary to other techniques, Raman scattering spectroscopy measurements can be applicable for microscopic region characterization even if these are located inside of a

transparent material. No special treatment of the sample is needed and the ability to carry out the analysis in the open air or controlled atmosphere represents an important advantage.
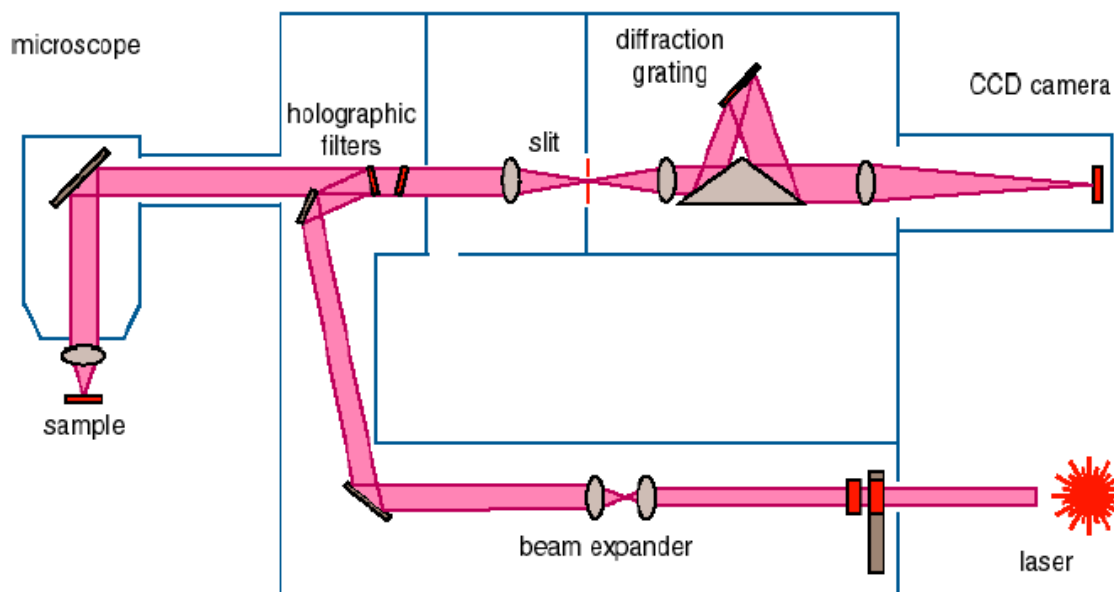
Figure II.15. Optical layout of the Renishaw inVia Reflex Raman confocal microscope and spectrometer (© Renishaw).

In our case, the Raman spectroscopy measurements were performed using an InVia Reflex spectrometer (Renishaw, 250 mm focal length), which includes an Olympus BXFM free-space confocal microscope. Spectral positions were calibrated against the silicon line yielding a stable value of 520.4 ± 0.3 cm^{-1}. The experiments were carried out at room temperature with two excitation radiations of $\lambda = 514.5$ nm produced by an air-cooled Ar^{+} laser source (Modu-Laser, Stellar-pro) and $\lambda = 785$ nm produced by an air-cooled High Power NIR Diode Laser (300 mW). Raman shifts can be measured at excitation wavelengths of either 514.5 nm or 785 nm with a spectral resolution of ~1 cm^{-1} and 0.05 cm^{-1} repeatability. An Olympus 50× objective (0.5 N.A.) was used for our measurements.

Due to the fact that Raman spectroscopy is a technique sensitive to local ordering and as these materials are susceptible to rather low temperatures, the vibrational spectra were recorded at different excitation laser powers (for 785 nm wavelength) and in

different regions of the samples. Another reason for excitation laser power variation was to determine the optimum excitation laser characteristics for acquisition so that no modifications in structural properties of the samples are induced. The excitation laser power at the sample surface was measured by a Lasercheck powermeter (Coherent). The excitation laser power was varied in the range 0.18 - 36mW. However, the irradiance calculation proved to be rather difficult. We measured the dimension of the laser spot imprinted on the sample surface, after analysis, at different excitation power densities. Due to the initial rectangular geometry of the laser beam we did not observe a perfect circular spot, but rather an elliptical one. As observed for the fluence calculation upon laser ablation, it is difficult to specify an exact value of the irradiance. The dimension of the interaction area on the sample surface depends on the optic and structural properties of the deposited material. The threshold intensity value for a visible surface mark differs from one material to another. For low excitation laser powers (e.g.: 1.36 mW), no imprint induced by the 785 nm radiation action was detected while for the 4.4 mW and 36 mW excitation laser powers the spot dimensions were 2.5 μm/9.3 μm and 5 μm/18.6 μm, respectively giving areas of 18.25 and 73 μm^2. Using the measured area values, we estimated a power density of 0.241mW/μm^2 and 0.493mW/μm^2.

The changes in as-obtained Raman spectra indicated an evolution in crystallinity as the excitation energy was increased. The differences were not only related to peak position but also to the appearance of other bands. To investigate the influence of the temperature generated by the high excitation laser power (36 mW), the same area was re-analyzed using a lower intensity of the laser radiation. Considering that no quantitative information was achieved, some spectra were normalized to the maximum peak intensity value for a better representation. All spectra are baseline-corrected, and the peak positions of the collected spectra were determined using a least-squares fitting procedure.

II.3.3.2   X-Ray diffraction

The X-ray diffraction (XRD) is a technique used to obtain information on the crystalline structure of a sample. Various types of materials can be analyzed: bulk samples, powders or thin films. This type of investigation is based on the interference

process of spherical waves generated by the atoms periodically arranged in the crystal when a monochromatic X-ray beam is focused on the material. These re-emitted waves interfere with each other either constructively or destructively producing a diffraction pattern on a detector. For a constructive interference, the XRD pattern will present diffraction lines characteristic to a type of structure. If the used wavelength is close to the inter-atomic distances, the diffraction direction is described by Bragg's law:

$$2d \sin \theta = n\lambda \qquad\qquad\qquad (II.1)$$

where n is a integer and λ is the wavelength of the incident radiation, d is the spacing between the planes in the atomic lattice, and θ is the angle between the incident ray and the scattering planes.

Depending on the geometry of the system, two configurations can be used: $\theta - \theta$ or $\theta - 2\theta$. In $\theta - \theta$ configuration, the X-ray tube and detector rotate at an θ angle related to the sample surface (which is fixed). This set-up is used when analyzing samples at different temperatures where the cryostat or heating devices need to be kept still during the measurements. For the second mentioned configuration, the X-ray tube is fixed, while the sample holder and detector are rotated with θ and 2θ respectively. The latest XRD models allow an analysis in both configurations.

In most cases, the $\theta - 2\theta$ geometry (called the Bragg-Brentano geometry) is used. Figure II.16 presents a schematic representation of this configuration. The phase identification is done by comparing the experimentally obtained diffraction patterns with the ones recorded in the database. Beside the determination of the crystalline structure, several other characteristics can be obtained by this technique: quantitative analysis of different phases, phase change study, determination of internal stress etc.

For the samples discussed in this thesis, the XRD data were obtained at the Faculty of Chemical Technology, University of Pardubice, Czech Republic by means of a D8-Advance Diffractometer (Bruker AXS, Germany) in Bragg-Brentano geometry using CuKα radiation (λ = 0.15405 nm, 40 kV, 40 mA) [Nemec et al. 2011a,b]. The patterns were recorded in the 5-65° 2θ region.
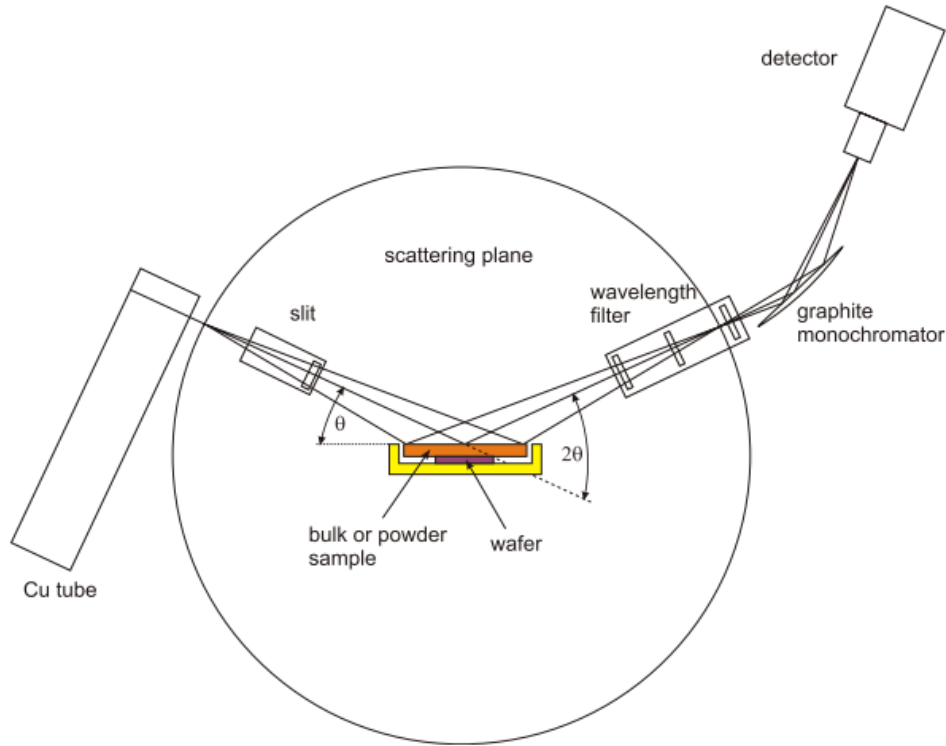
Figure II.16. Schematic representation of the Bragg–Brentano geometry of the X-ray diffractometer [Gilles et al. 2006].

II.3.4 Optical properties

II.3.4.1   Variable angle spectroscopic ellipsometry

As mentioned in Chapter I, chalcogenide materials are used in various applications that rely on their optical properties. These characteristics can be analyzed by ellipsometry, which measures the change in polarization of light upon reflection on the sample. The advantage of this technique is the simultaneous measurement of both the amplitude ratio upon reflection (tan Ψ) and phase difference (Δ) of orthogonally polarized light, more exactly between the normalized components s (oscillating perpendicular to the plane of incidence) and p (oscillating parallel to the plane of incidence) of the reflected light (Figure II.17).
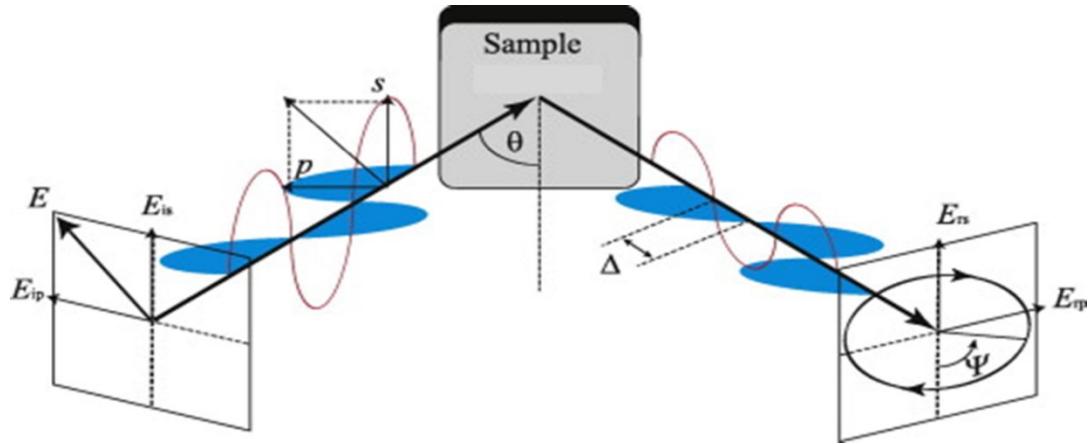
Figure II.17. Representation of the ellipsometric measurement geometry [Oates et al. 2011].

These measured parameters can then be used to calculate the real and imaginary parts of the dielectric function, ε_1 and ε_2. Having these parameters established, one can further calculate the extinction coefficient (k) and refractive indexes (n) using the following set of equations [Nemec et al. 2009a, Xu et al. 2008]:

$$k = \left\{ \left[\left(\varepsilon_1^2 + \varepsilon_2^2 \right)^{1/2} - \varepsilon_1 \right] / 2 \right\}^{1/2}$$

$$n = \left\{ \left[\left(\varepsilon_1^2 + \varepsilon_2^2 \right)^{1/2} + \varepsilon_1 \right] / 2 \right\}^{1/2}$$

$$(II.2)$$

Variable Angle Spectroscopic Ellipsometry (VASE) performs the above mentioned measurements as a function of both wavelength and angle of incidence. Further information that can be obtained using this technique is related to sample thickness and optical band gap determination. To obtain correct near-gap and above-gap optical responses, the imaginary part of the dielectric function is calculated as the product of variable band edge function and Lorentz oscillator function. For amorphous semiconductors, two such band edge functions were found to best characterize the optic response [Nemec et al. 2009a]. One of them (which was used to study our samples) is called the Cody-Lorentz model [Ferlauto et al. 2002, Orava et al. 2008, Nemec et al. 2011a] and describes the imaginary part of the dielectric function in the entire measured spectral ranges:

$$\varepsilon_2(E) = \begin{cases} \dfrac{E_1}{E} \exp\left\{\dfrac{(E-E_t)}{E_u}\right\}, \ 0 < E \le E_t \\[4mm] G(E)L(E) = \dfrac{\left(E - E_g^{opt}\right)^2}{\left(E - E_g^{opt}\right)^2 + E_p^2} \dfrac{ACE_oE}{\left(E^2 - E_o^2\right)^2 + C^2E^2}, \ E > E_t \end{cases} \qquad \text{(II.3)}$$

where A is the amplitude (oscillator strength), E_o - the peak transition energy, E_g^{opt} - the optical band gap energy, C - the broadening, E_p - the transition energy separating the absorption onset from the Lorentz-oscillator behavior. E_t represents the demarcation energy between the Urbach tail transitions and the band-to-band transitions [Nemec et al. 2009a]. All these parameters (including sample thickness also) are adjusted in a least-square fitting procedure to describe the experimental data.

Optical properties of some thin films synthesized in this thesis were obtained from spectroscopic ellipsometry analysis performed by P. Nemec at the Faculty of Chemical Technology, University of Pardubice, Czech Republic, using an ellipsometer with an automatic rotating analyzer (VASE, J. A. Woollam Co., Inc.). The refractive indices and extinction coefficients were monitored in the 300–2300 nm spectral region (i.e. 4.13–0.54 eV). The incident angle variation for this type of ellipsometer can be modified automatically in the 15°-90° range with accuracy of 0.01°.

II.3.4.2   *Spectrophotometry*

For some samples deposited on SiO_2 glass, transmission measurements were performed using an Agilent Cary 5000 UV-VIS-NIR spectrophotometer available in our laboratory (Figure II.18). These measurements are based on the well-known Beer-Lambert law:

$$T = \frac{I_t}{I_0} = e^{-\alpha d} \qquad \text{(II.4)}$$

where T is the transmission, I_t and I_0 - the intensities of the transmitted and incident beams, respectively, α - the optical absorption coefficient, and d – the sample thickness.
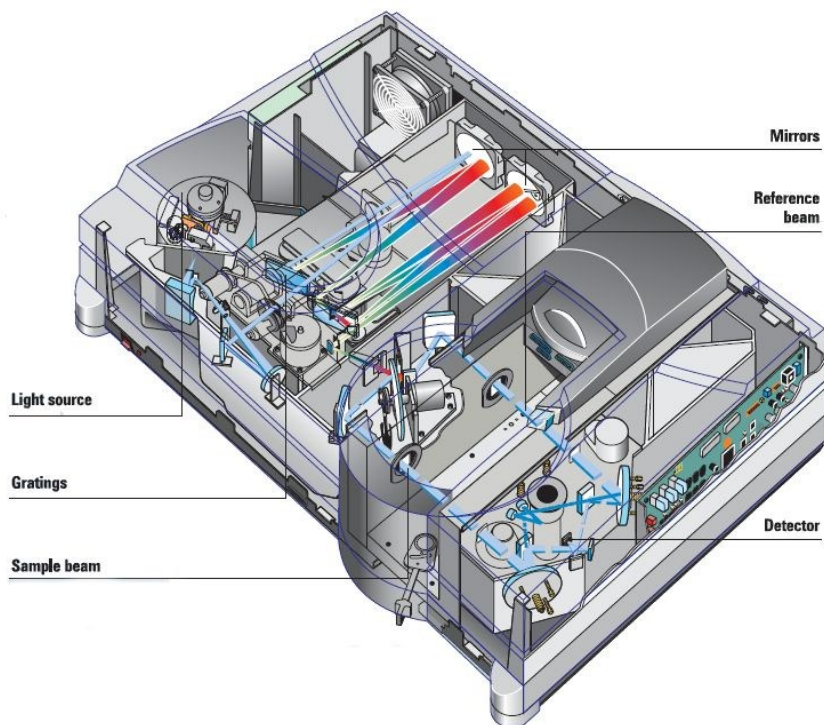
Figure II.18. Agilent Cary 5000 UV-VIS-NIR spectrophotometer.

The Cary 5000 apparatus is a double-beam spectrophotometer, able to work in the range 200 – 3300 nm, with a limiting resolution of 0.05 nm in UV-VIS and 0.2 nm in NIR range, wavelength accuracy of ±0.1 nm in UV-VIS and ±0.4 nm in NIR, and wavelength reproducibility of 0.025 nm. We recorded transmission spectra of thin films in the spectral range 300 – 2500 nm, in 2 nm steps. The contribution of the substrate (absorption, reflections) was removed by recording a "baseline" spectrum with a "blank" substrate (i.e. without any film deposited on it). This baseline was then used as 100% transmission reference in the recorded spectra, thus giving only the contribution of the thin films.

Because of the μm-range thickness of the samples, interference fringes occur in the spectra (one example can be seen in Figure II.19). By measuring the wavelength positions of the maxima and minima, and knowing the value of the refractive index on a given spectral range, one can get an approximate value of the sample thickness. With this, the values of the refractive index can be further calculated on an extended spectral range. Inversely, if the exact value of the film thickness is known from another

measurement (e.g. profilometry), the refractive index can be calculated for the wavelengths corresponding to the fringes maxima and minima, and then an interpolation procedure can be applied.
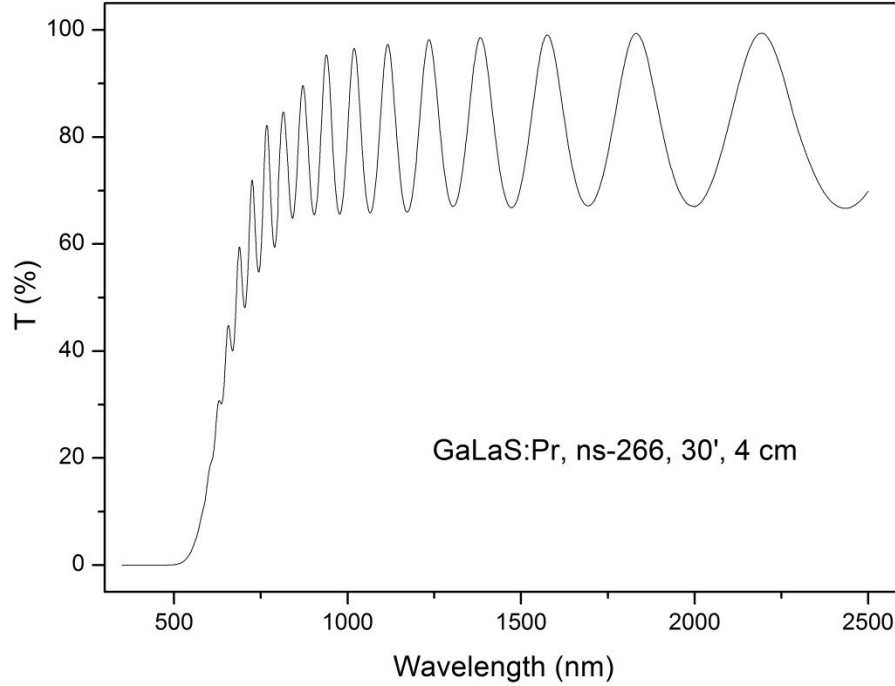
Figure II.19. Transmission spectrum of a PLD deposited GLS chalcogenide thin film (SiO$_2$ substrate).

These calculations are based on the well-known interference formula:

$$2nd = m\lambda \qquad \text{(II.5)}$$

where n is the refractive index, d – the film thickness, m – the interference order (integer for maxima, half-integer for minima) and λ is the wavelength. As we don't know the actual m value for a given maximum or minimum, we note:

$$m = m_0 + X \qquad \text{(II.6)}$$

where m_0 is an integer to be determined from the fit and X = 0, 0.5, 1, 1.5, … for the successive maxima and minima observed, when going from higher to lower wavelengths. The equation (II.5) becomes:

$$X = -m_0 + (2nd)\frac{1}{\lambda} \qquad \text{(II.7)}$$

54

By representing X as a function of $1/\lambda$, one can get m_0 from the ordinate at origin. An example is given in Figure II.20. As n is a function of λ, care must be taken in calculating the slope and the intercept only for the first points (at high λ, where n is approximately constant). The deviation from linearity at lower wavelengths can be seen in Figure II.20.
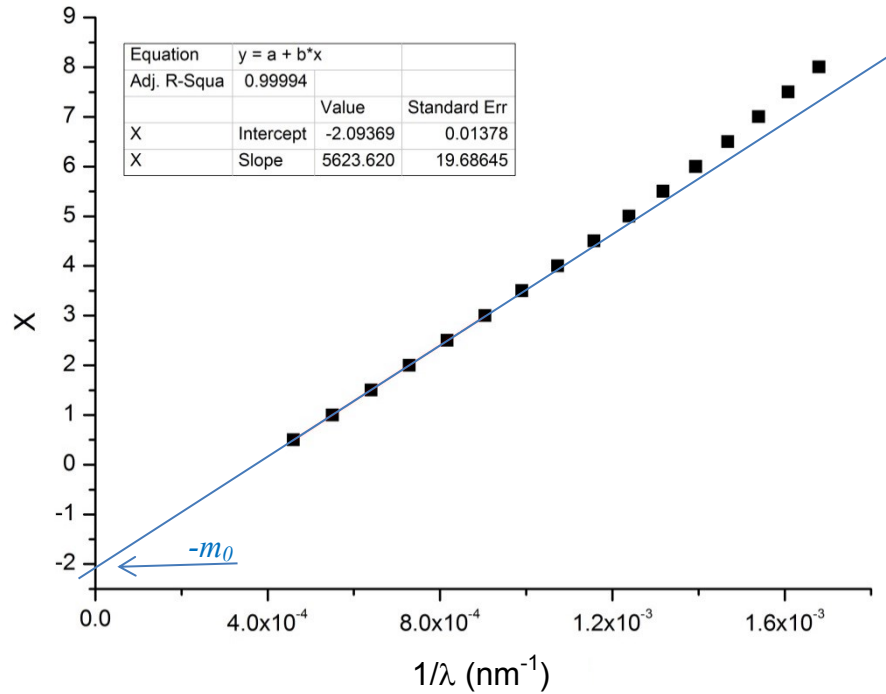
Figure II.20. Plot of equation (II.7) for a GLS:Pr sample (d = 1.1 μm).

Once m_0 is known, the *nd* quantity can be calculated using the actual $m = m_0 + X$ interference order for each wavelength (maxima and minima). As explained above, one can thus get (at least approximate) values of *d* (if *n* is known), or *n* (if *d* is known). However, we must warn about the sensitivity of this method to the precision of the parameters: for instance, 5% error bar on *d* will lead to ~5% error bar on *n*, which can be quite a lot for the studied materials.

Furthermore, fringes-free transmission *T* can be derived from the measured data, by plotting the envelopes corresponding to maximum and minimum transmission (see Figure II.21) and using the formula [Swanepoel 1983]:

$$T = \sqrt{T_{Max} T_{min}} \tag{II.8}$$

Based on equation (II.4), the absorption coefficient α can be calculated if the thickness *d* is known. The imaginary part of the refractive index can be calculated from:

$$\alpha = \frac{4\pi k}{\lambda} \qquad\qquad (II.9)$$
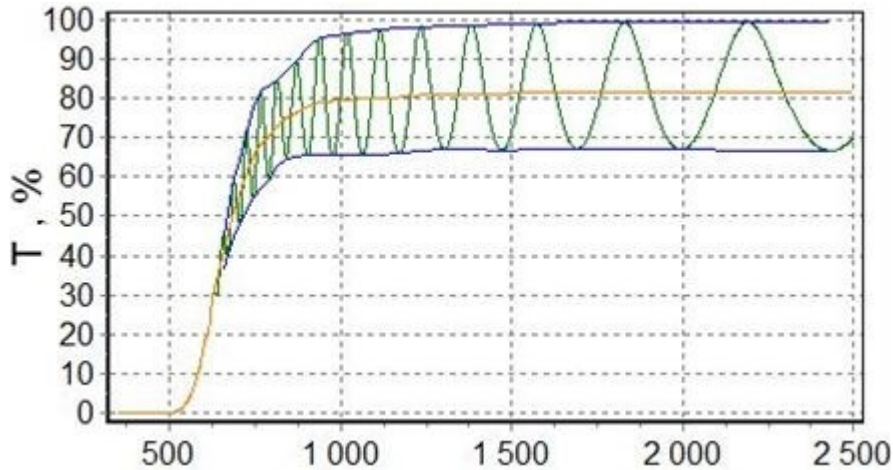
Figure II.21. Fringe-free transmission *T* (orange curve) calculated from T_{Max} and T_{min} envelopes (blue curves).

By plotting the $(\alpha E)^{1/2}$ quantity as a function of the photon energy *E* (Tauc plot [Tauc 1974]), the optical band gap E_g^{opt} can be estimated, as shown in Figure II.22. This procedure can be done (semi-)automatically with the PARAV-V2 free software [Ganjoo and Golovchak 2008, http://www.chalcogenide.org/parav-v2-0-2/], which uses the theory initially developed by Swanepoel [1983]. The program is able to calculate *d*, *n*, α and E_g^{opt} , however it has some flaws, as the use of Cauchy dispersion law, or the use of substrate transmission in the calculations (our data are free of substrate transmission, as we use a dual-beam spectrophotometer). These features can lead to erroneous results, especially for low thickness films.
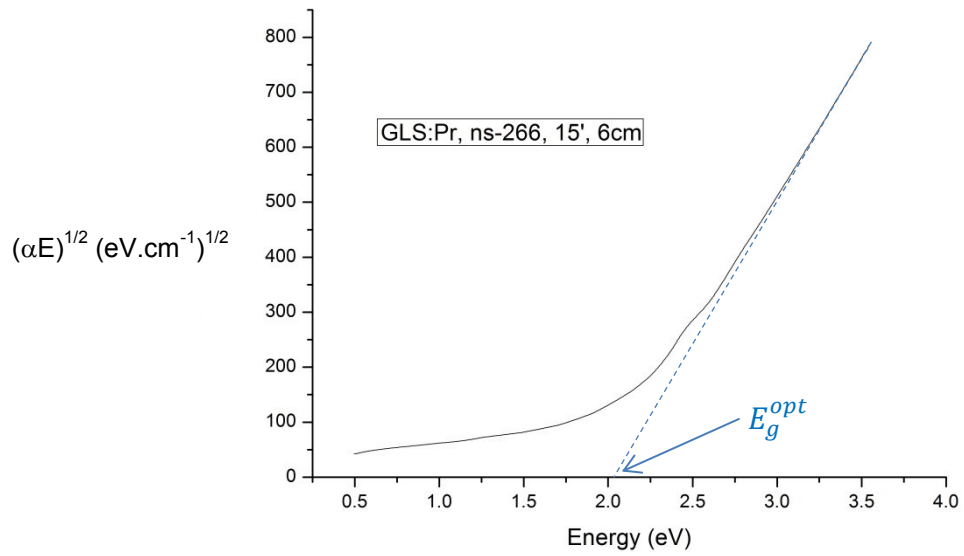
Figure II.22.   Tauc plot for determination of the optical band gap.

Chapter III

Thin films of Germanium Antimony Telluride (GST) based compounds

III.1 Introduction

Considering the promising applications mentioned in Chapter I, the first research subject studied in this thesis concerned thin films of Germanium – Antimony – Telluride (GST) based compounds deposited by laser ablation. A short description of the properties of GST materials and a compact literature survey on GST thin films obtained by various methods are presented in this chapter.

A significant advance in non-volatile solid state memory devices was driven by the discovery of Ge-Sb-Te alloys along the GeTe–Sb_2Te_3 tie-line by Yamada et al. in the mid 1980's [Yamada et al. 1987]. The rapid laser-induced crystallization with large property changes represented the grounds for many research studies [Kolobov et al. 2005, 2006, Nemec et al. 2012, Kolobov and Tominaga 2012, Vinod et al. 2012a]. Beside this quality, other requirements need to be addressed in order to obtain a good material for information storage devices (e.g.: good thermal stability of the amorphous phase and the possibility of applying large number of write-erase cycles). Figure III.1 shows the compositional dependences of the crystallization temperature (T_x) and of the laser heating time required for crystallization (τ_{cry}). It is clear that these materials present T_x larger than the room temperature but in the same time accessible for phase transitions by electric pulses. Moreover, the values of τ_{cry} were below 70ns which ensures a rapid recording. The investigated samples were 100nm thick GST films deposited by electron beam evaporation.
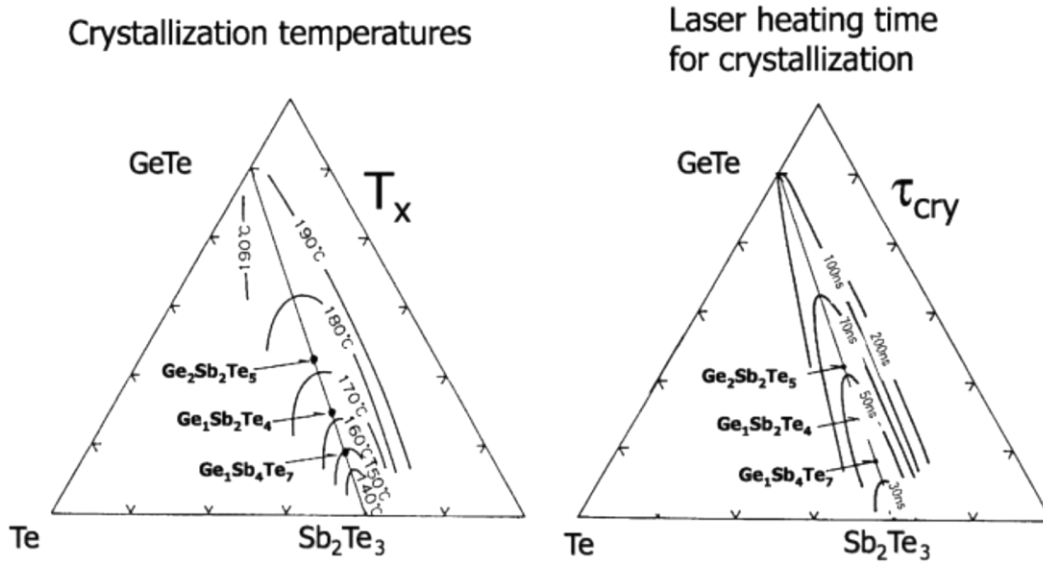
Figure III.1. Dependence of crystallization temperature (left) and laser heating time for crystallization (right) on Ge-Sb-Te composition [Yamada et al. 1987].
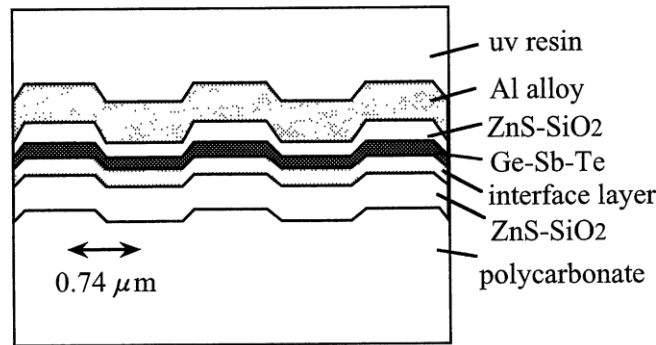
Figure III.2. Cross section view of the experimental optical disk; the layers were deposited by sputtering on a pre-grouved substrate [Yamada et al. 1998].

Yamada et al. [1998] reported results of repetitious data rewriting test, more exactly the deviation of the recorded mark from the correct position. For a DVD- RAM system this value needs to be <8.5%. The Ge–Sb–Te disk deposited on ZnS–SiO$_2$ with a germanium nitride interface layer (Figure III.2) showed a very clear and unchanged signal even after 500,000 cycles of data rewritings [Yamada et al. 1998]. It is to be noted that when using Ge$_2$Sb$_2$Te$_5$ the important and the exploited phase transition in any optical disk and electrical memory devices it is not the transition from amorphous to the stable hexagonal structure, but the phase change between the amorphous and a metastable phase described by a face centered cubic rocksalt-like structure (Figure III.3) where Te atoms

60

occupy the Cl sublattice, while the Na sub- lattice is randomly occupied by Ge/Sb atoms and intrinsic vacancies. The stable crystalline structures in the $(GeTe)_{1-x}(Sb_2Te_3)_x$ pseudobinary system can be viewed as trigonal structures with cubic periodicity formed by close-packed arrangement of NaCl-type cells along the c-axis in hexagonal notation. The binary GeTe compound has a rhombohedral (distorted rocksalt) structure at room temperature and a cubic phase at high temperatures. The other end of the GST system, Sb_2Te_3 has only the rhombohedral structure in the crystalline phase and can also be described as hexagonal for a conventional cell [Němec et al. 2011a].

An improved crystallization speed of the Ag-doped $Ge_2Sb_2Te_5$ thin films was observed by Song et al. [Song et al. 2008]. The un-doped and Ag-doped $Ge_2Sb_2Te_5$ thin films were obtained by thermal evaporation technique. The amorphous to crystalline phase transformation was investigated by focusing a laser beam with diameter <10µm. For laser powers of 7 mW, the threshold pulse durations for $Ge_2Sb_2Te_5$ and $Ag_{0.1}$ $(Ge_2Sb_2Te_5)_{0.9}$ films were approximately 70 ns and 30 ns, respectively.
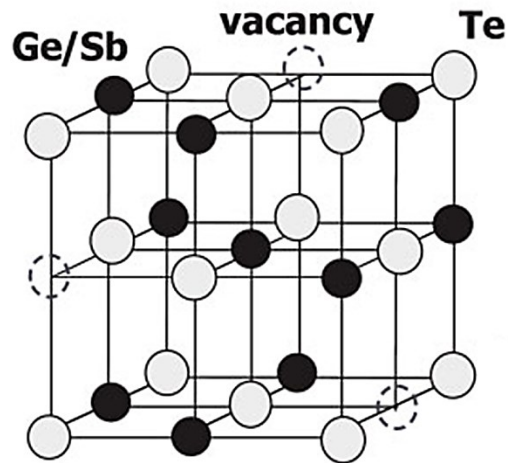
Figure III.3. Identified atomic arrangement of the NaCl type crystals in the laser crystallized $Ge_2Sb_{2-x}Te_5$ films deposited by sputtering (100W, 0.13Pa Ar pressure) [Yamada 2012].

As mentioned above, one key condition which needs to be fulfilled in order to distinguish the two states in the write-erase process is the drastic variation of optic or electric parameters upon phase change. Morales-Sánchez et al. [2005] investigated the electric properties of four GST-based thin films deposited by thermal evaporation on glass substrates at room temperature. Their thicknesses were ~100nm. From the

resistivity-temperature variation (Figure III.4) two abrupt declines were observed: the first one indicating an amorphous to fcc (face centered cubic) crystalline phase change and the second one for fcc to hexagonal structure transformation. For $Ge_2Sb_2Te_5$ thin film, the resistivity decreased from 220 $\Omega \cdot cm$ at 303K to $1.5 \cdot 10^{-2} \Omega \cdot cm$ at 443K. Since the sample thickness varies as the temperature is increased, a more precise measurement would be the monitoring of the sheet resistance vs. temperature. The electric properties of 80nm thick $Ge_2Sb_2Te_5$ thin films grown by sputtering were also investigated by Friedrich et al. [2000] using the sheet resistance dependence on applied temperature. By this method, the transition temperatures are more evident. The sheet resistance of $Ge_2Sb_2Te_5$ thin films obtained by Sun et al. [2008] presented a significant decrease from 10^7 to $10^3 \Omega/sq$ when the sputtered samples were irradiated with a pulsed laser of 580mW.
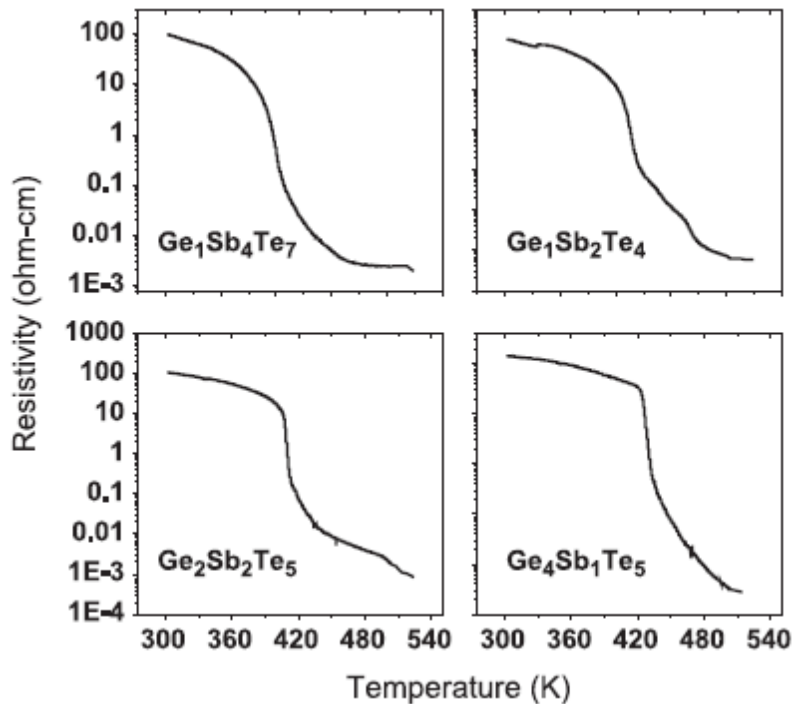
Figure III.4. Temperature dependence of the resistivity for several GST thin films [Morales-Sánchez et al. 2005].

Other parameter that can present changes from one phase to another is the absorption coefficient. Figure III.5c presents the spectral dependence of the absorption coefficients of $Ge_2Sb_2Te_5$ amorphous and crystalline thin films [Kolobov and Tominaga

2012]. Considering that in most cases, the PC memory devices rely on the optical reflectivity of the material, the n (refractive index) and k (extinction coefficient) optical constants are usually analyzed. For fcc and hexagonal structures, these parameters are very similar but in the visible range, a clear distinction between these parameters for amorphous and crystalline structure can be observed (see Figure III.5a,b) [Lee and Bishop 2009].
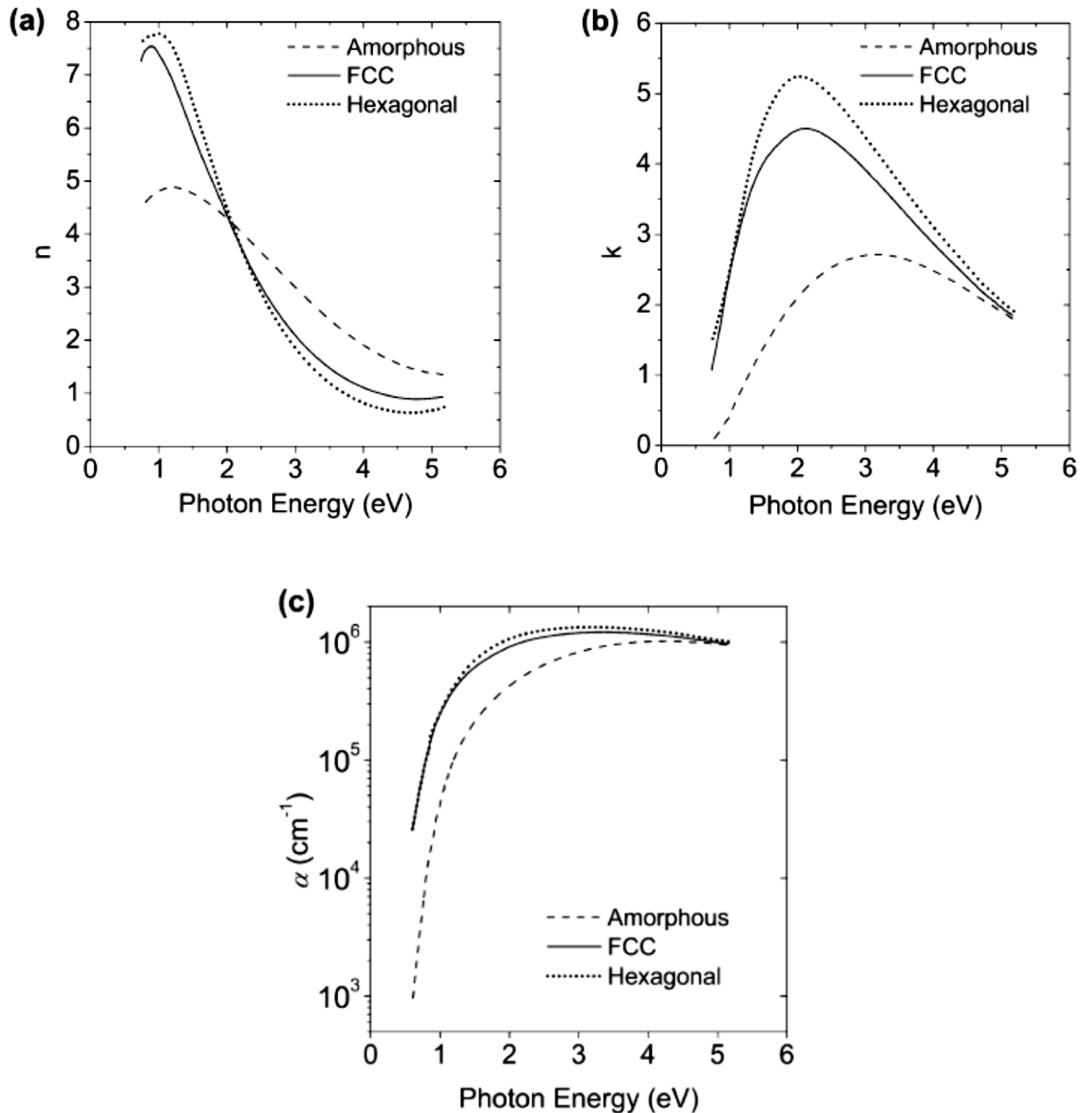
Figure III.5. Spectral dependence of the refractive index (a), extinction coefficient [Lee and Bishop 2009] (b), and absorption coefficient [Lee et al. 2005] (c) of 250nm thick $Ge_2Sb_2Te_5$ films deposited by RF magnetron sputtering (spectroscopic ellipsometru results).

The same conclusion can be drawn when taking into account the variation of $(\alpha h\nu)^{1/r}$ (where r=2) with the photon energy. The optical band gaps determined by Lee et al. [2005] were 0.7eV and 0.5eV for the as deposited amorphous and crystalline thin film of $Ge_2Sb_2Te_5$, respectively.

As reported by Yamada et al. [2012] the degree of the optical change n,k(crystalline) - n,k(amorphous) on the $GeTe$–Sb_2Te_3 pseudo-binary line increases with increasing the Ge content. Thus, for Blu-ray Discs that rely on optical characteristics, materials with GeTe rich compositions are more suited. However, GST chalcogenides with higher Sb concentrations present faster phase changes. Figure III.6 reveals a ternary composition diagram of phase-change alloys with annotations related to their years of discovery as a phase-change material and their use in optical storage products. The large arrow indicated the decrease of the crystallization time from ∼10µs (left side) to ∼30 ns (right side).
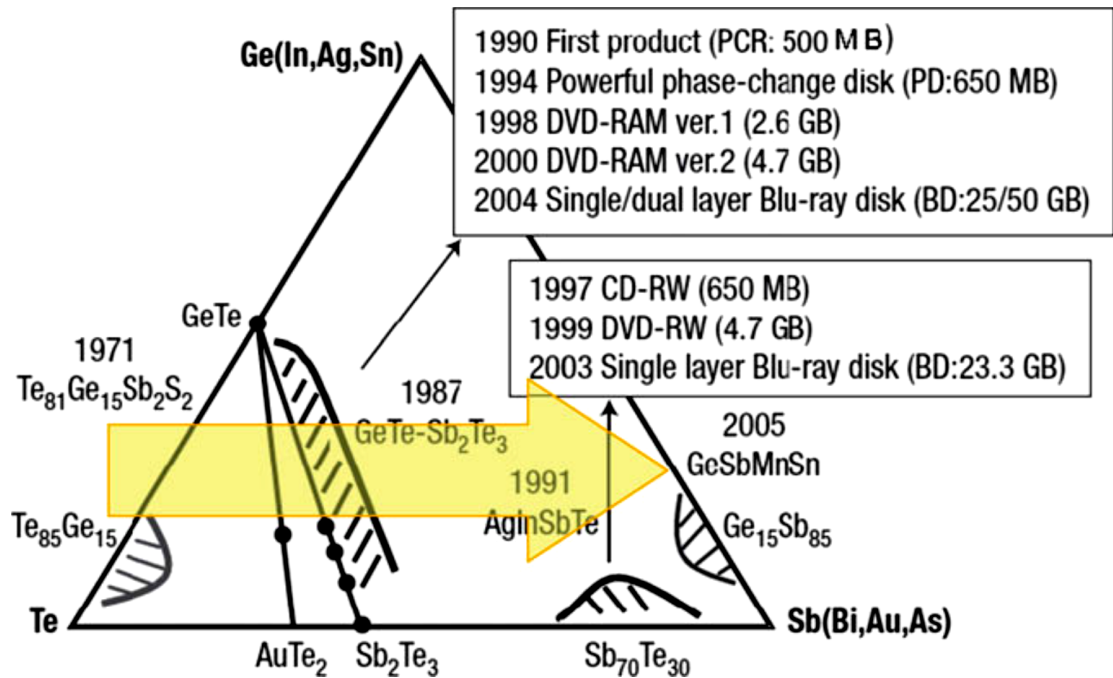
Figure III.6. A ternary composition diagram of phase-change alloys with annotations related to their years of discovery as a phase-change material and their use in optical storage products [Tanaka and Shimakawa 2011].

In 2010, the best DVD system available had a memory capacity of 50 GB/disk and utilized a blue semiconductor laser (wavelength of 405 nm). The film also presented

fast phase changes upon electrical pulses and thus electrical RAMs have been developed [Tanaka and Shimakawa 2011].

III.2 Previous studies on GST thin films

Most of the applications mentioned in Chapter I are based on thin films of chalcogen alloys. Although a large variety of deposition methods have been developed to date (e.g.: spin coating [Vlček et al.2003], magnetron sputtering [Gutwirth et al. 2009], thermal evaporation [Musgrave et al. 2011], atomic layer deposition [Lee et al. 2007], etc.) only a few of them can be considered when talking about specific properties of the resulting samples. It is important to obtain stoichiometric thin films of complex materials with good adhesion to the substrate and high homogeneity over a large area and, with several set-up adjustments (e.g.: laser beam splitting leading to multiple laser – target impact points), pulsed laser deposition (PLD) technique can ensure all these properties. The major drawback when using PLD is the deposition (in some cases) of large particles on the thin film surface but even in this case several solutions such as off-axis deposition [Chen et al. 2002], mask assisted or ultrafast laser ablation [Eason 2007] were employed.

Jeong et al. [1999] studied the crystallization mechanisms in $Ge_2Sb_2Te_5$ thin films deposited by magnetron sputtering. The ICP-AES revealed that the as-deposited thin films are slightly Ge and Sb rich in composition. Moreover, cross section TEM images revealed that as the annealing temperature increases, the number of nucleation sites increases until it saturates at the surface of the thin film, after which, the crystallization proceeds by the growth of the grains in the sample volume. Samples with amorphous and crystalline regions were also obtained by De Bastiani et al. [2010]. The reported results were achieved by analyzing $Ge_2Sb_2Te_5$ films deposited by RF sputtering on a 100nm thick layer of SiO_2 thermally grown on a Si (100) substrate. The as-obtained thin films with thicknesses of 50nm were then annealed at 150 and $400^{o}C$ in order to obtain samples with fcc and hexagonal structures, respectively. The phase formation was determined by XRD analysis. Moreover, the crystalline layers near the surface region were amorphyzed by Ge ion implantation (10^{14} ions/cm^2). The amorphous (top)/crystalline (bottom) layered structures were confirmed by cross-section TEM images.

Thin amorphous $Ge_2Sb_2Te_5$ films were also obtained by Gutwirth et al. [2009] using RF magnetron sputtering in Ar plasma. By EDX measurements, they observed that the samples are chemically homogeneous but with deviations from the nominal composition of the target. An approximately 4 at% increase of Ge content was observed for the film deposited in 1Pa Ar pressure in 60min with a 20W RF power while the Sb concentration was close to the nominal value of 22.2at%. Different chemical compositions were recorded for the films deposited at various angle divergencies from the normal direction when using the off axis configuration of the set-up. Moreover, slight changes of the atomic percentage of the main elements were observed even when the deposition conditions were the same, but the substrate was changed from silicon to silica glass. Although the accuracy of the EDX analysis is better than 0.5%, the Sb and Te signals are affected by the overlapping of the Te L- and Sb L-lines. The refractive indexes measured for wavelengths above 2000nm were lower than the ones reported by Dieker and Wuttig [2005]. Their study was focused on the influence of the Ar pressure (0.2-5 Pa) during the deposition on the structural, optical and electrical properties of magnetron sputtered thin films. The second varied experimental parameter was the applied power during sputtering (in the range from 20 to 100 W) but beside a linear change of the deposition rate no other influences were observed. The increase of the Ar pressure determined a decrease in density and consequently in refractive indexes of the 100nm thick samples. Unfortunately, due to the increased roughness of the thin films deposited at high argon pressures, the three dielectric functions used for describing the optical properties (Looyenga, Bruggermann and Maxwell-Garnet model [Dieker and Wuttig 2005]) deviated from the experimental plots.

Kato et al. [2005] studied the crystallization process of $Ge_2Sb_2Te_5$ and $Ge_4Sb_1Te_5$ thin films by XRD analysis with *in-situ* heating. The $Ge_2Sb_2Te_5$ (20 nm) or $Ge_4Sb_1Te_5$ (20 nm) samples were fabricated on Si substrate by sputter deposition. While for the first film two transition temperatures of 160^oC and 280^oC were observed, the XRD results of the second film indicated only one phase transformation process around 180^oC.

Studies of thermally evaporated GST-based materials were reported by Kumar et al. [2012]. The aim of their work was to investigate the properties of three chalcogenide materials along the tie line GeTe (GT) - Sb_2Te_3 (ST). The absence of the diffraction lines

in the XRD patterns confirmed the amorphous nature of the GT and GST ($Ge_2Sb_2Te_5$) deposited samples but the ST thin films presented peaks corresponding to three different structures: Sb_2Te_3, Sb_2Te and Sb_7Te. No measurements on the chemical composition were reported. Both XRD and temperature dependence sheet resistance measurements revealed crystallization temperatures of $150^{o}C$ and $180^{o}C$ for the GST and GT thin films. Along the sequence GT-GST-ST the optical gap and dc activation energy of the films decrease and the conductivity increases. The sufficiently high optical contrast of 30% for the GST film makes the material suitable for optical data storage.

The crystallization temperature observed by Vinod et al. [2012a] on $Ge_2Sb_2Te_5$ thin films deposited on glass substrate by the same method was slightly over $125^{o}C$, but the AFM analysis indicated an increase of the RMS roughness from 2.8 nm for the as-deposited samples to 6.7 nm for the thin films annealed at 360 °C. Moreover, the band gap values obtained for the amorphous and thermally treated samples were 0.58 and 0.36eV respectively, which are lower than the ones obtained by Lee et al. [2005] on RF sputtered thin films. Unfortunately no EDX measurement results were reported.

In order to improve the overwrite cyclability of $Ge_2Sb_2Te_5$ material, a small amount of nitrogen doping seems to be an attractive approach [Shin et al. 2005, Feng et al. 2007]. The study of Kölpin et al. [2009] revealed that by varying the addition of Si and N in the $Ge_2Sb_2Te_5$ thin films deposited by magnetron sputtering one can induce an increase of crystallization temperature and a decrease of crystallite size. The thin films were deposited using a $Ge_2Sb_2Te_5$ target in argon and nitrogen gas mixture and a Si target (combinatorial DC sputtering). A more pronounced effect was observed for the N-containing samples. These results were correlated with *ab initio* data. The effect of N-implantation on the structural and electrical characteristics of $Ge_2Sb_2Te_5$ thin films obtained by RF sputtering on $Si(100)/SiO_2$ substrate was investigated by Liu et al. [2005]. The as-obtained samples were N^{+} implanted (with nominal implant dose ranging from $6.44 \cdot 10^{15}$ to $6.44 \cdot 10^{16}$ ions per cm^2) and then annealed at different temperatures. They observed that both XRD and Raman spectroscopy analysis indicated a structural deformation as the N content was increased. In consequence, the sheet resistance decreases with N implant dose. The effect of Si and N doping on the phase transition of $Ge_2Sb_2Te_5$ thin films were studied by other research groups [Ling et al. 2006, Qiao et al.

2006]. Their conclusions were that the Si addition determined an increase in both crystallization temperature (as the other research group) and phase transition temperatures and that electrical properties and thermal stability of the samples were improved.

Musgraves et al. [2011] compared the structural, optic and electric properties of Ge-Sb-S thin films deposited by two methods: thermal evaporation (TE) and laser ablation. The EDS results revealed a slight variation of the Sb/S ratio from the stoichiometric value in the TE samples, while the PLD thin films presented atomic percentages of the main elements as in the target. The refractive indices of the deposited thin films, amorphous and annealed, were higher than the one of the bulk material, but the as-deposited PLD sample presented the highest value. Thus improved optical parameters and chemical properties were obtained when using PLD technique.

Only a few research papers that present results on GST thin films deposited by PLD can be found. A significant contribution was done by Nemec et al. [2009a, 2011a, 2012]. The main information was related to structural and optical properties of Ge-Sb-Te based thin films. In 2009 they reported a paper presenting the Raman spectroscopy and ellipsometry analysis results of $Ge_2Sb_2Te_5$ thin films [Němec et al. 2009a]. For target ablation, they used a 532nm radiation of an Nd-YAG laser with pulse durations of 3–7 ns and repetition rate of 10 Hz. The fluence was estimated at 2.3 J/cm^2 and the pressure inside the chamber was 10^{-4}Pa. To ensure a uniform thickness and to avoid extended damage of the target, both the substrate and the target holder were rotated during the deposition. The amorphous and crystalline natures of the as-deposited and annealed samples were confirmed by Raman spectroscopy.
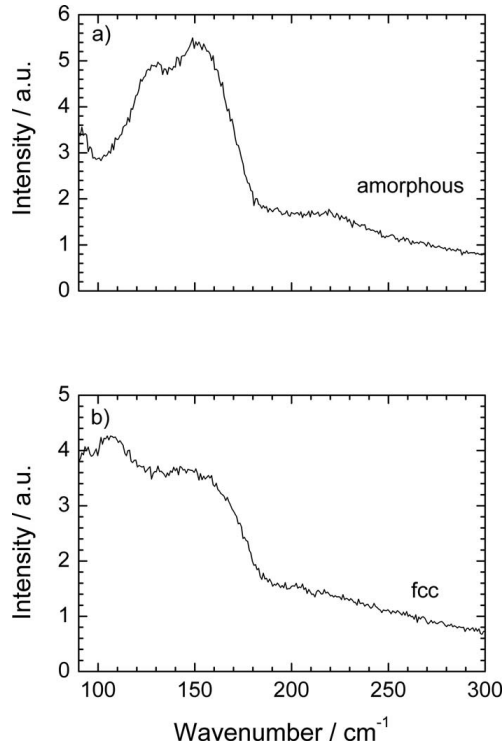
Figure III.7. Raman spectra of amorphous (a) and fcc (b) PLD GST thin films [Němec et al. 2009a].

The Raman spectra of the amorphous thin film presented a large band between 110 and 190 cm^{-1} which is due to the contribution of at least two peaks at 130 and 150 cm^{-1} (Figure III.7). They attributed the first peak to the A$_1$ mode of the GeTe$_{4-n}$Ge$_n$(n=1, 2) corner-sharing tetrahedral and the second one to the Sb-Te bonds in Sb–Te$_3$ units. The Raman spectroscopy results of the crystallized samples led to the conclusion that the GeTe component of the Ge-Sb-Te alloys is responsible for the phase transition. The ellipsometry results revealed optical band gap energy of 0.6–0.7eV for the amorphous film and of 0.4–0.5eV for the sample with fcc phase. Compared to the values found by other authors, they concluded that this parameter is independent on the deposition method. Moreover, the real part and the imaginary part of the dielectric function of the samples were simulated using the TL and CL models. The calculated values were found to be in good agreement with the experimental ones.

A more detailed study on ellipsometry results were further published in 2011 [Němec et al. 2011a]. In this paper, several chalcogenide alloys along the ternary line GeTe-Sb$_2$Te$_3$ were investigated in thin film form. Several experimental parameters

(pressure, fluence, target-substrate distance) were the same as the ones used in the previously reported paper. In this case, for target ablation they used the 248nm radiation of the KrF excimer laser (30ns, 20Hz). The Ge-Sb-Te thin films were found to be over-stoichiometric in Sb content. Very small variations of Ge concentration from the nominal composition were observed. In both GeTe and Sb_2Te_3 thin films the at% of Te was smaller than the stoichiometric value. Their results concluded that the thickness variation upon crystallization is strongly dependent on the GeTe content. The GeTe thin film presented the highest thickness variation (~13% decrease) but also the highest optical contrast at 400 nm (-1.98+i1.45) and reflectivity change upon amorphous-fcc phase transition. A complex Raman spectroscopy investigation of the bulk materials, as-deposited thin films and annealed samples was presented in [Nemec et al. 2012]. All the Raman peaks were correlated to the vibrational modes of the Ge-Sb-Te samples.

Franta et al. [2008] deposited $Ge_2Sb_2Te_5$ thin films by PLD on a crystalline Si wafer. Using the dispersion model of the optical constants, they studied phase change processes by optical methods. Upon annealing, they observed that the roughness of the thin film increased. The phase change was accompanied by an increase in density of electronic states and a change in the conductivity of the deposited films.

Lu et al. [2012] deposited $Ge_2Sb_2Te_5$ thin films on polymer substrates by PLD using a KrF laser (20ns, 10Hz, 248nm). The laser fluence was maintained at 1.5 J/cm^2 and the pressure was kept at 10^{-5}Pa. For references, several thin films were deposited on silicon wafers. The phase transformation processes were confirmed by XRD measurements at annealing temperatures of 140 and 300°C. The (200) diffraction line displacement was correlated to the tensile stress in the crystalline film. The reflectivity contrast between the amorphous and thermally treated samples increased with the annealing temperature, reaching 23% for the sample annealed at 240°C.

A notable study on the influence of the laser energy on the structural and optical properties of the deposited thin films was done by Hu et al. [2011]. For target ablation they used a KrF laser (248nm, 10Hz). The laser impact area was estimated at 0.1cm^2 while the pulse energy was varied from 58 to 190mJ. The thin films were deposited in Ar atmosphere (1Pa). The results of the chemical composition analysis (XPS technique) revealed that the deviations in concentration of the main elements were below 2at% and

no influence of the laser energy was observed. The XRD patterns of the as-deposited samples (with thicknesses of 120nm) presented small diffraction lines positioned close to the ones of the fcc and even hexagonal structures (sample deposited with the highest fluence). This analysis was performed again after the samples annealing at 200^oC for 2h and the results confirmed the formation of crystalline phases. The electrical measurements revealed that lower crystallization temperatures are needed when high pulse energies are used.

Ge-Sb-Te based nano-particles were also deposited on Si wafers by PLD. The paper published by Cho et al. [2006] and Yoon et al. [2005, 2006] all reported structural and chemical composition results of GST nano-particles synthesized using an ArF (193 nm, 5 Hz, 30ns) excimer pulsed laser. The fluence was about 2 J/cm^2 and the pressure inside the chamber was 1Torr. The EDS results indicated that the temperature of the thermally treated sample has a significant influence on the stoichiometry of the deposited thin films. The vibrational peaks observed for the GST bulk samples were correlated with the ones obtained by other research groups, but recorded Raman spectra of the annealed particles presented peaks at different wavenumbers.

III.3 Deposition and characterization of GeTe and Sb_2Te_3 thin films

Considering the reported results mentioned in the previous section, our study was based on the investigation of Ge-Sb-Te chalcogenide thin films (GeTe, Sb_2Te_3, $GeSb_2Te_4$, $GeSb_4Te_7$ and$Ge_2Sb_2Te_5$) deposited by PLD in various conditions. We present in this section the deposition and characterization of thin films based on the two ends of the GeTe–Sb_2Te_3 tie-line, while the Ge-Sb-Te pseudo-binary alloys studies will be presented in section III.4.

For target ablation we used three types of lasers which operate in different conditions: a) a nanosecond Nd-YAG laser (10ns, 10Hz) for which we used all four harmonics (1064, 532, 355 and 266nm), b) a Ti-Sa picoseconds laser (2ps, 100Hz) and c) a Ti-Sa femtosecond laser (~120fs, 1kHz). In each set of depositions, other experimental parameters were varied (e.g.: target-substrate distance – d_{t-s}, fluence, deposition time).

For easier reading, specifics on the deposition conditions are given as the thesis proceeds. The structural and optic properties of the as deposited thin films were investigated by stylus profilometry, optical microscopy, Energy-dispersive X-ray spectroscopy, Time of Flight – Secondary Ion Mass Spectroscopy, Raman spectroscopy, X-ray Diffraction, ellipsometry and spectrophotometry.

III.3.1 GeTe thin films

III.3.1.1   Nanosecond regime

In this regime, seven thin films were deposited using different wavelengths (λ) and fluences of the Nd-YAG laser (10ns, 10Hz). The target to substrate distance was varied from 3 to 6 cm, the deposition time was between 15' and 60', and pressure was kept constant during deposition in the $\sim 10^{-5}$ Torr range. The experimental parameters are listed in Table III.1. The first five films (G1-G5) were deposited on a circular area with 8mm diameter on crystalline Si (100) using configuration 2 (see section II.1.4) where the substrate was not rotated and the target was moved in the XY plane. For the D1 and D2 samples we used a microscope slide glass as substrate and the dimensions of the deposited areas were 2.6x3.5 cm and 2.6x4.5 cm, respectively (see Figure III.8). These depositions were carried on in Ar atmosphere using configuration 1 (see section II.1.4). The substrate was not moved and the target was rotated and translated along the X axis.
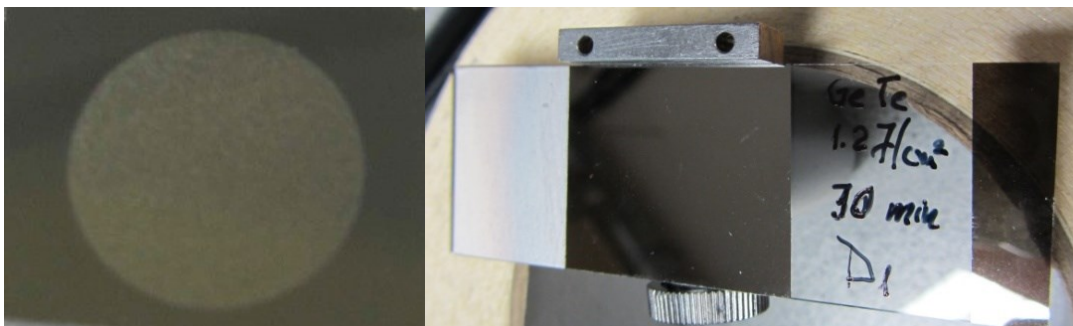
Figure III.8. Photographs of the G4 sample deposited on Si (100) (left side) and of the D1 thin film deposited on glass substrate (right side)

Table III.1   Deposition conditions used for GeTe thin film growth.

Sample label	P (Torr)	d_{s-t} (cm)	Laser characteristics	t (min)	Thickness (nm)	Deposition rate (nm/min)
G1	$1.3 \cdot 10^{-5}$	4	λ=1064 nm, fluence ~6.4 J/cm^2		400	6.7
G2	$1.2 \cdot 10^{-5}$	3	λ=1064 nm, fluence ~6.4 J/cm^2		540	9
G3	$1.2 \cdot 10^{-5}$	4	λ=532 nm, fluence ~6.4 J/cm^2	60	200	3.3
G4	$9.8 \cdot 10^{-6}$		λ=355nm, fluence ~6.4 J/cm^2		220	3.7
G5	$1.2 \cdot 10^{-5}$	3	λ=266nm, fluence ~3.8 J/cm^2		450	7.5
D1	$4.5 \cdot 10^{-5}$	6	λ=266nm fluence ~1.2 J/cm^2	30	120	4
D2	$4.5 \cdot 10^{-5}$			15	N/A	N/A

The surface topography and the thickness of the as-deposited samples were studied using the optical microscope (part of the Raman spectroscopy set-up) and stylus profilometry. The as-obtained images and thickness profiles of several thin films are revealed in Figures III.9 and III.10, respectively. All the investigated samples from G-series presented droplets on the surface and high roughness. These are due to the elevated fluence used for target ablation. Another important parameter that can have great influence on the microstructure of the deposited samples is the laser wavelength which, depending on the thermal properties of the material can determine the ejection of different sized particles. As the laser wavelength decreases, the penetration depth is lower. Thus the deposition with the 266nm laser radiation presents an advantage, especially when lower fluences are used. Improved results were obtained for the D1 and D2 samples. The lower fluence used for ablation determined the deposition of only a few droplets but also of a thinner thin film. One should consider that the thickness value listed in Table III.1 for the D1 sample is obtained when analyzing the ends of the deposited area, but the thin film can present a greater thickness in the center region. It is well known that due to the strong directionality of the plume to the perpendicular direction related to target surface, a typical PLD set-up cannot ensure a uniform thickness distribution on large areas.
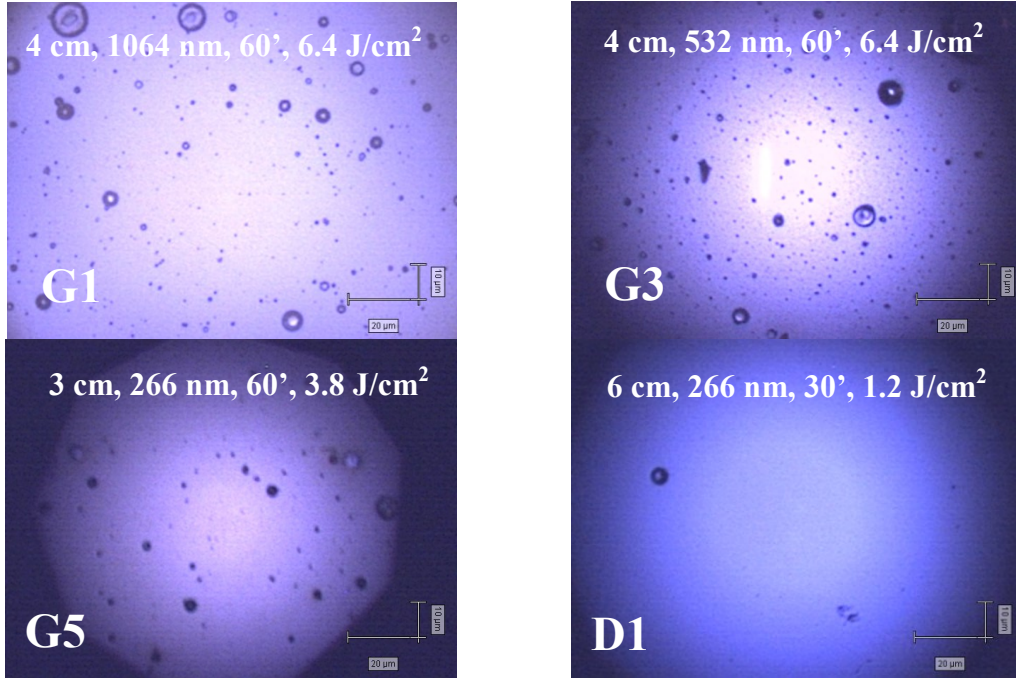
Figure III.9. Optical microscopy images of the GeTe thin films deposited by ns-PLD

In some cases, due to the high roughness of the measured samples, the thickness determination was quite difficult. We measured the distance between the substrate surface and the lowest feature of the thin films surface. Moreover, for some samples, it turned out that the substrate surface was not perfectly flat, making it more difficult to give a precise thickness value. In these cases, we estimated the thickness from the step height on both sides of the profile. Depending on the deposition configuration, the thickness in the center can be higher. The estimated values are listed in Table III.1. Considering these samples, the best combination of deposition conditions is the one used for D-samples. The use of a short target-substrate distance usually determines the deposition of a large number of micro-sized particles on the substrate surface. To diminish this effect, low fluences are needed to ensure a fine particle ejection but the deposition rate is substantially decreased. Although a larger target-substrate distance, a shorter deposition time and a lower fluency were used to deposit the D-samples, the thickness is still reasonable while the uniformity is improved. The estimated deposition rates are also listed in Table III.1. For the D1 sample, the film thickness increase is more likely due to the sample leveling during the measurements and not to the sample features.
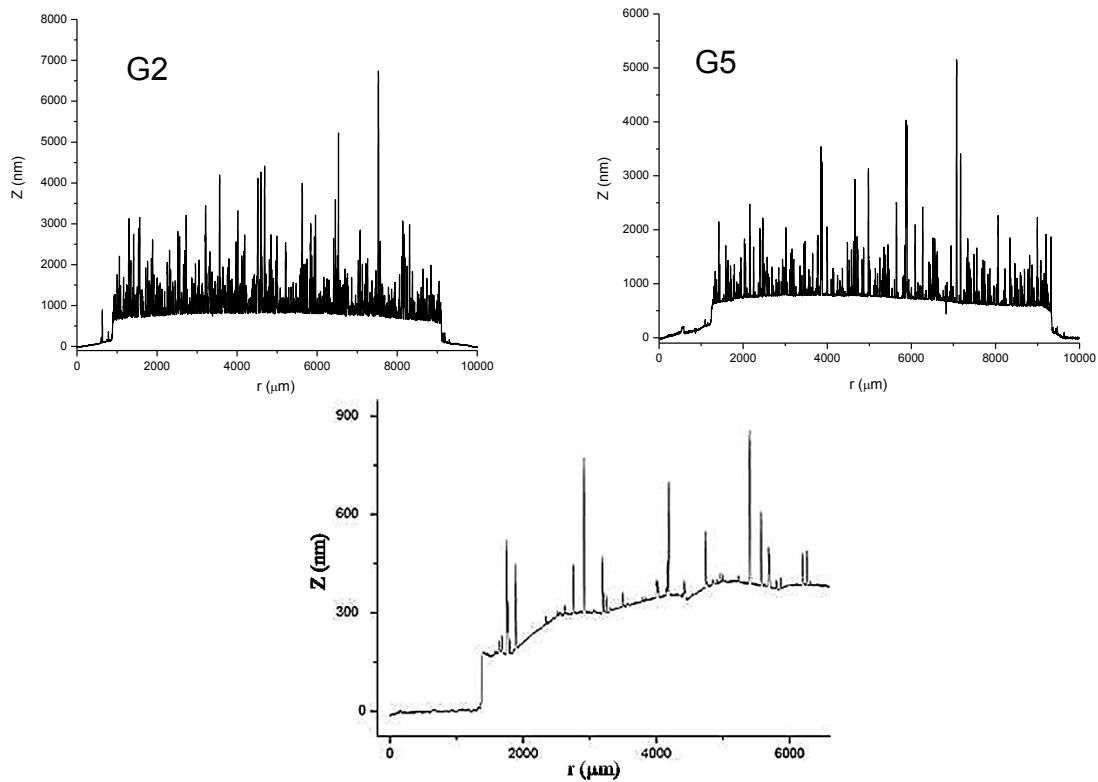
Figure III.10. Stylus profilometry of GeTe thin films deposited in nanosecond regime.

EDS results were obtained using the two instruments described in Chapter 2. The obtained results are summarized in Table III.2. All the samples present an increased Ge content. EDS measurements on the G5 sample were carried out using JEOL JSM 6400 instrument with 10kV accelerating voltage. Two types of analyzes were performed: on large areas (~100x100 μm^2, 1 μm depth) and on some deposited droplets (1 μm^3 volume). In both analyzing conditions, the G5 sample presents higher Ge content in report to the nominal composition. When large areas were investigated, the variations of Ge and Te concentrations were below 1% but higher differences in compositions were recorded from one droplet to another.

A higher Ge concentration was also observed by Nemec et al. [Nemec et al. 2012] in their study on GeTe thin films deposited by PLD using a KrF excimer laser (248 nm, 30 ns, 20 Hz) for target ablation and a fluence of 2.6 J/cm^2. Their samples presented only a 2.9at % over-stoichiometry in Ge. The large deviations from the nominal composition in our study can be explained by the higher fluence used for target ablation. The high

temperature induced at laser-target interaction could induce a more rapid evaporation of Te in report to Ge, depending on the chemical properties of each species.

Table III.2   Chemical composition from EDS measurements (uncertainty ±0.5%).

Sample	Atomic %		Instrument	Analyzing conditions
	Ge	Te		
	50	50		Nominal composition
G1	56.3	43.7	Tescan Vega II LMH	Surface: 550x550μm
	58.3	41.6		Surface: 55x55μm
G3	61	38.9		Surface: 550x550μm
	59.9	40.1		Surface: 55x55μm
G4	54	46		Surface: 550x550μm
	56	43.9		Surface: 55x55μm
G5	61.4	38.6		Surface: 550x550μm
	59.5	40.5		Surface: 55x55μm
	58.9	41.1	JEOL JSM 6400	Droplets
	63.6	36.4		
	62.7	37.3		
	60	40		Surface: 120x80μm
	59.6	40.4		

EDS measurements on the D1 sample were done using the Tescan Vega II LMH instrument in different points on the thin film surface, starting from the center of the deposited area and continuing towards the lateral ends of the sample (up to 10 mm left side and 20mm right side). The obtained distributions of Ge and Te content with r (distance from the center of the film to the analyzed point) are plotted in Figure III.11. One can observe that while in the center of the thin film the composition is stoichiometric, large variations from the nominal composition of Ge and Te concentrations are found in the regions close to the lateral ends, where an increased Te content was recorded.
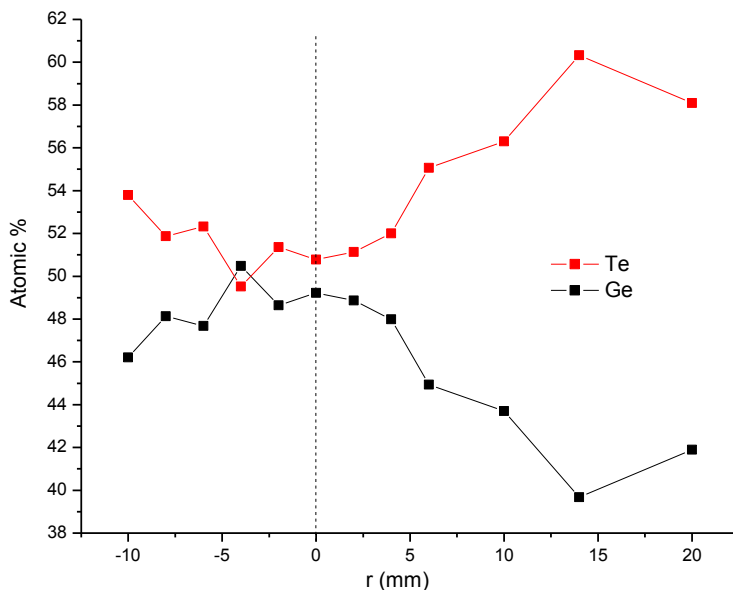
Figure III.11. Distribution of Ge and Te concentration on different points on the D1 sample.

The structural properties of the samples were investigating using Raman spectroscopy (with 785 nm and 514 nm excitation laser wavelength) and XRD analysis. Only one sample - G5 - was characterized by XRD while Raman spectra at different excitation laser powers were obtained for all deposited samples. The diffraction pattern of the G5 sample indicated an amorphous deposition. As indicated in Figure III.12 a), the two observed diffraction lines correspond to the silicon substrate.
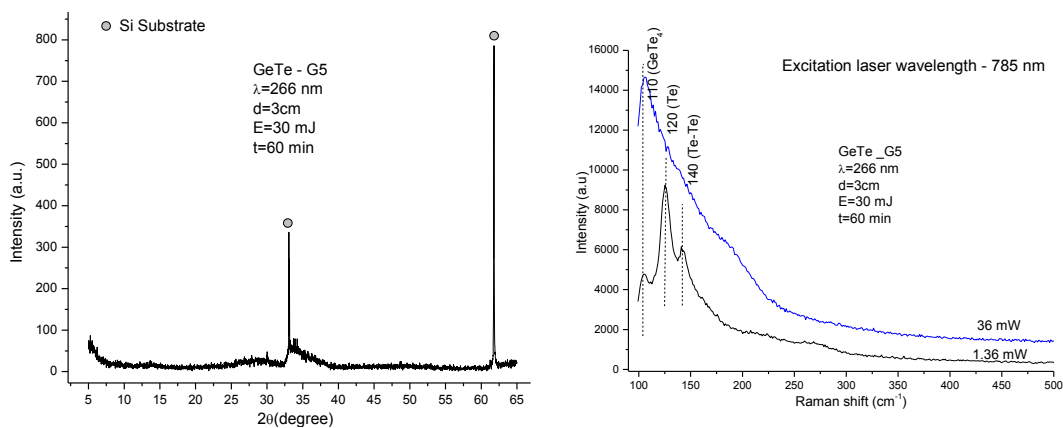
Figure III.12 XRD pattern (a) and Raman spectroscopy results (b) of G5 sample.

The reported studies on Raman spectroscopy of GeTe materials revealed that the amorphous GeTe(a-GeTe) present four peaks at 83, 125, 162 and 218 cm^{-1} and the crystalline GeTe (c-GeTe) shows dominant vibrational modes at about 80 and 120 cm^{-1} [Andrikopoulos et al. 2006, 2007, Nemec et al. 2012]. Moreover, Andrikopoulos et al.[2006] observed several similarities between the peaks of the a- and c-GeTe samples [Andrikopoulos et al. 2006]. These were related to the much wider peak of the crystalline phase and to the narrower peak of the amorphous sample compared to the Raman response of other materials. These Raman features indicated that GeTe chalcogenide crystals present a distorted rock salt structure while the a-GeTe seems more ordered than other glasses. The excitation laser power used was lower than 0.4mW. Figure III.13 presents the Raman spectra of the thin films from our study deposited using a 4cm target-substrate distance and a 6.4 J/cm^2 fluence. The similarities between the spectra recorded at 1.36mW indicate that the deposition laser wavelenght does not have an effect on the crysallization nature of the grown films. At low excitation laser powers (1.36mW), two main peaks were observed: one arround 125cm^{-1}and anotherone at ~143cm^{-1}. Their narrow width do not sugest an amorphous deposition but neither the presence of the second peak does indicate a GeTe crystallization. The Raman measurements do not support the ones obtained by XRD that indicate a presence of an amorphouse phase.
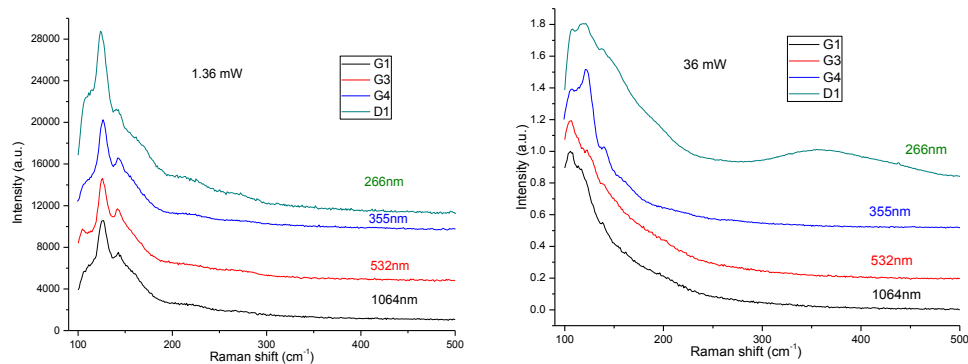
Figure III.13. Raman spectra of the deposited GeTe samples recorded using an excitation laser power of a) 1.36mW and b) 36 mW.

For a clear assignment, we took into consideration the contribution of any individual elements phase to Raman response. The bulk Te spectra present two peaks: one at 121 cm^{-1} which represents A1 mode and a second one at 140.8 cm^{-1} which

represent E_{TO} modes in crystalline Te–Te chain [Vinod et al. 2012a]. Considering the large deviations of Ge and Te concentrations from the nominal composition and that Te crystallizes at room temperature [Vinod et al. 2012b] a more adequate assignment of the two Raman peaks observed in our study (125 and 143cm^{-1}) would be based on Te segregation rather than GeTe crystallization.

Moreover, two other peaks seem to have a contribution to the Raman response at 1.36mW excitation laser power: one at 110 and another one at 160cm^{-1}. These bands can be associated with Ge-Te based vibrational modes in amorphous structures [Yoon et al. 2006, Nemec et al. 2012]. Andrikopoulos et al. assigned the 120 and 160cm^{-1} bands to GeTe$_{4-n}$Ge$_n$ (n=0, 1, 2, 3, 4) corner-sharing and edge-sharing tetrahedral units respectively [Andrikopoulos et al 2007].

Different features of the Raman spectra were observed as the excitation laser power was increased to 36mW. The wide band in the 110-200cm^{-1} region it is probably due to parasitic luminescence and not to crystallization processes.

III.3.1.2   *Femtosecond regime*

The deposition conditions used for this set of samples are summarized in Table III.3. For these films we used configuration 2 (Fig. II.7b) where the substrate was rotated and the target was moved in the XY plane during the growth process. The 800nm laser radiation (E=1.60mJ, repetition rate 1kHz) was focused on the target with f = 25cm lens at a 45° incidence angle. The varied experimental parameters were the target substrate distance (d_{s-t}) and the laser fluence. The pressure ($\sim 10^{-6}$Torr) and the deposition time (30min) were maintained constant.

Table III.3   Experimental parameters used for GeTe thin film depositions

Sample	P (Torr)	d_{s-t} (cm)	Laser fluence	t (min)	Thickness (nm)	Deposition rate (nm/min)
B1	$1.7*10^{-6}$	6	0.3 J/cm^2		800	26.6
B2	$1.8*10^{-6}$	2			900	30
B3	$3.1*10^{-6}$	4	0.1 J/cm^2		N/A	N/A
B4	$1.3*10^{-6}$	6			N/A	N/A
B5	$1.3*10^{-6}$	2		30	450	15
B6	$1.3*10^{-6}$	4	0.5 J/cm^2		1400	46.6
B7	$1.3*10^{-6}$	6			700	23.3
B8	$1.6*10^{-6}$	6			< 20	< 0.6
B9	$1.6*10^{-6}$	4	0.05 J/cm^2		N/A	N/A
B10	$1.6*10^{-6}$	2			< 20	< 0.6
GeTe_4	$2*10^{-5}$	1.6	0.26 J/cm^2	10	1010	101

The microstructure, chemical composition and elemental distribution were investigated by optical microscopy, EDS and ToF-SIMS analysis. Figure III.14 presents the optical microscopy images of four thin films obtained using the Olympus BXFM free-space microscope coupled with the Raman spectroscopy set-up. Compared to the thin films deposited in nanosecond regime, these samples present a more uniform surface, with no large particles.
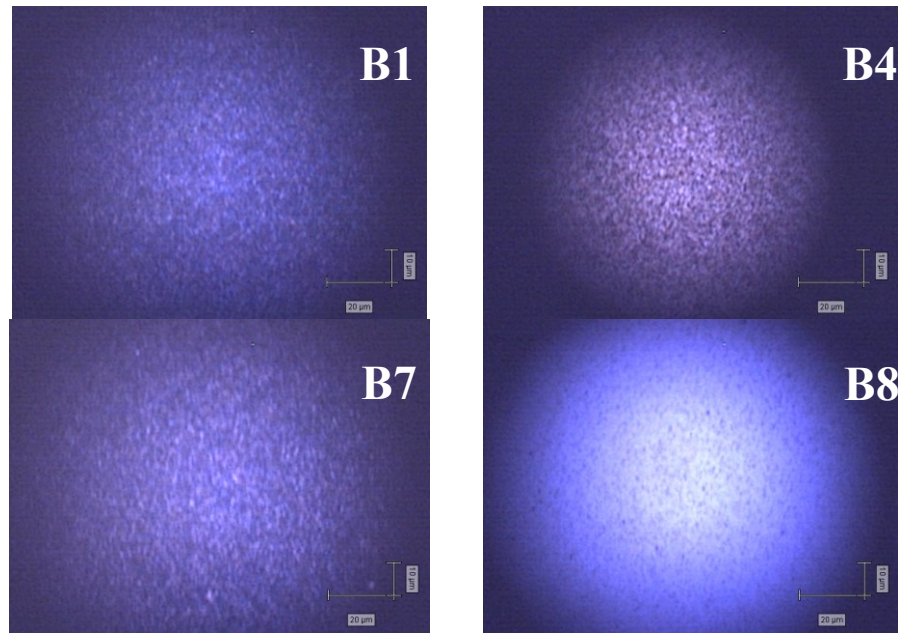
Figure III.14. Optical microscopy images of the GeTe thin films deposited by fs-PLD using 6 cm target-substrate distance and different fluences.
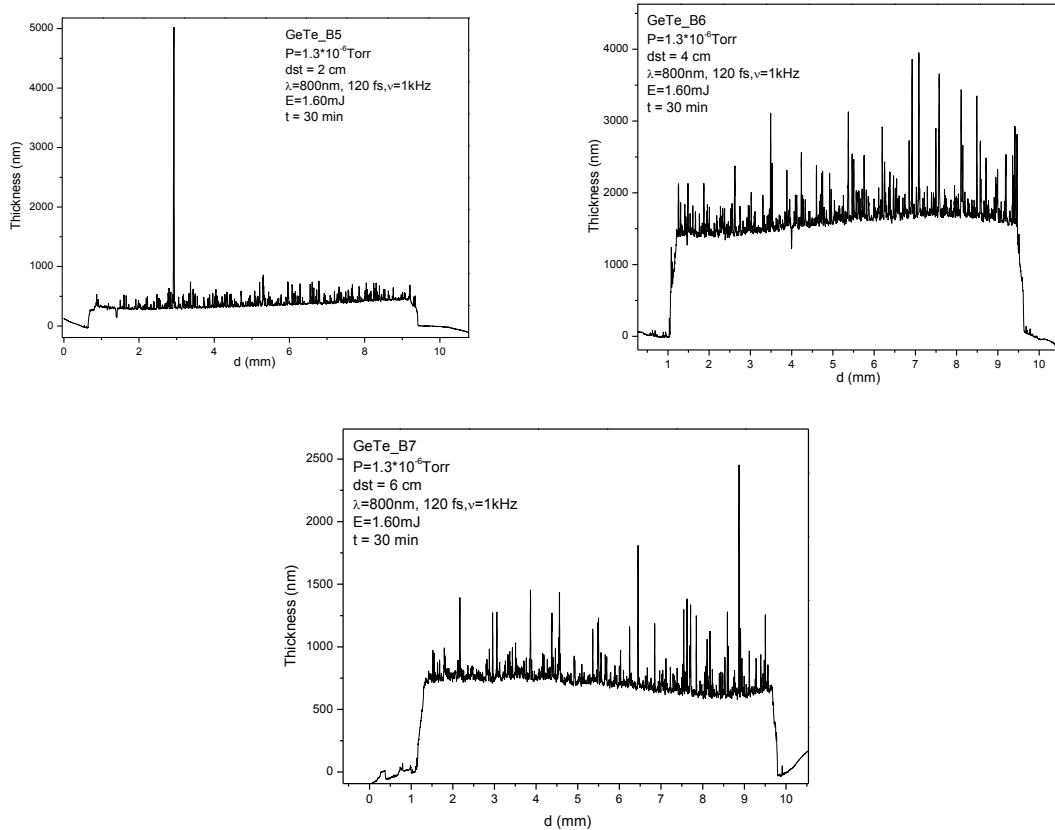
Figure III.15. Thickness profiles of three GeTe thin films deposited by fs-PLD.

As one can observe from the microscopy images of the ns- and fs-PLD thin films, the surface microstructure is quite different. Beside the absence of micro-sized particles, the samples deposited in femtosecond regime present very small fragments. The thin films presented in Figure III.14 were deposited using a target-substrate distance of 6cm. The use of a larger distance between the source material and the substrate usually determines the deposition of more uniform thin films. Thus, we also investigated the optical microscopy images of the samples deposited at 2 cm distance from the target surface. The varied experimental parameter in their case was the fluence. Even for these, a smooth surface microstructure with no large particles was observed.

The surface microstructure was investigated by profilometry measurements (Figure III.15). These confirmed the improved uniformity of the fs-PLD samples suggested by optical microscopy. The estimated thicknesses are listed in Table III.3. In some cases, the influence of experimental parameters variation on the sample thicknesses is evident. For example, comparing the B2 and B5 samples one can observe a two time

thickness increase when the laser fluency is augmented from 0.1 J/cm^2 to 0.3 J/cm^2. Also, a two times thinner thin film was obtained when the target to substrate distance was increased from 4 to 6 cm (B6 and B7). However, some discrepancies were still observed. These were assigned to the instability of the plume in this temporal regime. The generated plasma does not always propagate in the perpendicular direction related to the target surface. In a short time, more material is ejected from the target surface than in the nanosecond regime due to the high repetition rate and, in some cases, the laser beam can sputter an already irradiated surface which suffered a modification. Thus the velocity of the target movement in the XY plane should be increased to always sputter a fresh area. However one should consider that the target displacement is limited by its reduced dimensions. Moreover, the much smaller thicknesses observed for the last three samples (B8, B9, B10) indicates that the fluency used is close to the threshold value. The use of a lower power density cannot insure an efficient deposition even at 2cm distance from the target. Considering that the estimated thickness were below 20nm, the higher luminosity of the B8 sample image it is most probably due to the contribution of the substrate surface which has a higher reflectivity than the film.

EDS measurements on B2 and B8 samples were done using the JEOL JSM 6400 instrument from Rennes University, France. For the evaluation of Ge and Te concentrations the L-series of every element were analyzed and a 10kV accelerating voltage was applied. An example of the energy dispersive X-ray spectra, together with a SEM image of the analyzed area from the B2 sample is given in Figure III.16.
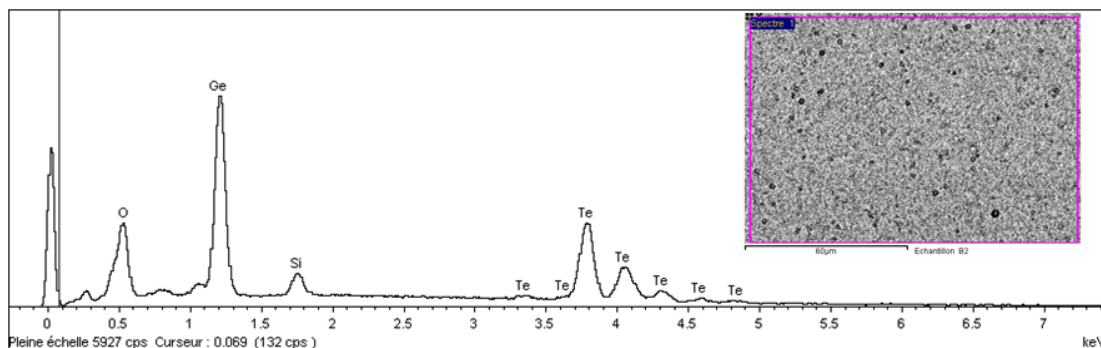
Figure III.16. Energy dispersive X-ray spectra and SEM image of the analyzed are from the B2 sample.

Table III.4   EDS results of the B2, B5 and B8 samples. The B5 sample was analyzed using the Tescan Vega II LMH instrument.

Sample	Atomic %		Instrument	Obs.
	Ge	Te		
	50	50		Nominal composition
Target	46	54		Surface 550x550μm
B1	50.2	49.9	Tescan Vega II LMH	Surface 550x550μm
	49.3	50.7		Surface 55x55μm
B2	51.8	48.2	Tescan Vega II LMH	Surface 550x550μm
	52.9	47.1		Surface 55x55μm
	49.2	50.8	JEOL JSM 6400	Surface 120x80μm
	49.7	50.3		No droplets were
	49.8	50.2		observed
B5	57.8	42.2	Tescan Vega II LMH	
B6	51	49	Tescan Vega II LMH	Surface 550x550μm
	49.1	50.9		Surface 55x55μm
B7	51.9	48.1	Tescan Vega II LMH	Surface 550x550μm
	51.4	48.6		Surface 55x55μm
B8	53.3	46.7	JEOL JSM 6400	Surface 120x80μm
	54.2	45.8		No droplets were
	56.1	43.9		observed
GeTe_4	48.7	51.3	Tescan Vega II LMH	Surface 550x550μm
	47	53		Surface 55x55μm

Beside Ge and Te, two more elements were detected: silicon (coming from the substrate) and oxygen (probably justified by the contamination of the sample due to its handling after deposition). The EDS results are listed in Table III.4. Part of the samples was analyzed using the Tescan Vega II LMH instrument with a 30kV accelerating voltage. For the Ge and Te concentration determination the K and L series, respectively, were considered. The concentration errors were ~1-2at%.

The EDS results indicated that these films have different chemical composition. While most film present very small deviations of Ge and Te atomic % from the nominal composition (below 1at%), two samples (B5 and B8) are highly over-stoichiometric in Ge content. Although improved EDS results were observed for the fs-deposited samples, both ns- (G5) and fs-PLD (B8) GeTe thin films presented higher concentrations of Ge as Nemec et al. [2011a] and Wagner [2007] observed in their study on chalcogenide thin films deposited by ns-PLD. However, the Ge concentration in their study was higher only

by 3at% compared to the nominal composition. Taking into consideration that the stoichiometric thin film was the one deposited at the shortest target-substrate distance and highest fluence (parameters which would determine a more energetic particle ejection and deposition), the possible re-sputtering processes cannot explain the concentration variation. For more information on the chemical properties of the deposited samples, in-depth profiles were obtained using ToF-SIMS analysis.

Figure III. 17 presents the distribution of Ge, Te and their compounds in the B5 sample obtained in negative polarity. For this acquisition, a beam of Cs ions (1keV, 93 nA) was used to sputter a 300x300µm area and a beam of Bi^{3+} ions (25kV) to generate secondary ions from a 100x100µm inner-surface.

A typical analysis obtained by this technique cannot offer quantitative information. The as recorded signal of Te had a much higher intensity than the one of Ge. Their intensities depend not only on the difference between the amount of sputtered ions but on the electronegativity of each element as well. Thus, for a more clear representation, the normalized depth profiles of the main elements found in the sample were plotted.
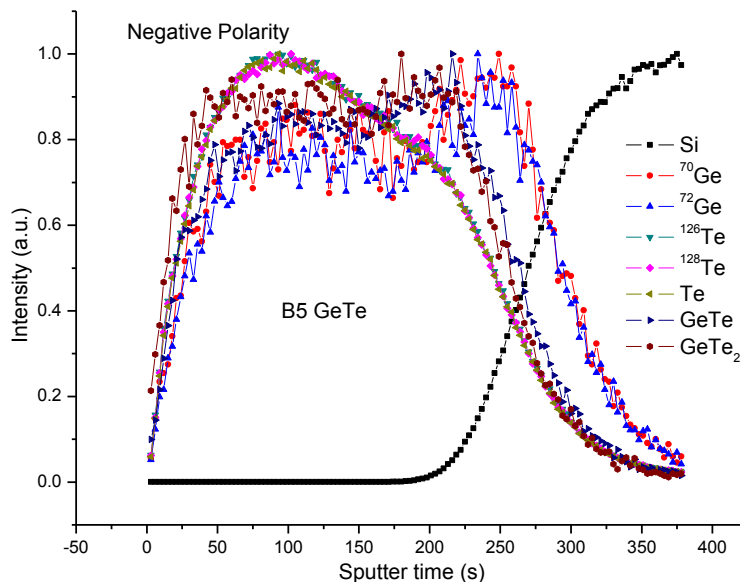
Figure III.17. Depth profiles obtained analyzing the B5 sample obtained in negative polarity using Cs ions for sputtering.

Different distribution of Ge and Te ions were recorded: a higher concentration of Te was found in the first pulverized part of the thin film while an elevated Ge content was observed in the region close to the substrate, but GeTe compound present a rather uniform distribution. Moreover, Ge ions were found at a deeper distance into the substrate than Te ions.
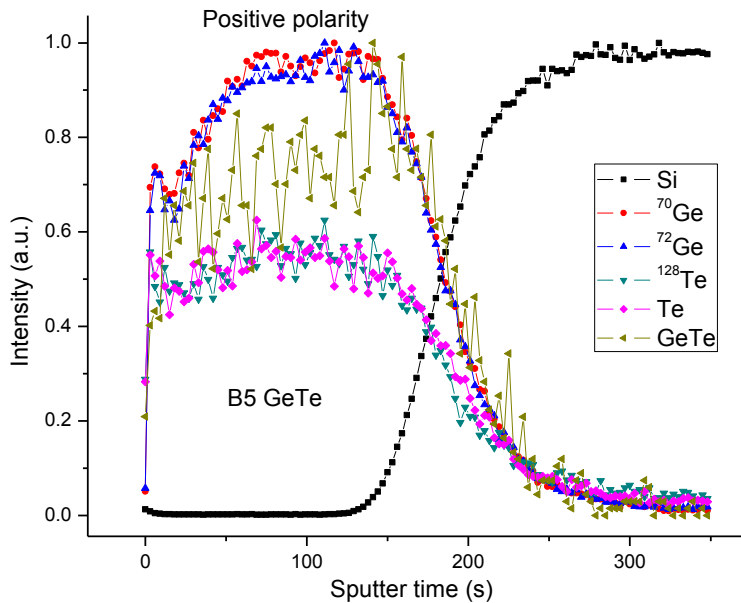
Figure III.18. Depth profiles of the B5 sample obtained in positive polarity using a beam of oxygen ions to sputter the material.

Using this same technique, a second analysis was done on the B5 sample. The next figure present the depth profiles obtained in positive polarity but, in this case, instead of Cs ions, we used a beam of oxygen ions (1kV, 243nA) to sputter a 300x300µm area.

Beside the detection of GeO and TeO compounds, other differences were observed when comparing these results with the ones obtained in the previous case (where Cs ions were used for sputtering). Here, Te and Ge ions present a more uniform distribution. However, one can still observe a variation of the Ge content in the samples volume. Although the depth profiles from Figure III.17 indicated an increased Te content in the first part of the film, its distribution in the second case is uniform. Moreover, the sputtering time at which the Si signals increase differs from one analysis to another. Assuming that there are no thickness variations in the thin film, this difference is due to

85

the sputtering beam characteristics. Furthermore, the Ge and Te signals decrease at approximately the same sputtering time, contrary with what was observed in the previous analysis.

As mentioned before, the recorded signal depends on the properties of each element. In negative polarity, the Te signal is more evident while in positive polarity, Ge detection presents an advantage. Thus, in Figure III.19 we present the ToF-SIMS mapping images obtained in the best suited acquisition conditions of each element. The ToF-SIMS images are obtained analyzing a quite large area of 100x100μm. As one can observe the distribution of the main elements and of their isotopes is uniform.

The XRD patterns of the GeTe sample presented in Figure III.20 suggest a crystalline thin film deposition. The red lines indicate the 2θ position of the diffraction peaks corresponding to GeTe bulk material recorded in the database.
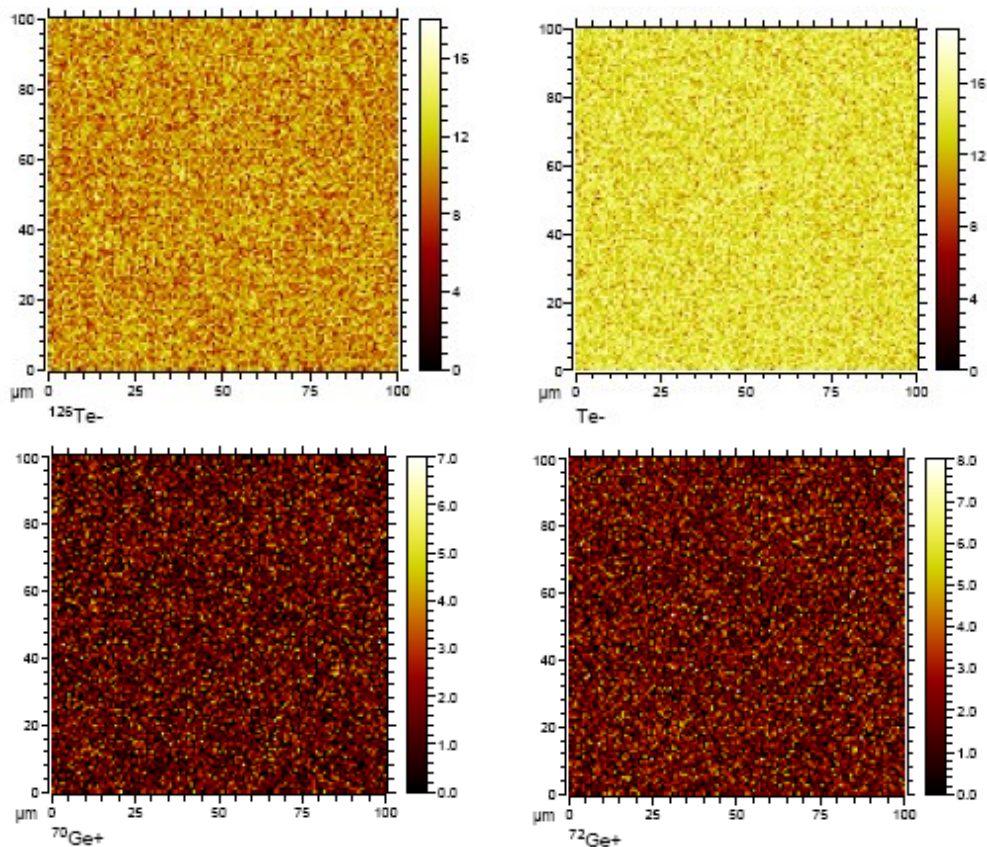
Figure III.19. Tof-SIMS images of the B5 sample. The images of Te distribution are obtained in negative polarity and the ones of Ge in positive polarity.

For further investigations of the crystalline structure of the deposited thin films, Raman spectroscopy measurements were done using the conditions mentioned in Chapter II. The Raman spectra are presented in Figures III.21 and III.22.
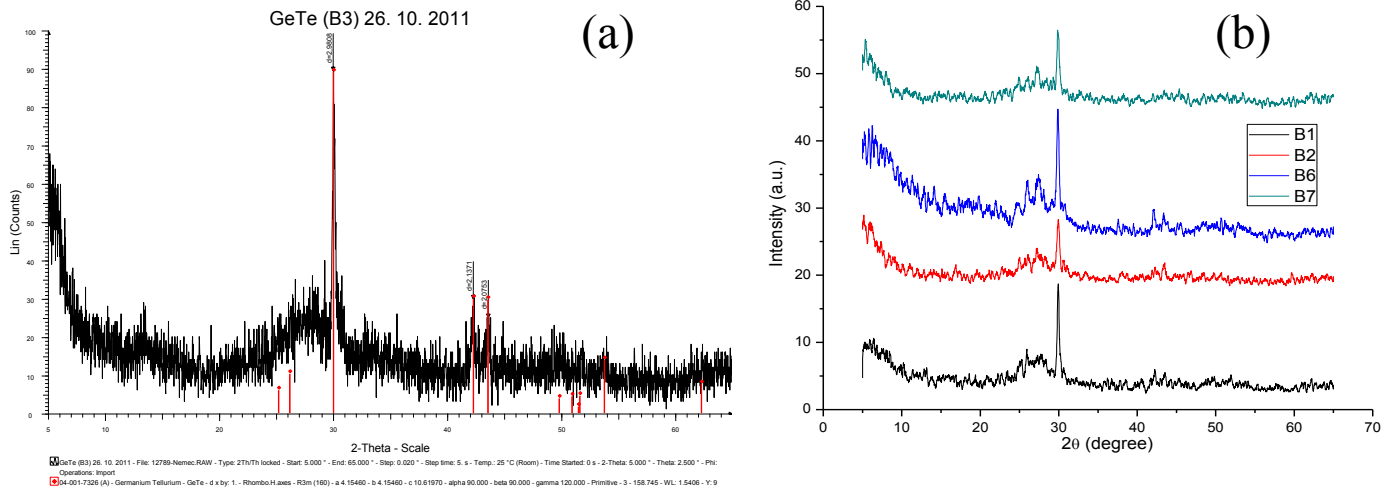
Figure III.20. XRD patterns of the GeTe samples.
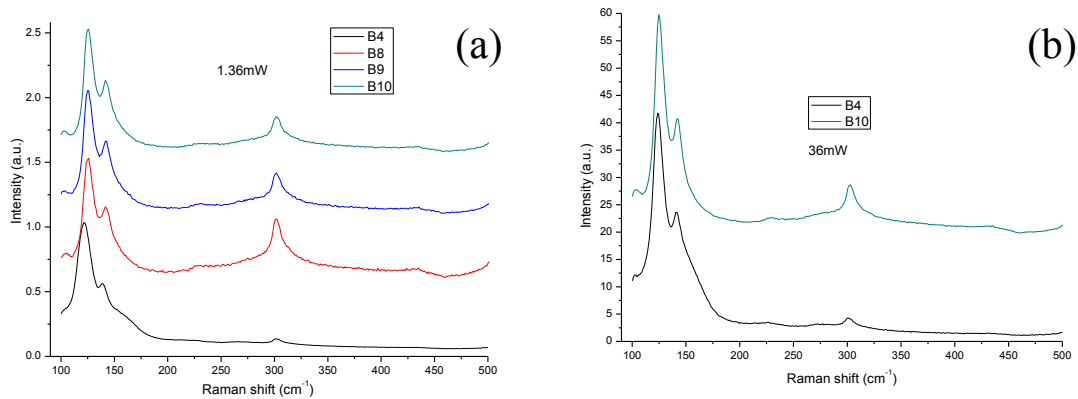
Figure III.21. Raman spectra of four thin films recorded using a (a) 1.36mW and (b) 36mW excitation laser power.

Figure III.21 presents the Raman spectroscopy analysis on four thin films (B4, B8, B9 and B10) when using two excitation laser powers. The B8, B9 and B10 samples were deposited at low fluences (d_{l-t} = 17cm) and target-substrate distances of 6, 4 and

2cm, respectively. For the B4 sample we used a higher fluence (d_{l-t} = 20cm) and a target-substrate distance of 6cm (the largest used in this set).

The main features of the recorded Raman spectra, in both cases were three peaks at 124, 140 and 301cm^{-1}. The first two peaks were also observed at the samples deposited by ns-PLD and coincide with A1 and E_{TO} modes in crystalline Te–Te chain. The peak at 301cm^{-1} is due to the contribution of the substrate and its presence indicates that these films are thinner than the other samples. The similarities between the Raman spectra recorded using different excitation laser powers do not suggest the presence of a phase change transformation process. The Raman spectra of the other six deposited samples are presented in Figure III.22.
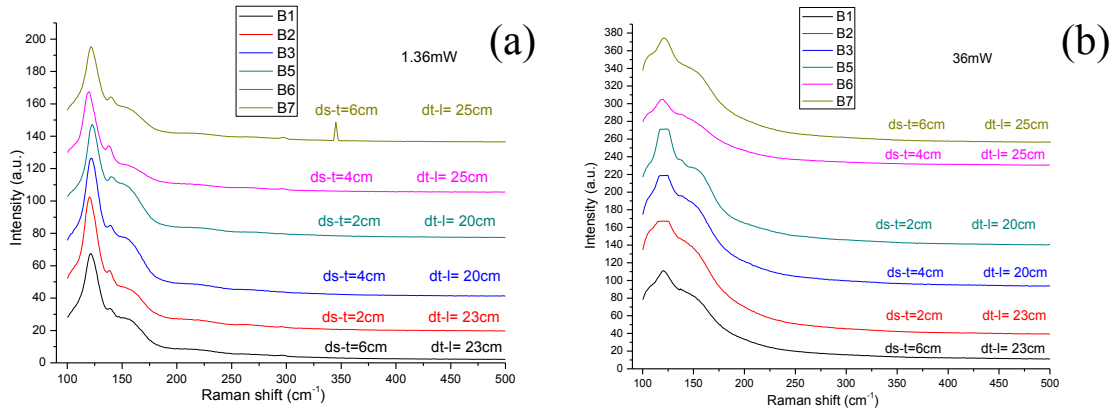
Figure III.22. Raman spectra of the GeTe thin films recorded at different excitation laser powers: (a) 1.36mW and (b) 36mW.

These films present different Raman spectra at 1.36mW excitation laser power which are characterized by the presence of an intense peak around 121cm^{-1}. However, one can still observe the contribution of two other bands (at ~140 and 160cm^{-1}) of the amorphous structure. As the thin films deposited in nanosecond regime, the Raman spectra recorded at 36.9mW present a wide band that is more likely to be coming from parasitic luminescence than from the material structure.

III.3.1.3   Conclusions on GeTe samples

The profilometry and optical microscopy images revealed great differences between the surface morphology of the thin films deposited in the two temporal regimes. While the samples deposited with an Nd-YAG laser present a rough surface with micro-sized particles, the fs-PLD thin films are uniform with fine « debris ». Although in the femtosecond regime lower fluences were used, the growth rate was not significantly decreased due to the high repetition rate of the Ti-Sa laser. EDS results on ns-PLD thin film revealed an up to 10% over-stoichiometry of Ge. The differences between the recorded content and the nominal composition were larger than the ones observed by Nemec et al. [2011a]. The Raman spectra acquired at 1.36mW excitation laser power were similar to the ones observed by Vinod et al. [2012a]. The main features of these spectra were two peaks at 125 and 141cm^{-1} which indicated Te segregation but at a molecular level. If there was Te segregation at a macroscopic range we would expect the images obtained by ToF-SIMS to reveal regions with an increased amount of Te and also the XRD patterns to present diffraction lines of Te structure. Moreover, the large vibrational bands recorded at 36mW did not suggest a phase transformation process induced by the increase in excitation power density.

Improved results related to thin film uniformity and stoichiometry were observed for the samples deposited in femtosecond regime. The deviations of Ge and Te concentrations from nominal ones for most films were below 2%. Depth profiles were obtained by ToF-SIMS analysis using two types of sputtering ion beams. The distributions of the main elements were slightly different in the two analyzing conditions. When oxygen ions were used to sputter a 300x300μm area, the Ge and Te distributions were much more uniform than the ones recorded when sputtering with a Cs ion beam.

The Raman spectroscopy results resemble from one deposition set to another. In femtosecond regime, correlations between the Raman response and the sample thicknesses were observed. For the thinner films, the silicon substrate vibrational modes were detected and no changes in Raman spectra were observed as the excitation laser power was increased.

III.3.2 Sb_2Te_3 thin films

III.3.2.1   Nanosecond regime

For this set of depositions, an Nd-YAG laser (10ns, 10Hz) was focused at 45° incidence on the target using the same lens (25 cm focal length) as for the GeTe samples. The deposition was done using configuration 2, the substrate was not rotated and the target was moved in the XY plane. The other varied experimental parameters were: target-substrate distance, laser energy and wavelength (see Table III.5). All the thin films were grown using $\sim 10^{-5}$ Torr pressure and 60 min deposition time.

Table III.5   Deposition parameters used for Sb_2Te_3 thin film growth

Sample	P (Torr)	$d_{s\text{-}t}$ (cm)	Laser (10Hz, 10ns)	t (min)	Thickness (nm)	Deposition rate (nm/min)
S1	$1.1 \cdot 10^{-5}$		λ=1064 nm, E=30 mJ, fluence ~3.8 J/cm^2		380	6.3
S2	$1.4 \cdot 10^{-5}$		λ=1064 nm, E=50 mJ, fluence ~6.4 J/cm^2		330	5.5
S3	$1.3 \cdot 10^{-5}$	4	λ=532 nm, E=50 mJ, fluence ~6.4 J/cm^2	60	230	3.8
S4	$9.8 \cdot 10^{-6}$		λ=355 nm, E=50 mJ, fluence ~6.4 J/cm^2		160	2.7
S5	$2.2 \cdot 10^{-5}$	3	λ= 266nm, E= 30mJ, fluence ~ 3.8 J/cm^2		620	10.3

As for GeTe thin films, the surface morphology of the deposited samples was investigated by stylus profilometry and optical microscopy. All the films present large particles on the surface due to the high fluence used for ablation. The estimated thicknesses are displayed in Table III.5. Comparing the S2, S3 and S4 samples, we observed that as the Nd-YAG laser wavelength decreases, the thickness of the deposited thin films presents a decrease from 330nm to 160nm. Considering that the other parameters were maintained, these thickness variations are due to the absorption mechanisms at laser-target interaction. A much higher thickness was observed for the S5 sample deposited using the lower laser wavelength, but a correlation with the previous

samples cannot be done since other parameters such as target-substrate distance and laser energy were varied. However, all the Ge-Sb-Te based thin films deposited in nanosecond regime using the 266nm laser wavelength present a much higher thickness among the samples of each set.

The presence of micro-sized particles on the surface of every thin film was confirmed by optical microscopy analysis. These results suggest that the experimental parameters used for deposition need to be reviewed in order to obtain samples with smooth surfaces. However, the increase of the target-substrate distance or the decrease of laser fluence will determine the use of a deposition time greater than 60 min in order to obtain 300nm thick films. This is another reason for which we used laser with high repetition rate for target ablation.

The presence of droplets at the sample surface was confirmed by SEM analysis as well. The EDS results obtained using both mentioned instruments are listed in Table III.6.

Table III.6   Chemical composition from EDS measurements

Sample	Atomic %		Instrument	Obs.
	Sb	Te		
	40	60		Nominal composition
Target	43.7	56.4	Tescan Vega II LMH	550x550μm
S1	48.6	51.5		550x550μm
	47.4	52.6		55x55μm
S3	47.2	52.8		550x550μm
	49.3	50.7		55x55μm
S4	47.8	52.2		550x550μm
	44.8	55.2		55x55μm
S5	50.5	49.5		550x550μm
	50.5	49.5		55x55μm
	50.6	49.4	JEOL JSM 6400	Analyzed area: droplets
	48.6	51.4		
	48.8	51.2		
	49.4	50.6		120x80μm
	49.5	50.5		

Higher concentrations of Sb and lower concentrations of Te were found, whether the analyzed area was on the droplets or not. A Sb over-stoichiometry was also observed

by Nemec et al. in their study on Sb_2Te_3 thin films obtained by PLD [Nemec et al. 2011a]. One should consider that even the target presented higher concentrations of Sb but the deviations were smaller than the ones observed for the thin films. However, this surely contributed to the increased Sb content found in the deposited samples.

The structural characteristics of the deposited samples were investigated by vibrational spectroscopy technique. The Raman spectra obtained using two different excitation laser powers (at 785 nm) are presented in Figure III. 23.
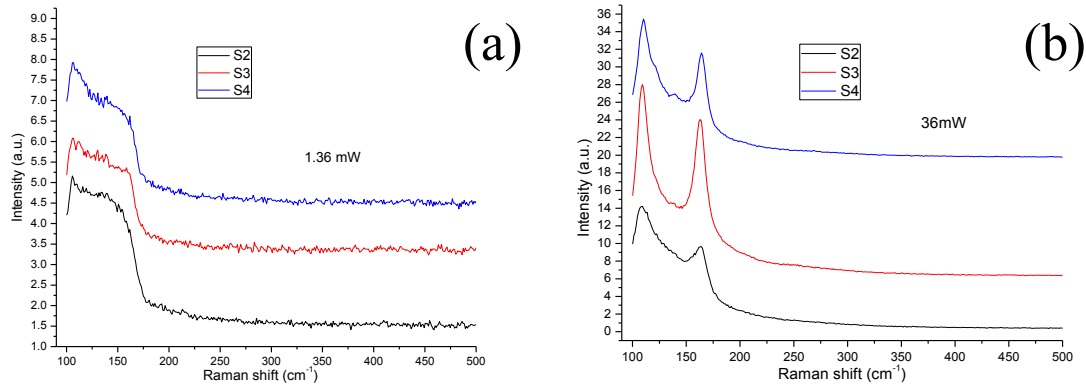
Figure III.23. Raman spectra recorded using (a) 1.36mW and (b) 36mW excitation laser powers.

Sb_2Te_3 has a rhombohedral (D_{3d}^5 symmetry) structure, with the following Γ point representation:

$$\Gamma = 2\left(A_{1g} + E_g\right) + 3\left(E_u + A_{2u}\right)$$

where the u-modes are Raman active and g-modes are IR active. Using density functional perturbation theory, Sosso et al. [2009] represented the IR and Raman spectra of crystalline Sb_2Te_3. The good agreement of their observations to the experimental vibrational spectra allowed them to assign each peak to specific phonons: E_g at 46 and 113 cm^{-1} and A_{1g} at 62 and 166 cm^{-1}. A sketch of the displacement patterns of phonons is also presented in their paper. Two peaks at 110 and 165cm^{-1} were also observed by Nemec et al. [2012] in their Raman study on Sb_2Te_3 bulk materials used as targets in the deposition process.

In our work, the Raman spectra of the thin films obtained at 1.36mW excitation laser power suggest an amorphous deposition, presenting a broad band between 106 and 165cm^{-1}. As the excitation laser power increases, the Raman spectra indicate that a phase transformation process occurs. The spectra recorded at 36mW are described by two peaks: 110 and 163cm^{-1}. In accordance with the data published in [Sosso et al. 2009] and [Nemec et al. 2012], the first peak was attributed to the active Raman E_g mode, while the second one to the A_{1g} vibrational mode.

Further structural investigations were done using the XRD technique. The pattern for the S5 sample is presented in Figure III.24. The right side figure is a magnified representation of the same pattern in the 23-44 degrees 2θ region.
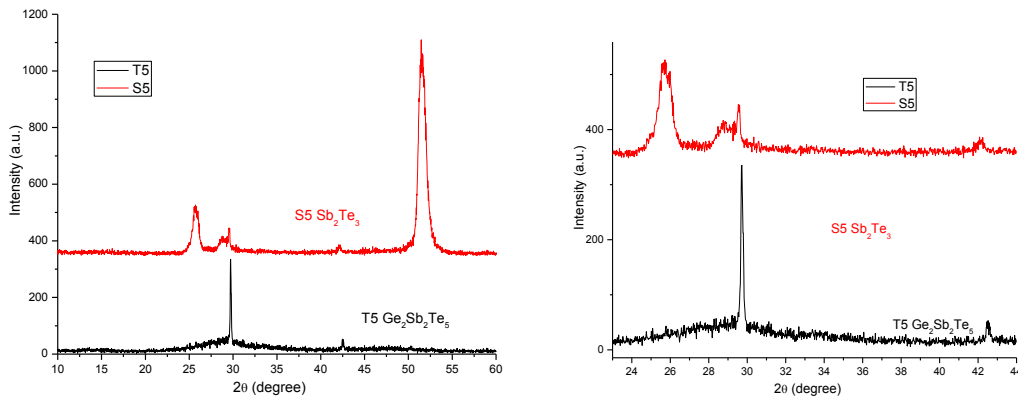
Figure III.24. XRD patterns of the S5 and T5 samples.

For comparison, in the same figure we presented the XRD results of one Ge$_2$Sb$_2$Te$_5$ thin film (T5) deposited by ns-PLD in the same conditions as S5 (266nm, 30mJ, 3.8 J/cm^2, 3cm, 60min). The XRD pattern of the S5 sample presents peaks with large widths (25.7, 28.8 and 42.16 degrees) that indicate small crystallite size. Moreover, another peak with shorter peak width at the same 2θ angle as the (200) diffraction line (at ~30 degrees) of the GST fcc structure was observed. One should consider that the XRD patterns of the thin films do not always resemble the ones of the bulk material due to their nanostructure and to the crystalline nature of the substrate. The XRD lines of the nanostructured sample can present different intensity ratios or could not be present at all. Our XRD results of the S5 sample indicated that two crystalline phases are present: one

characterized by the wider peaks and another one represented by the narrower diffraction line of the fcc structure. The first mentioned phase can be due to the excess of Sb in this sample. The larger diffraction lines from our XRD pattern were found at the same 2θ angles as the ones observed by Prokhorov et al. [2007] when analyzing thin films of Sb-Te with a higher Sb atomic %.

III.3.2.2   *Femtosecond regime*

In this temporal regime, three thin films of Sb_2Te_3 were deposited. The experimental parameters were: pressure=10^{-5}Torr, target-substrate distance=15mm, fluence=0.1 J/cm^2, deposition time=10min. These depositions were done using configuration 2 where the substrate was kept still and the target was moved in the XY plane.

The structural characteristics of the samples were investigated using optical microscopy and stylus profilometry. As seen for the GeTe samples an important uniformity improvement was observed from one temporal regime to another. The samples deposited using the fs Ti-Sa laser did not present micro-sized particles on the surface. Because of the reduced deposition time and fluence, the maximum thickness obtained was around 200 nm. EDS results were obtained for the $Sb_2Te_3\_1$ sample on two areas with different dimensions. When analyzing a 55x55μm region, the deviations from the nominal composition were below 1% while a 62.28% Te concentration (nominal composition 60%) was found when a 550x550 μm area was analyzed.

The Raman spectra of the analyzed samples at 1.36mW presented the same two peaks (120 and 140cm^{-1}) as the GeTe thin films detailed above where Te segregation was assumed (see Figure III.15). For the Sb_2Te_3 thin films deposited by fs-PLD the same two peaks (at 122cm^{-1} and 140cm^{-1}) were observed, regardless of the laser intensity used for analysis, whereas the Raman spectra of the samples obtained by ns-PLD pointed out a phase transformation process as the excitation laser power was increased from 1.36 to 36mW. These results support the ones observed for the $Ge_2Sb_2Te_5$ thin films deposited using different ablation regimes which suggested that the ns-PLD samples present more crystalline film deposition.

III.3.2.1   Conclusions on Sb$_2$Te$_3$ samples

The micro-structural analysis results revealed a uniformity improvement for the thin films deposited in femtosecond regime. While the ns-deposited samples present large particles on the surface, the thin films grown by fs-PLD have a lower roughness. The EDS measurements made on the thin film deposited in nanosecond regime presented an increased Sb content and a deficit of Te. Raman spectroscopy analysis revealed a more crystalline deposition for the ns-PLD samples. For high excitation laser powers, the observed vibrational modes for the ns-PLD samples were correlated to the ones of the bulk Sb$_2$Te$_3$ material. The XRD and Raman spectroscopy analysis suggested that the thin films grown in nanosecond regime are partially crystallized, with amorphous regions.

III.4 Deposition and characterization of Ge-Sb-Te thin films

III.4.1 GeSb$_2$Te$_4$

After having an insight on the two end points of the GeTe–Sb$_2$Te$_3$ pseudo-binary line we continued studying the intermediate materials based on Ge-Sb-Te compounds: GeSb$_2$Te$_4$ (GST 124), GeSb$_4$Te$_7$ (GST 147) and Ge$_2$Sb$_2$Te$_5$ (GST 225). We will start by presenting the structural results of GeSb$_2$Te$_4$ thin films deposited by ns-PLD. In this temporal regime, eight thin films were deposited: the first five were grown using configuration 2 (still substrate, target moved in the XY plane) and the last three using configuration 1 (still substrate, rotated target). The varied experimental parameters were the laser wavelength, energy, target-substrate distance and pressure. All these conditions are presented in Table III.7. The laser radiation was focused at 45° incidence angle. The substrate was not rotated during the deposition. Only the target was moved in the XY plane to ensure a fresh area ablation. No GST124 thin films were deposited by fs-PLD. The N-noted samples were deposited on glass substrate in Ar atmosphere. The rest of the samples were deposited on Si substrate.

Table III.7   Experimental conditions used for GeSb$_2$Te$_4$ thin film deposition

Sample	P (Torr)	d_{s-t} (cm)	Laser characteristics (10 ns, 10Hz)	t (min)	Thickness (nm)	Deposition rate (nm/min)
C1	$2.4 \cdot 10^{-2}$		λ=1064nm, E=50mJ, fluence~6.4 J/cm^2		400	6.7
C2	$1.6 \cdot 10^{-5}$	4	λ=1064nm, E=50mJ, fluence~6.4 J/cm^2		390	6.5
C3	$1.3 \cdot 10^{-5}$		λ=532nm, E=50mJ, fluence~6.4 J/cm^2	60	250	4.2
C4	$1.3 \cdot 10^{-5}$		λ=355nm, E=50mJ, fluence~6.4 J/cm^2		100	1.7
C5	$1.2 \cdot 10^{-5}$	3	λ=266nm, E=30mJ, fluence~3.8 J/cm^2		600	10
N1	$4.5 \cdot 10^{-5}$		λ=266nm, E=56mJ, fluence~2.4 J/cm^2	15	180	1.2
N2	$4.5 \cdot 10^{-5}$	6	λ=266nm, E=28mJ, fluence~1.2 J/cm^2	15	130	0.9
N3	$4.5 \cdot 10^{-5}$		λ=266nm, E=28mJ, fluence~1.2 J/cm^2	30	150	5

As observed for the other thin films grown by ns-PLD, the deposited samples present a high roughness. Moreover, the thickness diminishes as the wavelength of the laser radiation decreases from 1064 to 355nm (see Table III.7). The same tendency was observed for Sb$_2$Te$_3$ thin films. Again, the sample deposited with the lowest laser wavelength (λ=266nm) on Si substrate presented the highest thickness. The smaller thicknesses observed for the last three samples (N1, N2 and N3) is explained by the higher target-substrate distance and low fluence. The deposition of large particles on the sample surface was confirmed by optical microscopy. No significant changes from one sample surface to another were observed.

The chemical compositions of the C1 and C5 sample were investigated by EDS. The results are listed in Table III.8. While the Ge content is close to the nominal composition, the Sb concentration was found to be higher than the stoichiometric value. Same behavior was observed for the N1, N2 and N3 samples but the differences between the recorded values and the theoretical ones were smaller. As observed for the Sb$_2$Te$_3$ target, even the bulk material used for deposition presents small deviations from the nominal composition. This is probably due to the limited precision in concentration estimation of the EDS instrument.

Table III.8   EDS results for the C5 sample

Sample	Atomic %			Instrument	Obs.
	Ge	Sb	Te		
Nominal composition	14.28	28.57	57.14		
Target	13.7	30.8	55.5	Tescan Vega II LMH	550x550μm
	15.8	29.3	54.9		55x55μm
C1	13.7	40	46.3		550x550μm
	13.2	37.4	49.4		550x550μm
C5 $GeSb_2Te_4$	13.1	35.8	51.1	JEOL JSM 6400	Droplet
	13.4	35.7	50.9		120x80μm
N1	14.7	32.4	52.9	Tescan Vega II LMH	550x550μm
	15.2	33.9	50.8		55x55μm
N2	14.8	31.2	54.1		550x550μm
	15.7	31.7	52.6		55x55μm
N3	15.5	30	54.5		550x550μm
	14.2	31.4	54.4		55x55μm

Uniform distribution of the main elements and of their compounds was observed when analyzing the C1 and C5 sample in positive and negative polarity by ToF-SIMS.

The structural properties were further investigated using Raman spectroscopy. The vibrational spectra recorded using 1.36 and 36mW excitation radiation powers are presented in Figure III.25.
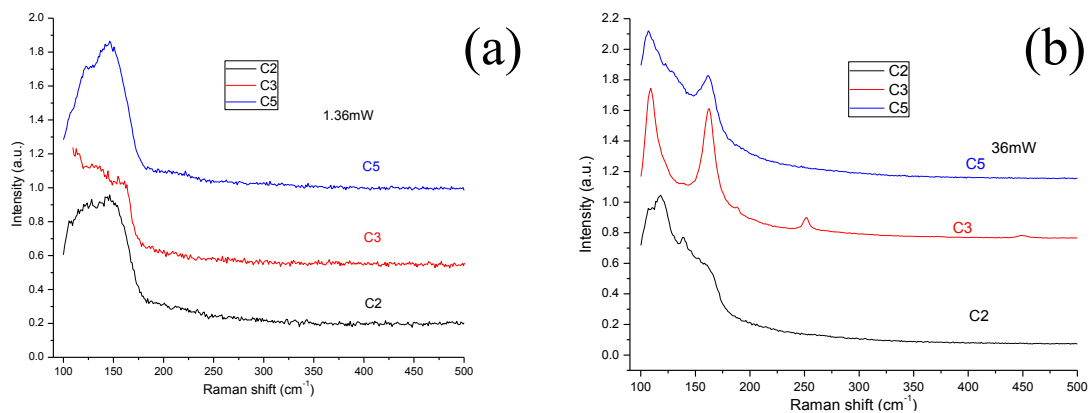
Figure III.25.   Raman spectra recorded at (a) 1.36mW and (b) 36mW excitation laser powers.

The different Raman spectra recorded at 1.36 mW and 36 mW excitation laser powers suggest a phase transformation process, but the different vibrational modes observed in each above representation suggest different chemical compositions. The broad bands observed in the spectra recorded at 1.36mW indicate the formation of amorphous thin films. The Raman modes in the spectra recorded at 36mW are different. While the C3 and C5 samples present two clear peaks at 110 and 160cm^{-1}, in the case of C2 sample two additional peaks appear: at 120 and 140cm^{-1}. The GeSb$_2$Te$_4$ bulk material studied by Nemec et al. [2012] also presented two vibrational modes when analyzed by Raman spectroscopy (110 and 160cm^{-1}). Based on the interpretation of the Raman spectra of GeTe and Sb$_2$Te$_3$ crystals, they attributed the bands of GST materials at ~115-110 cm^{-1} and 165 cm^{-1} as corresponding to $\Gamma_1(A_1)$, E_g (2) and A_{1g} (2) modes, respectively [Nemec et al. 2012]. The Raman response of the GST124 crystal studied by Cho et al. [2006] was characterized by four phonon modes, three of which were observed above 100cm^{-1}, at ~115, ~140 and ~165 cm^{-1}. A clear assignment of these bands to the vibrational modes was not reported. The Raman spectra recorded at 36mW from our study indicate the formation of an fcc crystalline structure for the C3 and C5 samples but also that the C2 thin films can present regions with Te segregation. The Raman spectroscopy results of the N1, N2 and N3 samples revealed an amorphous deposition. However, only spectra at low excitation laser powers (0.71mW) were acquired. The XRD spectrum of the C5 sample indicates that the thin film is crystalline presenting an fcc structure.

The structural analysis techniques (Raman spectroscopy and XRD) indicate that the deposited thin films present a combination between an amorphous phase and a crystalline structure. While the XRD analysis reveals a long range order, the Raman spectra recorded at low excitation laser powers suggest the presence of an amorphous region.

III.4.2 GeSb$_4$Te$_7$

Another intermediate material in the GeTe – Sb$_2$Te$_3$ tie line is GeSb$_4$Te$_7$. In the nanosecond regime, six GST147 thin films were deposited by varying several deposition parameters: target-substrate distance, fluence, Nd-YAG laser wavelength and deposition time. The experimental conditions are summarized in Table III.9. The incidence angle of

the laser beam was 45°. for these depositions we used configuration 2 with a non-rotated substrate and a target moved in the XY plane. No samples were deposited by femtosecond PLD using this material as target.

Table III.9   Experimental conditions used for GST147 thin film depositions

Sample	P (Torr)	d_{s-t} (cm)	Nd-YAG Laser (10 ns, 10Hz)	t (min)	Thickness (nm)	Deposition rate (nm/min)
P1	$1.2 \cdot 10^{-5}$		λ=1064nm, E=50mJ, fluence~6.4 J/cm^2		360	6
P2	$1.2 \cdot 10^{-5}$		λ=1064nm, E=30mJ, fluence ~3.J/cm^2	60	340	5.7
P3	$1.2 \cdot 10^{-5}$	4	λ=532nm, E=50mJ, fluence ~6.4 J/cm^2	30	130	4.3
P4	$1.3 \cdot 10^{-5}$		λ=532nm, E=50mJ, fluence ~6.4 J/cm^2		170	2.8
P5	$1.3 \cdot 10^{-5}$	3	λ=355nm, E=30mJ, fluence ~3.8 J/cm^2	60	200	3.3
P6	$2.2 \cdot 10^{-5}$		λ=266nm, E=30mJ, fluence ~3.8 J/cm^2		600	10

All the thin films present large particles on the surface. However the last two samples present an improved uniformity. These films were deposited using a lower fluence but a shorter target-substrate distance. Comparing the P2, P5 and P6 samples one can observe that as the laser wavelength is decreased from 1064nm to 355nm the thickness of the samples decreases as well (Table III.9). The laser wavelength was not the only varied parameter for these films, but the target-substrate distances as well. Still, the larger target substrate distance usually determines a shorter thickness. Moreover, the P6 sample deposited using the 266nm of the Nd-YAG laser is the thickest among the six samples. These conclusions were also drawn when the Sb_2Te_3 and GST124 thin films were discussed. The thickness variations were small when the laser energy (P1-P2) or deposition time (P3-P4) were varied. These indicate a non-linear deposition rate as the two mentioned experimental parameters are varied, at least for the GST147 material. This is probably due to the high fluence regime. The optical microscopy images support the results observed from profilometry measurements, namely the presence of micro-sized particles and the improved uniformity of the last two deposited samples: P5 and P6 (see Figure III.26).
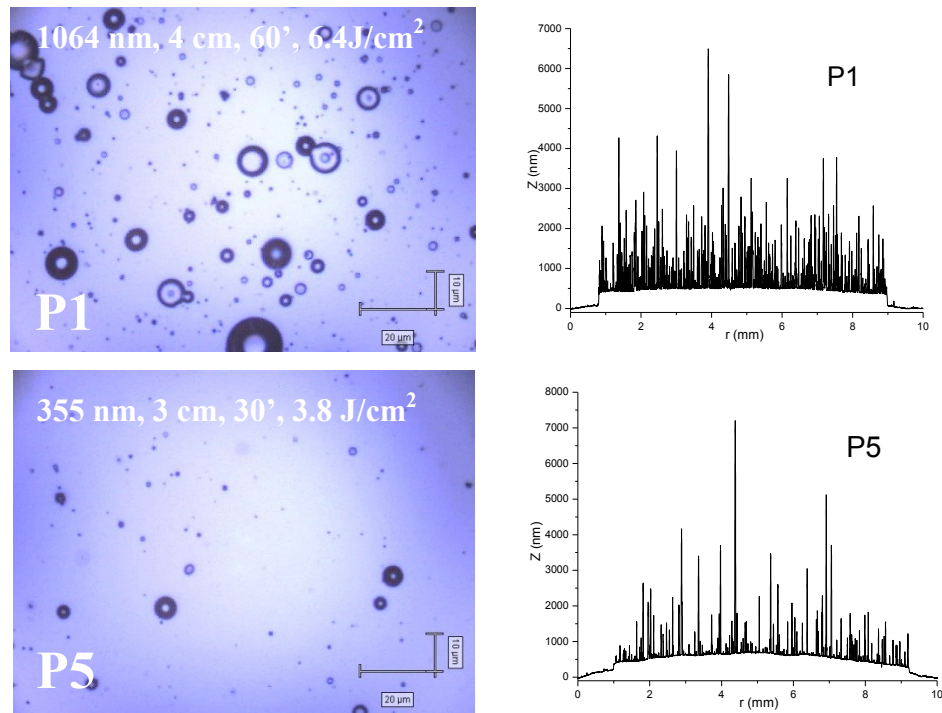
Figure III.26. Optical microscopy images (left side) and stylus profilometry (right side) of the P1 and P5 samples.

Information on the composition of the samples was obtained by EDS technique using the two instruments (see Table III.10). Whether the measurements were done on droplets ore large areas the trend is the same: increased Sb content and decreased Te concentration related to nominal composition. The same behavior was observed for thin films of GST147 obtained by Nemec et al. [2011a] by ns-PLD, but their deviations were below 4%. For Ge instead, fluctuations around the stoichiometric value (±2at%) were observed from one acquisition to another.

Table III.10   EDS results of the GST 147 samples

Sample	Atomic %			Instrument	Obs.
	Ge	Sb	Te		
	8.33	33.33	58.33		Nominal composition
Target	12	33.4	54.6	Tescan Vega II LMH	550x550µm
	11.1	33.9	55.0		55x55µm
P1	11.8	39.3	48.9		550x550µm
	9	42.3	48.8		55x55µm
P4	15.3	38.5	46.2		550x550µm
	17.6	38.9	43.5		55x55µm
P5	9.9	39.5	50.7		550x550µm
	11.1	38.2	50.7		55x55µm
P6	9.6	39.8	50.6	JEOL JSM 6400	Droplet
	7.2	42.4	50.4		
	9.8	39.5	50.7		
	10.5	37.1	52.5		
	9.1	45.1	45.9		
	8.4	45.3	46.3		120x80µm
	8.4	44.4	47.7		
	7.8	44.8	47.3		

To analyze the composition in the inner layers of the thin film, in-depth profiles of the main elements in P4, P5 and P6 samples were obtained using ToF-SIMS technique. The as obtain distributions of Ge, Sb, Te and of their isotopes and compounds are represented in Figure III.27. A surface of 500x500µm was sputtered with a Cs ions beam (1kV, 60nA) and a 400x400µm area was analyzed using a Bi_3^+ ion beam (25kV). These results revealed a uniform distribution of Ge and Sb while an elevated Te content was observed at the region close to the thin film surface. This can come also from matrix effect due to oxidation at interface. As Te has a more pronounced metallic character, it can be more affected by this. The same behavior was observed in the GST 225 thin films deposited by Krusin-Elbaum et al. [2007] by magnetron sputtering on Si substrate. Their work revealed that the deposited samples present Te segregation on grain boundaries and surfaces. The composition of the main elements on the thin film surface was determined by proton induced x-ray emission (PIXE) and Rutherford back-scattering (RBS). These results also revealed lower Ge and Te contents and higher Sb concentrations than the nominal composition, but no Raman spectroscopy measurements were reported.

Moreover, correlations between the thickness of the sample and the sputtering time at which the Si composition increases (time when the Cs ions reach the substrate) were observed. From this dependence we obtained information on the sputtering rate of GST147 thin films by the Cs ion beam. The analyzing conditions were the same for all three samples. From the linear fitting of this dependence we estimated a mean sputtering rate of 0.6 nm/s.

The structural characteristics of the samples were investigated by Raman spectroscopy. As observed for the GST 124 thin films, a wide band recorded for low excitation laser powers indicated an amorphous deposition. As the Raman laser intensity increases, a phase transformation process is induced. For 36mW analyzing conditions, the Raman spectra present two narrow peaks around 107 and 162cm^{-1}. However, slightly different vibrational spectra were observed for the P6 sample, in both analyzing conditions. These variations on Raman response related to other samples can be due to different chemical concentrations.

The XRD analysis indicates that the P6 thin film is crystalline. Two sets of diffraction lines were observed: one corresponding to the silicon substrate and another one associated with the GST147 fcc structure. The Raman spectroscopy analysis and XRD measurements indicate that the thin films present both amorphous and crystalline phases. While the micro-volumes analyzed by Raman spectroscopy appear to be amorphous, the XRD pattern suggests the existence of a long range order.
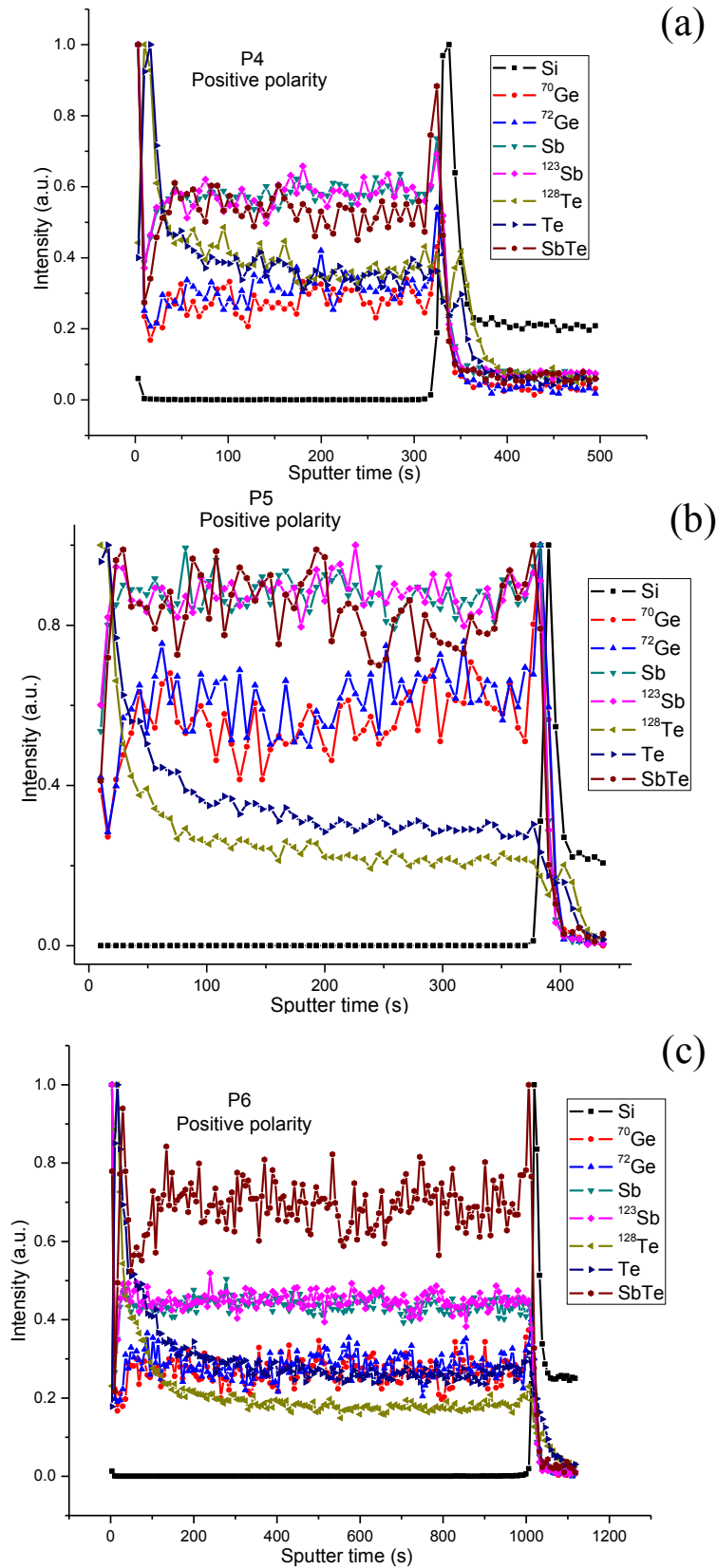
Figure III.27. ToF-SIMS depth profiles of (a) P4, (b) P5 and (c) P6 samples.

III.4.3 Ge$_2$Sb$_2$Te$_5$

III.4.3.1   Nanosecond regime

Finally, the third material based on GeTe and Sb$_2$Te$_3$ compounds studied in this thesis is the Ge$_2$Sb$_2$Te$_5$ chalcogenide. In the nanosecond regime, the radiation from an Nd-YAG laser with different wavelengths was focused on the target at 45° incidence. The T-noted samples were deposited using configuration 2 (the substrate was not rotated but the target was moved in the XY plane) while the last two samples were deposited using configuration 1 (the substrate was kept still and the target rotated and translated along the X axis). The target was moved in the XY plane while the substrate was kept still. The other varied experimental parameters were: target-substrate distance and laser fluence (see Table III. 11). The deposition of the last two samples (F1 and F2) was done in Ar atmosphere on glass substrate while the first five films were grown on Si.

Table III.11   Detailed experimental conditions used for GST 225 thin film depositions

Sample	p (Torr)	d$_{s-t}$ (cm)	Laser characteristics (10 ns, 10Hz)	t (min)	Thickness (nm)	
					Profilometry	Ellipsometry
T1	$1.3 \cdot 10^{-5}$		λ=1064 nm, fluence~6.4 J/cm^2		350	440
T2	$1.2 \cdot 10^{-5}$	4	λ=1064 nm, fluence~3.8 J/cm^2		250	240
T3	$1.2 \cdot 10^{-5}$		λ=532 nm, fluence~6.4 J/cm^2	60	190	210
T4	$1.3 \cdot 10^{-5}$	3	λ=355 nm, fluence ~3.8 J/cm^2		110	120
T5	$1.2 \cdot 10^{-5}$		λ=266 nm, fluence~3.8 J/cm^2		690	770
F1	$4.5 \cdot 10^{-5}$ (in Ar gas)	6	λ=266 nm, fluence~4.3 J/cm^2	15	90	-
F2	$4.5 \cdot 10^{-5}$ (in Ar gas)		λ=266 nm, fluence~2.4 J/cm^2	30	350	-

For most thin films, the thicknesses obtained by stylus profilometry were confirmed by ellipsometry measurements (Table III. 11). With T1 as an exception, the variation between the thicknesses obtained by the two techniques is below 10%. The

profiles indicate a rough surface for all samples. As observed for the other thin films obtained in nanosecond regime, the surface morphology is affected by the presence of large particles. Comparing the results for the t-noted samples the use of the 266 nm radiation did not result in smoother surface films, contrary with what was observed for the previous compositions. However, some similarities such as: the decrease of thin films thickness as the laser radiation is decreased from 1064nm to 532nm or the deposition of a much thicker sample when the 266nm radiation is used (T5) for ablation were also observed. Comparing the T1 and T2 samples, one can observe that as the energy of the laser decreases the thickness of the deposited samples is reduced. This is to be expected due to the lower amount of particles that are ejected from the target surface. The optical microscopy images suggest the same uniformity related conclusions as the ones drawn from profilometry measurements.

The chemical compositions of the deposited thin films were investigated by EDS measurements using two instruments: Tescan Vega II LMH (Technical University of Iasi, Romania) and JEOL JSM 6400 (Université de Rennes, France). The EDS results obtained using the Tescan Vega II LMH instrument are displayed in the next table. The atomic percentages were obtained analyzing the K, L and L series of Ge, Sb and Te, respectively using a 30kV accelerating voltage. These results revealed a higher concentration of Ge and Sb and a lower concentration of Te, an exception being observed for the T5 sample in which the Ge atomic percentage was smaller than the nominal composition.

Table III.12 EDS results on the GST 225 samples obtained using the Tescan Vega II LMH instrument.

Sample	Atomic %		
	Ge	Sb	Te
Nominal composition	22.22	22.22	55.55
Target	21.9	23.6	54.5
T1	27.5	29.6	42.9
T2	23.6	28.6	47.8
T3	31.9	25.7	42.4
T4	26.9	27.9	45.2
T5	19.6	28.6	51.8
	20.4	29.3	50.2

The EDS results recorded using the JEOL JSM 6400 instrument were obtained analyzing the L-series of the main elements using a 10kV accelerating voltage.

Table III.13   EDS results of the GST 225 thin films

Sample	Atomic %			Obs.
	Ge	Sb	Te	
	22.22	22.22	55.55	Nominal composition
T1	24	30.3	47.5	Droplet
	21.8	29	49.2	Large area
T2	19.8	27	53.2	Droplet
	20.6	25.6	53.8	Large area
T3	22.6	25	52.4	Droplet
	22.5	26.7	50.8	Large area
T4	21.4	26.9	51.7	Droplet
	24.6	26.6	48.8	Large area
T5	12.8	31.8	55.5	Droplet
	25.2	26.8	48	Droplet

As observed from the EDS results detailed earlier, the thin films present regions with different chemical properties. All the samples present higher concentrations of Sb and lower concentrations of Te. In most cases, Ge content is lower than the stoichiometric value, especially when droplets are analyzed. Comparing the EDS results, we observed that differences in chemical concentrations are recorded when the analyzing conditions such as accelerating voltage or element series are varied. For example the concentration values found for Ge are closer to nominal composition when the second instrument was used. Different series were used to obtain the concentrations: K-series for the first instrument and L-series for the second one.

ToF-SIMS analysis was used to obtain further information on the chemical distribution. The figure below presents the distribution of the main elements and other compounds inside the F2 thin film. The profiles were obtained using a beam of Cs ions (2keV, 240 nA) to sputter a 300x300μm area and a beam of Bi ions (25kV, 1.2pA) to analyze a 100x100μm inner-surface.
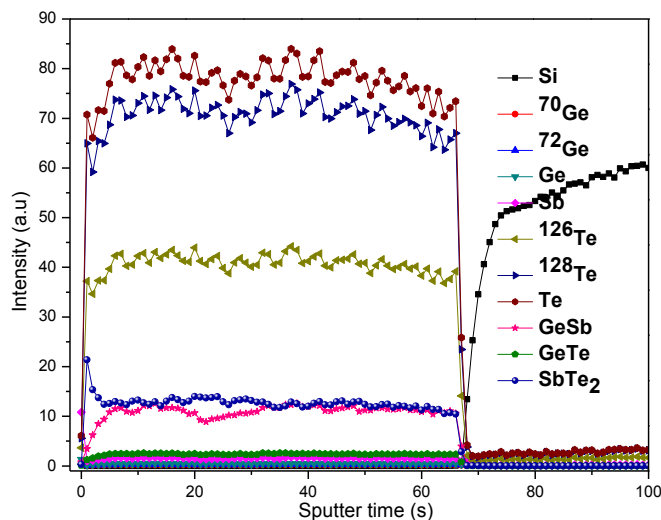
Figure III.28. ToF-SIMS depth profiles of the F2 sample obtained in negative polarity.

The Raman spectroscopy results are presented in Figure III.29. As observed for the other types of thin films, the Raman spectra differ when various laser powers are used for analysis. For low excitation laser powers, two vibrational modes can be observed at 120 and 146cm^{-1} which suggest an amorphous phase deposition. The Raman spectra at 36mW indicate an evolution in crystallinity. The main features are represented by two peaks: the one at 109 cm^{-1} that may correspond to the tetrahedral GeTe$_4$ and the one at 161 cm^{-1} to the Sb-Sb bonds, connected to other four Te or Sb atoms. For the T3 and T4 samples, these peaks are not well defined, suggesting a lower crystallization of the analyzed volume.
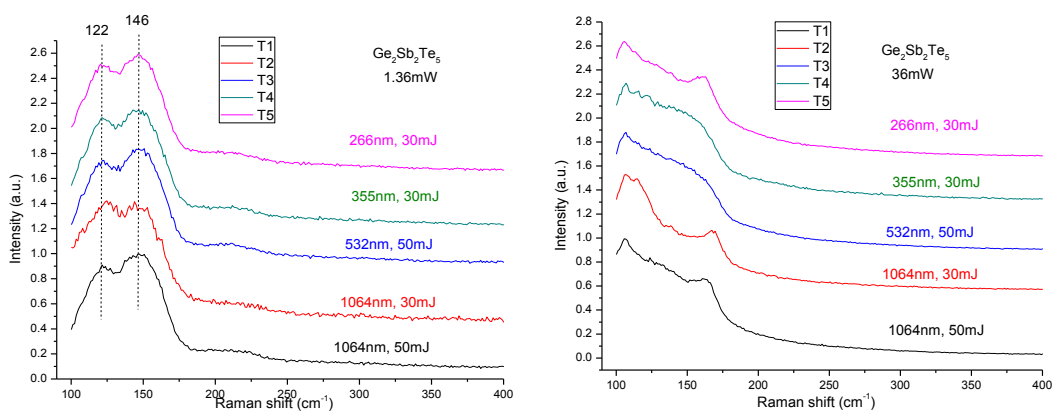
Figure III.29. Raman spectra of the GST 225 thin films recorded using (a) 1.36mW and (b) 36mW excitation laser power.

For more information on the structural characteristics of the deposited samples, XRD measurements were performed at room temperature. The recorded patterns are presented in Figure III.30. Beside the diffraction lines of the silicon substrate, two additional peaks, that were assigned to the distorted fcc structure, were observed. Thus all the diffraction patterns indicate that the thin films are crystallized but in different proportions. For example, the highest crystallinity was observed for the T3 sample deposited using the second harmonic of the Nd-YAG laser while the T1 sample present the lowest intensity of the (200) diffraction line. The single varied parameter for the last two mentioned samples was the laser wavelength. Thus the ablation processes can also affect the cristallinity of the sample, not only the surface morphology.
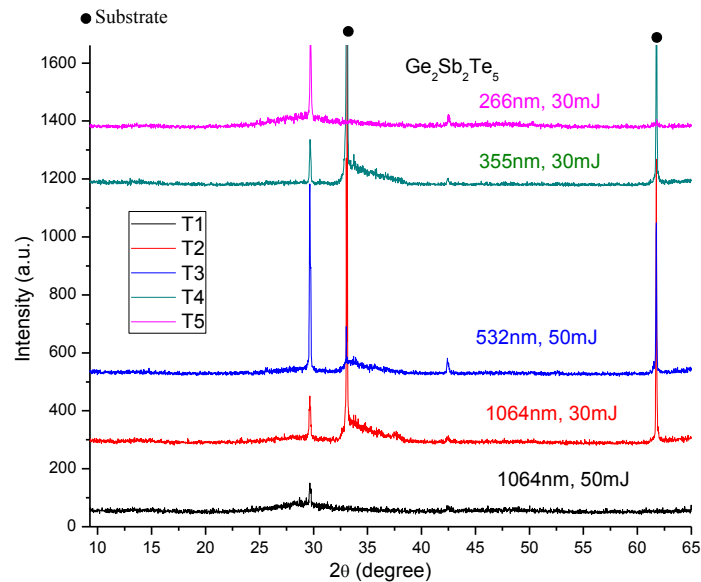
Figure III.30. XRD patterns of the GST 225 thin films.

As observed for the Sb_2Te_3 samples, the structural analysis results indicate that the GST 225 thin films are partially crystallized with amorphous areas. Moreover, Raman spectroscopy results revealed that structural transformations can occur when high enough excitation laser powers are used.

108
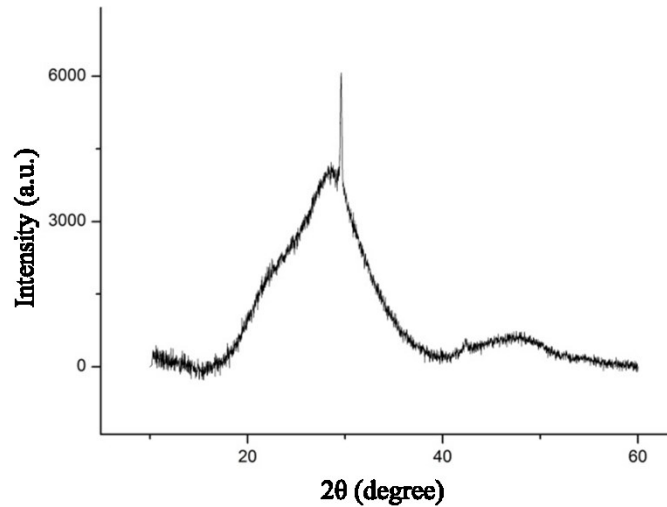
Figure III.31. XRD pattern of the F2 sample.

The XRD pattern of the F2 sample is presented in Figure 31. Even in this case one can observe the diffraction line of the crystalline material at $\sim 30^{\circ}$ 2θ angle. For this sample, the glass substrate contribution is superimposed on the thin film signal.

III.4.3.2   *Femtosecond regime*

In this temporal regime, three sets of depositions were performed. The experimental conditions are presented in Table III.14. For target ablation we used the 800nm radiation from a Ti-Sa laser, with energy of 1.6mJ and a repetition rate of 1kHz. The pressure inside the deposition chamber was maintained at approximately 10^{-5} Torr.

The deposited thin films were analyzed using stylus profilometry and optical microscopy. The obtained thickness values are summarized in Table III.14. The increase in deposition time determined an expected increase in thickness values. However, some discrepancies were detected when comparing the profilometry results of $Ge_2Sb_2Te_5\_2$ - $Ge_2Sb_2Te_5\_6$ samples. Although in some cases, the time of deposition was three times higher, the thicknesses of the deposited samples were approximately the same. Compared with the GST 225 thin films deposited in the nanosecond regime, these samples present a much smoother surface as optical microscopy images reveal as well (see Figure III.32).

Table III.14 Deposition conditions and thickness values of the GST 225 thin films deposited by femtosecond PLD

Sample	$d_{s\text{-}t}$ (cm)	Fluence (J/cm^2)	t (min)	Thickness (nm)	Deposition rate (nm/min)
Set 1: For these depositions we used configuration 2. The substrate was not rotated but the target was moved in the XY plane
Ge$_2$Sb$_2$Te$_5$_1	1.5		20	N/A	N/A
Ge$_2$Sb$_2$Te$_5$_2			10	90	9
Ge$_2$Sb$_2$Te$_5$_3			15	185	12.3
Ge$_2$Sb$_2$Te$_5$_4			20	110	5.5
Ge$_2$Sb$_2$Te$_5$_5		0.1	30	84	2.8
Ge$_2$Sb$_2$Te$_5$_6			5	100	20
Ge$_2$Sb$_2$Te$_5$_7	1.6		20	220	11
Ge$_2$Sb$_2$Te$_5$_8			10	92	9.2
Ge$_2$Sb$_2$Te$_5$_9			5	N/A	N/A
Ge$_2$Sb$_2$Te$_5$_10			20	1277	63.8
Ge$_2$Sb$_2$Te$_5$_11		0.21	20	690	34.5
Ge$_2$Sb$_2$Te$_5$_12			10	200	20
Ge$_2$Sb$_2$Te$_5$_14			5	50	10

Sample	$d_{s\text{-}t}$ (cm)	Fluence (J/cm^2)	t (min)	Thickness (nm)	Deposition rate (nm/min)
Set 2: For these depositions we used configuration 2. The substrate was rotated and the target was moved in the XY plane
H1			30	750	
H2			20	N.A.	N.A.
H3			10	N.A.	N.A.
H4	4	0.108	30	600	20
H5				N.A.	N.A.
H6			20	130	6.5
H8				N.A.	N.A.
H10			10	N.A.	N.A.

Sample	$d_{s\text{-}t}$ (cm)	Fluence (J/cm^2)	t (min)	Thickness (nm)	Deposition rate (nm/min)
Set 3: For these depositions we used configuration 3. The substrate was kept fix and the target was rotated and translated along the X axis
GST225_1	4	0.27	30		
GST225_2				300	10
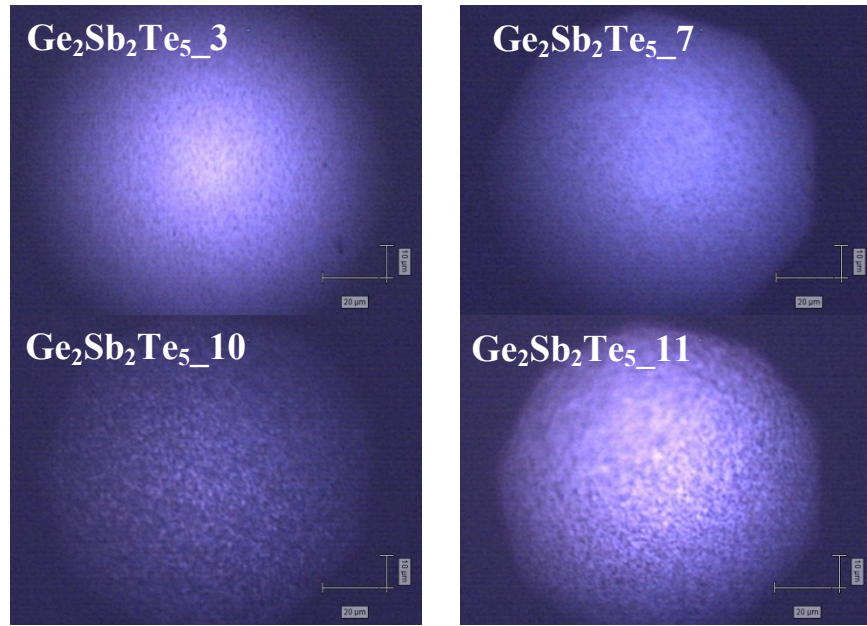
Figure III.32. Optical microscopy images of GST 225 samples deposited in femtosecond regime.

The chemical composition was investigated using EDS technique (both Tescan Vega II LMH and JEOL JSM 6400 instruments). Table III.14 summarizes the atomic percentages found when analyzing different areas on the sample surface using the K, L and L lines of Ge, Sb and Te respectively and a 30kV acceleration voltage (Tescan Vega II LMH). The H3 and GST225_2 samples were analyzed using the JEOL JSM 6400 instrument with a 10kV accelerating voltage. For concentration determination, the L series were taken into consideration.

Except H1 and GST225_2 samples for which the atomic% were close to nominal composition, the other thin films present a much higher concentration of Ge, as compared to the ns-PLD samples where a surplus of Sb was found. Due to the over-stoichiometry of Ge/Sb, a deficit of Te and Sb/Ge was detected for both types of thin films. The atomic percentages of the main elements in the thin films deposited by fs-PLD are much closer to the stoichiometric ones than the concentrations found in ns-deposited films.

Further investigations on the structural properties of the samples were done using ToF-SIMS analysis. The figures below present the distribution of the main elements and other compounds inside the thin film. The profiles from Figure III.33 were obtained using

a beam of Cs ions (1keV, 93 nA) to sputter a 300x300μm area and a beam of Bi ions (25kV) to analyze a 100x100μm inner-surface.

Table III.15   EDS results on GST 225 thin films deposited by femtosecond regime

Sample	Atomic %		
	Ge	Sb	Te
	22.22	22.22	55.55
Target	21.9	23.6	54.5
H1	22.3	22.8	54.9
	22.4	22.6	54.9
H2	29	22	49
	31.2	21.1	48.8
H3	26.8	19.4	53.9
	25.5	19.3	55.2
	25.8	20	54.2
H4	24.5	23.3	52.2
	25.3	22.8	51.9
H5	29.7	21.1	49.2
	30.1	20.8	49.1
GST225_2	21.4	22.5	56.1
	22.8	21.4	55.8
	22.6	22.3	55.2
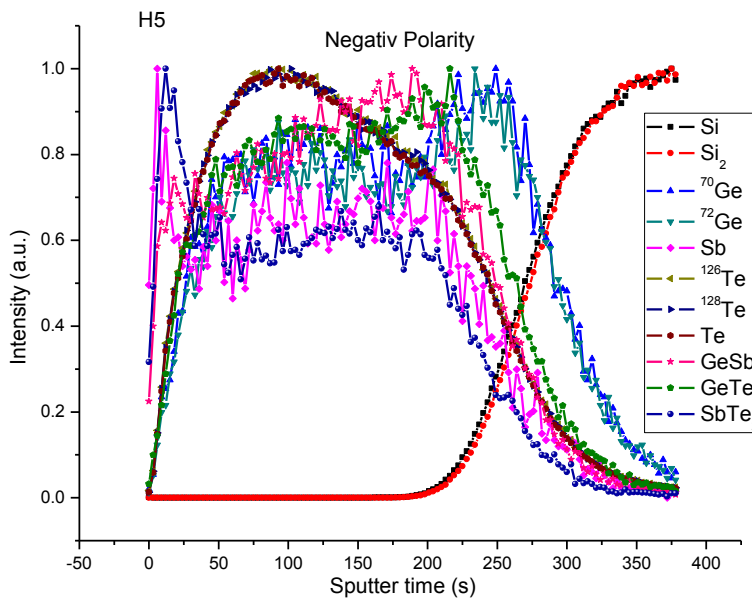
Figure III.33. ToF-SIMS depth profiles of Ge, Sb and Te and of their compounds for the H5 sample.

The Ge and Te ions present the same trend as in GeTe thin film (B5): a higher concentration of Te in the first half of the thin film and an elevated content of Ge in the region close to the thin film-substrate interface. Antimony ions present a higher concentration in the first 20seconds of the acquisition. These results, together with the ones obtained by EDS measurements indicate that the Ge and Sb concentration variations from the nominal composition are larger in the samples volume than on the surface. Another set of depth profiles were obtained using, instead of Cs ions, oxygen ions (1kV, 243nA) to sputter the samples. The Bi ion beam characteristics were: 25kV and 0.25pA.
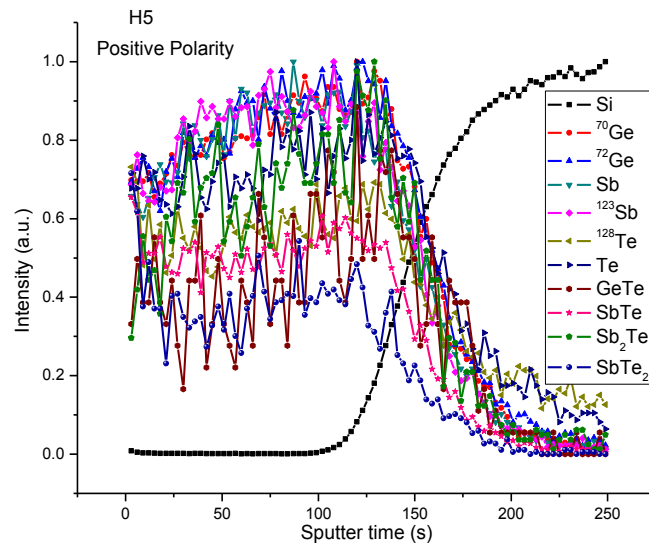
Figure III.34. ToF-SIMS measurements on H5 sample using oxygen ions for sputtering.

As it was observed for the GeTe B5 sample, the profiles recording using oxygen ions for sputtering are more uniform than the ones obtained by Bi ion sputtering.

Structural characteristics of the deposited samples were investigated by Raman spectroscopy in different conditions. The results are represented in the next figures. Two types of Raman spectroscopy responses were observed, depending on sample thickness. The first type is represented in Figure III.35.
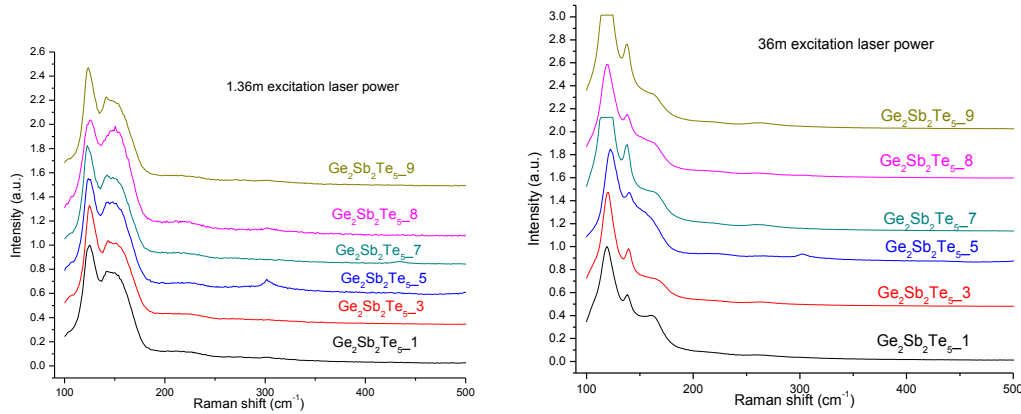
Figure III.35. Raman spectroscopy analysis of several thin films deposited by PLD in femtosecond regime.

The Raman spectra obtained using a 1.36mW excitation laser power is characterized by two peaks: one large centered at 150cm^{-1} which represents the contribution of the amorphous part of the sample [Nemec et al. 2009a, Jang et al. 2010] and a narrower peak at 124cm^{-1} which could indicate a Te segregation [Krusin-Elbaum et al. 2007, Vinod et al. 2012a]. Fine Raman peaks at 120 and 140cm^{-1} were also observed by Cho et al. [Cho et al. 2006] when analyzing Ge-Sb-Te based particles deposited by ns-PLD. In their work, the Raman spectra were recorded using the 514.4nm radiation of an Ar^{+} laser and the excitation laser power at the sample surface was estimated at 0.7mW. Although some of the samples were annealed, they presented the same Raman spectra as the one deposited at room temperature. The authors explained the difference between the Raman response of the annealed samples and bulk crystals on the basis of the contribution of phonons that are not near the Brillouin zone center.

Moreover, the different Raman spectra recorded when varying the excitation laser power suggest a phase transformation process. The features of the Raman spectra recorded at 36mW are two peaks at 119 and 138cm^{-1}, together with a shoulder around 163cm^{-1}. A similar Raman response was observed for the GeTe thin films deposited by fs-PLD recorded with a 1.36mW excitation laser power. The peaks at ~120 and ~140 cm^{-1} were in good agreement with Te vibrational modes.

A second type of Raman response was the one presented in Figure III.36.
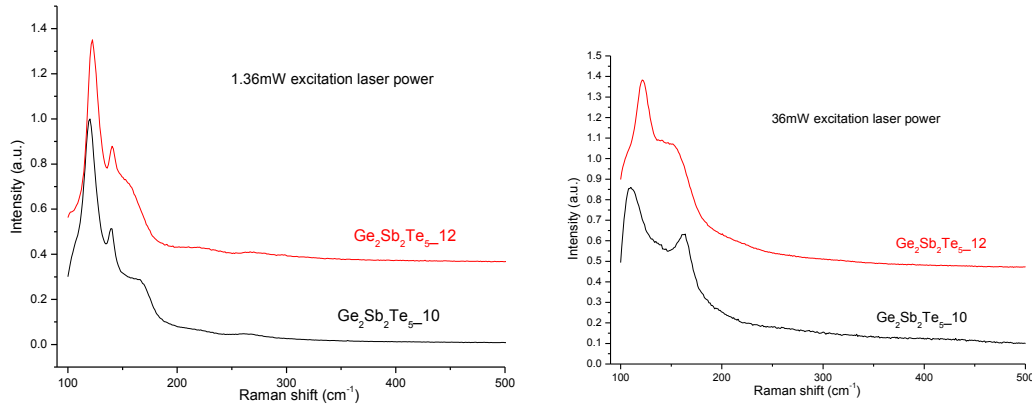
Figure III.36. Raman spectra of two thin films grown using different deposition times.

The two thin films compared in this case were deposited using a higher fluency than for the ones mentioned above. The sample $Ge_2Sb_2Te_5\_10$ was deposited in 20min and the sample $Ge_2Sb_2Te_5\_12$ in 10min. The Raman spectra recorded using a 1.36mW excitation laser power present the same features as the ones from the previous case but recorded using 36mW. Moreover, the $Ge_2Sb_2Te_5\_10$ sample present two peaks when a high excitation laser power is used for analysis. These vibrational modes correspond to the crystalline GST 225 materials. Thus, the Raman spectroscopy results indicate that when higher laser fluences are used for target ablation, the films have a higher crystallinity or at least indicate that a lower temperature is needed to crystallize the material to the fcc structure. The Raman spectra recorded using 1.36 and 36mW of the $Ge_2Sb_2Te_5\_12$ sample resemble the ones obtained for the GeTe thin films deposited in femtosecond regime. The vibrational spectroscopy response can be explained by the variation of Ge, Sb and Te concentration from the stoichiometric value. No EDS measurement were performed on these films, but composition information were obtained for the GST 225 samples deposited by fs-PLD from the next deposition set. As ,mentioned above, the GST 225 samples deposited in the femtosecond regime present lower concentration of Sb, as opposed to the EDS results of the ns-PLD samples where a higher Sb at % was detected.

Two distinct Raman behaviors were also observed for the H-noted samples. These are represented in Figure III.37 and III.38.
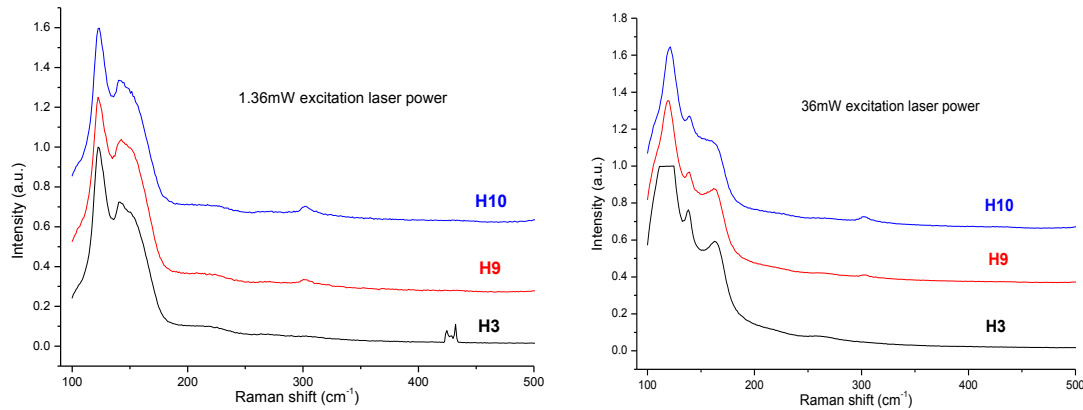
Figure III.37. Raman spectroscopy results of the GST 225 thin films deposited by fs-PLD in 10 min.
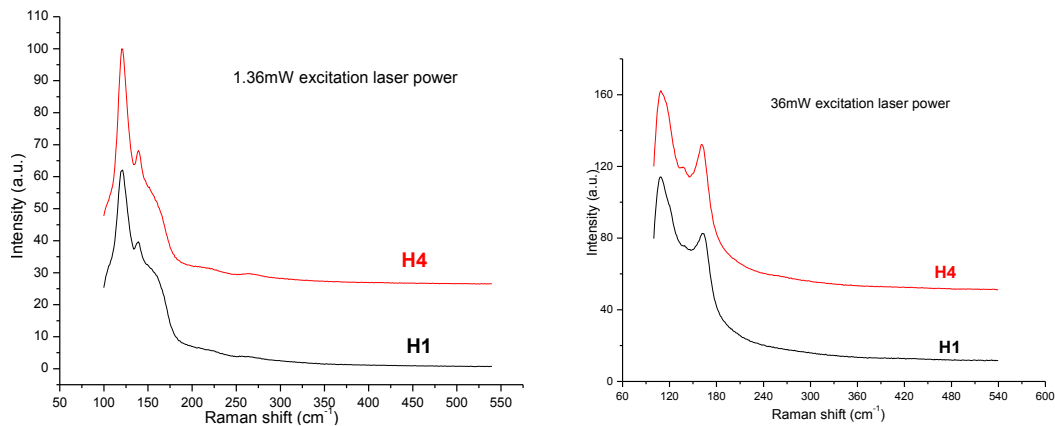
Figure III.38. Raman spectroscopy results of the GST 225 thin films deposited by fs-PLD in 30 min.

The thin films deposited in 10 and 20min present the same Raman behavior. In both cases, the increase in excitation laser power induced a phase transformation process but the vibrational modes observed when using 36mW analyzing condition were not the ones of the GST 225 bulk material. The thin films deposited in 30 min present different Raman characteristics. A variation of the Raman response was observed when the analyzing laser intensity was increased but this time, the spectra recorded at 36mW resembled the ones of the crystalline material. Thus, the vibrational spectroscopy results are different depending on the thickness of the samples. These indicate that the thicker

films have a more ordered structure and lower temperatures are needed to crystallize the sample.

For the samples from the third set, the Raman spectrum recorded using 1.36mW excitation laser power presents two wide peaks at 124 and 148cm^{-1}, suggesting an amorphous deposition. Increasing the excitation laser power, other vibrational modes appear, indicating a phase transformation process. These Raman results are comparable with the ones of the other GST 225 samples deposited in femtosecond regime.

Further Raman spectroscopy analysis revealed information on the stability of the induced phase. Figure III.39 presents the Raman spectra of the H5 sample recorded using 1.36mW, before and after the irradiation of the analyzed surface with a 36mW excitation laser power.
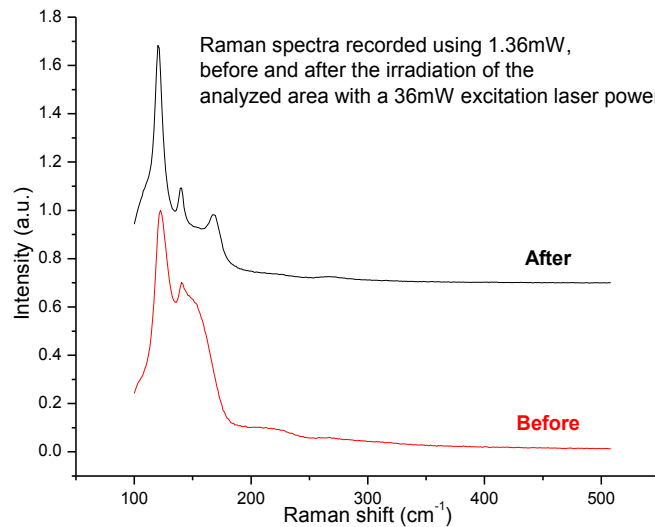
Figure III.39. Raman spectra of the H5 sample recorded using 1.36mW, before and after the irradiation of the analyzed surface with a 36mW excitation laser power.

As one can observe, the Raman spectra recorded with 1.36mW resembles the one acquired with a 36mW excitation laser power of the same analyzed area. Thus, the induced phase transformation does not present a reversed process.

The XRD pattern of the GST225_1 sample indicated an amorphous deposition (Figure III.40).

GST 225 (I) 18. 06. 2012 - File: 12786-Nemec.RAW - Type: 2Th/Th locked - Start: 5.000 ° - End: 65.000 ° - Step: 0.020 ° - Step time: 5. s - Temp.: 25 °C (Room) - Time Started: 0 s - 2-Theta: 5.000 ° - Theta: 2.500 ° - Phi
Operations: Import
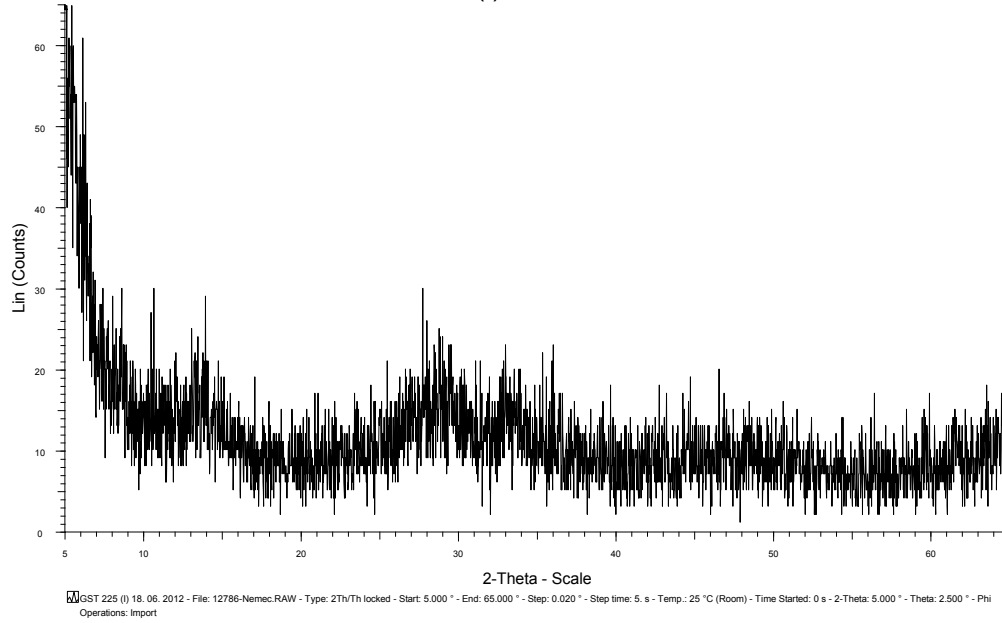
Figure III.40. XRD pattern of the GST225_1 sample.

III.4.3.3   Picosecond regime

Another deposition set was done using a pulsed laser with pulse duration of 2ps and a repetition rate of 100Hz for target ablation. The deposition conditions are summarized in Table III.16. The only varied experimental parameter was the target-substrate distance. For these experiments we used configuration 3 where the substrate was fixed and the target was rotated. By profilometry measurements, the thickness for the GST225 II sample was estimated at 390nm.

Table III.16   Experimental conditions for the thin films deposited in the picoseconds regime

Sample	P (Torr)	d_{s-t} (cm)	Laser	t (min)	Thickness (nm)	Deposition rate (nm/min)
GST225 I	$8 \cdot 10^{-6}$	4	λ=800nm, 100Hz, 2ps, E=1.78mJ fluence=0.3 J/cm^2	30	260	8.7
GST225 II	$8 \cdot 10^{-6}$	3			390	13
GST225 III	$8 \cdot 10^{-6}$	2			N/A	N/A

The profilometry results and optical microscopy images (Figure III.41) revealed that the deposited thin films are more uniform than the ones obtained in nanosecond regime. No large particles were observed.
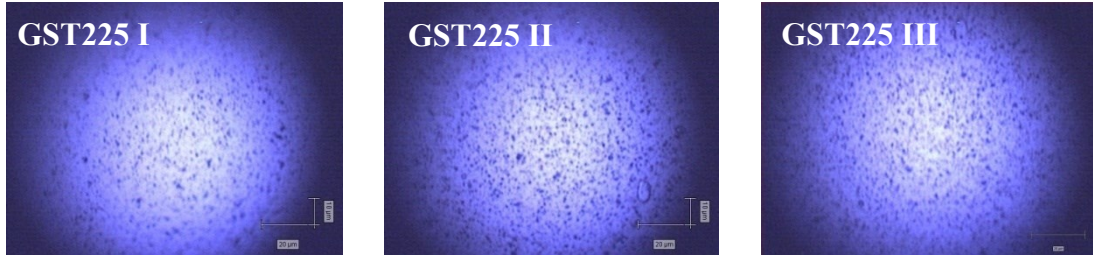
Figure III.41. Optical microscopy images of the GST 225 samples deposited in picoseconds regime.

The chemical concentration of the main elements was obtained using the JEOL JSM 6400 instrument with a 10kV accelerating voltage, considering the L series of every element.

Table III.17   EDS results of the GST 225 thin films deposited in femtosecond regime

Sample $Ge_{22.22}Sb_{22.22}Te_{55.55}$	Atomic %			Obs.
	Ge	Sb	Te	
GST225 I	23.5	21.7	54.9	Surface 120x80µm
	22.3	22.1	55.6	
	23.4	22.2	54.5	

As recorded for the fs-PLD samples, improved EDS results were observed for the thin films deposited in picosecond regime. The atomic % were close to the nominal composition.

The distributions of the main elements in the inner-layers of the samples were investigated by ToF-SIMS analysis, using two types of ion beams to sputter the material in the same conditions as the samples mentioned above. Figure III.42 present the depth profiles of the GST225 II thin film obtained when sputtering a 300x300µm area and analyzing a 100x100µm surface.
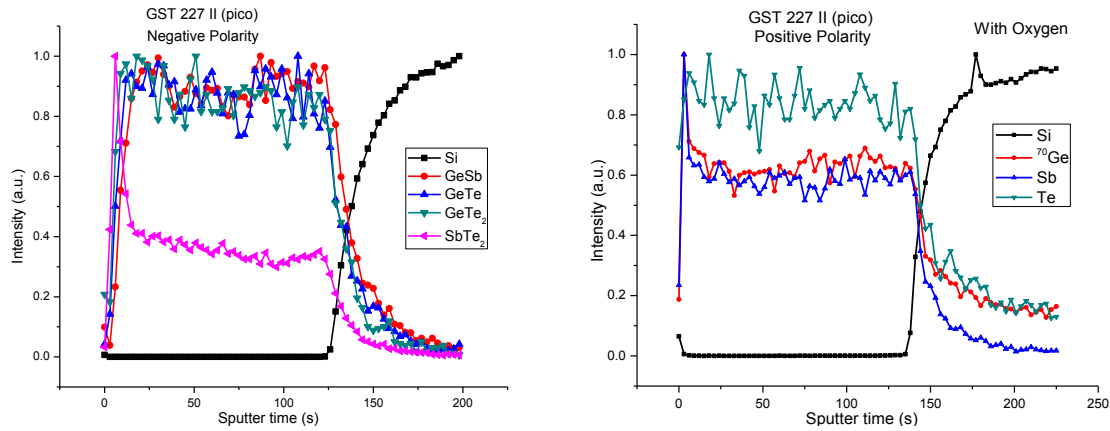
Figure III.42. ToF-SIMS analysis of the GST225 II thin film deposited in picosecond regime (Cs ions were used for sputtering).

Compared to the sample deposited in the nanosecond regime, a much more uniform distribution was observed for the ps-deposited samples. The increased $SbTe_2$ content at the air-film interface is most probably due to the different surface matrix from the rest of the film due to the sample expositor to air.

The structural properties of the deposited thin films were investigated by Raman spectroscopy and XRD analysis. As the other Raman results revealed, a phase transformation process is induced by the high excitation laser powers. The Raman spectra at 1.36mW present two peaks (124 and 148cm^{-1}) which suggest an amorphous phase deposition [De Bastiani et al. 2008]. The Raman spectra of the GST 225 II thin film recorded using 36mW excitation laser power resembles to the one of the crystalline material. The other two thin films present different Raman features. The structural analysis results obtained by Raman spectroscopy are influenced by chemical composition variations. The EDS results revealed a stoichiometric deposition of the main elements for the GST 225 II sample and a slightly elevated Ge concentration for the other two samples. XRD analysis revealed that the GST 225 III thin film is amorphous.

III.4.4 Conclusions on Ge-Sb-Te samples

Thin films of Ge-Sb-Te based compounds were deposited using PLD technique. $GeSb_2Te_4$ and $GeSb_4Te_7$ samples were obtained only in nanosecond regime. The profilometry results were confirmed by optical microscopy. All the sample surfaces were affected by the presence of large particles. For both sets of depositions, the thicknesses of the deposited samples decrease as the laser wavelength is decreased from 1064 nm to 355 nm. The thin films deposited using the fourth harmonic of the Nd-YAG laser presented the highest thickness. The $GeSb_4Te_7$ thin films grown when using short wavelengths (355nm and 266nm) and low laser fluences presented an improved uniformity compared to others from the same set. The chemical composition and distribution of the main element in the sample volume were investigated by EDS and ToF-SIMS analysis. A higher Sb concentration and a deficit of Te were found for the $GeSb_4Te_7$ samples. The depth profiles recorded for the same sample revealed a uniform distribution of Sb and Ge and an increased Te content at the air-film interface due to matrix differences that appear as a consequence of outer-layer oxidation. Knowing the thicknesses of the $GeSb_4Te_7$ thin films, we estimated a sputtering rate of 0.6nm/s. The Raman spectroscopy results recorded in different conditions indicated that a phase transformation process occurs when the laser intensity used for analysis is increased. While the Raman spectra recorded at low excitation laser powers revealed an amorphous deposition, the XRD patterns presented diffraction lines corresponding to the crystalline material.

$Ge_2Sb_2Te_5$ samples were deposited by PLD in three temporal regimes. As observed for the other types of thin films, an improved surface uniformity is achieved when using short pulse lasers. The chemical concentrations were determined using two EDS instruments in different analyzing conditions. Both measurements revealed an increased content of Sb and lower Te concentrations than the nominal composition. However, the observed variations were different, depending on the instrument used. A distinct behavior was observed for Ge. While some areas (usually on droplets) presented a deficit of Ge, others were over-stoichiometric. Different Raman spectra were recorded for various excitation laser powers. For 1.36mW analyzing condition the samples presented an amorphous deposition. The XRD patterns revealed the presence of a long

range ordered structure. The samples deposited in femtosecond regime presented different Raman behaviors. The vibrational spectroscopy results indicated that the thicker films are easier to crystallize. The Raman spectra of these samples recorded at 36mW resembled the one of the crystalline material, while the thinner films presented additional peaks. EDS measurements of the fs-PLD samples revealed an increased Ge content related to the nominal composition. However, several thin films presented concentration values close to the stoichiometric ones. The depth profiles of Ge and Te presented the same dependence as in GeTe thin films while an increased Sb content was detected for low sputtering times. A more uniform distribution of the main elements was recorded when, instead of Cs ion beam, oxygen ions were used for sputtering. In picoseconds regime, three thin films were deposited. The structural results of these samples were similar to the ones observed in femtosecond regime.

III.5 Ellipsometry measurements

Because of their applications in optical disks, the reflectivity of materials is one of the most important optical parameters considered in phase-change optical storage and optical waveguides [Xu et al. 2008]. Its value can be derived from [Hilton 2010] [Xu et al. 2008]:

$$R(E) = \frac{(n(E)-1)^2 + k^2(E)}{(n(E)+1)^2 + k^2(E)} \qquad \text{(III.1)}$$

Considering the parameters included in the above equation it is necessary to know the behavior of the real part (n) and imaginary part (k) of the refractive index in order to obtain the reflectivity-energy dependence. With this aim, the optical properties (refractive indices and extinction coefficients) of some prepared thin films were investigated using variable angle spectroscopic ellipsometry (VASE, J. A. Woollam Co., Inc. ellipsometer type) with an automating rotating analyzer. The optical responses of thin films in the entire measured spectral region (300-2300 nm) where calculated using Cody-Lorentz (CL) model [Ferlauto et al. 2002, Orava et al. 2008, Nemec et al. 2011a]. The surface

122

layer was defined by Bruggeman effective medium approximation (EMA) where the thin films consisting from the same bulk material with void density of 50% [Aspnes et al. 1979, Bruggeman 1935].

Figure III.43 presents the spectral dependence of refractive index, extinction coefficient, reflectivity and $(\alpha E)^{1/2}$ for the T-series thin films (GST225, ns regime), while Figure III.44 presents a comparison of the same parameters for samples of various composition deposited in ns regime. The calculated values of the optical band gap are listed in Table III.18.
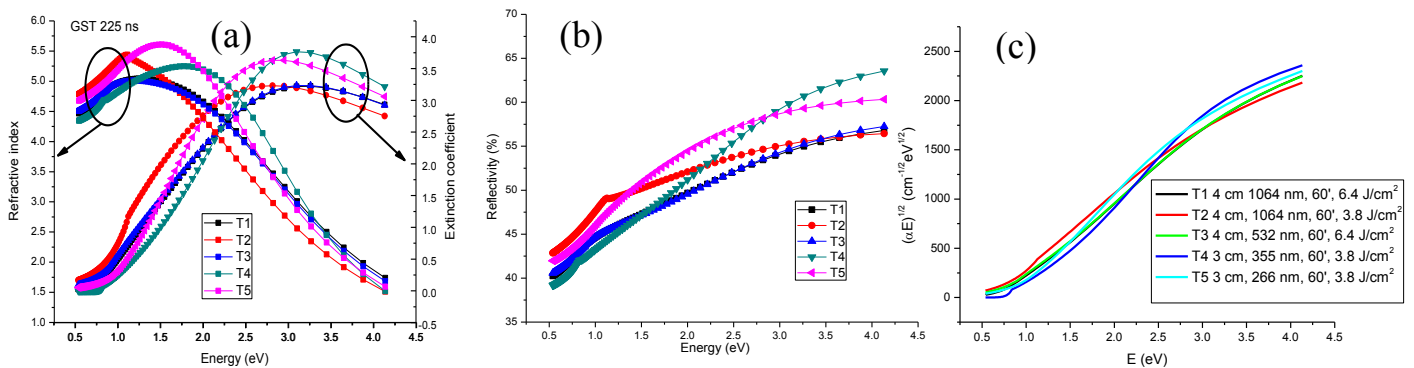
Figure III.43. Ellipsometry results of the $Ge_2Sb_2Te_5$ thin films: energy dependence of refractive index and extinction coefficient (a); reflectivity (b) and $(\alpha E)^{1/2}$ for band gap energy calculation (c).

Comparing these results with the ones reported by Nemec et al. [2011a] and [2009a], some similarities were observed: the refractive index presented an increase up to 1.2eV and then a decrease for higher energies. The same type of dependence was observed for the extinction coefficient which reached its maximum value around 2.5eV. However there were still some differences between our results and the ones reported by Nemec et al. These indicated that the optical behavior of the samples discussed in this thesis presented features between those found for the amorphous and crystalline samples reported by the other group. Comparing the plots of the refractive indexes, we observed higher maximum values than the amorphous chalcogenide thin films deposited by Nemec et al. (and in the same time lower than the crystallized samples) but, a more rapid decrease at large energy values was recorded, comparable with the optical features of the

crystalline thin films. These results support the ones found from structural measurements which indicated only a partial crystallization of the deposited samples. Moreover, we did not observe a clear dependence between the maximum values of the refractive index or extinction coefficient with the Sb_2Te_3 content. This can be explained by the different structural characteristics mentioned in the previous sections. For the Sb_2Te_3 sample, the XRD results indicate a mixture between two phases, one corresponding to the GST structure and another one characterized by an increased Sb content.
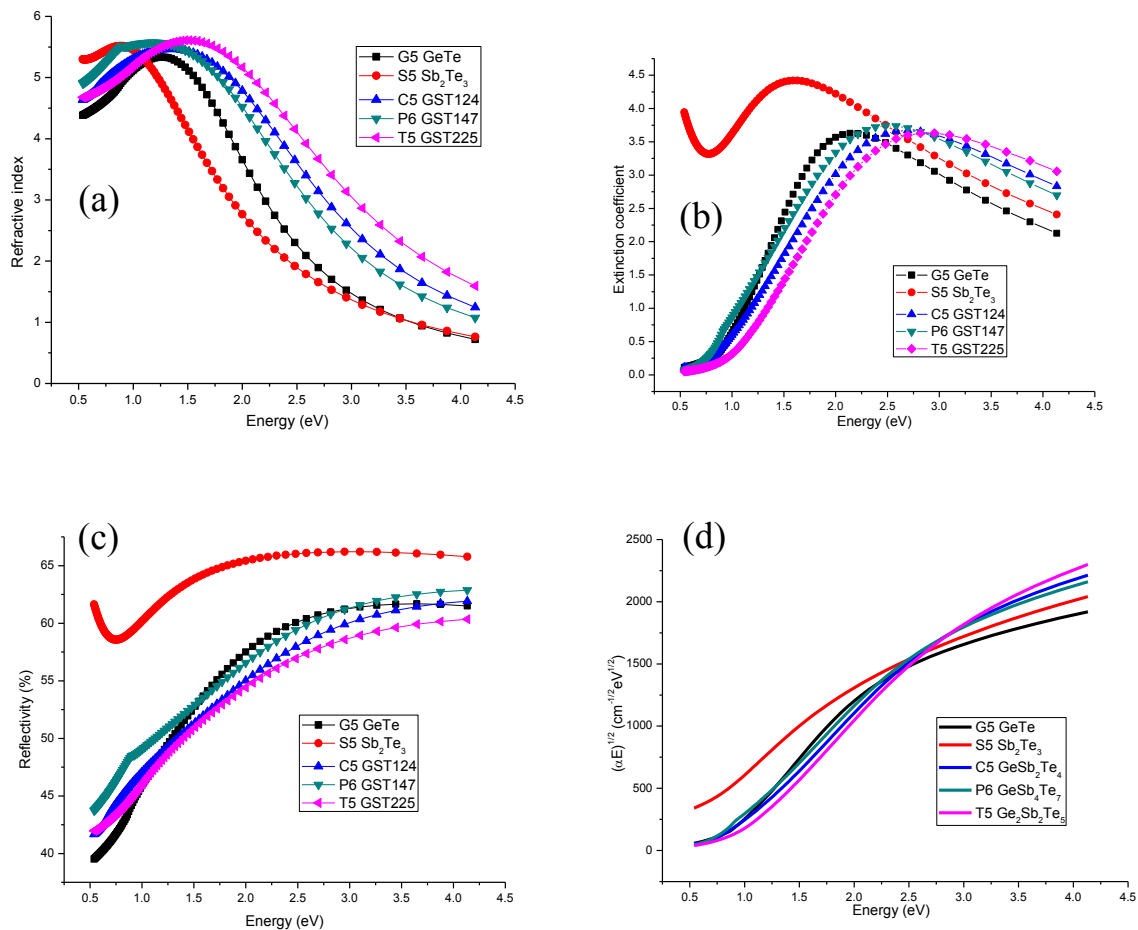
Figure III.44. Ellipsometry results: energy dependence of refractive index (a), extinction coefficient (b), reflectivity (c), and $(\alpha E)^{1/2}$ (d) for the Ge-Sb-Te based thin films (deposition conditions: 3cm, 266 nm, 60', 3.8J/cm^2).

Regarding the calculated energy gaps, our calculations showed comparable values with the ones reported in [Nemec et al. 2011a] for the as-deposited samples. However, the poor microstructural quality of the deposited films determined in some cases, slightly

increased error values. However Lee et al [2005] found that the optical band gaps of their samples deposited by RF magnetron with amorphous, fcc and hexagonal structure are 0.7, 0.5, and 0.5 eV, respectively. A unusual value of the optical band gap was observed for the Sb_2Te_3 sample. However the XRD results of this thin film revealed the presence of two phases, one of them induced by the increased Sb content.

Table III.18   Calculated E_g^{opt} values of several samples, together with the deposition conditions and thicknesses

Sample	Chalcogenide	Deposition conditions	Thickness (nm)	E_g^{opt} (eV)
T1	$Ge_2Sb_2Te_5$	λ=1064nm, t=60min, d_{t-s}=4cm, fluence~6.4 J/cm^2	350	0.5673
T2	$Ge_2Sb_2Te_5$	λ=1064nm, t=60min, d_{t-s}=4cm, fluence~3.8 J/cm^2	250	0.5333
T3	$Ge_2Sb_2Te_5$	λ=532nm, t=60min, d_{t-s}=4cm, fluence~6.4 J/cm^2	190	0.61072
T4	$Ge_2Sb_2Te_5$	λ=355nm, t=60min, d_{t-s}=3cm, fluence ~3.8 J/cm^2	110	0.56791
T5	$Ge_2Sb_2Te_5$	λ=266nm, t=60min, d_{t-s}=3cm, fluence~3.8 J/cm^2	690	0.57973
G5	GeTe	λ=266nm, t=60min, d_{t-s}=3cm, fluence ~3.8 J/cm^2	450	0.54843
C5	$GeSb_2Te_4$	λ=266nm, t=60min, d_{t-s}=3cm, fluence ~3.8 J/cm^2	600	0.61567
P6	$GeSb_4Te_7$	λ=266nm, t=60min, d_{t-s}=3cm, fluence ~3.8 J/cm^2	600	0.40126
S5	Sb_2Te_3	λ=266nm, t=60min, d_{t-s}=3cm, fluence ~3.8 J/cm^2	620	0.21038

Some preliminary measurements were also performed on fs and ps deposited samples, but due to the lower thickness of these samples, only the transparent region (up to 1eV) could be investigated for the moment. These measurements will be extended in the near future using thicker fs and ps samples. Due to the narrow range in which we obtained a signal, no calculations of the E_g^{opt} were allowed.

III.6 Comparative study and main conclusions

This chapter presents the structural characteristics of several thin films based on five types of materials found along the tie line GeTe-Sb_2Te_3, including endpoints. As a review on Ge-Sb-Te based thin films obtained in nanosecond regime, we will represent the structural results of the chalcogenide samples deposited using the 266 nm radiation of the Nd-YAG laser. The five thin films of GeTe, Sb_2Te_3, $GeSb_2Te_4$, $GeSb_4Te_7$ and $Ge_2Sb_2Te_5$ were deposited in the same conditions. Table III.19 re-summarizes the profilometry results. Although the absorption mechanisms depend on the material properties, the estimated thicknesses are comparable. Figure III.45 gives a comparative view of the surface quality of the five thin films. Both profilometry and optical microscopy images indicate that all the thin films were affected by the presence of droplets, but a higher uniformity was observed for the GeTe and GST 147 thin films.

Table III.19   Thickness values of the samples deposited using the following conditions: 3cm, 266 nm, 60', 3.8 J/cm^2

Sample	Target	Thickness (nm)
G5	GeTe	450
S5	Sb_2Te_3	620
C5	$GeSb_2Te_4$	600
P6	$GeSb_4Te_7$	600
T5	$Ge_2Sb_2Te_5$	690
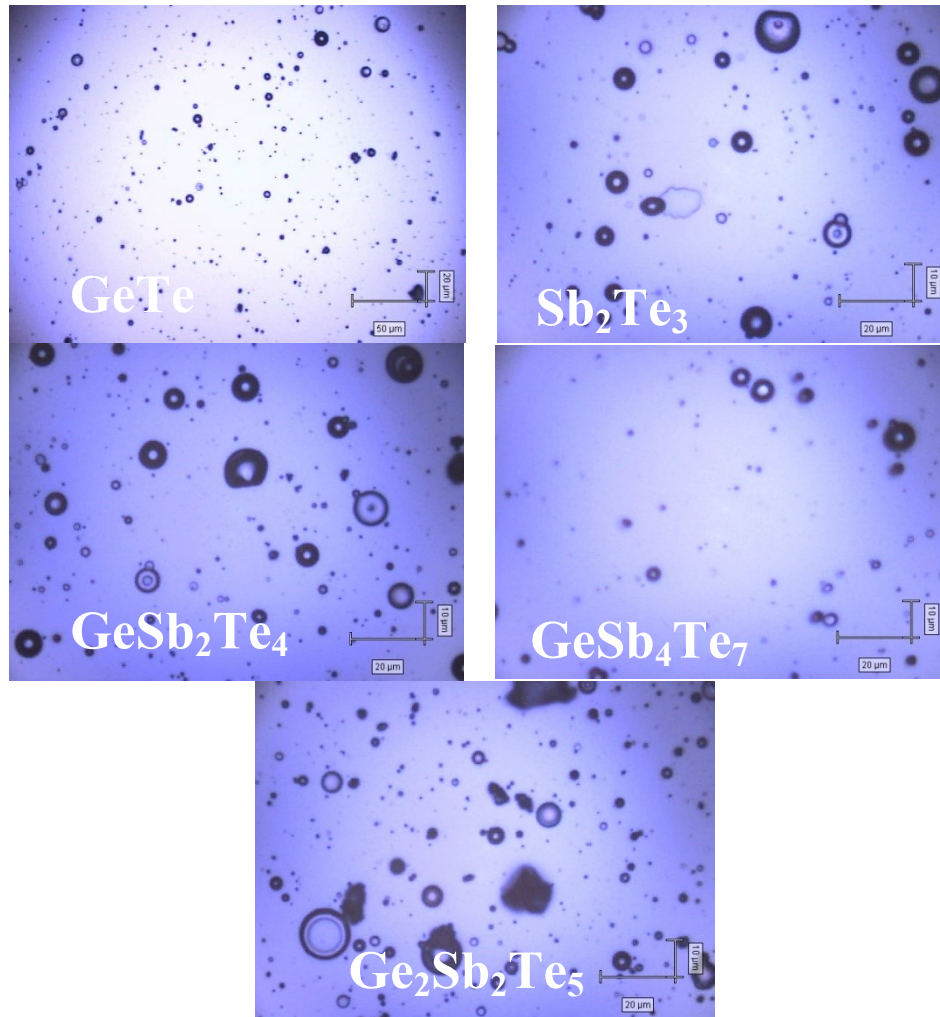
Figure III.45. Optical microscopy images of Ge-Sb-Te based thin films deposited by ns-PLD.

Concerning the EDS results, all the thin films present concentrations different from the nominal composition. The same stoichiometric behaviors of Ge, Sb and Te were observed by Nemec et al. [2011a] but the deviations recorded by their group were lower.

Table III.19 EDS results of the chalcogenide thin films deposited using the 266nm radiation

Sample	Atomic %			Obs.
	Ge	Sb	Te	
G5	62.68	-	37.32	Droplet
GeTe $Ge_{50}Te_{50}$	60	-	40	Large area
S5 Sb_2Te_3	-	48.78	51.22	Droplet
$Sb_{40}Te_{60}$	-	49.5	50.5	Large area
C5 $GeSb_2Te_4$	13.14	35.78	51.08	Droplet
$Ge_{14.28}Sb_{28.57}Te_{57.14}$	13.42	35.67	50.92	Large area
P6 $GeSb_4Te_7$	9.57	39.8	50.63	Droplet
$Ge_{8.33}Sb_{33.33}Te_{58.33}$	8.4	45.31	46.29	Large area
T5 $Ge_2Sb_2Te_5$	12.75	31.81	55.45	Droplet
$Ge_{22.22}Sb_{22.22}Te_{55.55}$	25.23	26.81	47.97	Droplet

The XRD patterns of the GST 147,225 and 124 thin films indicate the formation of an fcc crystalline structure (Figure III.46). The GeTe and Sb_2Te_3 thin films have a different behavior.
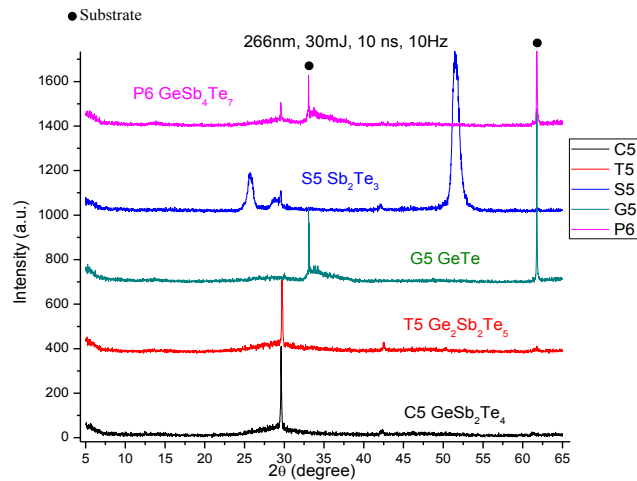
Figure III.46. XRD patterns of the chalcogenide thin films deposited using the 266nm harmonics of the Nd-YAG laser.

The XRD measurements indicate that the GeTe thin film is amorphous while the Sb_2Te_3 sample presents peaks that can be associated with two types of structures. Different structural responses of the GeTe and Sb_2Te_3 thin films were also detected by

Raman spectroscopy analysis when 1.36 and 36mW excitation laser powers were used (Figure III.47).
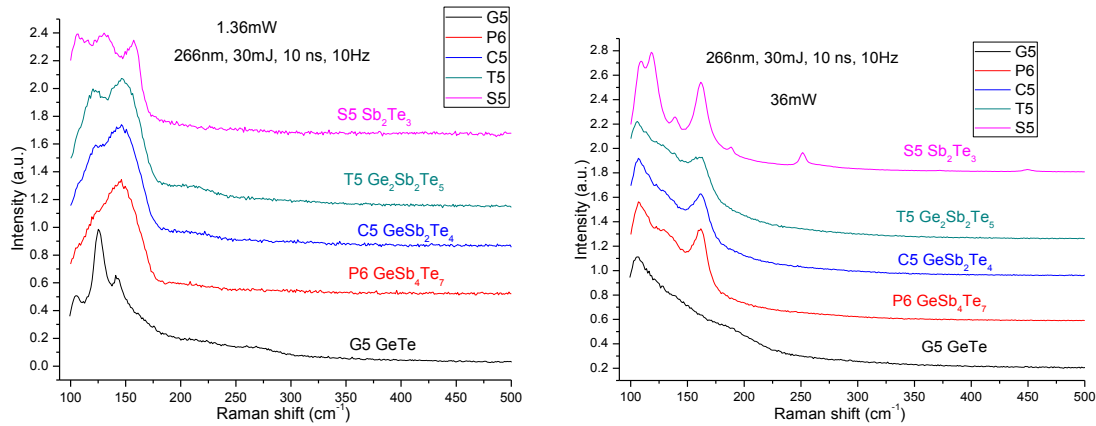
Figure III.47. Raman spectroscopy results of the Ge-Sb-Te based thin films deposited using the 266nm radiation of the Nd-YAG laser.

The results of the thin films deposited by ns-PLD were compared to the ones obtained for other samples deposited in different temporal regimes and these main conclusions can be drawn (with some exceptions):

- The profilometry and optical microscopy images revealed an improved uniformity of the fs-deposited thin films as compared to the samples obtained in nanosecond regime.

- The thickness of the ns-deposited thin films deposited on Si substrate decreases as the laser wavelength decreases from 1064nm to 355nm. A much larger thickness was observed for the thin films deposited using the fourth harmonic of the Nd-YAG laser (266nm), although the experimental parameters would suggest otherwise. This behavior could be explained by analyzing the optical properties of the target material (absorption coefficient) but these were not yet carried on.

- The element concentrations recorded using EDS measurements were different from the stoichiometric values. The chemical compositions of the analyzed films were obtained using two types of instruments. The differences between the atomic percentages found for the same sample in the two cases were influenced by the different analyzing conditions (accelerating voltage and investigated series).

- Improved EDS results were observed for several fs-deposited thin films. The Ge, Sb and Te concentrations were close to the values of the nominal composition.

- Different ToF-SIMS depth profiles of the main elements were recorded when instead of Cs ions, O_2 ions were used for sputtering. The inconsistencies between these results are not related only to the element distribution but to the sputtering time at which the silicon substrate is reached as well.

- The Raman spectra recorded at different excitation laser powers indicate an evolution in crystallinity. The different vibrational modes observed when analyzing the same type of material are influenced by the changes in chemical concentration. The samples which present the same Raman spectra for various excitation laser powers usually present a low thickness.

- The XRD patterns of the ns-deposited thin films present diffraction lines corresponding to the fcc structure but the Raman spectra indicated an amorphous deposition. Thus, the as deposited thin films present a mixture between an amorphous and a crystalline phase.

- The n and k energy dependences recorded by ellipsometry measurements supported the conclusions of the structural analysis results that the films present a mixture between an amorphous phase and a crystalline structure. The calculated optical band gap values were found to be close to the ones reported by other research groups.

Chapter IV

Thin films of pure and rare-earth doped gallium lanthanum sulphide (GLS)

IV.1 Introduction

The second family of compounds investigated in this thesis was the gallium lanthanum sulphide, pure or doped with rare-earths (Erbium or Praseodymium). Since their initial discovery in the 1970s [Loireau-Lozach et al. 1974, 1976, 1977], gallium lanthanum sulphide (GLS) and gallium lanthanum oxysulphide (GLSO) glasses have provided an attractive non-toxic alternative to As- and Ge-based chalcogenide glasses. The low vibrational frequencies of the sulphide bonds allow these materials to have a wide transmission window (0.5 – 10 μm, see Figure IV.1) which, along with good chemical and mechanical properties (they are stable, easy to polish, hard, and non-hygroscopic), makes them appropriate for the manufacturing of optical elements at infrared wavelengths. Its high glass transition temperature (~600 °C) makes GLS appropriate for use in high-temperature applications.
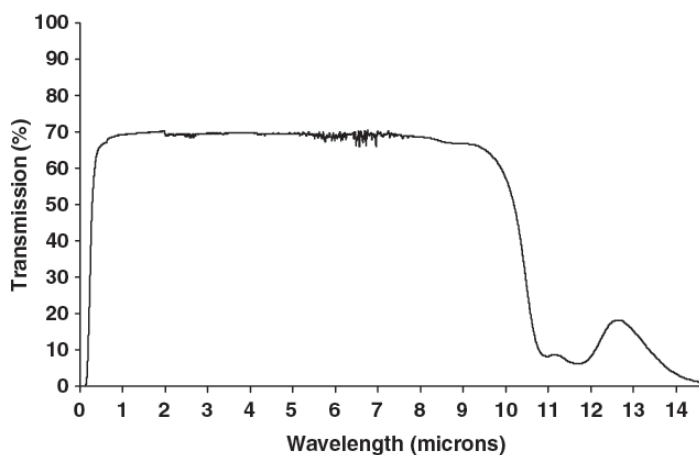
Figure IV.1. Optical transmission spectrum of a 10-mm thick bulk GLS sample [Curry et al. 2005].

The low maximum phonon energy of these materials ensures low non-radiative relaxation rates, which makes them ideal candidates for laser host media. Additionally, the GLS family has a wide region of glass formation, centered at about 70% Ga_2S_3 – 30% La_2S_3 (see Figure IV.2), and exhibit good rare-earth solubility, as the high lanthanum content is readily partially substituted by other lanthanide dopants. When doped with rare-earths such as Nd^{3+}, Er^{3+} etc., these glasses, due to their low phonon energy and high refractive index (2.4) open up the possibility of operating lasers in the mid-infrared, and the use of energy levels which are non-radiatively quenched in oxide glasses. For instance, laser action at 1080 nm has been demonstrated in Nd-doped GLS glass, both in bulk (2.7 mW maximum output power, [Schweizer et al. 1996]) and fiber (1.2 mW maximum output power, [Schweizer et al. 1997a]) forms. Doping of GLS glasses with Holmium [Schweizer et al. 1999a], Erbium [Frantz et al. 2006a,b, Schweizer et al. 1997b], Dysprosium [Schweizer et al. 2001], Praseodymium [Hewak et al. 1994], Thulium or Terbium [Schweizer et al. 1999b] showed promising results in enhanced fluorescence / frequency upconversion.
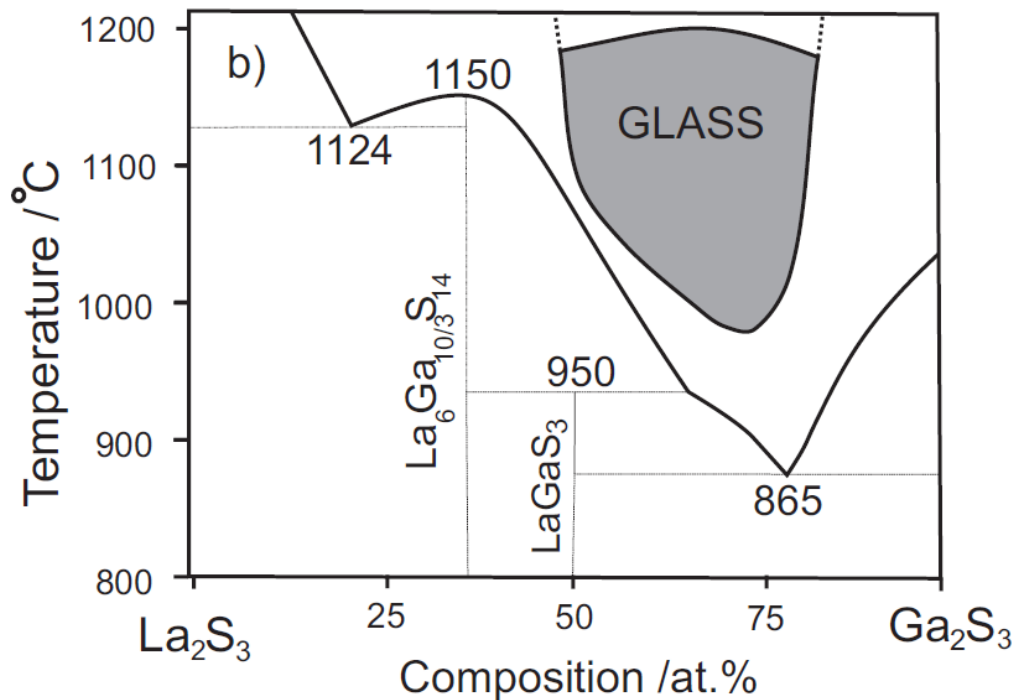
Figure IV.2. Phase diagram of the Ga_2S_3 – La_2S_3 system (redrawn after [Flahaut et al. 1983]).

In addition, the GLS glasses exhibit a wide range of interesting photo-stimulated properties, including subtle effects as shifts in the absorption edge, and more substantial atomic or molecular reconfigurations such as photo-induced refractive index changes [Elliot 1986, Owen et al. 1985]. The permanent photo-induced changes in refractive index can be up to 1%, thus opening the possibility of writing high spatial resolution grating structures and waveguides. Grating structures have been written using either laser or e-beams [Gill et al. 1995], and photonic crystals fabrication has been demonstrated using ion beams [Pollard et al. 2012]. These have applications like mode converters, waveguide couplers or Bragg reflectors in integrated optical devices. Moreover, it has been reported that GLS has high optical nonlinearity (200 times higher than conventional silica glass) [Kang et al. 1995], which suggests that single-mode operating GLS glass planar waveguides could potentially be beneficial in a variety of nonlinear applications, e.g. generation of supercontinuum and all-optical switching.

Despite all these attractive properties, the GLS glasses have also some practical drawbacks, as the still limited visible transparency and potentially damaging photosensitivity. Their low thermal conductivity and strong thermal lensing make them impractical for bulk glass lasers, thus requiring the use of geometries capable of efficiently dissipating heat, such as optical fibers or thin films. As the subject of this thesis is related to the thin films, we will not address in the following the optical fibers research on these materials. We present in the next section a brief review of the previous studies conducted in this field.

IV.2 Previous studies on GLS thin films

Among the various deposition techniques cited above, the thickest amorphous GLS films have been obtained by Mairaj et al. [2004, 2005] using a modified version of the conventional spin coating technique (combination of inverted deposition of the molten glass phase and high-velocity spinning). These authors created relatively uniform (±0.5 μm thickness variation across 25 mm) and homogeneous (±5% composition accuracy) films with increased refractive index (Δn up to +0.005 with respect to the substrate GLS glass), thus recommending this method for the fabrication of planar

waveguides. The propagation loss at 1064 nm was as low as 0.2 dB.cm^{-1} over a 15 mm path length in a 6 μm thick single-mode waveguide fabricated with this technique. Despite these promising results, a potential drawback of this method is the incompatibility with pre-existing structures on the substrate; it is likely that any pre-existing features would either melt or cause thickness non-uniformity in the spun films.

Another deposition method used to obtain GLS thin films is the RF sputtering [Pollard et al. 2012, Frantz et al. 2006a,b, Popescu et al. 2011]. Using this technique, Pollard et al. [2012] deposited GLS (162 nm thick), GLSO (100 nm) and Er:GLSO (150 nm) thin films on 2 inch silicon wafers, and further created photonic crystals in annealed Er:GLSO films with a focused ion beam, for the express purpose of demonstrating enhanced visible upconversion. Popescu et al. [2011] obtained a refractive index of 2.48 for GLS thin films (220 nm thick) deposited by RF sputtering (2 hours, 25 W, 0.8 Pa Ar pressure), versus 2.55 for the bulk glass used. In earlier works, Frantz et al. [2006a,b] fabricated Er:GLS thin films with excellent surface roughness (< 8 Å RMS) and thickness in the range 0.15 – 3.8 μm (11 Å/min deposition rate) using a substrate heated at 100°C, in an Ar atmosphere of 5 mTorr. However, a relatively high variation of the Ga:S ratio has been evidenced in the 0 – 2 μm thickness range. The authors announced achievement of deposition rates of more than 100 Å/min for GLS [Frantz et al. 2006b], but, up to our knowledge, no paper demonstrating or using this has been published afterwards.

The first application of the PLD technique to the deposition of amorphous GLS thin films was done 20 years ago by Youden et al. [1993] using a KrF excimer laser (248 nm, 20 ns pulse duration) in vacuum (10^{-4} mbar). The average fluence was 4 J/cm^2 and the target – substrate distance was 5 cm. Films with average thickness of 1.5 μm were deposited at room temperature on CaF$_2$ and microscope slide substrates for 20 minutes each at a laser repetition rate of 40 Hz (i.e. ~50 000 pulses), which gives a maximum deposition rate of 0.3 Å/pulse. The authors claimed good quality films with only few droplets on a sub-micrometer scale, but no picture of the surface was shown. Rutherford backscattering (RBS) and EDX composition analyses indicated a slightly sulphur deficient film compared to the target material. Some photoinduced effects (photobleaching, photodiffusion, refractive index changes) were demonstrated by the

authors using an Ar^+ laser (514 nm) for illumination. The waveguide properties of a 1 μm film were analyzed using a prism coupling technique, and a refractive index of 2.53 was deduced.

This work was extended two years later by Gill et al. [1995], who investigated the influence of the substrate temperature and laser fluence on the deposited films properties. They concluded that heating the substrate (up to 410°C) led only to more opaque films at all wavelengths. The most transparent films were obtained at room temperature, and the authors even suggested cooling the substrate to improve the transmission properties of the films. The KrF laser fluence was varied in the $2 - 16$ J/cm^2 range, leading to very interesting results. A clear difference was found between films deposited at fluences $\geq$ 3.5 J/cm^2, and those deposited below this value. For F $\geq$ 3.5 J/cm^2 the films exhibited properties similar to the bulk glass (Ga:S ratio of 0.7, refractive index of 2.45, cut-off wavelength of ~480 nm), while the films deposited at lower fluence were more transparent (cut-off wavelength ~350 nm), had a lower refractive index (n $\approx$ 2.3), and (somehow curiously) were sulphur-rich, with Ga:S ratios in the range $0.4 - 0.6$. Moreover, these low-fluence films were stable to photoinduced effects, while the high-fluence films were not. It seems thus that use of higher fluences must be favored. Nevertheless, the authors acknowledge the occurrence of undesirable micrometric spherical droplets on the surface of the films for high laser fluences. An EDX analysis in 12 points on the surface showed fair homogeneity, with variations in the 10-15% range for the three components. A high optical loss (6 dB/cm) was measured for these films.

The effect of the KrF laser fluence on the optical properties of GLS thin films deposited in vacuum (10^{-6} mbar) was studied in more detail by Asal and Rutt [1997]. A quasi-linear dependence of the deposition rate (in the range 0.4–0.8 Å/pulse) on the laser fluence (3 to 6 J/cm^2) was found for a target-substrate distance of 8 cm. This time, a clear increase of the refractive index with the laser fluence was demonstrated. The absorption coefficient also rose when the laser fluence was increased and a gradual shift of the absorption edge to lower energies was observed, along with a decrease in the optical gap from 1.9 eV at 3 J/cm^2 to 1.4 eV at 6 J/cm^2 (Tauc gap). These changes were explained by a subsequent EXAFS study [Asal et al. 1997] in terms of structural modifications, namely the existence of "wrong bonds" Ga-Ga and S-S leading to chemical disorder in the

structural network of the GLS thin films. The number of these "wrong bonds" slowly increases with increasing fluence, thus reflecting a gradual change from the predominantly tetrahedral structure (ordered-bond network) at low fluence (<4 J/cm^2) to the random-bond network at high fluence (>4 J/cm^2). The authors proposed a thin film growth mechanism and concluded that the deposition conditions should be chosen as to minimize the ablated species energy (down to ~4 eV, which is the order of magnitude of the heat of formation per bond in GLS) by using fluences close to threshold.

Darby et al. [2008a] performed a comprehensive study on the influence of various deposition parameters on the composition and refractive index of gallium lanthanum oxysulphide (GLSO) thin films. Two different lasers were used: nanosecond Nd:YAG at 266 nm (10 Hz repetition rate) and femtosecond Ti:Sa at 800 nm (1 kHz repetition rate), with comparable fluences (in the range $0.6 - 2.4$ J/cm^2 for ns and $0.2 - 4$ J/cm^2 for fs). The effects of the background Ar pressure (between 2×10^{-4} mbar and 2×10^{-1} mbar) and target – substrate distance (2 to 6 cm) were also investigated. Film thicknesses in the range of $0.2 - 2.5$ μm were obtained (the authors mention however non-uniform thickness profiles, without giving further details). The compositions measured by EDX ranged well outside the conventional glass-formation region reported for the $La_2S_3 - Ga_2S_3 - La_2O_3$ system [Flahaut et al. 1983]. A notable point is that the ns PLD films have a roughly constant Ga percentage, while the fs PLD films have compositions that are richer in La at the expense of Ga. In order to give insight on the off-axis deposition, composition measurements were made at different distances from the film center (i.e. the intersection of the substrate and plume axis), up to 10 mm (for a target-substrate distance of 2.5 cm), revealing a difference in stoichiometric transfer between ns and fs off-axis deposition. For fs PLD, the Ga content decreases and the composition becomes considerably richer in La at distances farther away from the film center, while the S content remains roughly constant. For ns PLD, the film material deposited at higher off-axis geometries is increasingly deficient in S, while the La and Ga content remains relatively unchanged. The film composition was only weakly affected ($<10\%$) by changing the laser fluence in both regimes (at least above 1 J/cm^2). The target-substrate distance showed some effect on the film composition, with S content decreasing at higher distances in both regimes, while Ga and La content exhibited more peculiar evolutions.

The conclusion of the authors was that closer target-substrate distances resulted in film compositions more closely comparable to the target stoichiometry, which in our opinion was only partly supported by the experimental results. The ambient gas pressure was the most influential parameter on film composition, reducing the Ga:La ratio by a factor of 2 when increased from $2x10^{-4}$ mbar to $5x10^{-2}$ mbar, in both regimes.

The first PLD study using a visible laser (Nd:YAG, 532 nm) was reported by Nemec et al. [2009b]. Fluence of 3-4 J/cm^2 led to film thicknesses in the range 0.42 – 1.67 μm, depending on the number of laser pulses and deposition geometry. The chemical composition of the films was quite close to that of the targets, with only a few percent excess of Ga and La, and deficit of S. Some differences between Raman spectra of GLS bulk glasses and thin films were evidenced and explained by the slightly different stoichiometry. Variable angle spectroscopic ellipsometry (VASE) revealed a decrease of thickness (~30%) and refractive index (~4%) when moving ~18 mm outwards the plasma plume center at fixed target-substrate distance (5 cm). Negative irreversible photorefraction changes (~1-2%) were observed under cw (473 nm) or pulsed (248 nm) laser irradiation.

IV.3 Deposition and characterization of pure GLS thin films

Pure GLS thin films were deposited by PLD in various conditions using three types of lasers with distinct characteristics: nanosecond Nd:YAG laser, Ti:Sa picosecond laser and Ti:Sa femtosecond laser. The varied deposition parameters were: time of deposition (number of laser pulses), target-substrate distance, laser fluence and background pressure. The as-obtained thin films were analyzed using stylus profilometry, Raman spectroscopy, X-Ray Diffraction (XRD), Energy Dispersive X-Ray Spectroscopy (EDX), Time-of-Flight Secondary Ion Mass Spectrometry (ToF-SIMS) and Variable Angle Spectroscopic Ellipsometry (VASE). We present hereafter the results obtained in the three laser regimes.

IV.3.1 Nanosecond regime

In this regime, only four thin films were deposited, because of limited availability of targets. Three different laser wavelengths were used (1064 nm, 532 nm, and 355 nm). The background pressure in the vacuum chamber was kept almost constant at about 10^{-5} Torr. A high fluence ($\sim$10 J/cm^2) was used for these preliminary depositions. The number of laser pulses was 36000 (60 min. at 10 Hz) for λ = 1064 nm and 532 nm, and 27000 for λ = 355 nm. Target-substrate distances (d) of 4 cm and 6 cm were used. All these parameters are summarized in Table IV.1.

Table IV.1 Experimental parameters for the deposition of GLS thin films in the nanosecond regime.

Sample label	P (Torr)	d (cm)	Laser	t (min)	Thickness (nm)	Deposition rate (nm/min)
L1	$1.2 \cdot 10^{-5}$	4	λ=1064nm, E=50mJ/pulse, F = 10 J/cm^2		1500	25.0
L2	$1.2 \cdot 10^{-5}$	6	λ=1064nm, E=50mJ/pulse, F = 10 J/cm^2	60	600	10.0
L3	$1.3 \cdot 10^{-5}$	4	λ=532nm, E=50mJ/pulse, F = 10 J/cm^2		700	11.7
L4	$9.8 \cdot 10^{-6}$		λ=355nm, E=50mJ/pulse, F = 10 J/cm^2	45	270	6.0

The optical microscopy and stylus profilometry investigations revealed the presence of numerous "debris" on the surface of the thin films, as one can see in Figures IV.3 and IV.4. This is undoubtedly due to the use of high fluence, but could also be favoured by the laser wavelength, at least for 1064 nm and 532 nm, where thermal effects could be higher. In this sense, one can nottice the much better result obtained at 355 nm, where the penetration depth of the laser in the target must be lower, and the subsurface heating must be reduced. We note however that the shape of the droplets is somehow different compared to those observed for GST thin films, in the sense that we do not observe here (or at least not for most of the droplets) the characteristic spherical shape due to the melting of the material during laser heating. All these tend to suggest deposition at deeper UV wavelengths, e.g. 266 nm. Unfortunately the limited availability of the target didn't allow us to do it for pure GLS, this was done on doped GLS.
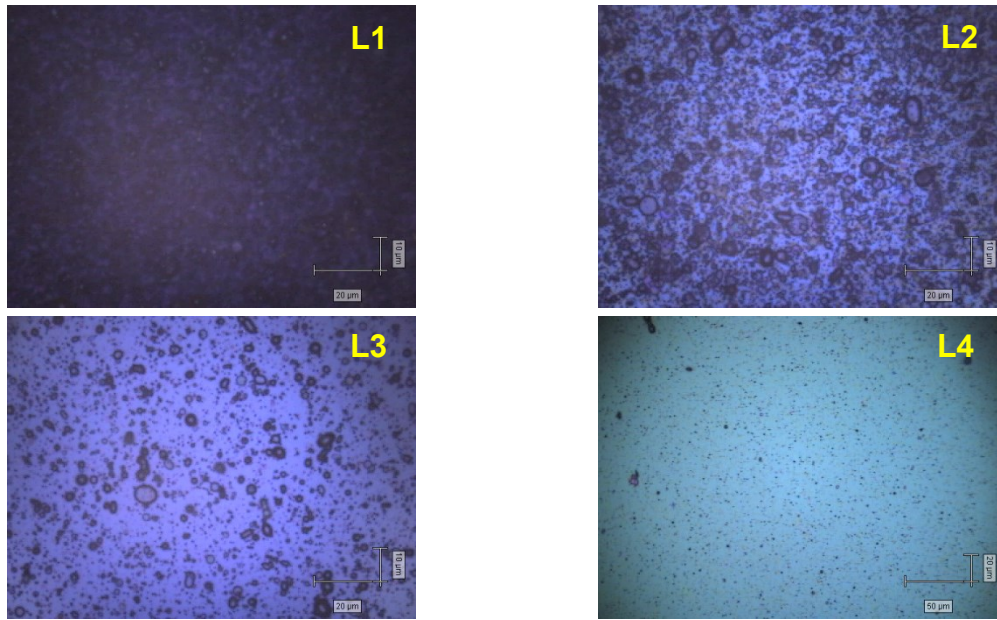
Figure IV.3. Optical microscopy of the surface of GLS thin films deposited in nanosecond regime.
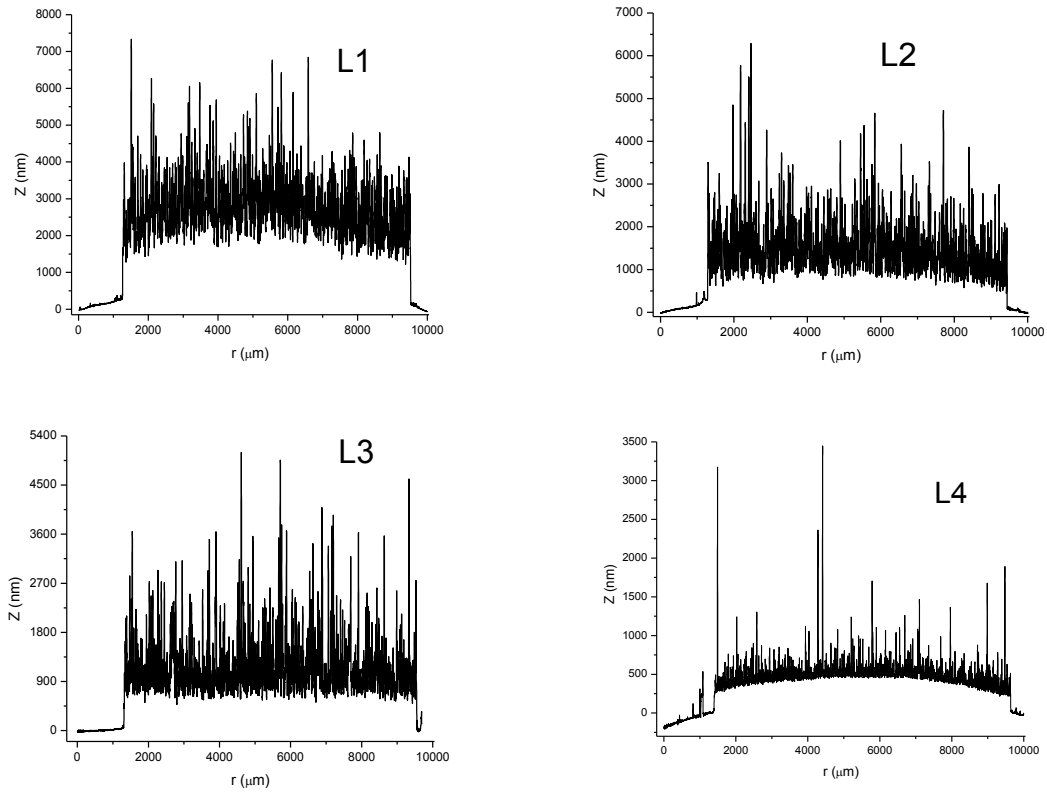
Figure IV.4. Stylus profilometry of GLS thin films deposited in nanosecond regime.

Measuring the thickness of the films was quite difficult because of the high non-uniformity of the surface. We decided to define the thickness as the distance between the substrate and the "bottom" of the profile on the films surface. The results obtained by stylus profilometry are presented in Table IV.1. They were also confirmed by VASE ellipsometry (see below). One can easily remark a better deposition rate for $\lambda = 1064$ nm, and for a shorter target – substrate distance (4 cm). For the L1 sample (1064 nm), we obtain a deposition rate of ~0.4 Å/laser pulse, while for L3 (532 nm) we get ~0.2 Å/laser pulse. For comparison, a deposition rate of ~0.3 Å/pulse was obtained by Nemec et al. [2009b] using a 532 nm laser and d = 5 cm but at lower fluence (~4 J/cm^2), and ~0.8 Å/pulse was obtained by Asal and Rutt [1997] using a 248 nm laser, d = 8 cm and F = 6 J/cm^2. Our UV deposition (355 nm, L4) exhibited a significantly lower rate, at ~0.1 Å/pulse. More systematic studies are needed in order to explain these results.

IV.3.1.1   Elemental composition of thin films

In order to check the stoichiometric transfer between the target and the thin films, we investigated the elemental composition using two techniques: EDX and TOF-SIMS. For EDX measurements, two instruments were used, one with 10 kV accelerating voltage (JEOL JSM 6400, Université de Rennes, France) and the other one with 30 kV (Tescan Vega II LMH, Technical University of Iasi, Romania). The first instrument used the L, L, and K series of Ga, La, and S, respectively, while the second one used the K, L, and K series for Ga, La, and S, respectively. An example of X-ray spectrum is given in Figure IV.5 (sample L3, 10 kV), along with a SEM image of the analyzed area. One can notice the presence of the Si peak, coming from the substrate.
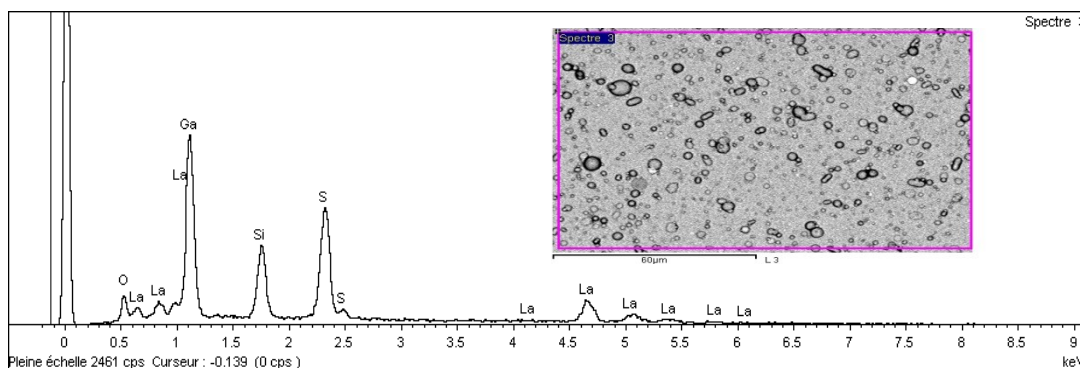
Figure IV.5. EDX spectrum and SEM image for sample L3 (JEOL instrument, Rennes).

With the JEOL instrument (10 kV accelerating potential) two types of analyses were performed: on large area ($\sim$100x100 μm^2, 1 μm depth) and on some deposited droplets using only 1 μm^3 analysis volume, while with the VEGA instrument (30 kV accelerating potential) only large areas have been analyzed ($\sim$50x50 μm^2). The EDX results are summarized in Table IV.2.

Table IV.2   GLS thin films EDX analysis results.

Sample	Composition			Analysis conditions.
	Ga	**La**	**S**	
Bulk	**26.47**	**14.25**	**59.26**	**Nominal composition**
L1	31.49	20.17	48.34	10 kV, large area
	31.59	20.30	48.11	10 kV, large area
	31.11	21.16	47.73	10 kV, large area
	31.57	19.05	49.38	10 kV, droplet
	35.45	16.36	48.19	10 kV, droplet
	33.18	17.88	48.94	10 kV, droplet
	33.09	14.11	52.8	10 kV, droplet
	34.81	14.77	50.41	10 kV, droplet
	27.85	13.18	58.96	30 kV, large area
L2	30.65	20.94	48.41	10 kV, large area
	32.31	21.47	46.22	10 kV, large area
	32.41	19.47	48.13	10 kV, large area
	31.77	16.98	51.25	10 kV, droplet
	31.98	14.08	53.94	10 kV, droplet
	29.53	16.43	54.05	10 kV, droplet
	31.32	17.67	51.01	10 kV, droplet
	19.53	30.43	50.04	10 kV, droplet
	26.80	13.39	59.80	30 kV, large area
L3	35.46	20.83	43.70	10 kV, large area
	35.73	20.20	44.06	10 kV, large area
	36.23	20.11	43.66	10 kV, large area
	31.12	15.87	53.01	10 kV, droplet
	35.54	18.17	46.29	10 kV, droplet
	33.00	22.79	44.21	10 kV, droplet
	33.43	19.28	47.29	10 kV, droplet
	32.31	15.34	52.35	10 kV, droplet
	32.24	12.97	54.78	30 kV, large area
L4	37.15	17.98	44.87	10 kV, large area
	37.30	17.05	45.66	10 kV, large area
	37.34	17.55	45.1	10 kV, large area
	24.28	27.72	47.99	10 kV, droplet
	31.46	19.18	49.37	10 kV, droplet
	25.01	26.69	48.30	10 kV, droplet
	32.56	10.94	56.49	30 kV, large area

The results in Table IV.2 show fairly constant (within 1-2%) composition when measured on large areas (100x100 μm^2) by the 10 kV electron beam, while a much larger variation is observed on the composition of individual droplets (1 μm^2 analysis area). The general trend is a high deficit of S in the film (this deficit is somehow reduced on certain droplets), with respect to the nominal value (~60 at%). This is of course expected because of the much higher volatility of this element compared to Ga and La, and has already been observed by other authors [Nemec et al. 2009b], but at less extent (4-5 at% only). The difference can arise from the higher fluence used in our case, which could favor higher temperatures at the target surface and thus even more volatility of sulphur. A composition closer to that of the bulk should exist (deeper) in the droplets, but for this a deeper penetration of the electron beam is needed (only 1 μm for the 10 kV experiments).

Surprisingly, when using the 30 kV beam, a composition much closer to the stoichiometric one has been evidenced on the L1 and L2 thin films, while for L3 and L4 Ga was overstoichiometric by ~6 at%, La understoichiometric by 2-3 at%, and S understoichiometric by 4-5 at%. This is encouraging (especially for L1 and L2), but it is not sure that this is coming from the film itself, it might be (as said above) just a major contribution from the droplets (largely present on these samples), which are now deeper penetrated in the volume by the 30 kV beam. Unfortunately, because of the very limited access to the 30 kV instrument, we could not proceed with further investigations in order to validate this hypothesis, but it would be interesting to verify it in the future.

In order to analyze the distribution of constituents on the surface and in the volume of the thin films, we performed some TOF-SIMS experiments using the ION-TOF instrument available at Université Lille 1. This instrument can work in both positive and negative polarities. We used both possibilities, as Sulphur is almost impossible to be detected in positive polarity, while La gives better signal using this polarity. In negative polarity however, La and Ga are detected in form of oxides or sulphides. An example is given in Figure IV.6 for the analysis of the L4 sample surface. From these pictures we can notice a quite uniform distribution of the Ga, La, and S elements on the surface of the film.
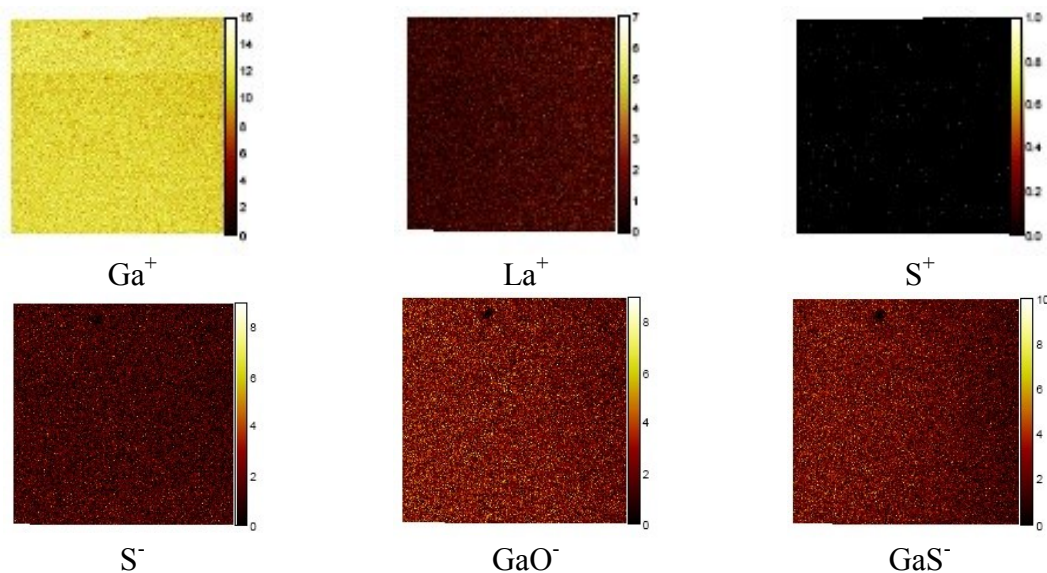
Figure IV.6. TOF-SIMS mapping (500 μm x 500 μm) of the L4 sample surface in positive (upper row) and negative (lower row) polarity.

We also performed depth-profiling studies using a Cs ion beam to progressively sputter the film on a 300 μm x 300 μm surface and a Bi ion beam to analyze a surface of 100 μm x 100 μm centered on the sputtered area. The result obtained for the L4 sample in negative polarity is given in Figure IV.7. We can notice a fairly constant signal of S and La over the entire thickness of the sample, while Ga adducts present a more peculiar evolution (the same was observed for the L3 sample), which is still to be explained. Note however that the increase in the oxide signal at the interfacial region between the film and the substrate has already been observed for other materials, especially when the substrate is heated [Dascalu et al. 2013]. In our case, the deposition is made at room temperature and, moreover, the La oxide does not show the same behavior as GaO.

The time needed to reach the substrate was ~800 s (decay of thin film components signals and growth of Si substrate signal), for a thin film thickness of ~270 nm, which gives a sputtering rate of ~0.34 nm/s. This rate depends of course on the analysis conditions (sputtered surface and Cs ion current and voltage – 60 nA and 1 kV in this case, respectively), but it could be used to get an estimation of the film thickness where this is not known and if the analysis is done in the same conditions.
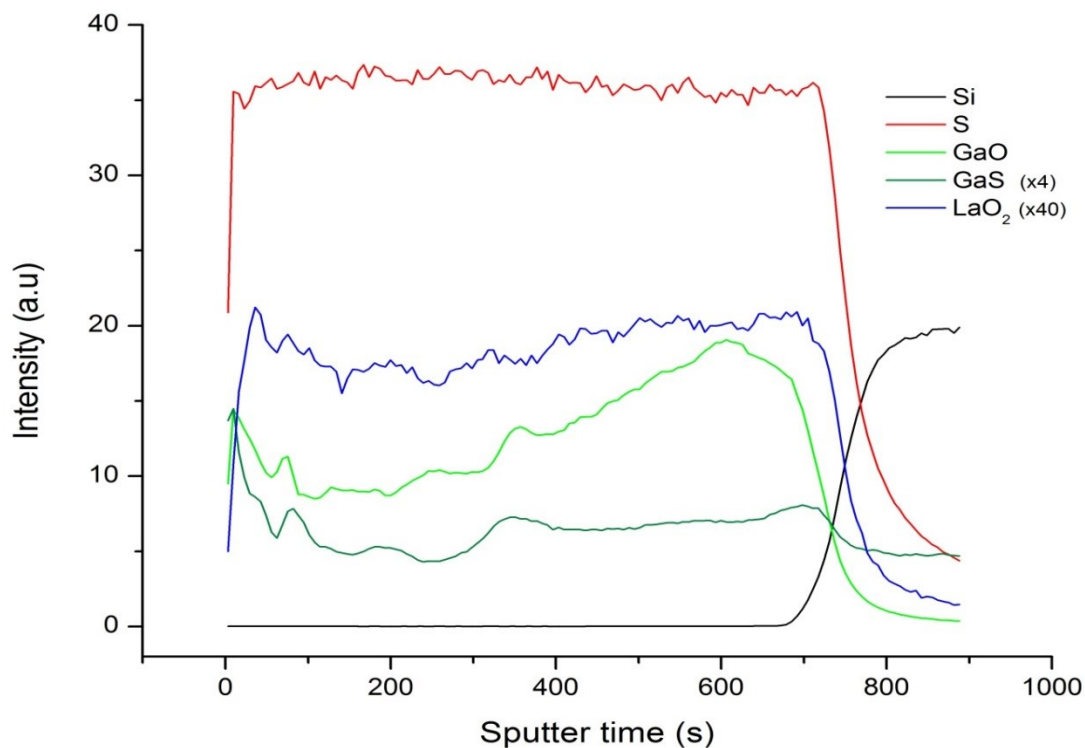
Figure IV.7. TOF-SIMS depth-profiling of the L4 sample in negative polarity.

IV.3.1.2   *Structural characterization of thin films*

The structural characterization of the deposited thin films was done by two techniques: X-Ray diffraction (XRD) and Raman spectroscopy. The XRD experiments (performed by P. Nemec at Pardubice University, Czech Republic) clearly proved the amorphous nature of the thin films, as one can see from Figure IV.8 where only the Si substrate crystalline features are present.

Raman spectroscopy was also performed on the deposited films and on the target (bulk), using 785 nm or 514 nm excitation. Previous studies [Hewak et al. 1994, Nemec et al. 2009b] showed that the main feature of the GLS glass Raman spectrum was a broad band between ~260 and 450 cm^{-1} with maximum around 330cm^{-1} (see Figure IV.9). Some lower intensity and almost featureless bands with maxima around 95, 135 and 220 cm^{-1} were also observed, both in bulk and thin films [Nemec et al. 2009b].
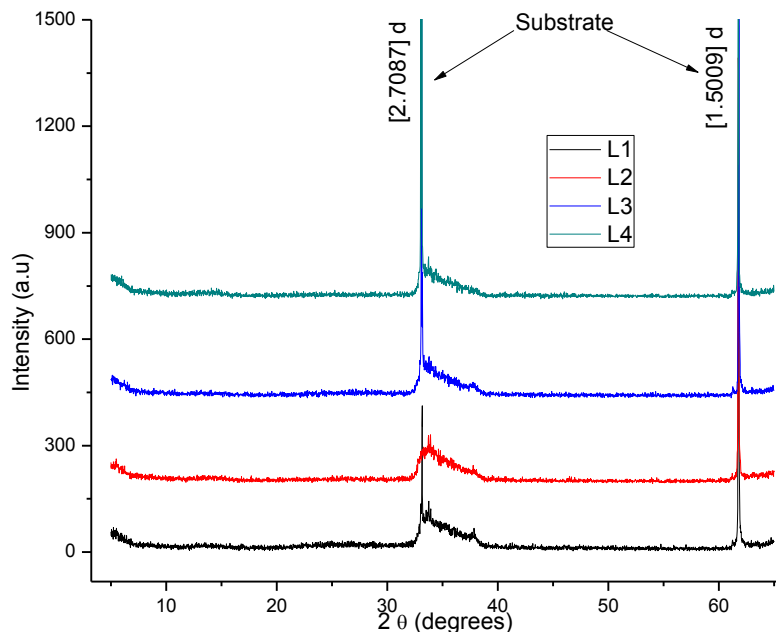
Figure IV.8. XRD spectra of the L1 - L4 samples.

Based on previous works [Lucazeau et al. 1978, Lucazeau and Leroy 1978, Barnier and Lucazeau 1976], Nemec et al. [2009b] tentatively assigned the main band (330 cm^{-1}) to F_2 ν_d GaS_4 tetrahedra vibrations overlapping with F_2 ν LaS_8 vibrations. The band at ~220 cm^{-1} was attributed to A_1 ν_s GaS_4 tetrahedra vibrations overlapped with A_1 or E, eventually F_2 ν LaS_8 vibrations, while the weaker bands at 135 and 95 cm^{-1} were connected with $F_1(F_2)$ δ GaS_4 and A_1/E T' LaS_8 vibrations, respectively. The authors concluded that the structure of GLS bulk glasses and corresponding thin films was formed by GaS_4 tetrahedra and LaS_8 structural units, and explained the small variations between Raman spectra of bulk and PLD thin films by the slightly different stoichiometry and some differences in bonds' length and angles present in the GaS_4 / LaS_8 basic structural units.

The Raman spectra we recorded with 785 nm excitation for the bulk GLS target confirmed the existence of this structure, but also evidenced a second one, with maximum around 600 cm^{-1} and extending to ~750 cm^{-1} (Figure IV.10a). There are two possibilities for the occurrence of this structure: either it is due to the presence of Ga_2O_3 and/or La_2O_3 oxides (but this structure was not observed for the Pr-doped samples, see below), or to the luminescence of possible Er impurities at 825 nm ($^4I_{9/2} - {}^4I_{15/2}$ transition)

following excitation at 785 nm. The Raman spectra of thin films using 785 nm excitation did not show the presence of GLS specific features, being dominated by the 520 cm^{-1} and 301 cm^{-1} peaks of the Si (100) substrate (Figure IV.10b). However, the thickest samples (L1 and L2) exhibited the characteristic GLS broad band between 260 and 500 cm^{-1} when excited with 514 nm (Figure IV.10c).
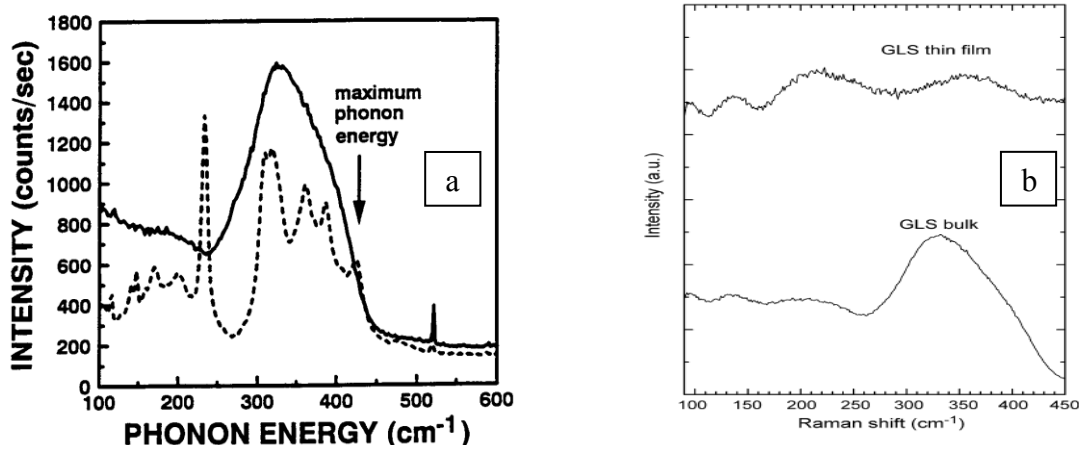
Figure IV.9. a) Raman spectra (514 nm excitation) of GLS glass fibre (solid line) and crystallized fibre core (dashed line) [Hewak et al. 1994]; b) Raman spectra (632.8 nm excitation) of GLS bulk and thin film deposited by PLD at 532 nm [Nemec et al. 2009b].
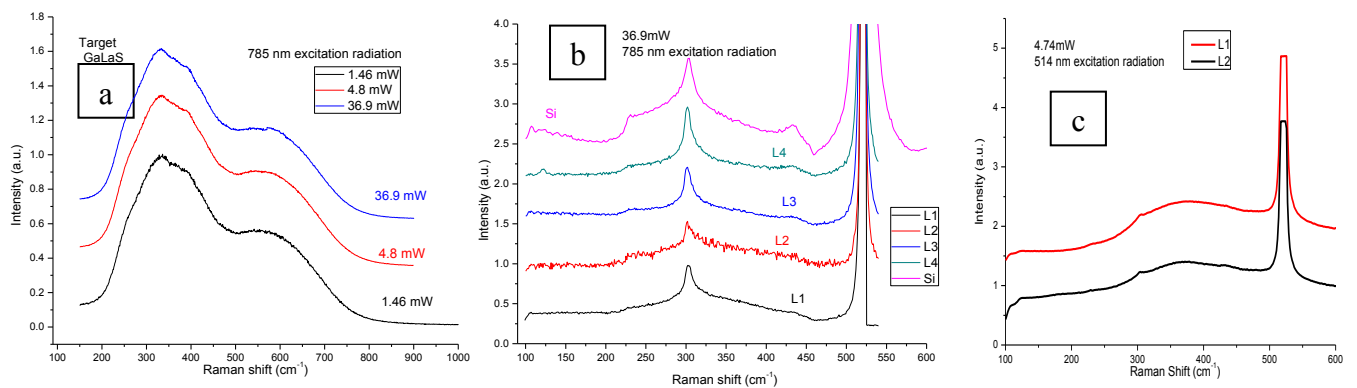
Figure IV.10. Raman spectra of a) GLS target (785 nm excitation) and deposited thin films, b) 785 nm excitation, c) 514 nm excitation.

IV.3.2 Picosecond and femtosecond regimes

Four pure GLS samples were deposited in picosecond regime and nine samples in femtosecond regime, using the Ti:Sa laser at λ = 800 nm, repetition rate = 100 Hz, pulse duration = 2 ps and 120 fs, respectively. The picosecond samples were deposited on Si (100) substrates under high vacuum conditions ($7\text{-}8\times10^{-6}$ Torr), while in the femtosecond regime a higher pressure ($6\text{-}7\times10^{-2}$ Torr, N_2 buffer gas) was also tested. The amplified Ti:Sa laser can deliver only <2 mJ /laser pulse, so a maximum fluence of 0.51 J/cm^2 was used. Depositions were made during 15 or 30 minutes, i.e. with 90 000 or 180 000 pulses. The distance between target and substrate was varied in the range 2-4 cm. Deposition parameters for both regimes are summarized in Tables IV.3 and IV.4.

Table IV.3 Experimental parameters for the deposition of GLS thin films in the picosecond regime.

Sample label	P (Torr)	d (cm)	Laser	t (min)	Thickness (nm)
GaLaS I	$8\cdot10^{-6}$	4	λ=800 nm, 100 Hz, 2 ps, E=1.78 mJ/pulse, F=0.29 J/cm^2		N/A
GaLaS II	$7\cdot10^{-6}$	4		30	700
GaLaS III	$8\cdot10^{-6}$	3			1100
GaLaS IV	$8\cdot10^{-6}$	2			1200

Table IV.4 Experimental parameters for the deposition of GLS thin films in the femtosecond regime.

Sample label	P (Trr)	d (cm)	Laser	t (min)	Thickness (nm)
GaLaS 1	$8\cdot10^{-6}$	4	λ=800 nm, 100 Hz , 120 fs, E=1.63 mJ/pulse, F=0.51 J/cm^2	15	N/A
GaLaS 2	$7\cdot10^{-6}$	4			100
GaLaS 3	$7\cdot10^{-2}$	4			30
GaLaS 4	$6\cdot10^{-2}$	3			80
GaLaS 5	$6\cdot10^{-6}$	3			55 (ellipso)
GaLaS 6	$7\cdot10^{-6}$	2			200
GaLaS 7	$7\cdot10^{-2}$	2			100
GaLaS 8	$8\cdot10^{-6}$	4	λ=800 nm, 100 Hz, 120 fs, E=1.67 mJ/pulse, F=0.27 J/cm^2	30	100 (ellipso)
GaLaS 9	$7\cdot10^{-6}$	4			150

The optical microscopy inspection of the thin films surface (Figure IV.11) showed a quite different picture with respect to the nanosecond regime, especially for the picosecond samples. This was further confirmed by stylus profilometry measurements displayed on the same Figure. We notice the absence of large droplets, which is somehow expected as the thermal effects are much more reduced in these regimes. However, the surface of the picosecond samples exhibits an important roughness, and looks like being an agglomeration of small chunks of matter (or like a compressed powder). On the contrary, the femtosecond samples do exhibit some small debris on the surface, but they are much smaller and dispersed than in the nanosecond regime. In fs-deposited thin films, the debris on the surface look more like "dust particles", and do not show the round shape characteristic to molten matter. These remarks are valid for all samples, i.e. we did not see any influence of pressure, target-substrate distance or laser fluence on the general aspect of the thin films surface.
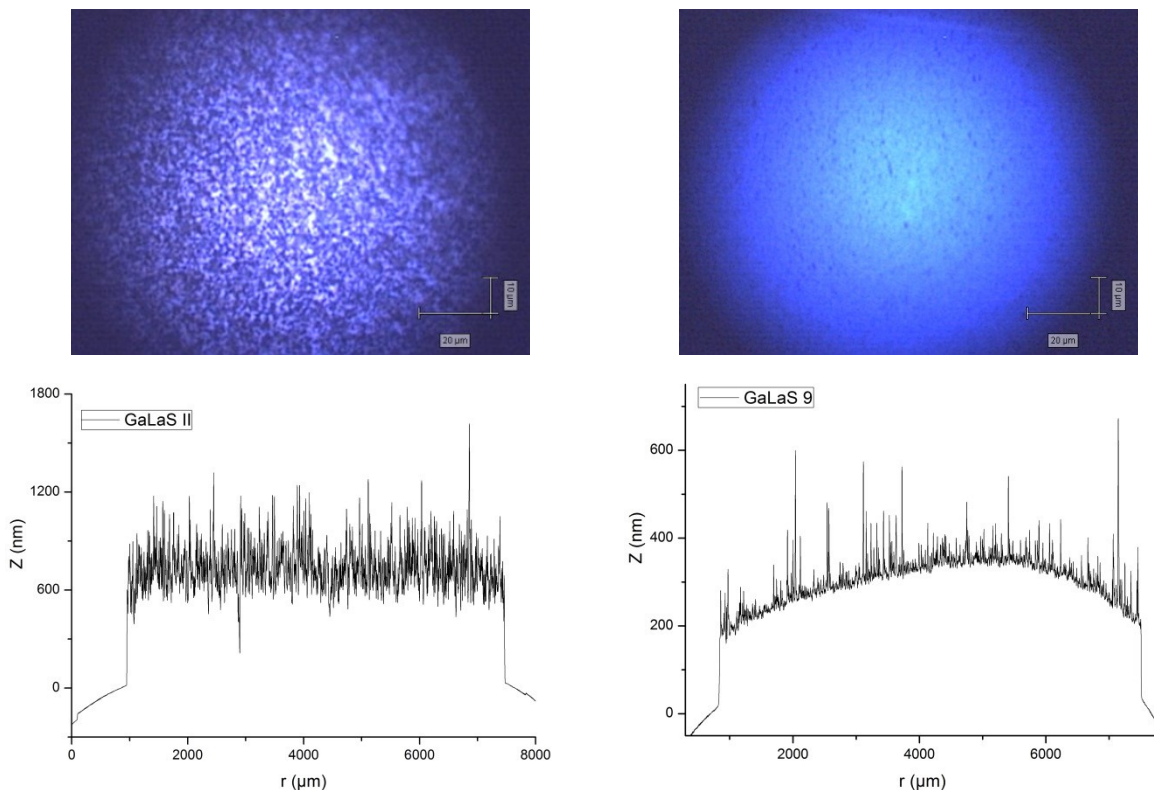
Figure IV.11. Optical microscopy and stylus profilometry for GaLaS II (ps, left column) and GaLaS 9 (fs, right column) samples.

The deposition rates were significantly different between picosecond and femtosecond regimes: in picosecond we obtained rather thick samples (in the range 700-1200 nm, deposition rate = 0.06 Å/laser pulse for GaLaS III), while in femtosecond the thickness was much less for similar laser fluence (100-200 nm in high vacuum). This points to different ablation mechanisms in these two regimes. Moreover, higher pressure seems to negatively affect the deposition rate, as one can see from the very low thickness (<100 nm) of samples GaLaS 3, 4 and 7. Reducing the distance between the target and the substrate results in higher deposition rate, as it is expected.

IV.3.2.1   *Elemental composition*

EDX measurements were performed on three samples (GaLaS II, 6 and 9) using the JEOL JSM 6400 instrument at Université de Rennes, France (10 kV accelerating voltage, L, L and K series for Ga, La and S, respectively). The results are summarized in Table IV.5. Due to the uniformity of the thin films surface (see SEM images in Table IV.5), only analyses on large areas were performed (~100x100 μm^2). Three distinct areas were measured for each sample. Each sample seems to be homogeneous (this was also confirmed by TOF-SIMS profiles recorded in both positive and negative polarities), within 1-2% variation for each element. However, important deviation from nominal composition is observed, especially for the femtosecond deposited samples. The picosecond sample shows 5-6% overstoichiometry for Ga, 2-3% overstoichiometry for La, and 7-8% understoichiometry for S. This is comparable with the results obtained on nanosecond samples in this work (using the 30 kV analyzing beam) and also by other authors [Nemec et al. 2009b]. On the contrary, the femtosecond deposited samples seem to have very different compositions, especially for Ga and La (10% variation !). When compared to the nominal composition, these samples are also far away, with 15-20% deficit in Sulphur. The two parameters changed when depositing these samples were the fluence (by a factor of 2) and the target-substrate distance (from 2 to 4 cm). The only comparison available in femtosecond regime is the work of Darby et al. [2008a] on GLSO: they evidenced an increase of Ga content, and decrease of La and S as the target-substrate distance is increased, which is the contrary of what is observed here. Note

however that their work was done at significantly higher fluence (1.5 J/cm^2). When the fluence is lowered at ~0.2 J/cm^2, very important variations (as high as 10%) are observed between the samples deposited, especially on Ga and S content (S in the low 40% is measured). This suggests use of higher fluence should be favored (which is difficult with the limited output energy of our laser). We note however that in the entire femtosecond work of Darby et al. [2008a], regardless of the varied parameter (background pressure, laser fluence, target-substrate distance), all the compositions were far away from the nominal: in the range 40-50% for S, 25-35% for La, and 15-25% for Ga.

All these observations raise the question about the applicability of femtosecond PLD for obtaining GLS thin films close to the nominal composition. This question is justified by the very different ablation mechanism in fs compared to ns regime, and certainly deserves a more thorough study, which was prevented here by the limited availability of the EDX instrument.

Table IV.5 Picosecond and femtosecond GLS thin films EDX analysis results and SEM images.

Sample	Composition			SEM image.
	Ga	**La**	**S**	
Nominal comp.	**26.47**	**14.25**	**59.26**	
GaLaS II	31.59	16.33	52.08	
	31.44	17.41	51.15	
	32.07	17.25	50.68	
GaLaS 6	36.93	21.50	41.57	
	37.53	20.80	41.67	
	37.14	20.56	42.31	
GaLaS 9	27.56	28.00	44.44	
	27.00	27.06	45.94	
	28.44	27.66	43.90	
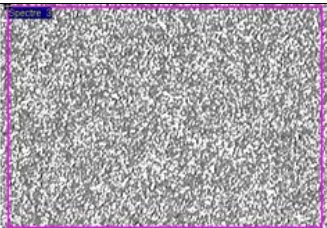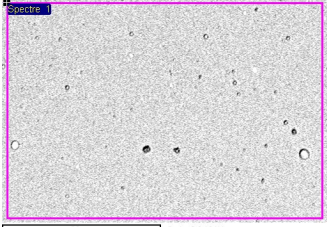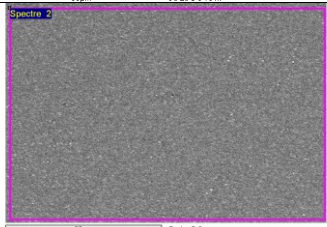
IV.3.2.2 Structural characterization

The XRD analysis (performed by P. Nemec at Pardubice University, Czech Republic) revealed the amorphous nature of both ps- and fs-deposited thin films (see Figure IV.12).
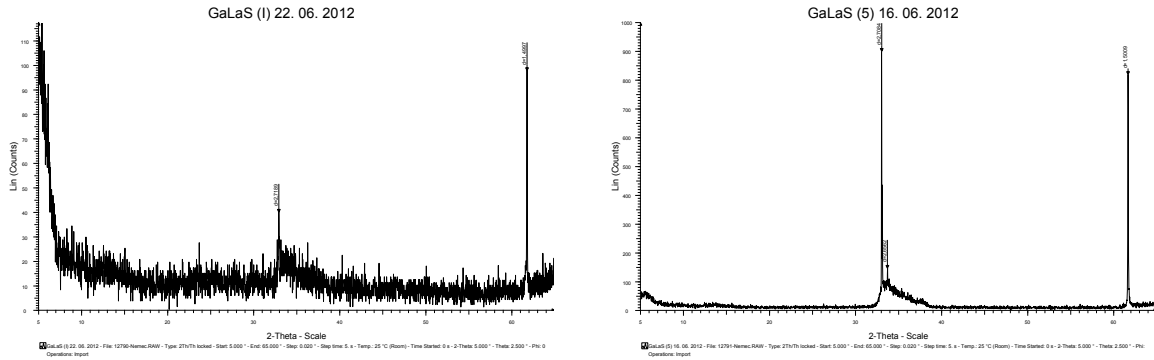
Figure IV.12. XRD spectra of samples GaLaS I and GaLaS 8.

The Raman spectra recorded with 785 nm excitation revealed the presence of the characteristic broad band between 200 and 500 cm^{-1} for all the ps-deposited samples. No phase transition was observed when increasing the excitation laser power from 1.46 mW to 36.9 mW (see Figure IV.13). On the contrary, the only feature visible in the fs-deposited samples Raman spectra was the peak at ~300 cm^{-1}, coming from the crystalline Si substrate. This could be related to the low thickness of the fs samples, compared to the ps ones. However, the same result was obtained for the ns-deposited samples (see above), which are much thicker. We have not a clear explanation on the origin of these observations, and new measurements should be envisaged in order to confirm/infirm our suppositions.
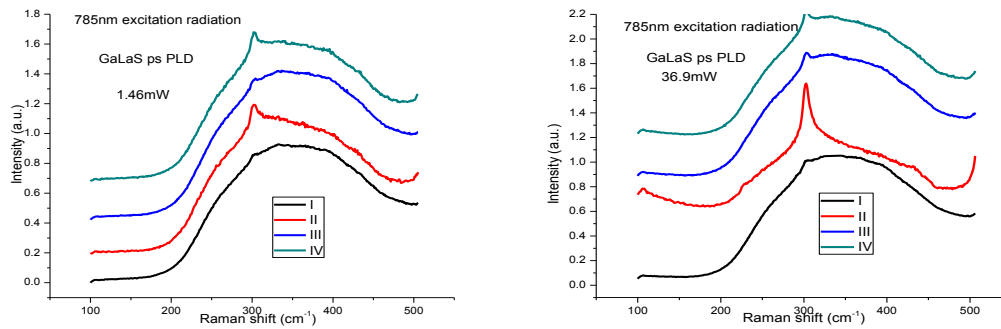
Figure IV.13. Raman spectra of ps-deposited samples recorded with 1.46 mW (a) and 36.9 mW (b) excitation laser power.

IV.4 Deposition and characterization of Er- and Pr-doped GLS thin films

IV.4.1 Nanosecond regime

Following the general trend observed for the previously studied thin films (better quality for deposition at deeper UV wavelength), we decided to deposit two series of samples (Er- and Pr-doped GLS) only at 266 nm. The experimental conditions are displayed in Table IV.6. The depositions were made under a very low flux of Ar (background pressure ~5×10^{-5} Torr), which seemed to improve the film quality and the plume stability. We worked in deposition configuration #1 (see Figure II.7a), with the target rotated and translated, and the substrate kept fixed on the axis of the ablation plume. All the depositions were made on silica glass (microscope slide) substrates. Target-substrate distances (d) between 3 cm and 6 cm were used, and deposition times between 15 minutes (9000 laser shots) and 60 minutes (36000 laser shots). Comparable fluences (around 4 J/cm^2) were used for the deposition of the two series, but with two different approaches: lower ablated surface and energy/pulse for GLS:Er, and higher for GLS:Pr.

Table IV.6 Experimental parameters for the deposition of Er- and Pr-doped GLS thin films in the nanosecond regime.

Target	Sample	P (Torr) (Ar)	d_{t-s} (cm)	Laser (AOI 45^0)	t (min)	Thickness (nm)	
						stylus	ellipso
GaLaSEr	A 2	$4.5*10^{-5}$	6	266 nm, 10 ns, 10Hz, 100mJ, 2.35mm^2, 4.28J/cm^2	15	570	
	A 5	$4.5*10^{-5}$	3			2400	
	A 6	$4.5*10^{-5}$	6		60	2500	
	A 7	$4.5*10^{-5}$			30	1100	1150
GaLaSPr	E 1	$4.5*10^{-5}$	6	266 nm, 10 ns, 10Hz, 150mJ, 4.23mm^2, 3.5J/cm^2	15	500	495
	E 2	$4.5*10^{-5}$	6		30	1000	940
	E 3	$4.5*10^{-5}$	4		15	1150	1108
	E 4	$4.5*10^{-5}$	4		30	2200	

Thin films deposited in these conditions exhibit much better surface quality, with only few small droplets (generally < 1 µm diameter), as one can see from optical (Figure IV.14) and electronic (Figure IV.15) microscopy.
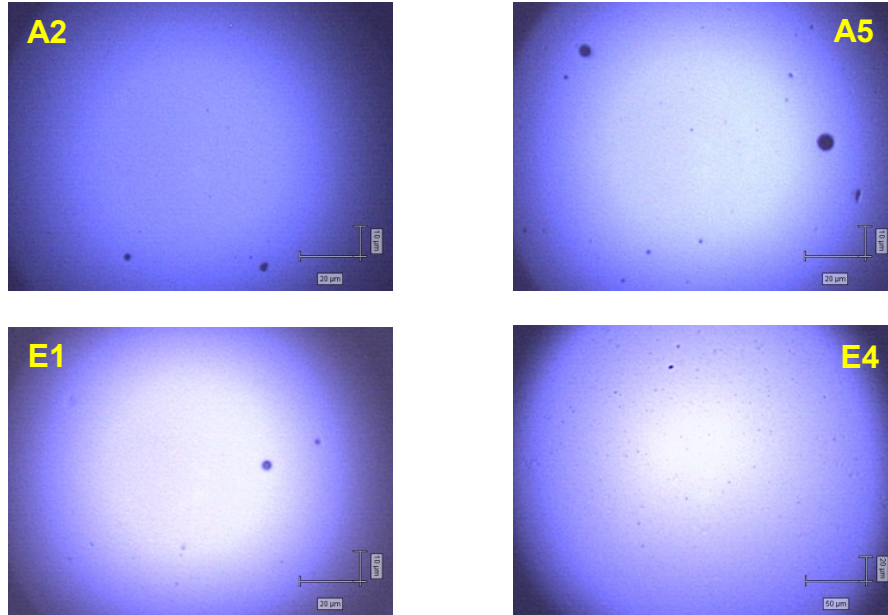
Figure IV.14.   Optical microscopy of the surface of Er- and Pr-doped GLS thin films deposited in nanosecond regime (266 nm).
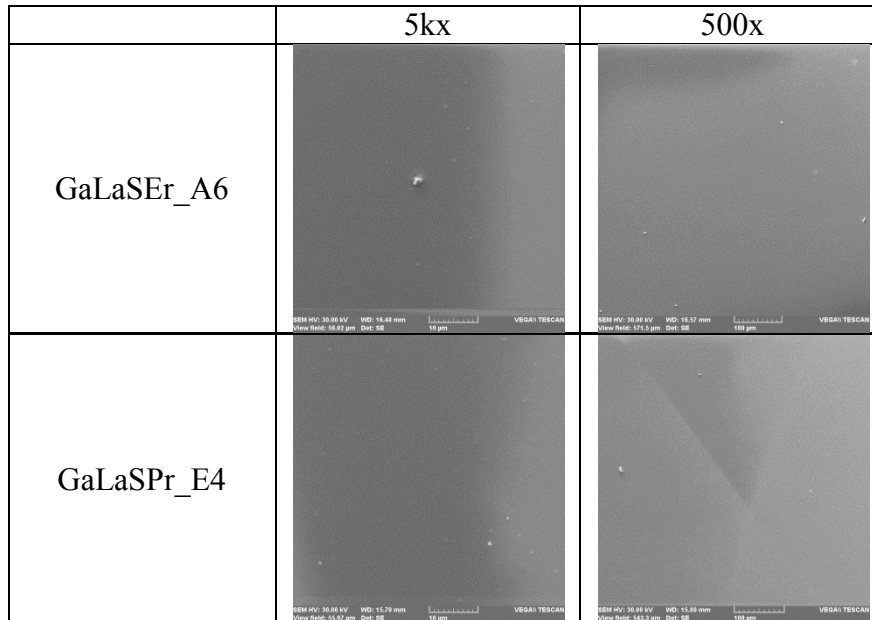
Figure IV.15. Scanning electron microscopy of the surface of Er- and Pr-doped GLS hin films deposited in nanosecond regime (5kx and 500x magnification).

This was further confirmed by the stylus profilometry measurements (Figure IV.16), which showed much smoother profiles compared to all previous depositions. We can remark a good uniformity of the film thickness, even if the substrate was not rotated and on-axis deposition was performed. The non-linear baseline apparent for the Pr-doped films is due to a slight flatness defect of the substrate and could not be removed automatically by the stylus profilometer software. However, even in this case, good thickness uniformity is observed. The film thickness values measured by profilometry are in good agreement (within 6%, see Table IV.6) with those measured by ellipsometry (see below).
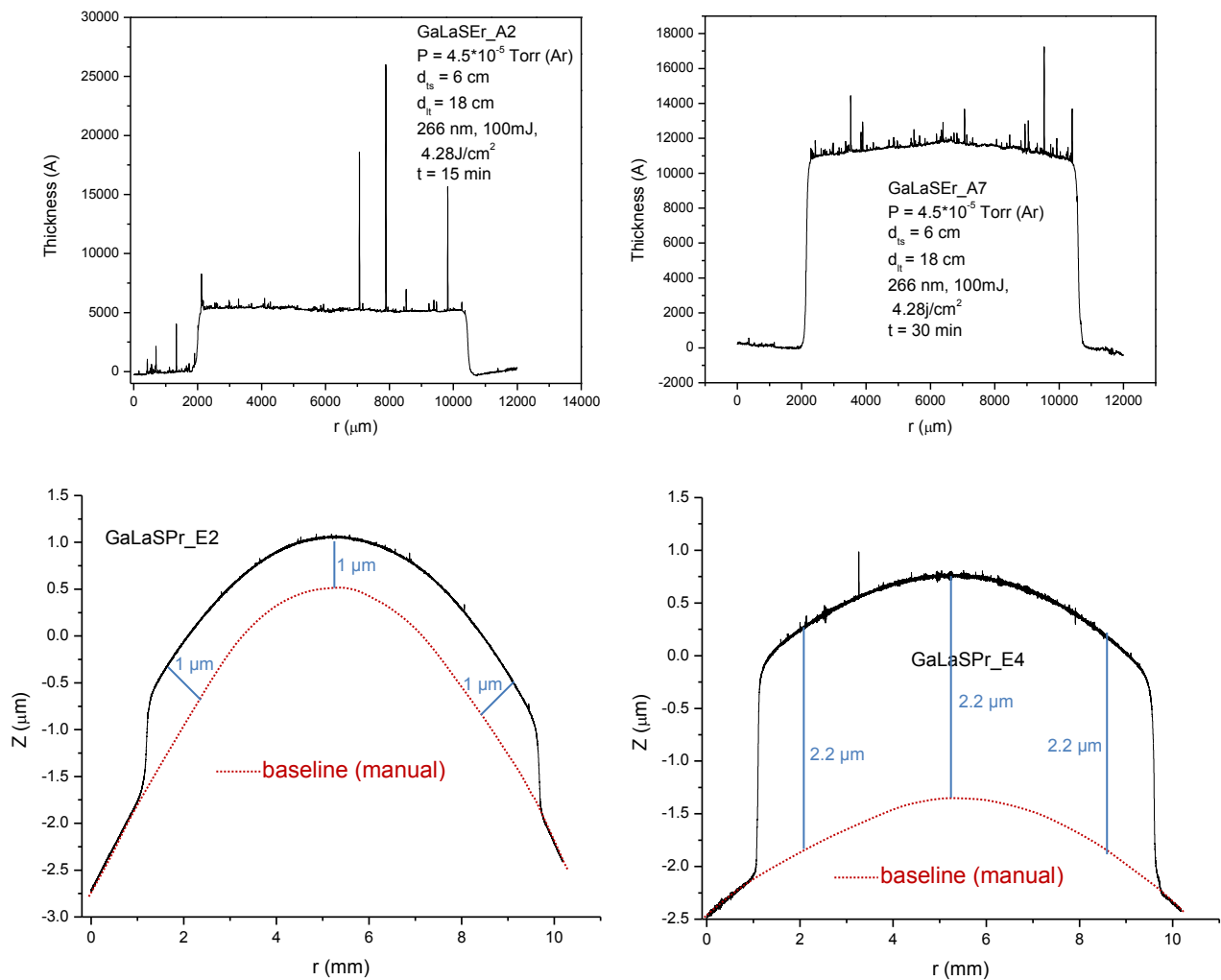
Figure IV.16. Stylus profilometry of Er- and Pr-doped GLS thin films deposited in ns regime (266 nm).

When looking to Table IV.6, one can remark a linear increase of the film thickness with the deposition time (for the same target-substrate distance, e.g. A2, A6 and A7 samples). From this linearity, a constant deposition rate of ~0.6 Å/laser pulse can be derived for d_{t-s} = 6 cm. For shorter target-substrate distance, this rate is increased, by a factor of ~2 for d_{t-s} = 4 cm, and ~4 for d_{t-s} = 3 cm. These values are in line with previous results for ns-PLD of chalcogenides [Assal and Rutt 1997, Nemec et al. 2009b]. We note that using shorter target-substrate distances doesn't seem to significantly affect the film surface quality. However, further roughness measurements by Atomic Force Microscopy (AFM) are envisaged in order to confirm this.

IV.4.1.1   Elemental composition

In order to check the stoichiometric transfer between the target and the thin films, we performed EDX measurements using the Tescan Vega II LMH instrument (Technical University of Iasi, Romania) with 30 kV acceleration voltage, and two magnifications: 500x (analyzed area ~500x500 μm^2) and 5000x (analyzed area ~50x50 μm^2). The results are summarized in Table IV.7. The measured compositions were fairly close to the nominal ones. In all the measurements, La was overstoichiometric by 5-6 at%. Curiously, for Ga and S composition, the two series of samples presented completely opposite behavior: the Er-doped films were slightly understoichiometric in Ga (by maximum ~6 at%) and slightly understoichiometric (or for some points even overstoichiometric!) in S, while for the Pr-doped films, overstoichiometry of Ga was measured (by maximum ~6 at%), along with more severe understoichiometry of S (by maximum 11 at%). The dopants were quantified at 1-2 at%, but these figures should be taken with caution, as they are comparable to the instrument precision. However, the dopants signals were well present in the EDX spectra. On the other hand, an EDX analysis performed on the GLS:Pr target gave the following results: Ga: 28.28 at%, La: 12.45 at%, S: 59.14 at%, and Pr: 0.13 at%, i.e. deviations of up to 1 at% with respect to the nominal composition, which is in our opinion representative of the instrument precision.

Table IV.7 EDX analysis results of Er- and Pr-doped GLS thin films deposited in ns regime.

Target	Sample	EDX				
		Magnification	Ga	La	S	Er
	Nominal		**27.44**	**11.76**	**60**	**0.8**
	A 2	500x	25.51	15.00	57.25	2.23
		5000x	21.86	14.75	61.43	1.95
	A 5	500x	26.76	15.98	54.95	2.30
		5000x	24.08	17.41	56.77	1.74
GaLaSEr	A 6	5000x	22.3	15.7	57.7	2.2
			21.5	15.8	60.5	2.14
		500x	25.5	17.5	55.0	2.1
			25.0	17.6	55.4	2.0
	A 7	500x	25.53	15.55	57.14	1.78
		5000x	23.00	17.38	57.50	2.11
			Ga	La	S	Pr
	Nominal		**27.44**	**11.76**	**60**	**0.8**
	E1	500x	30.96	15.26	52.37	1.41
		5000x	32.58	16.93	49.39	1.1
	E 2	500x	33.06	16.64	49.01	1.3
GaLaSPr		5000x	29.97	16.70	51.93	1.40
	E 3	500x	30.80	16.28	51.75	1.17
		5000x	26.64	16.62	55.47	1.27
	E 4	5000x	27.4	16.8	54.4	1.4
		500x	30.0	17.1	51.7	1.2
			29.5	17.3	52.0	1.3

TOF-SIMS depth-profiling was performed on some sample in order to check the uniform distribution of the elements in the film volume. An O_2 ion beam was used to progressively sputter the film on a 200 μm x 200 μm surface and a Bi ion beam to analyze a surface of 75 μm x 75 μm centered on the sputtered area. The ions were detected in positive polarity (which explains the low signal of S, see Figure IV.17). The profiles displayed in Figure IV.17 show good homogeneity of the main elements and also of the dopants in the deposited films. Moreover, when comparing the sputtering times needed to reach the substrate in similar conditions (e.g. E3 and E4 samples), we find a factor of ~2, corresponding to the thickness ratio of the two films.
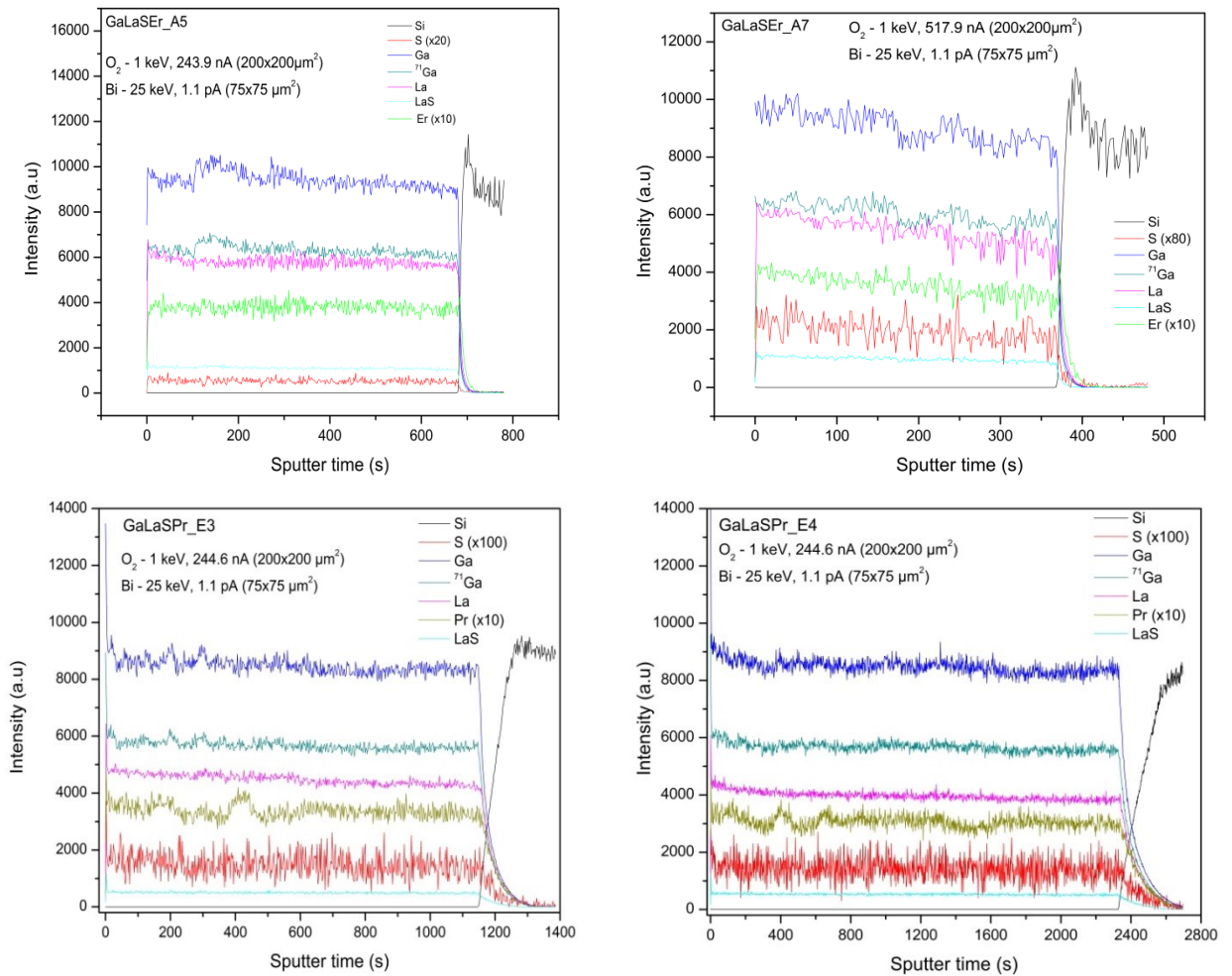
Figure IV.17. TOF-SIMS depth-profiles (positive polarity) of the some Er- and Pr-doped GLS thin films deposited in ns regime.

IV.4.1.2   *Structural characterization*

The XRD measurements performed on the Er- and Pr-doped GLS thin films deposited in ns regime showed an amorphous deposition (Figure IV.18), with one exception: the A7 sample, which exhibits a very surprising crystalline structure. Moreover, the crystalline phase could not be identified from the available databases! Future work on this sample has to be done in order to identify its structure

.
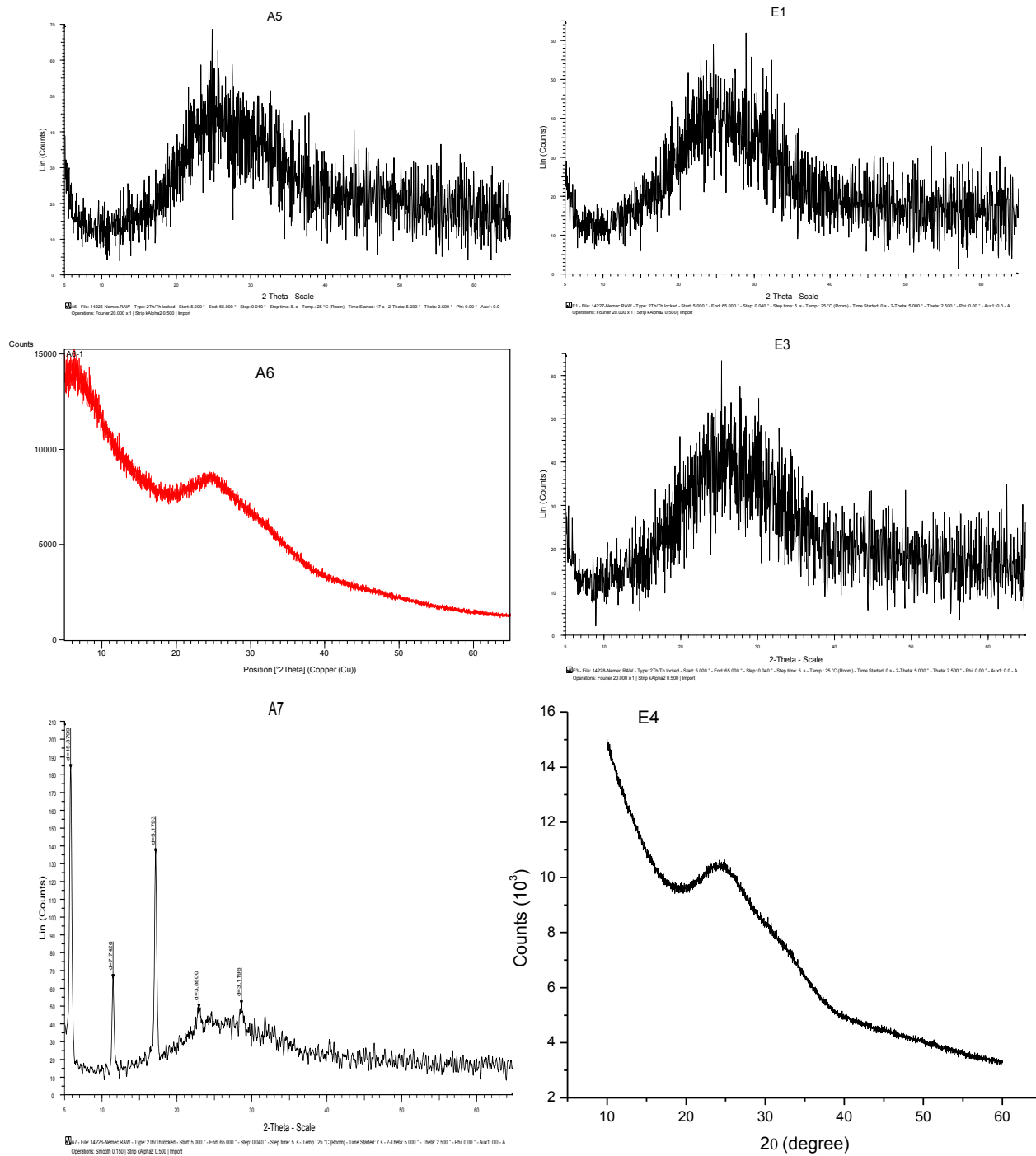
Figure IV.18. XRD spectra of Er- and Pr-doped GLS thin films deposited in ns regime.

Raman spectra of bulk GLS:Er and GLS:Pr are presented in Figure IV.19. The broad band centered at ~330 cm^{-1}, characteristic for GLS (see above), is present in both

spectra. The second structure (maximum at ~600 cm^{-1}) evidenced for the pure GLS targets is visible in the GLS:Er spectrum, but not in the GLS:Pr one, which corroborates the hypothesis made on its Er origin (as Pr has no absorption at 785 nm).
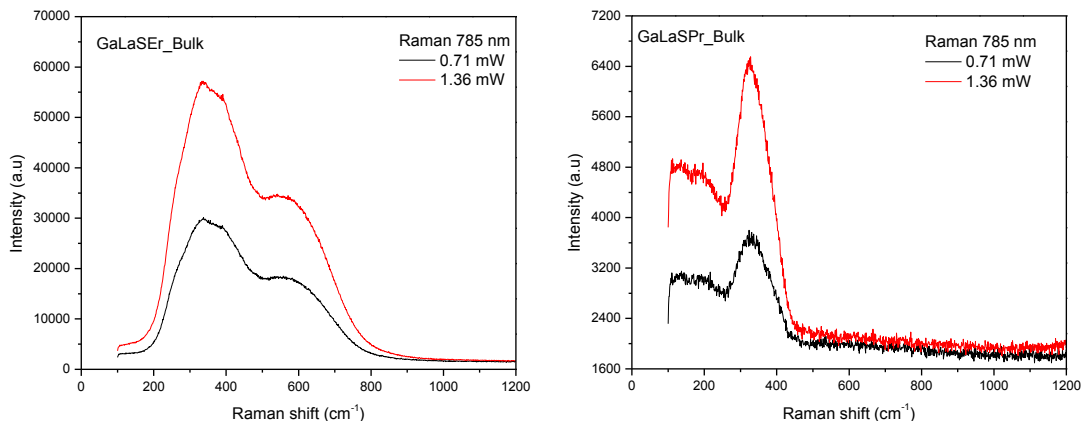
Figure IV.19. Raman spectra of GLS:Er and GLS:Pr targets (785 nm excitation).

Recording Raman spectra of GLS thin films deposited on silica glass was less straightforward than in the case of films deposited on crystalline Si. The main problem is that the glass substrate exhibits a strong band centered at 360 cm^{-1}, i.e. very close to the main GLS band, as one can see from Figure IV.20a (note in passing that a second structure is centered at ~550 cm^{-1}, i.e. close to the second structure observed in GLS and GLS:Er targets). In these conditions, only the thickest films gave enough Raman signal to be distinguished from the substrate signal. One example is presented in Figure IV.20b,c for the GLS:Pr E4 sample. One can see a shoulder around 330 cm^{-1}, and also another band centered at ~175 cm^{-1}.
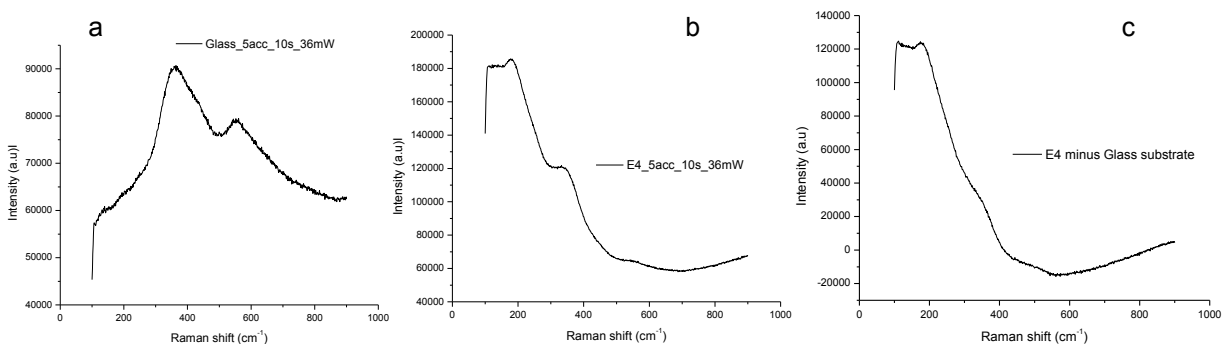
Figure IV.20. Raman spectra of a) SiO$_2$ glass substrate; b) E4 sample (raw data, i.e. with glass substrate contribution); c) E4 thin film without glass substrate contribution (i.e. difference between b) and a)).

The spectra recorded for the Er-doped thin films showed no interesting feature in the low wavenumber region. However, when extending the measurement range to 3000 cm^{-1}, a pronounced broadband situated between 1200 and 2000 cm^{-1} was evidenced. For the A7 sample, a very strong increase has been observed, with a maximum at ~1380 cm^{-1} (see Figure IV.21), and we had some hope in explaining the difference observed in the XRD spectra for this sample. Unfortunately, it seems that this is just coming from the glass substrate (Figure IV.21), due to the lower thickness of this sample.
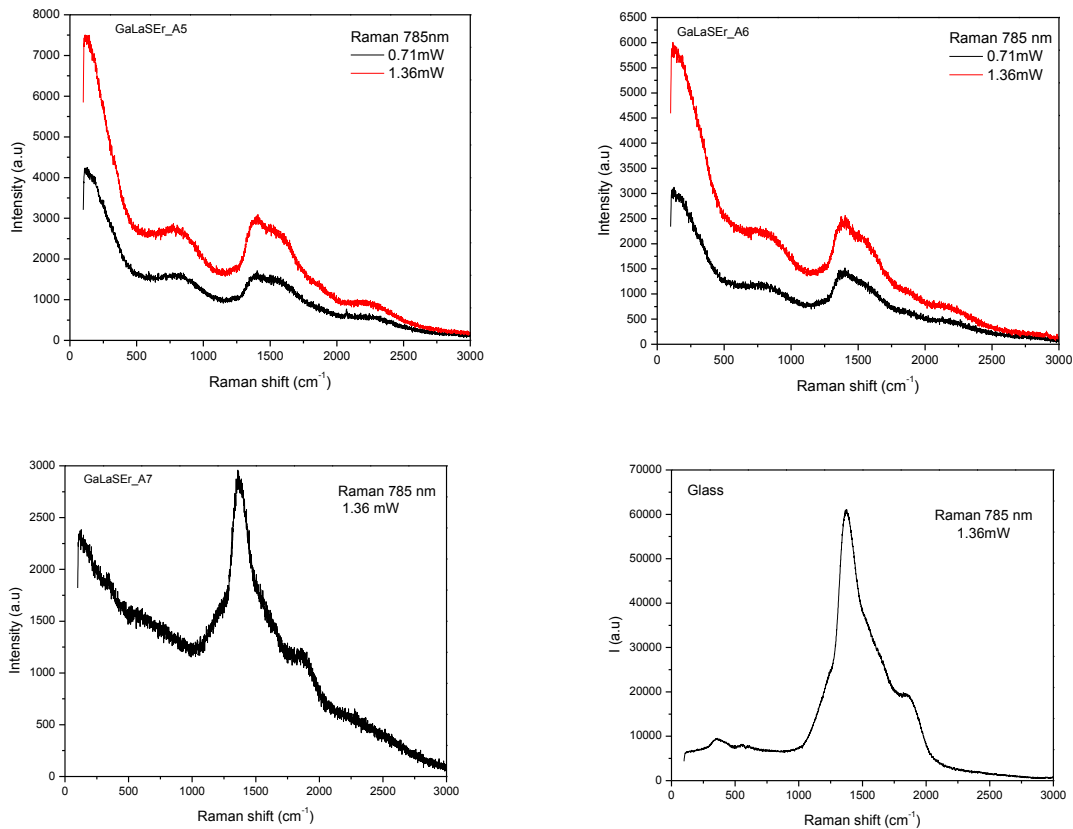
Figure IV.21. Raman spectra of GLS:Er A5, A6, A7 samples and of the glass substrate.

The pronounced increase observed in the spectra at lower wavenumbers (200 – 500 cm^{-1}) could come from fluorescence. Er-doped GLS fibers exhibit a fluorescence band with maximum around 800 nm (see Figure 3 in [Schweizer et al. 1997b]), which means ~240 cm^{-1} in the Raman spectrum excited by 785 nm radiation. On the other hand, Pr^{3+} exhibits fluorescence at ~1 µm (see Figure 3.4.1 in [Schweizer 1998]), i.e. ~2700

cm-1 in the Raman spectrum, or no signal has been observed at this wavenumber in our spectra.

IV.4.2   *Picosecond and femtosecond regimes*

Eight thin films of Er and Pr-doped GLS were deposited in fs regime (on crystalline Si substrates) and two films in ps regime (on microscope slides glass), using experimental conditions summarized in Table IV.8. The fs-deposited samples were very thin and did not allow obtaining reliable results by the various characterization methods employed. Consequently, we will focus our discussion on the two samples deposited in ps regime. These samples were deposited using rectangular masks placed on the substrate in order to delimitate larger deposition areas: 21x18 mm^2 for AP1 and 19x15 mm^2 for EP1.

Table IV.8 Experimental parameters for the deposition of Er- and Pr-doped GLS thin films in the ps and fs regimes.

Target	Sample	P (Torr)	d_{s-t} (cm)	Laser (AOI 45^0)	t (min)	Thickness (nm)
GLS 2% Er^{3+} doped	EX1	$1.6*10^{-6}$	4	λ=800nm, E=1.60mJ, ν=1kHz, 120fs, S = 1.47 mm^2, F = 0.108 J/cm^2	20	N/A
	EX2	$1.6*10^{-6}$			30	80-100
	EX3	$1.6*10^{-6}$			20	30-40
	EX4	$1.6*10^{-6}$			10	40-50
GLS 2000 ppm Pr^{3+} doped	R1	$1.2*10^{-6}$			30	N/A
	R2	$1.3*10^{-6}$			20	N/A
	R3	$1.6*10^{-6}$			10	<30 nm
	R4	$1.2*10^{-6}$			30	<30 nm
GLS 2% Er^{3+} doped	**AP 1**	$4.5*10^{-5}$	3	800 nm, 2ps, 100 Hz, 0.15mm^2,1.2J/cm^2	15	~1500 (central profile) ~1300 (side profile)
GLS 2% Pr^{3+} doped	**EP 1**	$4.5*10^{-5}$				~1800 (central profile) ~900 (side profile)

The surface quality inspection by optical and electronic microscopy revealed again a characteristic "granular" aspect (see Figure IV.22), with only few small droplets, as already observed for other ps regime depositions.
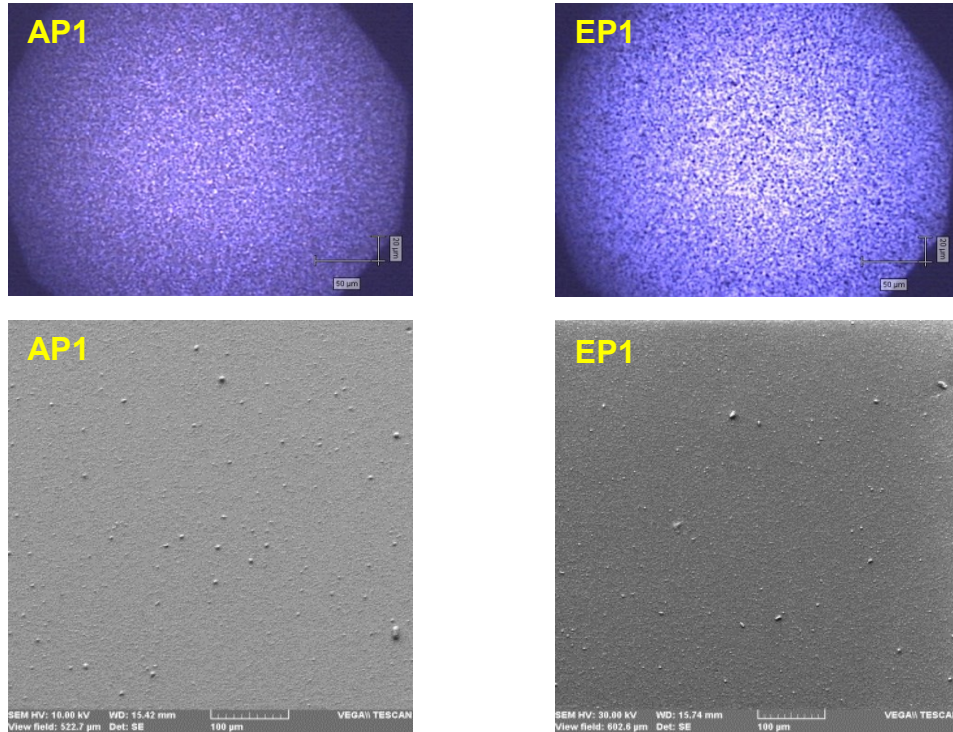
Figure IV.22. Optical (top) and electronic (bottom) microscopy of the surface of Er- (left) and Pr-doped (right) GLS thin films deposited in ps regime.

This was further confirmed by stylus profilometry (Figure IV.23). Two profiles were recorded for each sample, one on the film center, and another one 6 mm aside for AP1 and 10 mm aside for EP1. We note that because of the limited length range of the KLA Tencor stylus profilometer (10 mm), a complete profile (i.e. from side to side) could not be recorded in one acquisition. Consequently, the thickness values listed in Table IV.8 are actually step heights measured on the extremities of the "half-profiles" recorded, i.e. 9 mm from the profile center for AP1, and 7.5 mm for EP1, as displayed in Figure IV.24.
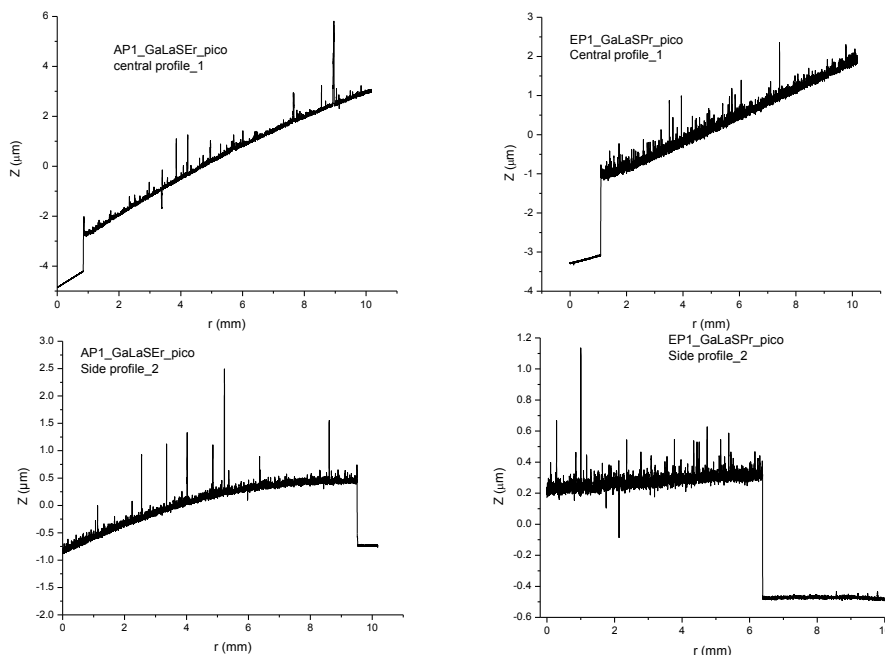
Figure IV.23. Stylus profilometry of AP1 (left) and EP1 (right) samples: central (top) and side (bottom) profiles.
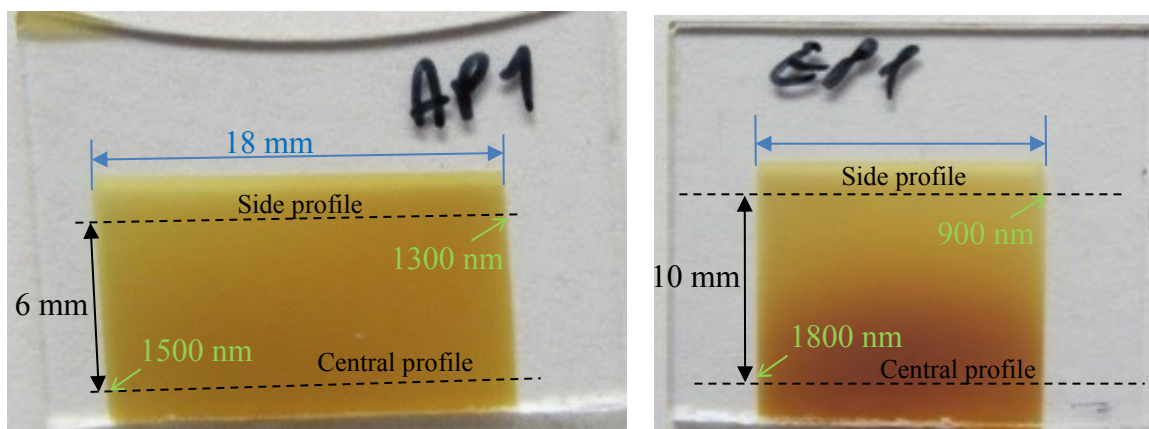
Figure IV.24. Central and side profile positions for AP1 and EP1 samples (see text).

EDX measurements were performed using the TESCAN VEGA instrument (30 kV accelerating voltage) in various points on the sample surface (see Table IV.9). A significant variation of the composition with the distance from the film center is not observed, on the contrary of results obtained for GST deposition (D1 sample, see Chapter III). Once again, Sulphur is understoichiometric (by as much as ~10 at%), while La is overstoichiometric by about the same amount and Ga is closer to the nominal value. The dopant concentration is probably overestimated by the instrument. TOF-SIMS depth-

profiling measurements performed in positive polarity showed a fairly uniform in-depth distribution of main constituents and dopants for both samples (comparable to ns-deposited films, see above). This corroborates the quite low standard deviations on the mean concentration values displayed in Table IV.9. We note that in a previous study (ns 248 nm excimer laser deposition of GLS thin films), Gill et al. [1995] obtained higher standard deviations when analyzing by EDX 12 points on the surface of a film (Ga: 26.8±2.9 at%, La: 15.2±2.5 at%, S: 50.4±5.6 at%) and concluded to a good homogeneity of the film across the surface.

Table IV.9   EDX measurements in various points on the AP1 and EP1 samples surface.

Sample	Magnification	EDX composition			
		Ga	La	S	Er/Pr
Nominal		**27.44**	**11.76**	**60**	**0.8**
AP 1 GaLaSEr	5kx_1	23.6	19.1	55.2	2.1
	5kx_2	22.8	19.6	55.6	2.1
	500x_1	24.2	18.6	54.6	2.5
	500x_2	23.5	19.0	55.0	2.4
	500x_3	22.97	18.45	56.22	2.35
	500x_4	26.64	19.36	51.58	2.42
	500x_5	26.10	19.86	51.53	2.51
	500x_6	27.65	18.37	51.64	2.33
Average values AP1		**24.7±1.8**	**19.0±0.6**	**53.9±2.0**	**2.3±0.2**
EP 1 GaLaSPr 	500x_1	27.61	20.36	50.41	1.62
	500x_2	29.41	20.76	48.13	1.70
	500x_3	27.76	20.30	50.22	1.72
	500x_4	26.10	19.61	52.65	1.64
	500x_5	28.25	20.33	49.75	1.67
	500x_6	28.50	18.37	51.65	1.48
	500x_7	24.58	20.87	52.92	1.63
	500x_8	24.44	20.51	53.45	1.60
	500x_9	26.70	19.74	51.91	1.65
Average values EP1		**27.0±1.7**	**20.1±0.8**	**51.2±1.7**	**1.6±0.1**

     XRD measurements showed the amorphous nature of both samples, see Figure IV.25. Recording Raman spectra was again difficult because of the silica glass substrate response. However, the 330 cm^{-1} band was visible in the subtracted spectra (sample – substrate) when using 2.5 mW excitation laser power, with better signal for the thicker

EP1 sample, as showed in Figure IV.26. The same steep increase at low wavenumbers as for the ns-deposited samples was observed.
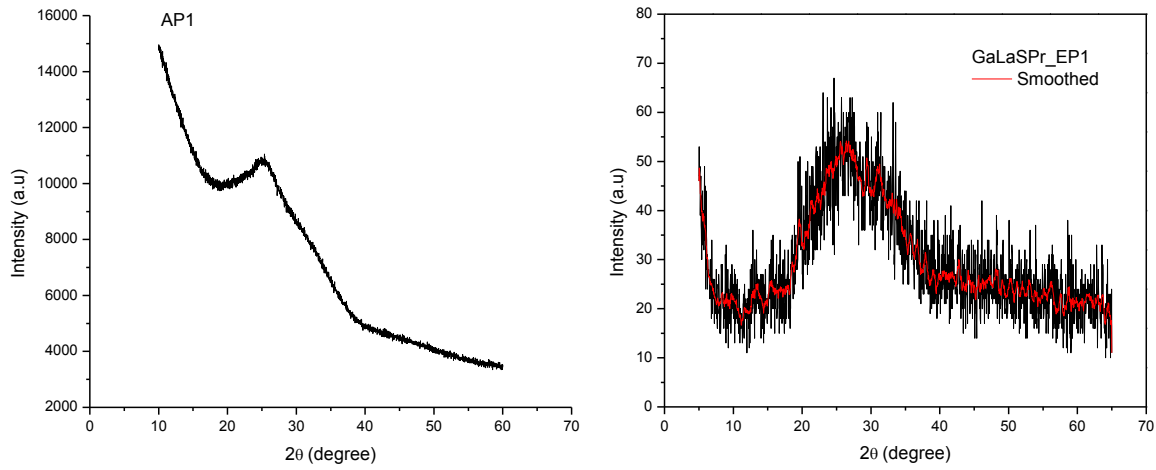
Figure IV.25. XRD measurements for AP1 and EP1 samples.
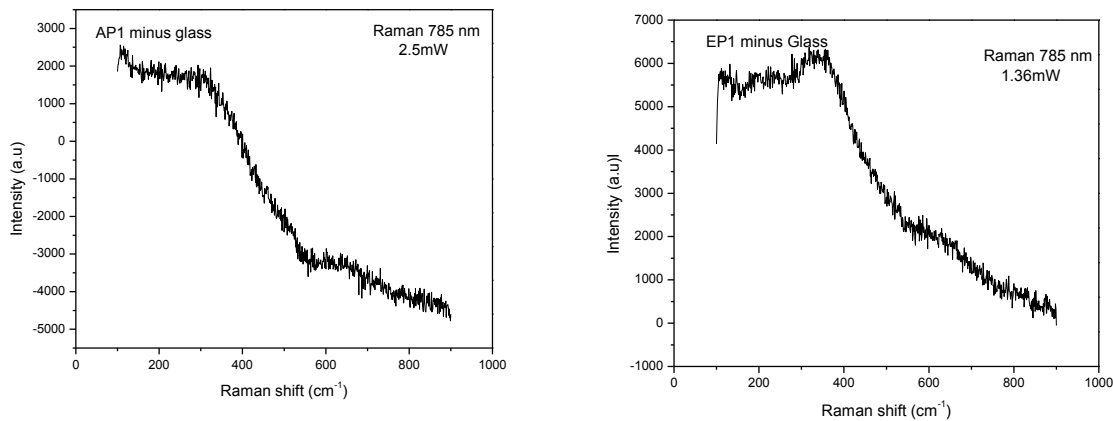
Figure IV.26. Subtracted (sample – substrate) Raman spectra of AP1 (GLS:Er) and EP1 (GLS:Pr) samples.

IV.5 Optical properties of GLS thin films

The optical properties of some GLS thin films were investigated by variable-angle spectroscopic ellipsometry (VASE) at University of Pardubice, Czech Republic (measurements done by P. Nemec and M. Olivier) and optical transmission spectrophotometry (in our laboratory). The results are presented in separate sections below.

IV.5.1 Variable-angle spectroscopic ellipsometry

Three pure GLS films deposited on crystalline Si substrates (L4 – ns regime, and GaLaS_5 and GaLaS_8 – fs regime) and four doped GLS films deposited on silica glass (A7, E1, E2, and E3 – ns regime) were investigated by the VASE technique. Figure IV.27 presents the variation with wavelength of the real and imaginary parts of the refractive index for the seven analyzed samples.
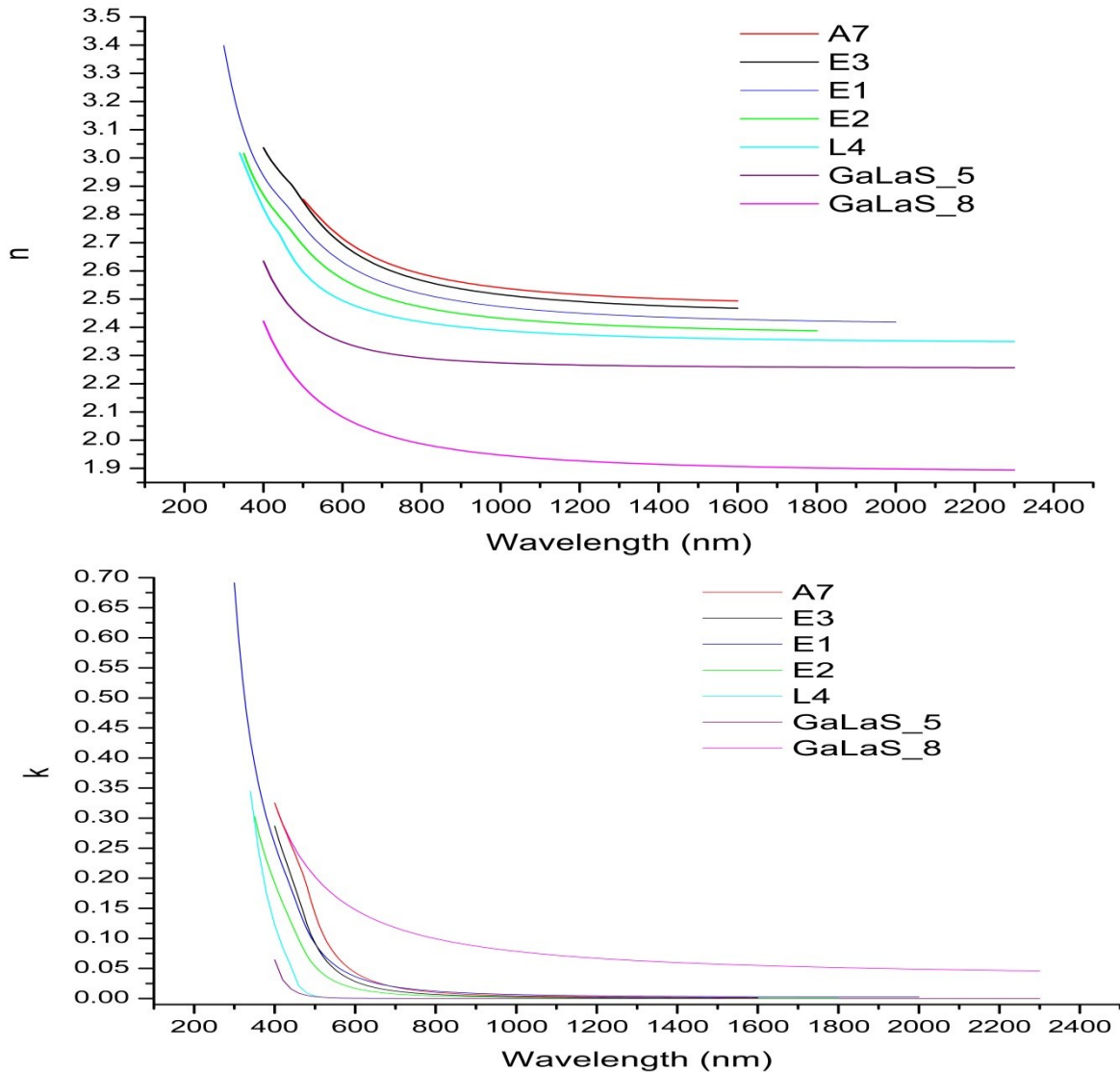
Figure IV.27. n and k values of some GLS thin films from VASE measurements.

One can easily remark the relatively good agreement between the n values of the fours samples deposited on glass substrate (and also the L4 sample deposited in ns on Si),

and the more peculiar values obtained for GaLaS_5 and (especially) GaLaS_8 samples, deposited in fs regime on Si substrate. We note however that these two samples presented much lower thickness (<100 nm) and that a Cauchy model was used to describe the ellipsometry data, instead of the Cody-Lorentz model (see Chapter II) used for the other five samples. We note also the non-zero imaginary part of the refractive index in the (normally transparent) IR range. Caution must thus be taken when comparing these data with the others.

Values of the real part of the refractive index measured at several discrete wavelengths of practical interest are displayed in Table IV.10, along with optical band gap energies (E_g), and, for comparison, with data available in the literature for PLD grown GLS thin films. We can remark that our data are in good agreement with the literature data, with the notable exception of the GaLaS_8 sample.

Table IV.10 Present study and literature n and E_g values.

Sample/Reference	n@1560 nm	n@1000 nm	n@800 nm	n@640 nm	E_g (eV)
A7	2.495	2.540	2.589	2.678	2.3±0.1
E3	2.469	2.516	2.566	2.658	2.3±0.1
E1	2.430	2.473	2.519	2.598	2.3±0.1
E2	2.394	2.432	2.472	2.536	2.2±0.1
L4	2.360	2.391	2.419	2.472	2.05±0.11
GaLaS_5	2.261	2.274	2.292	2.330	Cauchy
GaLaS_8	1.908	1.947	1.987	2.055	Cauchy
[Nemec et al. 2009b]	2.32-2.40			2.44-2.54	Cauchy
[Darby et al. 2008a] - GLSO		2.10-2.45			
[Asal and Rutt 1997]	2.4-2.75	2.5-2.85	2.6-2.9		1.4-1.9
[Gill et al. 1995]				2.27-2.47	
[Youden et al. 1993]				2.53	

It is interesting to discuss about the possible origin of the refractive index real part variations, based on previous results reported in the literature. For instance, Gill et al. [1995] reported a very high variation of n (between 2.27 and 2.47 @ 633 nm) when the

ablation laser (KrF, 248 nm, 20 ns) fluence was modified by just 1 J/cm^2, between 3 and 4 J/cm^2. They concluded that films deposited at lower fluence (typically below 3.5 J/cm^2) were sulphur-rich (Ga:S ratio of 0.4 – 0.6) and presented low n values (around 2.3), while films deposited at higher fluence (up to 9 J/cm^2) had Ga:S ratio (~0.7) and refractive index closer to the bulk values found in the same study (n = 2.45 @ 633 nm and Ga:S ratio of 0.69). We note in passing that a Ga:S ratio in bulk of 0.7 is surprising, since in our "standard" targets the nominal value is ~0.45, but the authors do not give any information on the actual composition of their target. Their conclusion is not verified by our data, as the film deposited at the highest fluence (L4, 10 J/cm^2) presents the lowest refractive index! On the other hand, using such a high fluence led indeed to Ga-rich/S-poor films (average Ga:S ratio of L1-L4 samples = 0.65±0.11 from data in Table IV.2), but with composition far from the target one. Reducing the fluence to 4.3 J/cm^2 (A samples) and 3.5 J/cm^2 (E series) led to Ga:S ratios closer to the nominal value (average of 0.42±0.05 and 0.58±0.06, for A and E series, respectively, from data in Table IV.7). On the other hand, for the fs-deposited samples much lower fluences were used: 0.51 J/cm^2 for GaLaS_5 and 0.27 J/cm^2 for GaLaS_8. We have no EDX measurements for these two samples, but data available for films deposited with the same fluences (GaLaS_6 and GaLaS_9, see Table IV.5) led to Ga:S ratios of 0.89±0.01 for F = 0.51 J/cm^2 and 0.62±0.03 for F = 0.27 J/cm^2. Once again, no clear relationship can be drawn between the Ga:S ratio and the refractive index, nor between the fluence and the Ga:S ratio.

One can argue that the ablation mechanisms involved in ns and fs PLD are different, thus a direct comparison of the fluence values in these two regimes would not be right. However, Darby et al. [2008a] performed an extensive ns-fs comparative study on the PLD of GLSO and showed that almost identical compositions (Ga:La:S ~ 30:17:53 at%, Oxygen was not quantified) are found for similar values of fluence in ns (1.8 J/cm^2) and fs (2 J/cm^2) depositions. Moreover, using targets of different composition, they investigated the influence of the deposition parameters on the deposited films Ga:La ratio, and concluded that the refractive index was linearly increasing with this ratio, from ~2.1 at Ga:La ~0.7 to ~2.45 at Ga:La ~1.7. This is again not verified for our GaLaS_5 and GaLaS_8 samples, as compositions of GaLaS_6 and GaLaS_9 films deposited with

the same respective fluences led to Ga:La ratios of 1.8 and 1.0, respectively. For the other series under investigation, the Ga:La ratio was quite spread, with average values of 1.8 ± 0.5 for F = 10 J/cm^2 (L series), 1.49 ± 0.14 for F = 4.28 J/cm^2, and 1.81 ± 0.15 for F = 3.5 J/cm^2, i.e. once again we cannot draw a clear relationship between the fluence, the Ga:La ratio and the refractive index.

Finally, Asal and Rutt [1997] found refractive indices greater than those of the bulk and increasing by 10-15% when the laser (KrF, 248 nm) fluence was increased from 3 to 6 J/cm^2, which is not verified by our data. Concerning the imaginary part of the refractive index, these authors found optical band gap values (derived from Tauc plots) decreasing from 1.9 to 1.4 eV when the fluence was increased from 3 to 6 J/cm^2. These values are far away from ours (2.2-2.3 eV for F = 3.5 - 4.28 J/cm^2, and 2.05 for F = 10 J/cm^2, see Table IV.10), and they are in contradiction with the study of Gill et al. [1995] which showed a decrease of the cut-off wavelength from 480 nm (similar to the bulk value) to ~350 nm, when the laser fluence was decreased below 3.5 J/cm^2. Our k values suggest cut-off wavelengths around 500 nm (again with the exception of the GaLaS_8 sample, see Figure IV.27), but this will be explored in more detail in the optical transmission study presented below.

IV.5.2 Optical transmission

Optical transmission spectra were recorded for ten GLS samples deposited on SiO$_2$ glass: A2, A5-7, E1-4 (in ns regime) and AP1, EP1 (in ps regime). A typical spectrum showing interference fringes was presented in Fig. II.19 for the E4 sample. Using the procedure described in II.3.4.2, one can determine the values of the refractive index at the wavelengths of these fringes maxima and minima, if the thickness of the sample is known (from ellipsometry or stylus profilometry). Figure IV.28 displays the results obtained for the eight samples deposited in ns regime.
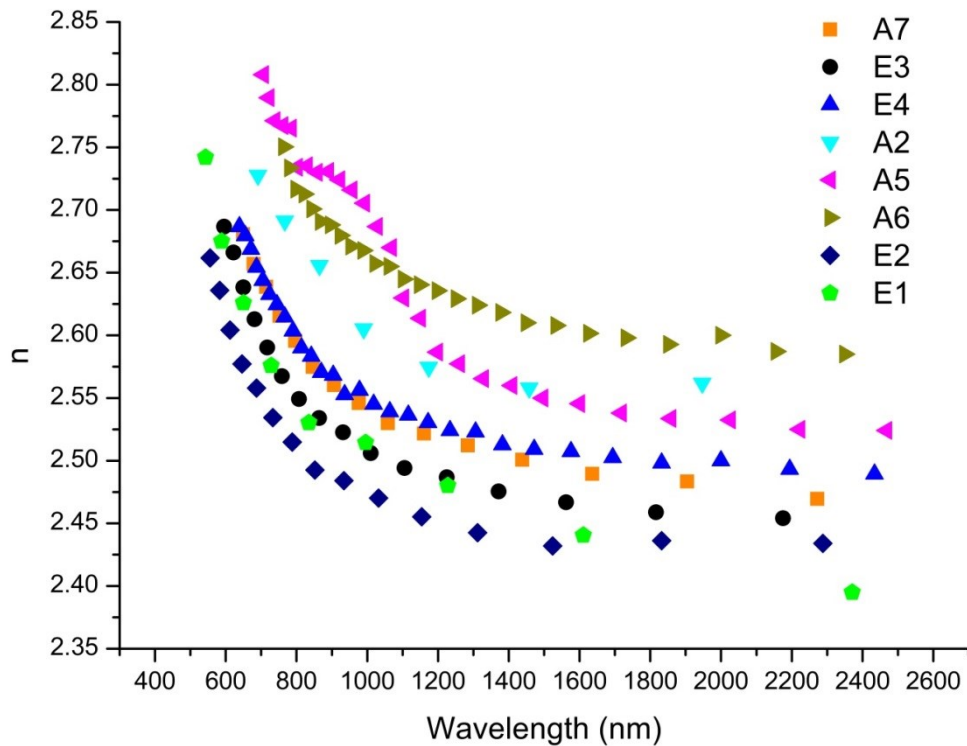
Figure IV.28 Refractive index (real part) values derived from optical transmission
               measurements for Er- and Pr-doped GLS thin films deposited on glass in
               ns regime.

To derive these n values, we used film thicknesses measured by ellipsometry
(where available) and stylus profilometry. One can remark a fair agreement between the
results obtained by optical transmission (n roughly in the range 2.4-2.5 in the transparent
IR region) and those from ellipsometry (see Figure IV.27) for the four samples (A7, E1-
3) studied by both techniques. Four the four other samples the n values are slightly higher
(2.5-2.6), but this can come from lower precision in measuring the probed thickness by
stylus profilometry, especially for uneven substrates (see Figure IV.16, E2 and E4
profiles). Our transmission measurements are done on a circular spot (~1 mm^2 area) in
the center of the film, while for stylus profilometry we have better precision on the sides
of the deposition (step between substrate and film surfaces).

For the imaginary part of the refractive index, we calculated the absorption
coefficient α from fringe-free transmission (see Chaper II) using the Beer-Lambert law

and film thickness measured by ellipsometry or stylus profilometry. However, our transmission measurements must be corrected for reflection at the film-air and film-substrate interfaces. As explained in II.3.4.2, the contribution of the substrate (absorption, reflections) was removed by recording a "baseline" spectrum with a "blank" substrate (i.e. without any film deposited on it), which was then used as 100% transmission reference in the recorded spectra. The air-substrate and film-substrate reflection coefficients are almost equal (4-5%), at least in the GLS transparent region, so we considered that the film-substrate reflection was compensated by the air-substrate reflection taken into account in the baseline subtraction. For the film-air interface, we used (where available) n and k values derived from ellipsometry to calculate the reflection coefficient at each wavelength according to formula (III.1). This placed the corrected transmission in the transparent range at ~100% (it was ~80% for the un-corrected one), in good agreement with the values obtained by ellipsometry. An example is given in Figure IV.29a for the E1 sample.

With the calculated absorption coefficients, we traced Tauc plots to determine the optical band gap energy (see Chapter II). Only slight differences were observed between the plots traced with α from corrected *vs* uncorrected transmission, as one can see in Figure IV.29b for the E1 sample. Generally, the uncorrected transmission led to a underestimation of the band gap by ~0.05 eV with respect to the value derived from corrected tranmission.
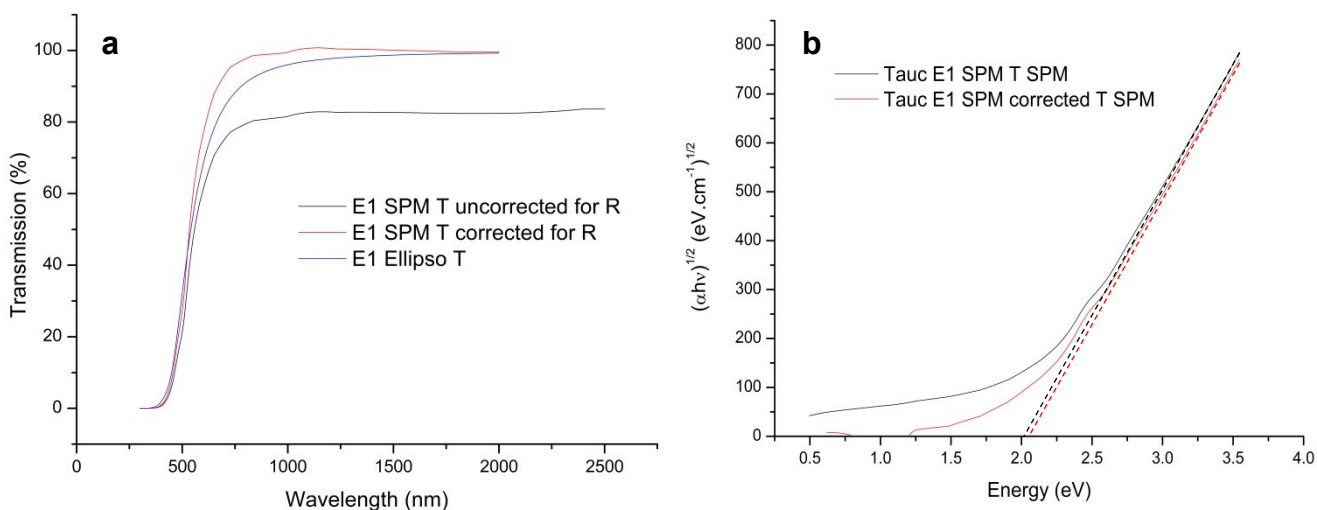
Figure IV.29   Corrected *vs* un-corrected transmission (a) and Tauc plot for E1 sample.

Along with the band gap energy, cut-off wavelengths were calculated. We have chosen to measure them at 50% transmission (as for optical filters). This was motivated by the fact that, although most of our films show important increase of absorption around 500 nm (see Figure IV.27), the transition between strong absorption and transparent regions seems quite different, thus measuring a point in this intermediate regime could better describe the quality of the film. For some films, corrected transmission was not available (no ellipsometry data), in these cases we measured the cut-off wavelength at 50% of the maximum film transmission (i.e. T~40%). The agreement between $\lambda_{cut\text{-}off}$ values measured from corrected and un-corrected data was better than 5 nm.

The optical band gap energies and the cut-off wavelengths derived from ellipsometry and spectrophotometry are listed in Table IV.11. One can remark important differences between the $\lambda_{cut\text{-}off}$ values derived from ellipsometry and SPM for A7 and E2 samples, while they are in good agreement for the E1 and E3 films. These differences are for the moment unexplained. On the other hand, the high $\lambda_{cut\text{-}off}$ values observed for some samples (e.g. 800 nm for A6) are disappointing as they could indicate important density of defects in the deposited films. The band gap energy values derived from optical transmission measurements (Tauc plot) are 0.1 – 0.5 eV lower than the values derived from the ellipsometry data fit (Table IV.10). The samples measured only by optical transmission (A2, 5, 6 and E4) exhibited even lower values, in the range 1.55 – 1.85 eV.This can explain the lower band gap energies (1.4 – 1.9 eV) found by Asal and Rutt [1997], who used the same optical transmission method as us.

Table IV.11 $\lambda_{cut\text{-}off}$ and E_g values derived from optical transmission (A and E series).

Sample	$\lambda_{cut\text{-}off}$ (nm)			E_g (eV) SPM
	ellipso	corrected SPM	uncorrected SPM	
A2	-	-	670	1.6
A5	-	-	725	1.65
A6	-	-	800	1.55
A7	564	652	653	1.80
E1	541	535	539	2.0
E2	498	553	555	2.1
E3	595	601	604	1.95
E4	-	-	657	1.85

Finally, the two large dimension doped GLS samples deposited in ps regime (AP1 and EP1), where investigated by optical transmission in various points on the surface, in order to check the evolution of the thickness and refractive index with the distance from the plume center. Transmission spectra for the 18 points measured are presented in Figure IV.30, along with their positions on the sample surface: for AP1 the vertical rows were spaced by 5 mm and the horizontal ones by 3 mm, while for EP1 both the vertical and horizontal rows were spaced by 5 mm.
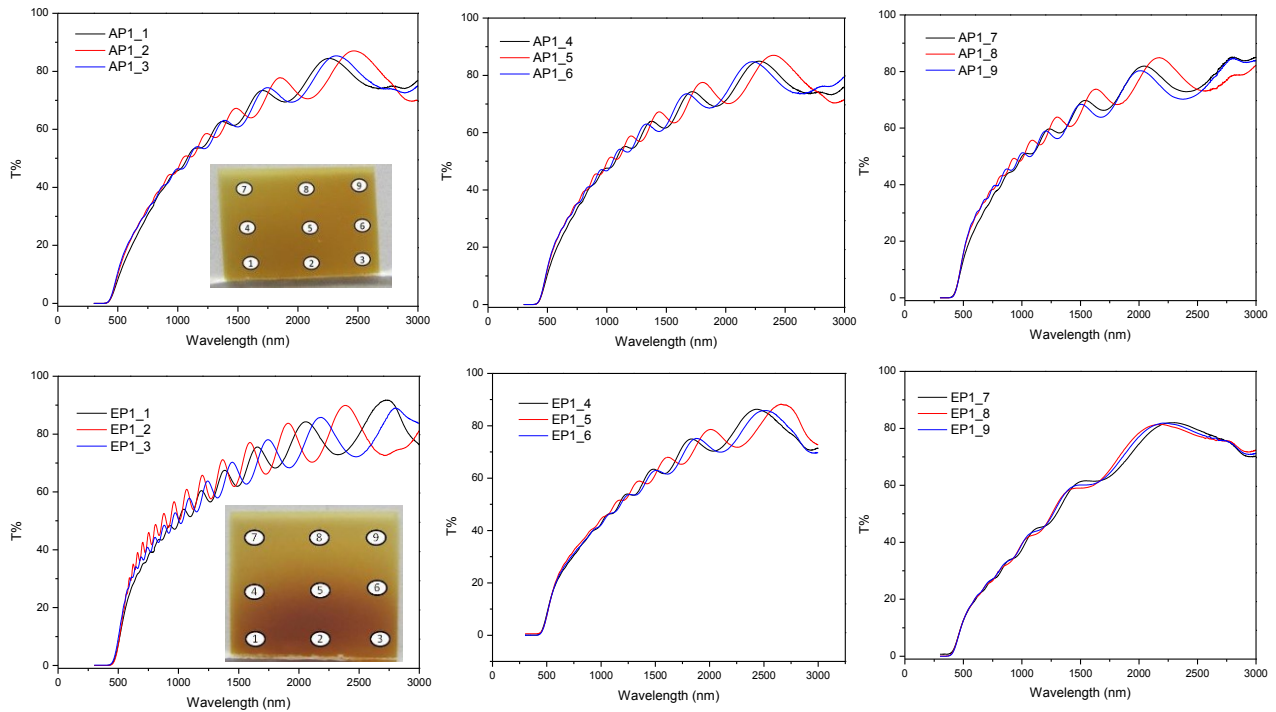
Figure IV.30 Transmission spectra of AP1 (GLS:Er) and EP1 (GLS:Pr) samples in various points.

Table IV.12 summarizes the thickness and refractive index (average on the 1.0 – 2.0 μm spectral range) values measured in six points on each surface, corresponding to the horizontal profiles measured by stylus profilometry. Using profilometry thickness for points 1, 3, 7 and 9, we first determined the refractive index in these points. The values obtained are very close, n = 2.28 – 2. 29, with one exception for the point 7 on AP1 sample (n = 2.24), which tends to validate the method and also to prove that the deposited

films have quite uniform refractive index across the surface (4% decrease was observed by Nemec et al. [2009b] at 18 mm from the center). Using this average value, we further determined the thickness in points 2 (center of the deposition) and 8. We obtain ~20% thickness decrease at ~8 mm from center for AP1 and ~60% decrease at ~11 mm from center for EP1. Nemec et al. [2009b] obtained ~30% thickness decrease in their ns (532 nm) PLD study, but using substrate rotation and off-axis deposition.

Table IV.12   Thickness, refractive index, cut-off wavelength and bad gap energy measured in various points of the AP1 (GLS:Er) and EP1 (GLS:Pr) samples.

Point	Thickness (nm)	n	$\lambda_{cut-off}$ (nm)	E_g (eV)
AP1_1	1470	2.29	910	2.14
AP1_2	1600	2.29	878	2.09
AP1_3	1500	2.29	894	2.11
AP1_7	1350	2.24	834	2.03
AP1_8	1400	2.26	786	2.22
AP1_9	1300	2.29	776	2.20
EP1_1	1800	2.28	820	2.04
EP1_2	2100	2.28	748	2.00
EP1_3	1900	2.28	764	1.95
EP1_7	950	2.29	1032	1.58
EP1_8	900	2.29	994	1.93
EP1_9	920	2.29	954	2.06

The cut-off wavelengths and the band gap energies derived from raw transmission data in various points are also listed in Table IV.12. One can notice E_g values around 2 eV, in line with the results obtained for the ns-deposited samples. However, the cut-off wavelengths are again disappointing, with values as high as 1000 nm.

IV.6 Summary

Pure and rare-earth doped GLS thin films were deposited by PLD in different conditions using three types of lasers with various characteristics: nanosecond Nd-YAG laser, picoseconds laser and Ti-Sa femtosecond laser. The varied deposition parameters were: time of deposition, target-substrate distance, background pressure, laser energy and

fluence. The as-obtained thin films were analyzed using optical and electronic microscopy, Raman spectroscopy, X-Ray Diffraction (XRD), Energy Dispersive X-ray Spectroscopy (EDX) and Time of Flight Secondary Ion Mass Spectrometry (ToF SIMS). The optical properties were measured by ellipsometry and spectrophotometry (transmission).

The main conclusion for the ns regime is that films deposited at moderate fluence (~4 J/cm^2) in UV (266 nm) presented the best surface quality (low number of droplets), while exhibiting acceptable composition uniformity and the lowest deviations from stoichiometry (A and E series). Using shorter pulse lasers (ps and fs) also led to lower surface roughness, but in some cases the film thickness was very low (because of the low fluence used) and did not allow obtaining reliable results by some of the characterization methods. From XRD and Raman measurements we deduced that all the films were amorphous, with one exception (A7) which crystallized in a not yet elucidated phase.

The optical properties were studied by ellipsometry and transmission measurements for some of the films, giving optical band gap values around 2 eV, but with quite high cut-off wavelengths, which is a possible indication of an important defect density. We observed a progressive decrease of the refractive index value when passing from ns to ps to fs deposition regimes (although in the last one the obtained values are not completely reliable), which cannot be related to the film chemical composition. Further physical properties measurements, e.g. film density (incorporation of voids?), thermal behavior, electrical (resistivity) and mechanical (adhesion, scratch resistance) properties etc., could bring some answers to the numerous questions opened by this study. Moreover, it would be interesting to investigate the photo-induced effects (photo-darkening, photo-bleaching etc.) on the deposited thin films

Chapter V

Optical investigations on the laser ablation plasma plume

V.1 Introduction

The interaction of high-intensity laser pulses with matter is a complex subject, and is far from being completely understood, albeit extensive literature is available. [Allmen et al. 1995, Cremers et al. 2000, Radziemski 2002, Rusak et al. 2002, Liu et al. 1997]. The last decades brought the occurrence of new techniques based on the laser-solid interaction, as MALDI (matrix-assisted laser desorption and ionization) [Karas et al. 1985, 1987], PLD [Chrisey and Hubler 1994], or MAPLE (matrix-assisted pulsed laser evaporation) [Chrisey et al. 2003]. All these developments led to an increased interest for a better fundamental understanding of the interaction of a laser pulse with multi-component targets, in order to fully exploit (and possibly extend) the analytical and technological capabilities of these methods [Dreisewerd et al. 2003, Georgiou and Koubenakis 2003].

In this frame, although the PLD technique has been employed for almost two decades to grow various thin films, the control and optimization of the deposition parameters are still generally done in an empirical manner. For the detailed understanding of the processes connected with PLD and particularly for the optimization of the PLD of amorphous chalcogenide films, studying the dynamics of the plasma plume formed during laser ablation is appealing. An important role in this dynamics is played by the balance between species production by elementary processes (e.g. direct and indirect ionization) and their loss, e.g. by recombination in the volume and at the walls. Knowledge of these processes is very important since it permits the controlled action at a molecular and atomic level during the operation of PLD for thin films growth.

The ejection of particles from a surface following the irradiation by a high-intensity laser beam leads to the formation of an ablated matter cloud which moves rapidly away from the surface. Generally, such a cloud (commonly named "plume") is made of neutrals (excited or in the ground state), electrons and ions. The physical parameters of the plume, as the mass

177

distribution, the ions and neutrals velocities, the angular distribution of the ejected species, play an important role in laser ablation applications, as mass analysis [Vertes et al. 1993] or thin film synthesis by PLD [Chrisey and Hubler 1994]. In particular, the thickness profile of a deposited thin film is determined by the shape of the plume, which varies during the expansion from the target surface to the substrate [Saenger 1994, Amoruso et al. 1999, Schou 2006]. This practical importance led to the occurrence of an extensive literature on a broad array of techniques devoted to the diagnostics of laser ablation plasma plumes [Chrisey and Hubler 1994, Lowndes 1998, Amoruso et al. 1999].

When looking to the plasma plume expansion part, the main parameters of interest are: shape and velocity of the plume at various times after the ablating laser pulse, the spatial distribution of density and temperature at various times after the ablating laser pulse, and the spatial and temporal variation of the plume composition, in terms of the atoms, molecules, excited states, clusters, nanoparticles etc. At a quick view, the "primary" diagnostic techniques can be divided into optical (fast photography, shadowgraphy, emission and absorption spectroscopy, laser induced fluorescence etc.) and electrical (Langmuir probes, energy analyzers, mass spectrometry) approaches. We used in this thesis the optical approach, namely fast photography by intensified CCD camera and space- and time-resolved optical emission spectroscopy. It has to be noted that these experiments were done separately from the deposition runs, but we tried to reproduce, as much as possible, the deposition conditions (e.g. in terms of typical fluence). In order to complete the experimental part description from Chapter II, the theoretical framework used to derive the plume parameters is presented below.

V.2 Theoretical framework

Generally, a plasma can be described by three theoretical models: i) the collisional – radiative model, ii) the coronal model (developed to describe the off-equilibrium plasmas), and iii) the thermodynamic equilibrium model. Due to its simplicity, in laser ablation plasmas the most used model is the third one.

A completely isolated system tends towards a complete thermodynamic equilibrium (CTE), which is described by four laws: Boltzmann, Maxwell-Boltzmann, Saha-Eggert and Planck. The Maxwell-Boltzmann law gives the kinetic energy distribution of the particles. The discrete states (electronic, vibrational, rotational excitation) populations are described by

the Boltzmann law, while the Saha-Eggert law describes the various ionized states, and the Planck law the radiation spectral distribution. For every law, one can define a temperature – a plasma is in CTE when all these temperatures are equal, in other words when all the energy exchange processes are counterbalanced by the reverse processes (this is called the micro-reversibility principle).

A laboratory plasma is never in CTE: because of its limited extension, the photons escape from the system and consequently the radiative de-excitation rate is greater than the absorption excitation rate (radiative disequilibrium). However, if the system verifies the first three laws cited above, it is said to be in a local thermodynamic equilibrium (LTE). If one of these three laws is not verified, the system is off-equilibrium. Actually, the plasma temperature and the density vary in space and time, but the population density distribution at each moment and in each space point depends entirely on the local values of temperature and density. Consequently, in the expansion plasma, the thermodynamic equilibrium is reached only locally and only for certain time laps during its evolution. Usually it is considered that if the plasma plume exceeds a threshold density of free electrons, the local thermodynamic equilibrium (LTE) is established. This is expressed by the McWhirter criterion [McWhirter 1965]:

$$N_e(cm^{-3}) \geq 1.6 \times 10^{12} \Delta E^3 (eV) T_e^{1/2}(K) \qquad (V.1)$$

where $\Delta E(eV)$ is the largest energy difference between two energy levels involved in a transition for which the condition is satisfied, and T_e is the excitation temperature in K.

It has to be noted that the McWhirter criterion is a necessary not sufficient condition for LTE [Cristoforetti et al. 2010]. Moreover, it limits the validity of the LTE model only to the densest plasmas, which is not always the case for laser ablation plume. On the other hands, when using optical emission spectroscopy one wants to have an optically thin plasma in order to avoid self-absorption of the spectral lines. So these two conditions are contradictory. In practice, the LIBS (Laser-Induced Breakdown Spectroscopy) community generally uses straight the LTE model to derive temperature and number densities, even if some deviations from the McWhirter criterion are found by subsequent calculations. We will adopt the same model in the following

Electronic temperature (T_e). In the LTE condition, the electron temperature (T_e) can be assumed equal to the excitation temperature (T_{exc}), and the plasma temperature (T) can be determined from the intensity ratio of two or more spectral lines belonging to the same ionization stage as following [Griem 1964]:

$$I_{ki} = N_0 \frac{1}{4\pi} \frac{hc}{Z(T)} \frac{A_{ki}}{\lambda} g_k e^{-\frac{E_k}{k_B T_e}}$$ (V.2)

where N_0 is the total number density of atoms (particles), λ is the transition wavelength, A_{ki} is the Einstein coefficient of the $k \rightarrow i$ transition, g_k the statistical weight of the upper level, E_k is the energy of the upper level, $Z(T)$ is the partition function [Lochte et al 1968], h is the Planck constant, k_b the Boltzmann constant, and c the light velocity.

The excitation temperature can be simply calculated from equation (V.2) using the intensity ratio (I_1/I_2) of two spectral lines originating from two upper levels E_1 and E_2 belonging to the same ionization state:

$$T_e = \frac{E_2 - E_1}{k_B \ln \left(\frac{I_1}{I_2} \frac{g_1 \lambda_1^3 f_1}{g_2 \lambda_2^3 f_2} \right)}$$ (V.3)

where f_1 and f_2 are the oscillator strengths of the two spectral lines. The spectroscopic data (E, A, f) can be found in various databases (e.g. [NIST ASD], Kurucz and Bell [1995]). We note however that the uncertainties in some data (especially oscillator strengths) can lead to significant uncertainties on the calculated temperatures. In order to minimize the relative errors, it is preferable to choose two spectral lines coming from levels which present the highest energy difference.

The calculated temperature error bars can be reduced by using the so called Boltzmann plot, which represents the logarithmic function of intensity versus the upper level energy:

$$\ln\left(\frac{I_{ki}\lambda}{g_k A_{ki}} \right) = \ln\left(N_0 \frac{1}{4\pi} \frac{hc}{Z(T)} \right) - \frac{E_k}{k_B T_e}$$ (V.4)

The slope of this plot gives the excitation temperature, and its linearity allows an indirect check of the LTE conditions validity.

Electron density. The electron density can be calculated from the Saha-Eggert equation [Griem 1964], relating the plasma ionization equilibrium temperature to the ratio of population of two successive ionization states. In the case of a neutral atom and a singly charged ion of the same element, this can be written as [Le Drogoff et al. 2001, Keszler and Nemes 2004]:

$$n_e(cm^{-3}) = 4.83\, x\, 10^{15}\, \frac{I^*}{I^+}\, \frac{g^+ A^+ \lambda^*}{g^* A^* \lambda^+}\, T^{\frac{3}{2}}\, e^{-\frac{V^+ + E^+ - E^*}{kT}} \tag{V.5}$$

where the (*, +) superscripts represent the neutral excited atom and the singly charged ion, respectively, I is the emission intensities of a spectral line of λ wavelength (in nm), T is the ionization temperature (in K), which is assumed to be equal to the excitation temperature in LTE conditions, V^+ is the first ionization potential, and E is the energy of the upper level of the transition.

V.3 Characterization of pure and rare-earth doped Gallium Lanthanum Sulphide laser ablation plasma

V.3.1 Pure GLS ablation. Influence of laser regime

We performed a comparative optical characterization study on GLS plasma plumes generated by laser ablation in ns [Pompilian et al. 2013], ps and fs regimes. Although this characterization was not done during the deposition runs, we tried to use ablation conditions typical for the PLD processes described in the previous chapters. These parameters are summarized in Table V.1. The laser beam was focused at normal incidence on the target, and the generated plasma, expanding normally to the target and visible with naked-eye, was investigated from lateral at 90°, as described in Chapter II.

Tabel V.1 Experimental conditions used for the optical investigation of pure GLS laser ablation plasma plume.

Laser regime	P (Torr)	Wavelength (nm)	Pulse width	Repetition rate	Energy (mJ)/pulse	Fluence (J/cm^2)
Nanosecond		532	10 ns	10 Hz	15	4
Picosecond	~ 2*10^{-6}	800	2 ps	100 Hz	1.27	1.25
Femtosecond		800	120 fs	100 Hz	1.8	1.78

In order to obtain a preliminary insight on the dynamics of the GLS laser ablation plasma plume, ICCD sequential snapshots of the spectrally unresolved plasma optical emission were recorded at various delays (100-1300 ns) with respect to the laser pulse (Figure V. 1). These pictures reveal the formation of a single plasma structure, not depending on the laser regime, and on the contrary of some previous studies showing a splitting of the plume in two components (fast and slow) [Ursu et al. 2009, 2010, Darby et al. 2008b, Focsa et al. 2009]. By plotting the position of the plume maximum emitting point as a function of time, one can derive the so called "center-of-mass" axial velocity of the plume. In our case, the obtained values (4.4 km/s in ns regime, 5.2 km/s in ps, and 6.2 km/s in fs) are very similar and are also comparable to the value obtained for the slow component of the plasma plume generated by ns laser ablation of another chalcogenide system (AsSe, [Focsa et al. 2009]). Although surprising (as different ablation mechanisms are involved in, e.g. fs *vs* ns regimes), this result can be an indication of a quite similar dynamics of the plume as a whole in its flight from the target to the substrate, i.e. after the initial ablation phase this dynamics would be rather governed by internal processes (e.g. collisions) in the plume itself.

We emphasize however that the "center-of-mass" velocity reflects only the evolution of the maximum emitting point in the plasma (which is ruled mainly by excitation collision and radiative de-excitation), yet individual species with significantly higher velocities can be present in the plume. In order to separate the contribution of each species present in the plasma plume, we performed a space- and time-resolved optical emission spectroscopy study using the technique described in Chapter II. First, some spectra were recorded from a 0.2-mm wide plasma "slice" located in the vicinity of the target (zone of maximum emission), using a "broad" 1 µs ICCD gate width, in order to get an overview of the whole spectral range (250 – 700 nm) and to select the wavelength regions of interest. Figure V. 2 displays these spectra corresponding to the three ablation regimes, along with the assignment of the most intense spectral lines. One can easily notice the presence of both neutral and ionic species in the spectrum, and even some signals from double-charged ions in the case of La (only in ns regime). Another observation is that the spectrum collected for the ns ablation is by far "richer" than the spectra corresponding to the other two regimes. This can be an indication of a higher collision rate (i.e. more frequent excitation processes), due to the higher fluence (and pulse energy) used in the ns regime.
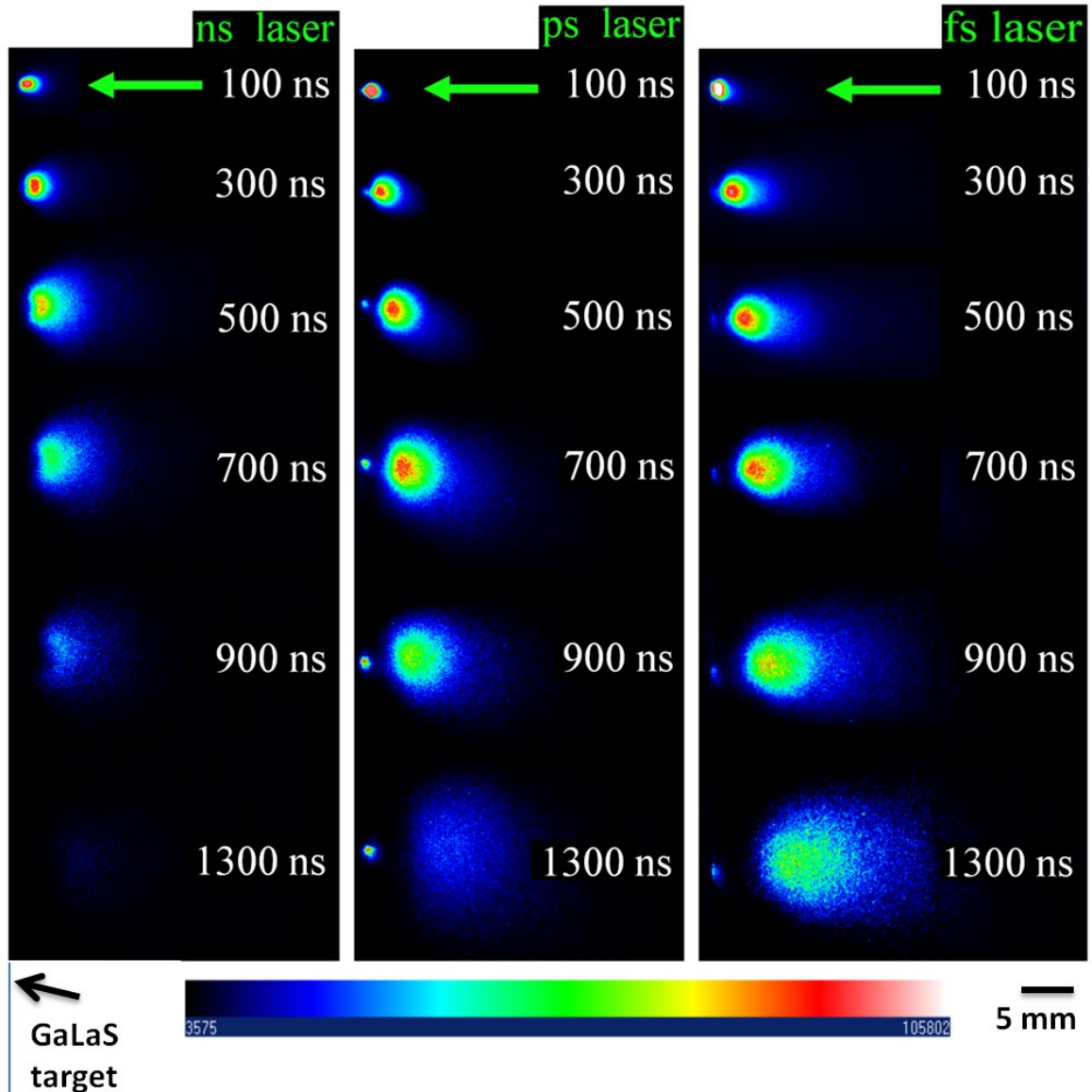
Figure V.1. Temporal evolution of the spectrally-integrated optical emission of the plasma plumes obtained by laser ablation of GLS in ns, ps and fs regimes. ICCD gate width = 5 ns in ns ablation regime, 20 ns in ps and fs ablation regimes..

We remark that two spectral lines of Ga (at 287.42 nm and 294.36 nm) were observed in all three temporal regimes. However, significant differences in the dynamics of the excited species associated with these transitions were evidenced, as the intensity ratio $\frac{I^*_{29436}}{I^*_{28742}}$ is close to 1 in picosecond regime, while in nano- and femtosecond regimes its value is ~2. The dynamics of these species doesn't seem to depend on the temporal regime, but rather on the fluence used. This behavior is difficult to explain, as the upper levels of these transitions are

quasi-degenerated, and the transition probabilities are very similar (see Table V.2). Probably other processes (as population by de-excitation from upper levels) have to be considered in order to explain it. The same discrepancy (this time in the reverse way) is noticed on the intensity ratio of the Ga I 403.29 nm and 417.20 nm lines, which is close to 1 in ns and fs regimes, and rather close to 2 in ps regime..
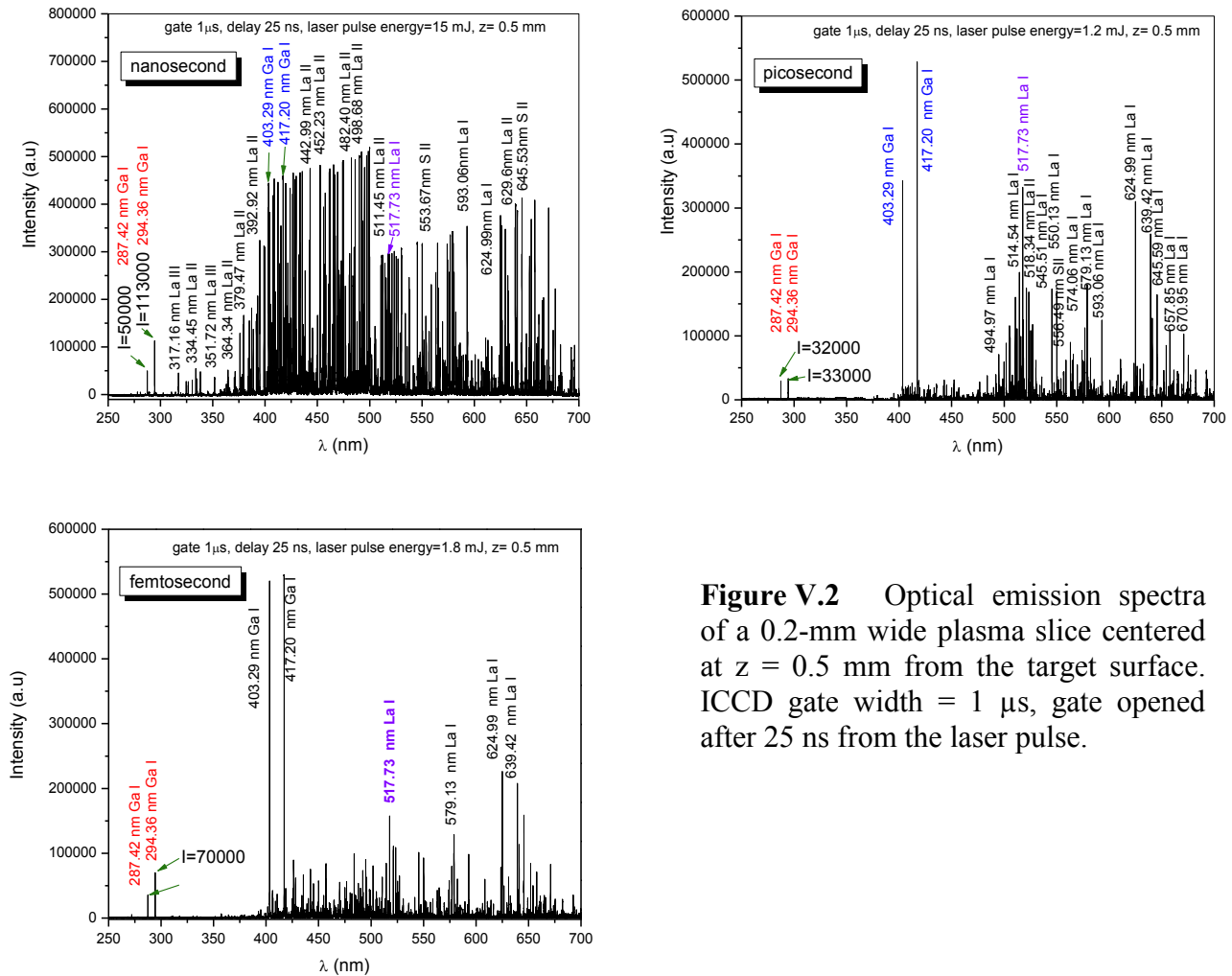
Figure V.2 Optical emission spectra of a 0.2-mm wide plasma slice centered at z = 0.5 mm from the target surface. ICCD gate width = 1 μs, gate opened after 25 ns from the laser pulse.

Table V.2 Spectroscopic data for the 287.42 nm and 294.36 nm Ga I spectral lines   [Kurucz and Bell 1995].

Wavelength (nm)	Rel. Int.	A_{ki} (s^{-1})	E_i (eV)	E_k (eV)	lower level Conf., Term, J			upper level Conf., Term, J		
287.4235	3	1.17e+08	0.000000	4.312376	$3d^{10}4s^24p$	$^2P°$	$^1/_2$	$4s^24d$	^2D	$^3/_2$
294.3636	3	1.34e+08	0.102434	4.313143	$3d^{10}4s^24p$	$^2P°$	$^3/_2$	$4s^24d$	^2D	$^5/_2$

The space- and time-resolved studies were conducted by selecting 0.2-mm wide plasma slices at various *z* distances from the target surface, and using the automatic delay incrementing capabilities of the ICCD camera (see Chapter II). Thus, at a given *z* distance,

temporal profiles of the emission lines can be readily recorded, as illustrated in Figure V.3. A fast ICCD camera gate width of 50 ns is used in this case for the recording of each individual spectrum at high resolution (2400 lines/mm grating).
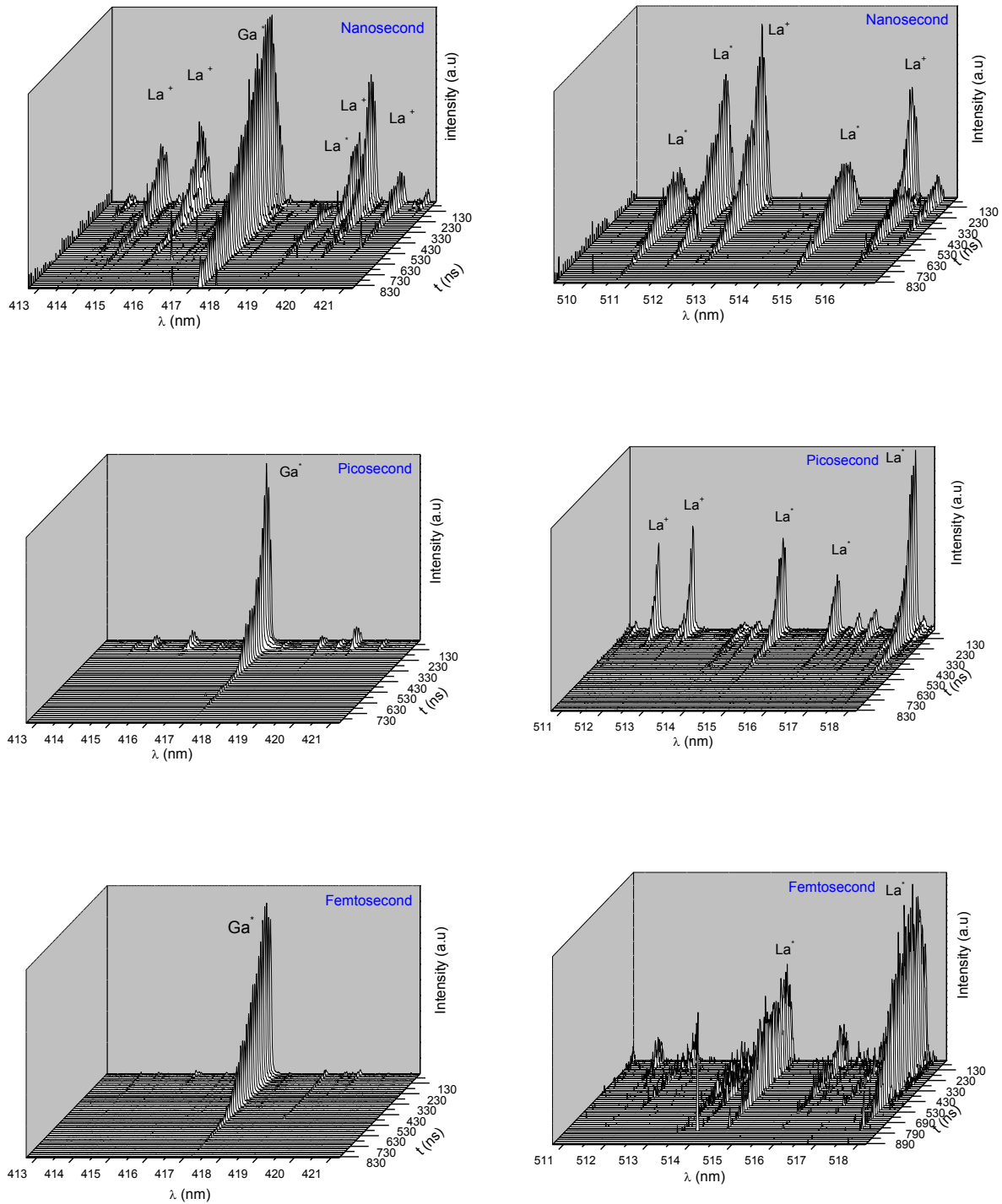
Figure V.3   Optical emission time–of–flight profiles of various spectral lines recorded at z = 0.5 mm from the target surface. ICCD gate = 50 ns.

By plotting the time corresponding to maximum emission vs z, one can easily derive the axial velocities for the individual species of interest. An example is given in Figure V.4 for the the case of neutral and singly-charged species of Ga, La, and S ablated in ns regime. The velocity values derived by this method for some species in the three ablation regimes are summarized in Table V.3.
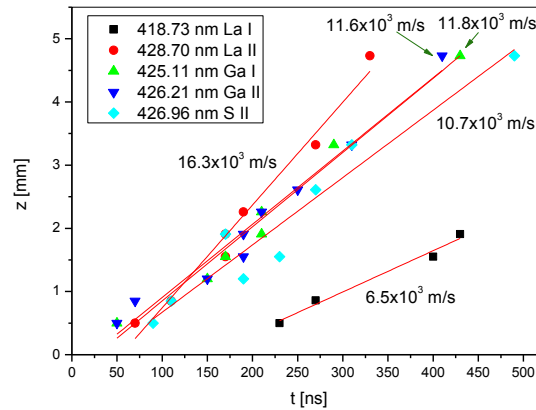
Figure V.4. Axial velocities of various Ga, La, and S species ablated in ns regime.

Table V.3 Axial velocities for some species present in the plasma plumes generated in the ns, ps and fs ablation regimes.

Species	Velocity (10^3 m/s)		
	Nanosecond	Picosecond	Femtosecond
Ga I (λ=417.20 nm)	9.9	10	9.4
Ga I (λ=425.11 nm)	11.8	-	-
Ga II (λ=426.21nm)	11.6	-	-
La I (λ=418.73 nm)	6.5	-	-
La I (λ=428.02 nm)	9.7	-	-
La I (λ=514.54 nm)	11.2	4.18	6.28
La II (λ=428.70 nm)	16.3	-	-
SI (λ=569.66 nm)	-	17.6	5.61
SII (λ=426.96 nm)	10.7	-	-
S II (λ=547.50 nm)	-	-	7.5

These data show the presence of high kinetic energy species in the plume, with velocities in the range of 10^4 m/s. This is of practical importance for PLD, as energetic particles hitting the surface of a growing film can influence the nucleation, energy and

mobility of atoms on the surface of the film, by colliding with atoms already adhered to the existing islands, causing bond breaking or even sputtering. The velocity values displayed in Table V.3 turn into kinetic energies as high as ~200 eV for La^+. It has been shown that for such high kinetic energies, sputtering rates exceeding 0.5 can be reached (Ag atoms, 4.5 J/cm^2 [Fähler et al. 1998]). A possible solution is of course to reduce the fluence, but in this case stoichiometric transfer issues may arise [Schou 2009].

Generally the expansion velocities of the ionized species are found to be higher than those of the excited neutral species [Ursu et al. 2009, 2010, Focsa et al. 2009]. This trend seems to be generally followed in our experiments (see Figure V.4), however some neutral (e.g. Ga in ns regime, or S in ps, see Table V.3) can exhibit velocities comparable to those of the corresponding ions. This can be an evidence for a different ionization/excitation mechanism for this species, possibly resulting from in-plume collisional/radiative processes rather than directly from the ablation step.

Figure V.5 presents the time-distance plots for two neutral species (Ga I 417.20 nm line and La I 514.54 nm) recorded in the three ablation regimes. One can easily remark a very different behavior for these two species: while Ga present almost equal velocities in the three ablation regimes, La shows completely different values, with much higher velocity in the ns regime. In order to explain this discrepancy, a complete model including all (or as much as possible of) the species present in the plasma, and the related processes, should be developed, but this is beyond the scope of this thesis.
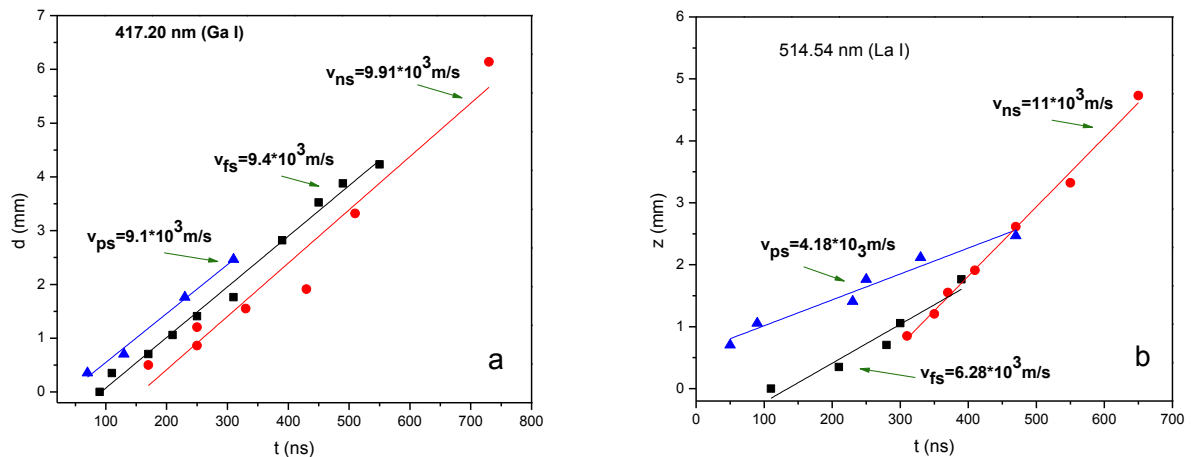
Figure V.5. Axial velocities of Ga and La neutral species associated with the 417.20 nm and 514.54 nm spectral lines, respectively, in the ns, ps and fs ablation regimes.

In order to get some insight on the internal energies of the species present in the plume, the excitation temperature can be calculated using the relative intensities of two or more spectral lines, based on the Boltzmann plot method described above. Using the spectroscopic data from [NIST ASD] and [Kurucz and Bell 1995], we derived the temperatures listed in Table V.4 for the three ablation regimes at z = 0.5 mm from the target surface. For exemplification, we displayed in Figure V.6 some Boltzmann plots obtained for La I and La II in these conditions. Note that these are somehow "averaged" temperatures, as the gate width of the detector was set to 1 μs.

Table V.4   Average excitation temperatures derived from Boltzmann plot at z = 0.5 mm from the target

Species	Temperatures (10^3 K)		
	Nanosecond	Picosecond	Femtosecond
Ga I	4.3±0.5	3.7±0.6	4.0±0.8
La I	5.3±0.5	4.0±0.3	6.5±0.5
La II	7.5±0.4	7.2±1.5	10.4±1.6
S II	-	8.2±0.8	7.5±1.7

.

The fact that significant differences are obtained between the various species temperatures can lead to the conclusion that we are not in LTE conditions, even in this region close to the target surface, where the plasma is very dense. On the other hand, the linear evolution observed in the Boltzmann plots represents an argument for the validity of the model. The quite important spread of the experimental points observed for some plots can come from deviations with respect to the LTE conditions, but also from significant uncertainties in the values of some spectroscopic data or from the fact that the line intensities used in the calculations were not corrected for the whole optical system response. We note that these differences in temperatures are commonly accepted in the literature when studying laser induced multi-component plasmas [Cremers and Radziemski 2006, Miziolek et al. 2006]. The temperature values (and the associated error bars) are usual for this range of laser fluences. It is interesting to remark that the S II temperature is comparable to that of La II, despite the fact that the ionization potential of Sulphur (10.36 eV [NIST ASD]) is significantly higher than that of Lanthanum (5.57 eV [NIST ASD]). This confirms the strong multi-photonic character of the laser-target interaction in fs and ps regimes.

When comparing the three ablation regimes, no significant differences are observed for a given element temperatures (maybe with the exception of La II in fs regime, but with high uncertainty), which tends to indicate that the dynamics and the energetics of the plasma plume would be governed rather by in-plume processes (e.g. collisions).
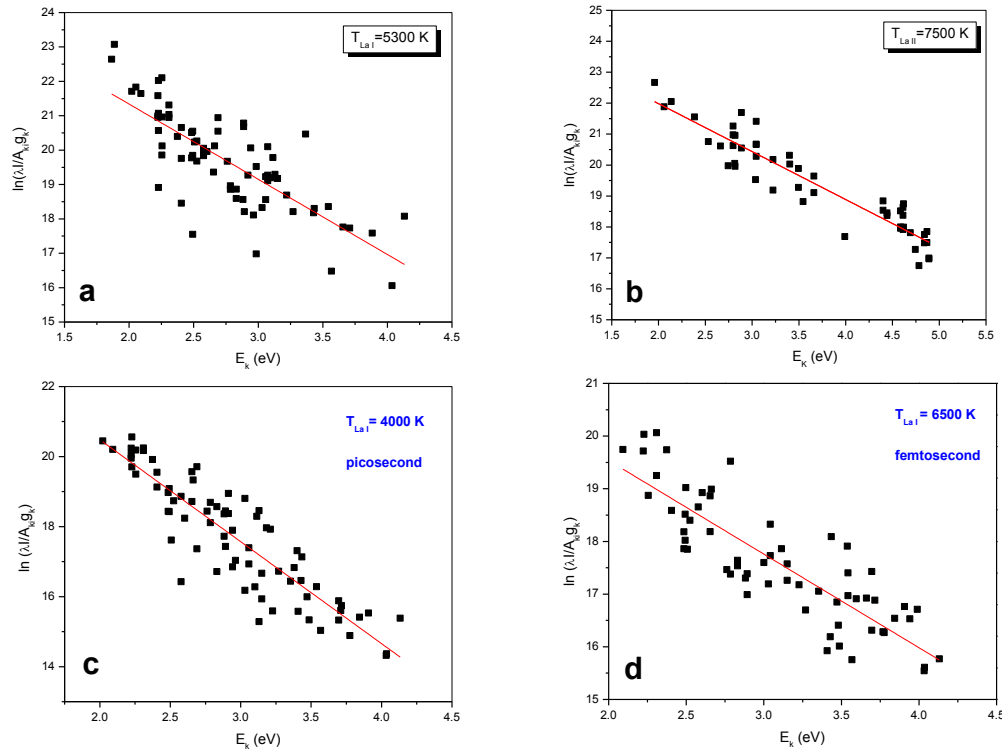
Figure V.6. Boltzmann plots for La I (a) and La II (b) in ns regime, and for La I in ps (c) and fs (d) regimes. Distance from the target z $=$ 0.5 mm, gate width $=$ 1 µs.

Deeper insight on the plasma plume dynamics can be granted by studying the space and time evolution of the excitation temperature and electronic density. For temporal temperature profiles, this can be done from series of snapshots taken at a given distance and various delays with respect to the laser pulse (as those in Figure V.2), calculating for each delay the ratio of two spectral lines intensities (this method was preferred here for simplicity and time-saving, instead of the "heavier" Boltzmann plot method used above to derive the "average" temperatures). Moreover, once the temperature is calculated, the electronic density can be derived from equation V.5. Figure V.7 presents the temporal profiles of the temperature (La$^+$ ion) and electronic density at two distances (z = 0.5 mm and z = 1.55 mm) from the target surface, in the three ablation regimes. The temperature of the excited ions was calculated from Eq. V.3 by using the 428.696 nm and 429.60 nm La$^+$ lines in ns regime, and the (567.15 nm, 570.33 nm) couple of La$^+$ lines in ps and fs regime.

The electron density was calculated from Eq. V.5 by using the 428.026 nm (in ns regime) and 565.77 nm (in ps and fs regimes) La* lines and the 428.696 nm (in ns regime) and 567.15 nm (in ps and fs regimes) La$^+$ lines. The spectroscopic parameters of these transitions are given in Table V.5.
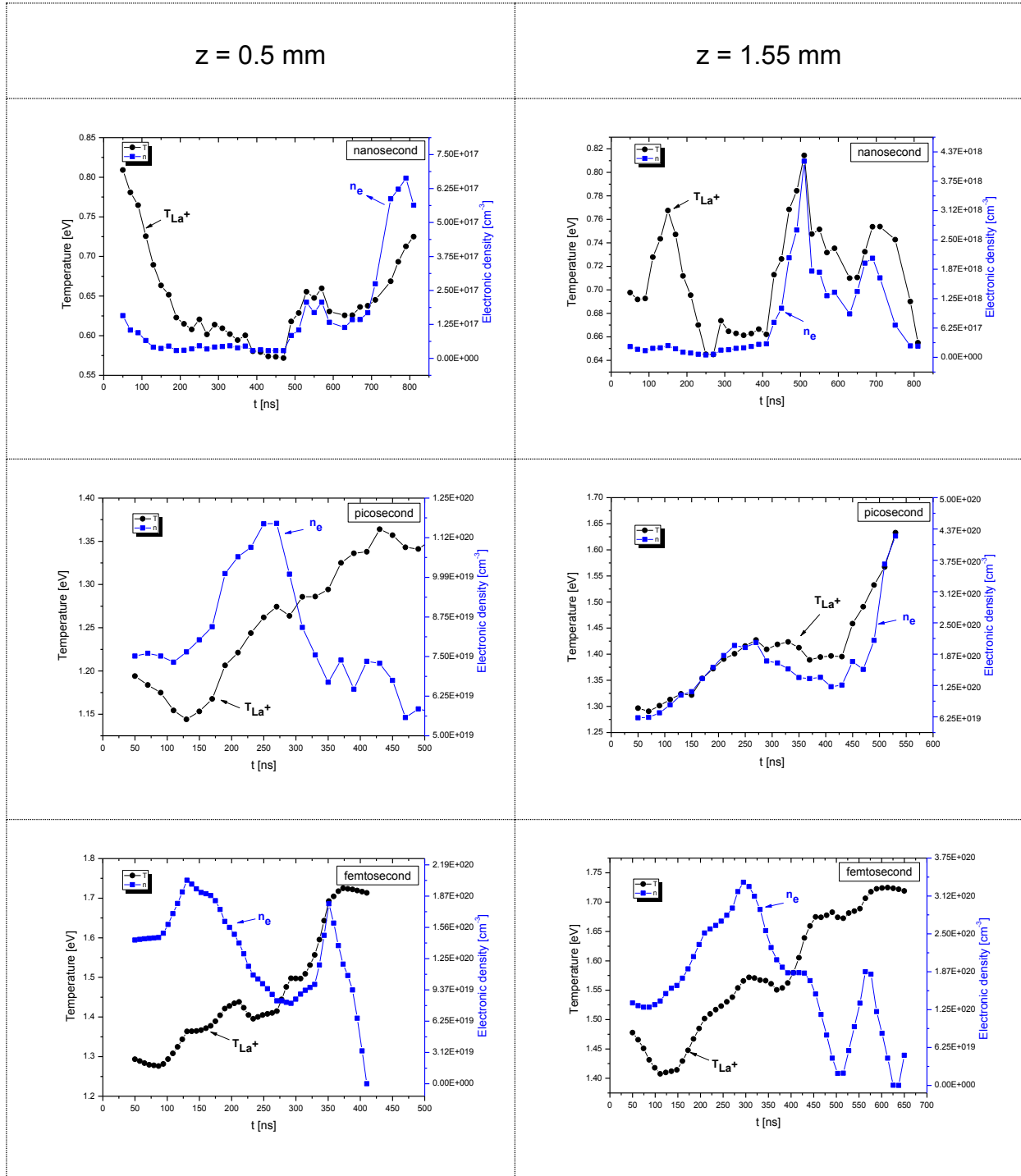
Figure V.7   Excitation temperature and electronic density temporal profiles at z = 0.5 mm and z = 1.55 mm from the target surface, in ns, ps and fs ablation regimes.

The time-resolved (50 ns ICCD gate width) excitation temperatures obtained are consistent with the average values (1 μs ICCD gate width) found at z = 0.5 mm in ns regime, and they are higher by a factor of ~2 in the ps and fs regimes. Nevertheless, the multiple maxima present in the temperature and electronic density profiles reveal a complex behavior of the plasma plume, probably driven by (excitation/ionization/recombination) collisions and electric interactions, leading to the idea of double-layer formation and self-structuring, as evidenced previously in [Eliezer et al. 1989, Gurlui et al. 2006a, Nica et al. 2010].

Table V.5 Spectroscopic data of the transitions used in the calculation of the temperature and electronic density temporal profiles [Kurucz and Bell 1995].

Wavelength (nm)	A_{ki} (s^{-1})	Element	E_i (eV)	E_k (eV)	g_i	g_k
428.0259	1.438e+07	La I	0.130589	3.026621	6	8
428.6958	5.473e+07	La II	1.946527	4.838033	9	11
429.6054	1.900e+07	La II	0.772154	3.657539	5	5
565.7707	2.694e+06	La I	0.330837	2.521798	4	6
567.1528	3.994e+06	La II	2.210244	4.395866	9	7
570.3311	5.043e+05	La II	0.709004	2.882446	3	5

The electron density and temperature values (at least up to the onset of the oscillations) seem to be in fair agreement with previous studies performed at comparable fluences, but on completely different materials (Ag [Toftmann et al. 2000] and Cu [Hendron et al. 1997]). This somehow suggests a quite universal behavior in this range of fluence, which can be related [Schou 2009] to the not so different cohesive energies (vaporization enthalpies) of e.g. Ag, Cu, Ga and La (at least in pure solid samples). Note however that S is much more volatile (by two orders of magnitude), which can also explain the different behavior evidenced above.

The values obtained for the electron density in the three regimes are largely sufficient to verify the McWhirter criterion (Equation V.1). Indeed, if one considers the highest temperature derived in this study (about 20 000 K, from the temporal profile in fs regime), and the highest energy transition (~4.3 eV, corresponding to the lowest wavelength transition observed – Ga I at 287.42 nm), Eq. V.1 gives a threshold value for N_e of about 1.8×10^{16} cm^{-3}, i.e. about one order of magnitude lower than the lowest electronic density obtained in ns regime. However, we stress once again that the McWhirter criterion is just a necessary (not sufficient) condition to be in LTE [Hahn and Omenetto 2010].

The lower (by two or three orders of magnitude) electron density values obtained in the ns regime compared to the ps and fs ones tend to indicate that the ns ablation would lead to the less ionized plasma. This is surprising, as the overview spectrum recorded in ns regime (Figure V.2) is by far richer in ionic lines (coming even from doubly-charged ions) than the spectra recorded in ps and fs regimes. Moreover, in the first 400 ns and close to the target surface, the temperature is decreasing in the ns regime (with low electronic density), while it is increasing in ps and fs regimes. This would again suggest that the ns ablation ejects mainly hot neutrals, which can further thermalize by collisions and lead to ionization rate increase. In fs regime, it seems that mostly "cold" ions are ejected (high electronic density), and their temperature is further increased by recombination processes. The ps regime presents an intermediate picture. The dynamic equilibrium between these processes can lead to the oscillatory behavior mentioned above. For now these are just speculative hypotheses, and complementary investigations by electrical methods (Langmuir probes and time-of-flight mass spectrometry) are needed in order to better understand the complex dynamics of the plasma plumes generated by laser ablation of the GaLaS system.

V.3.2 *Rare-earth doped GLS*

Some measurements were also performed on Er- and Pr-doped GLS targets ablation in ns and fs regimes, using the experimental conditions detailed in Table V.1. No significant differences with respect to the pure GLS targets were observed. The overview spectra (1 µs ICCD gate width) presented in Figure V.8 show again a much richer spectrum in ns compared to fs regime. Despite their low concentration in the targets, the dopants were observed in the spectra, however, only in neutral, singly- and doubly-ionized forms, but not in triply-ionized state (as one could expect from their incorporation in the GLS matrix). It is interesting to remark that the GLS:Er spectra are richer than the GLS:Pr ones, both in ns and fs regimes. This is somehow surprising, as the first ionization potentials of Er (6.11 eV [NIST ASD]) and Pr (5.46 eV [NIST ASD]) are very similar, and also very close to those of Ga (6.00 eV [NIST ASD]) and La (5.57 eV [NIST ASD]). The other physical parameters of the dopants (as melting and boiling points, heat of vaporization etc.) should not play a major role, when considering their low atomic percentage in the target.
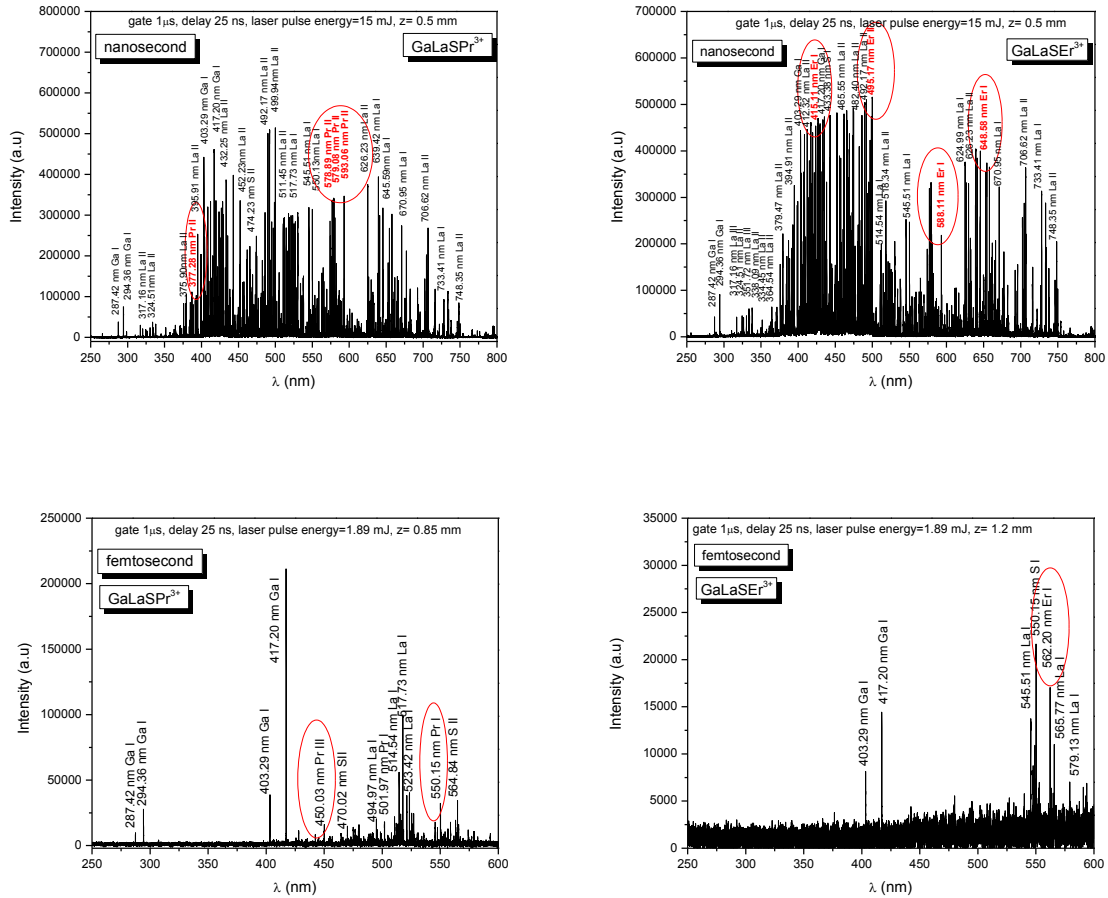
Figure V.8. Optical emission spectra of 0.2-mm wide plasma slices centered at z = 0.5 mm from the targets (GLS:Er and GLS:Pr) surface in ns and fs ablation regimes. ICCD gate width = 1 µs, gate opened after 25 ns from the laser pulse.

Using the same procedure as for the pure GLS samples, axial velocities and average temperatures were derived, but only in ns regime. They are summarized in Table V.6. One can easily notice that the dopants present axial velocities and average temperatures similar to those of the main constituents.

Table V.6 Axial velocities and average excitation temperatures (at 0.5 mm from the target) for some species present in the plasma plumes generated by GLS:Er and GLS:Pr targets ablation in ns regime.

Species	λ (nm)	Velocity (10^3 m/s)		Temperature (K)	
		GLS:Pr	GLS:Er	GLS:Pr	GLS:Er
Ga I	417.20	11.34	16.96	3800	3800
Ga I	425.57	19.70	16.24		
Ga II	426.21	18.81	13.90		
La I	428.02	8.81	13.91	4200	4400
La II	414.17	17.63	19.13	6600	8000
La II	415.19	17.63	40.53		
La II	419.23	24.44	18.04		
La II	419.65	33.22	19.63		
La II	420.40	18.22	42.61		
La II	423.09	17.46	10.02		
La II	423.83	21.89	34.05		
La II	426.35	27.7	35.25		
La II	427.56	18.19	17.88		
La II	429.60	13.02	30.07		
La II	430.04	5.92	17.21		
La II	432.25	17.63	35.25		
La II	435.44	5.24	17.63		
La II	436.46	10.67	44.06		
S II	416.23	35.25	35.25	9800	
S II	426.96	10.67	32.67		
S III	434.02	5.08			
Pr I	468.78	7.39		8400	
Pr I	513.98	17.39			
Pr II	472.86	8.59		6300	
Pr II	513.51	9.59			
Pr II	517.39	10.17			
Er I	413.15		19.3		4600
Er I	428.65		18.48		
Er I	588.11		7.78		
Er II	590.20		5.62		7000

V.4 Characterization of Ge-Sb-Te laser ablation plasma

Some investigations were performed on the dynamics of the GST family ablation plasma plumes, mainly in the ns regime (on $GeSb_2Te_4$, $Ge_2Sb_2Te_5$, Sb_2Te_3, and GeTe targets). For the $Ge_2Sb_2Te_5$ target, experiments were also done in the ps and fs regimes (they will be presented separately. The same experimental conditions as for the GLS system (Table V.1) were used. Because of the limited availability of spectral data for the Ge, Sb and Te elements, no calculations were performed on average temperatures and electronic densities.

V.4.1 Nanosecond regime

Figure V.9 presents pictures of the ablation plume spectrally-unresolved optical emission recorded by the ICCD camera (20 ns gate width) at two delays (225 ns and 425 ns) with respect to the laser pulse for the four GST targets investigated. On the contrary of the GLS results (see above), the GST images reveal a splitting of the plasma plume in two structures. This splitting process has already been observed in studies on As_xSe_{100-x} chalcogenides [Focsa et al. 2009], and also on several other targets as Cu [Gurlui et al. 2006 b], Al [Gurlui et al. 2008, Ursu et al. 2009] or graphite [Bulgakova et al. 2000], and has been numerically retrieved in the frame of a theoretical model based on fractal hydrodynamics [Gurlui et al. 2008]. The two structures exhibit distinct dynamics, with "center-of-mass" axial velocities usually in the range of 10^4 m/s for the former (fast) and 10^3 m/s for the later (slow).
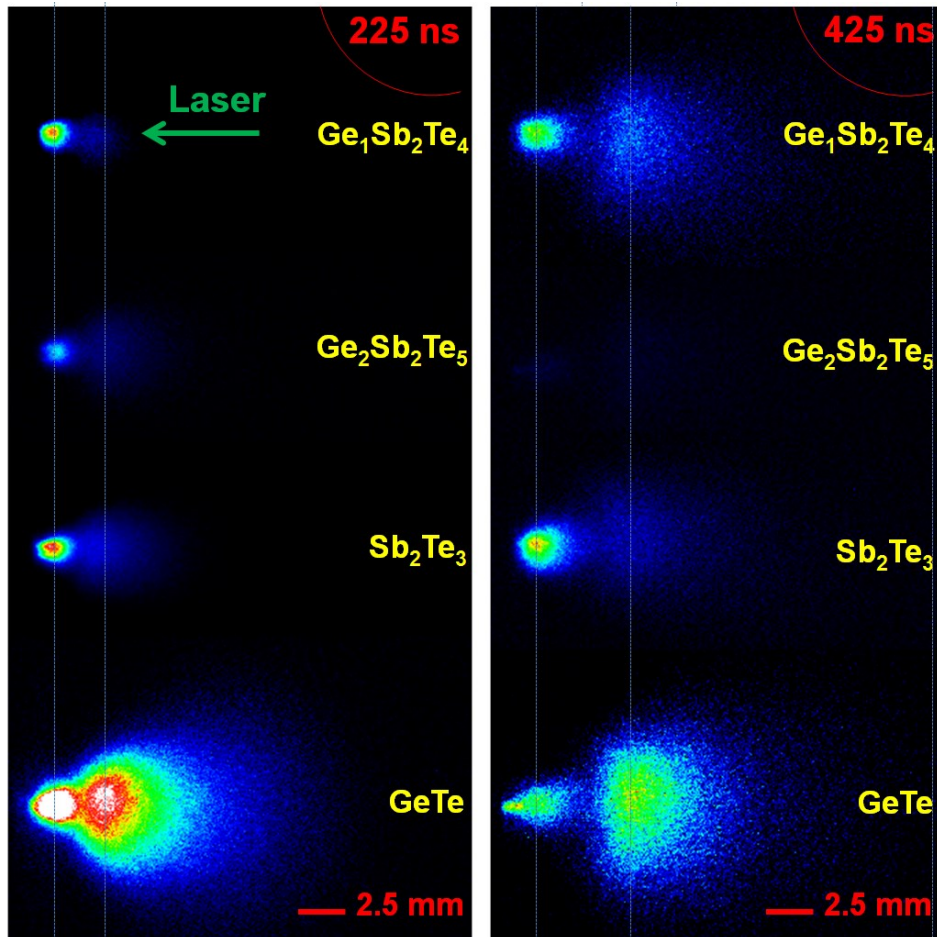
Figure V.9. Fast ICCD photography (20 ns gate width) of the spectrally-unresolved optical emission of plasma plumes generated by ns laser ablation of four GST targets, at 225 ns and 425 ns after the laser pulse.

Two distinct mechanisms have been proposed [Ursu et al. 2009, 2010] for the interpretation of the plume components origin: the first (fast) component would come from an electrostatic repulsion mechanism, i.e. electrons are removed from the surface in the very first instants of the ablation, and the net positive charge left on the surface would generate an intense electric field which accelerates the positive ions outwards the surface, with velocities that depend on their ionization degree and mass, while the second (slow) component would come from a subsequent thermal process, which needs more time to establish [Peterlongo et al. 1994, Harilal 2001].

In order to check this hypothesis, spectrally resolved emission has been recorded. Figure V.10 presents overview spectra obtained close to the target ($z = 0.5$ mm) for the four targets investigated, along with the assignment of the most intense lines. At a first view, presence of neutrals and (only) singly-charged ions is evidenced (however some weak signals from doubly-charged ions are present, see below).
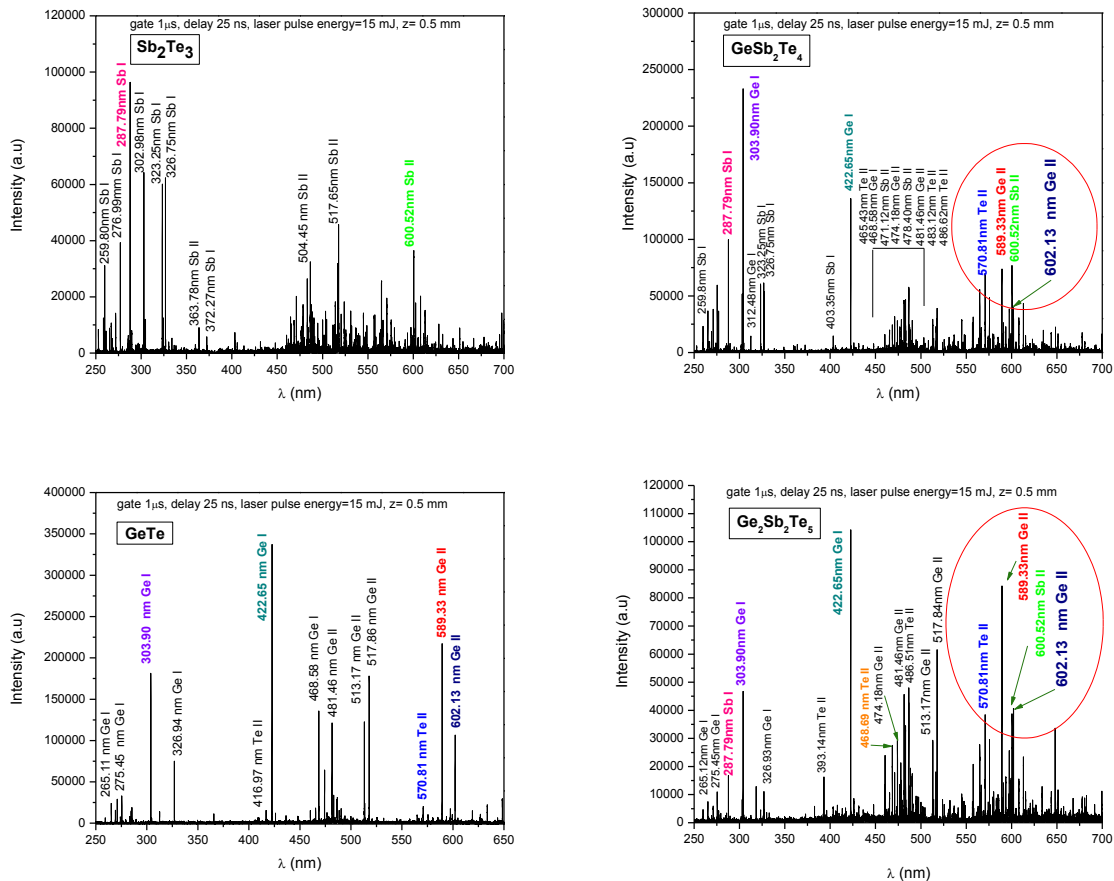
Figure V.10 Optical emission spectra of 0.2-mm wide plasma slices situated at 0.5 mm from the target surface for the ns ablation of $GeSb_2Te_4$, $Ge_2Sb_2Te_5$, Sb_2Te_3, and GeTe. ICCD gate width = 1 μs.

Furthermore, by applying the same method as for the GLS samples, individual velocities have been derived from the space-time resolved study. They are summarized in Table V.7, with an example of typical plot in Figure V.11 (for GeTe ablation).

Table V.7. Individual axial velocities for some species present in the plasma plumes and "center-of-mass" velocities derived from ICCD fast photography in ns regime.

Target/species	Wavelength (nm)	Velocity (10^3 m/s)	Center-of-mass velocity (10^3 m/s)	
GeTe			slow	fast
Ge I	303.90	8.81		
Ge II	481.46	14.8		
Ge II	482.40	18.05		
Ge II	513.17	21.04		
Ge II	517.86	23.12	$v_2 = 2.7$	$v_1 = 16.25$
Ge III	513.47	28.2		
Te II	483.12	24.3		
Te II	486.51	23.4		
Te II	486.62	17.37		
$Ge_1Sb_2Te_4$				
Ge I	303.90	8.81		
Sb I	302.98	7.54		
Sb II	464.73	7.04		
Sb II	471.12	7.76		
Sb II	487.72	7.97	$v_2 = 2.46$	$v_1 = 15.45$
Te II	465.43	6.47		
Te II	468.69	8.02		
Te II	486.51	9.06		
Te II	488.52	9.06		
Te II	490.44	8.14		
Sb_2Te_3				
Sb II	464.73	7.25		
Sb II	471.12	17.22		
Sb II	487.72	13.93		
Sb II	600.52	17.04		
Te II	465.43	13.85		
Te II	468.69	12.14		
Te II	470.65	18.01		
Te II	486.51	12.92	$v_2=3.74$	$v_1=18.69$
Te II	486.62	7.91		
Te II	488.52	12.32		
Te II	490.44	11.96		
Te II	566.61	11.51		
Te II	570.81	14.95		
Te II	597.46	18.31		
$Ge_2Sb_2Te_5$				
Te II	468.69	11.19		
Te II	483.12	10.20		
Te II	486.51	11.93		
Sb II	471.11	9.52	$v_2=2.65$	$v_1=14.94$
Sb II	516.63	8.08		
Ge I	303.90	7.61		
Sb I	302.98	11.02		
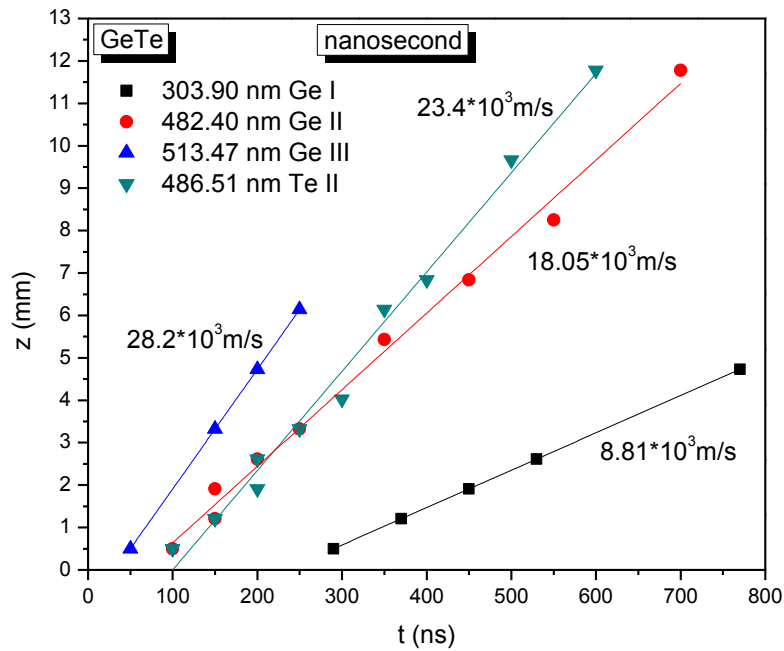
Figure V.11. Individual velocities of various species present in the plasma plume generated by ns laser ablation of GeTe.

For comparison, the "center-of-mass" velocities of the two plume structures, derived from spectrally-unresolved ICCD fast photography, are also listed in Table V.7. We note in passing that these values are very close to those found for the two structures (v_1=18.0 km/s and v_2=4.6 km/s) in the ablation of another chalcogenide (As2Se3 [Focsa et al. 2009]) in similar experimental conditions. Despite the lack of some more data on neutrals, the values displayed tend to corroborate the hypothesis made above on the electrostatic versus thermal mechanisms: the highest charge state (Ge III) exhibits the highest velocity, and most of the singly-charged ions have velocities which are closer to the center-of-mass velocity of the fast structure (i.e. in the 10^4 m/s range). This further indicates that the first (fast) plume component would consist mainly of ionized species, while the second (slow) one mainly of neutrals. However, as the plume evolves, the contribution of recombination processes cannot be neglected, leading to a less distinct separation.

V.4.2 Picosecond and femtosecond regimes

Only the $Ge_2Sb_2Te_5$ target was used for plasma plume investigations in ps and fs ablation regimes. Figure V.12 presents the evolution of the spectrally-unresolved optical emission recorded at 300 ns after the laser pulse by the ICCD camera gated at 20 ns, along with overview spectra (ICCD gate width = 1 μs) recorded close to the target (z = 0.5 mm) in these two regimes. Interestingly, the $Ge_2Sb_2Te_5$ plasma plume images reveal a splitting in ps regime (as in the ns one), while no splitting is evidenced in the fs regime. This behavior confirms the absence of the second (thermal) ablation mechanism in fs regime for this material, as it is generally observed, for instance in laser precision microfabrication [Sugioka et al. 2010, Phipps 2007].
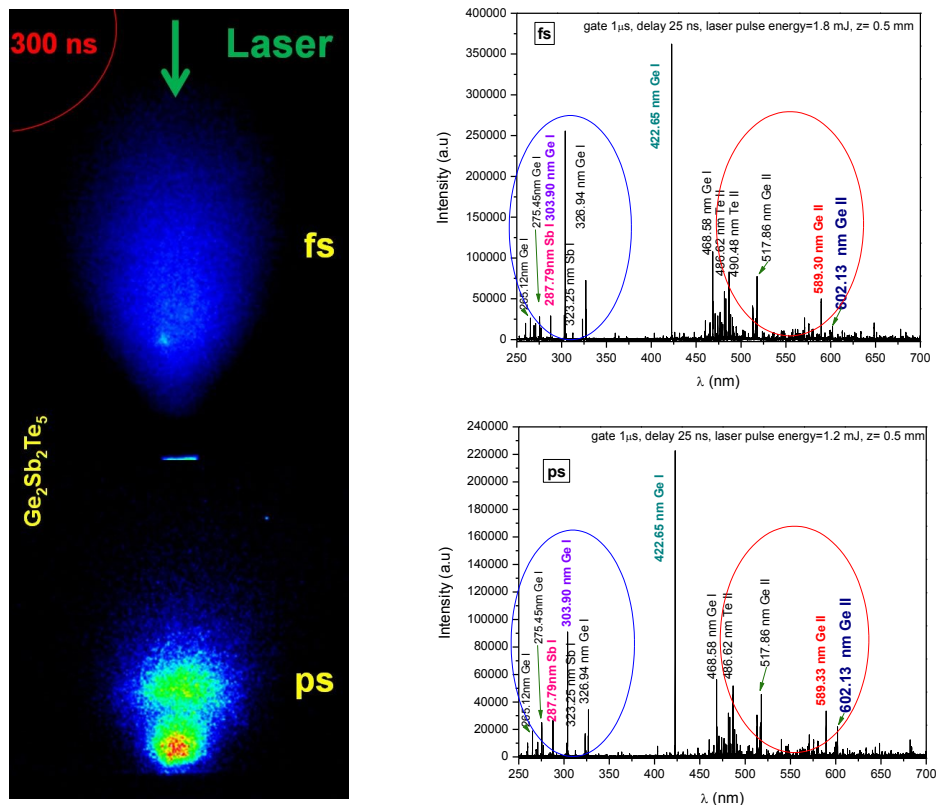
Figure V.12. (right) Spectrally unresolved emission of the plasma plume generated by laser ablation of $Ge_2Sb_2Te_5$ at 300 ns after the laser pulse in ps and fs regimes (ICCD gate width 20 ns); (left) Overview spectra of a 0.2-mm plasma slice at z = 0.5 mm from the target in fs (top) and ps (bottom) regimes ($Ge_2Sb_2Te_5$ target, ICCD gate width 1 μs).

Table V.8 summarizes the center-of-mass axial velocities derived for the $Ge_2Sb_2Te_5$ plasma structures in the three ablation regimes. For comparison, the velocities obtained for the GLS plasma (which presents only one structure) are reported. We remark that the GLS velocities are closer to the second structure ones in $Ge_2Sb_2Te_5$ plasma, which would indicate a "more thermal" interaction mechanism in GLS compared to GST.

Table V.8 Center-of-mass velocities of $Ge_2Sb_2Te_5$ and GLS plasma plume structures in the three ablation regimes.

target/laser regime	Center-of-mass velocity (10^3 m/s)				
	ns		ps		fs
$Ge_2Sb_2Te_5$	v_2=2.65	v_1=14.94	v_2=4.17	v_1=9.83	v_1=13.78
GLS	v_2 =4.36		v_2 =5.16		v_2=6.23

Individual species velocities were also derived from a space-time resolved study, mainly for singly-charged ions. Table V.9 presents a comparison of some values in the three temporal regimes, while Figure V.13 gives some examples of typical (z, t) plots. With one exception (Sb II 471.11 nm line), higher velocities are obtained in the ps and fs regimes.

Table V.9 Axial velocities of some species present in the $Ge_2Sb_2Te_5$ plasma plume in ns, ps and fs ablation regimes.

Species	λ (nm)	Laser regime	Velocity (10^3 m/s)
Ge II	481.44	ns	12.95
		ps	22.61
		fs	20.89
Te II	468.69	ns	11.19
		ps	17.63
		fs	17.63
	483.12	ns	10.20
		ps	17.64
		fs	17.63
	486.51	ns	11.93
		ps	13.85
		fs	15.51
Sb II	471.11	ns	9.52
		ps	17.63
		fs	8.12
	516.63	ns	8.08
		ps	14.25
		fs	16.19
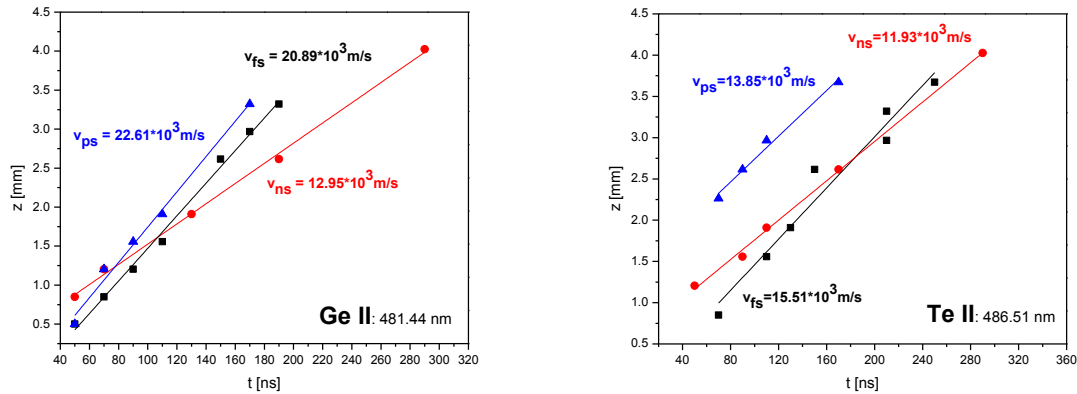
Figure V.13. Comparison of Ge$^+$ (481.44 nm) and Te$^+$ (486.51 nm) species axial velocities in ns, ps and fs ablation regimes (Ge$_2$Sb$_2$Te$_5$ target, ICCD gate width 50 ns).

V.5 Conclusions

We studied in this Chapter the dynamics of the plasma plumes generated by laser ablation of GLS and GST targets in ns, ps and fs regime. Although the initial aim of this study was to correlate the plume behavior with the grown thin films properties, no clear conclusions could be drawn on this relationship. Thus, a rather fundamental character, related to the ablation mechanisms and the plume dynamics itself in the three ablation regimes, has been brought into discussion. Some important differences have been observed between the GLS and the GST ablation. For GLS, only one plasma structure was evidenced in the three regimes, with center-of-mass velocities closer to those characterizing a thermal ejection mechanism, while for the GST targets, two structures were observed in ns and ps regime (as in a previous study on AsSe chalcogenides [Focsa et al. 2009]), and only one in fs regime. The derived individual velocities (neutrals and ions) allowed to infer on a second ablation mechanism (electrostatic repulsion [Ursu et al. 2009, 2010] or ambipolar diffusion [Tanaka et al. 1998]) in the case of the GST system.

Some previous comparative studies on the growth of oxide thin films by PLD in various temporal regimes (ns/ps/fs) [Perrière et al. 2002, Klini et al. 2005, Canulescu et al. 2011] concluded on the poorer quality (especially for roughness and crystallinity) of the films deposited in fs regime, which was attributed to the higher kinetic energies of the species reaching the surface of the growing film during deposition. This was not the case in our study (note in passing that we obtained better films in fs regime), as the species velocities were

roughly comparable in the three ablation regimes. We acknowledge however that high kinetic energy species (with energies of up to ~3 keV, see the case of La^+ ion in Er-doped GLS ns ablation) can lead to significant re-sputtering rates or to important defect concentrations.

The more abundant spectroscopic data available for the Ga, La and S species allowed us to perform a study on the plasma plume temperature and electronic density in the case of the GLS system. Comparable temperatures have been obtained for a given element in the three temporal regimes, and the validity of the McWhirter criterion for LTE has been verified for all of them. The higher electronic densities observed in ps and fs ablation led to the conclusion that the plasma plume was more ionized in these regimes compared to the ns one. This is in apparent contradiction with the much richer emission spectrum observed for ns ablation in all the studied systems. However, important differences can occur between the optical emission spectroscopy results and the actual composition of the plasma plume: for instance in the ablation of $LiMn_2O_4$, only neutral Li atoms were detected by OES [Canulescu et al. 2009], while mass spectrometry analysis showed that Li ions are the main species in the plume [D. O'Mahony et al. 2007]. On the other hand, the peculiar (oscillatory) behavior of the electronic density and temperature temporal profiles suggest a much more complex dynamic equilibrium, related to in-plume processes, as collisions, recombinations or even double-layer formation and self-structuring [Eliezer et al. 1989, Gurlui et al. 2006a, 2008, Nica et al. 2010].

Further studies in order to unveil this complexity are thus appealing, by use of both optical and electric probes. For the optical part, it would be interesting to visualize in real-time the distribution of a given species in the whole plume by using adequate interferential filters to isolate the corresponding spectral line and taking snapshots with the ICCD camera in imagery mode [Canulescu et al. 2009, 2011] in order to detect possible non-uniformities in the distribution of the plume constituents [Gonzalo et al. 1999], with direct effects on stoichiometry variations along the film surface (see our D1 sample, Chapter III). Moreover, the use of other optical techniques (as absorption spectroscopy, laser induced fluorescence, etc.) can give access to other pieces of this complex puzzle, for instance the density of species in their ground states. On the other hand, the study of the actual interaction between the plasma plume and the substrate (i.e. by optical experiments close to the substrate, placed at distances from the target which are representative for practical PLD) has been only scarcely addressed to date [Gonzalo et al. 2007, Nakata et al. 1994, Okada et al. 1992], although it is indispensable from a practical point of view in the understanding and optimization of the thin film growth.

On the electric methods side, the use of Langmuir probes [Gurlui et al. 2006a, Doggett and Lunney 2009], energy analyzers [Ursu and Nica 2013] or mass spectrometry [Mihesan et al. 2005, Pangavhane et al. 2010] can provide precious complementary information on the dynamics and energetics of the plasma as a whole or of the individual species. Finally, an interesting approach would be to "manipulate" the behavior of the plasma plume by adding external electric and/or magnetic fields which can further induce plume confinement or splitting, ionic acceleration, instabilities, or emission spectra modifications [Yeates and Kennedy 2011, Jordan et al. 1997, Neogi et al. 1999, Nica et al. 2010, 2012].

Chapter VI

General conclusions and perspectives

The present study was realized in the ANATRAC research group and in collaboration with laboratories from our university and other research centers. The thesis presents the main results regarding two groups of chalcogenide materials: Ge-Sb-Te based compounds and rare earth doped and undoped Ga-La-S alloys. Two main research directions were followed: the first one included thin film deposition (and their subsequent characterization) using the PLD technique with lasers that operate in different temporal regimes, and the second one was based on laser induced plasma analysis with an initial aim of correlating the plume characteristics with the ones of the grown samples.

In Chapter III we detailed the structural, chemical and optical properties of five chalcogenide materials found along the tie-line $GeTe-Sb_2Te_3$. The thin films were deposited by PLD in different configurations by varying several experimental parameters such as: target-substrate distance, deposition time, fluence etc. Another important studied aspect was the influence of pulse duration and repetition rate on the sample properties. The profilometry and optical microscopy images revealed an improved uniformity for the thin films deposited in picosecond and femtosecond regime. The samples obtained by ns-PLD presented large droplets on the surface. Their density decreased in cases where lower fluences were used but in the same time the deposition rate had lower values. Uniform thin films with higher thicknesses were obtained by fs- and ps-PLD in short deposition times. The lower fluence and high repetition rate ensured a fine particle ejection and determined a higher deposition rate. The EDS measurements revealed concentrations of the main elements different from the nominal composition for the samples deposited in nanosecond regime. These results were similar to the ones reported by Nemec et al. [2011a]. However their measured concentrations were closer to the stoichiometric values. Improved results were observed for the samples deposited by fs and ps-PLD. Uniform concentration distributions were observed in the ToF-SIMS depth profiles of the samples deposited using laser with short pulse duration, compared to the ones recorded for the ns-PLD thin films where regions with increased Te or Ge content were observed.

The structural analysis results of the ns-deposited Ge-Sb-Te based samples revealed that the grown thin films were partially crystallized. While the Raman spectra recorded at low excitation laser powers indicated an amorphous deposition, the XRD pattern revealed the presence of a long range order. The thin films deposited in femtosecond and picosecond regime were found to be amorphous. In general, the Raman spectroscopy results obtained at high excitation laser powers revealed a phase transformation process. The similarities between the Raman spectra recorded with low excitation power densities before and after the irradiation of the analyzed area with a high power laser beam (coming from the same Raman set-up) gave information on the stability of the formed structure. The existence of a mixture between an amorphous and a crystalline structure of the ns-deposited samples was also indicated by ellipsometry measurements. The determined values for optical band gap were comparable with the ones reported by other research groups [Nemec et al. 2011a, Kumar et al. 2012].

The second chalcogenide family investigated in this thesis was Gallium Lanthanum Sulphide (GLS), pure or doped with low concentration of rare-earths (Er, Pr). The same experimental procedures (deposition configurations and characterization methods) as for the GST system were employed. The main conclusions are relatively similar, indicated better film surface quality in short-pulse regimes (ps and fs) compared with the ns one, where the thermal ablation mechanism favors the ejection of numerous droplets. In the last regime, the droplets density was reduced when using UV wavelengths (355 and especially 266 nm). All the deposited films were amorphous, with one exception which is still to be explained. The chemical composition measured by EDX showed important deficit of Sulphur in the deposited films. Values closer to the nominal ones were obtained for two series of doped GLS samples deposited at moderate fluence ($\sim$4 J/cm^2) in ns regime at 266 nm, and also for two large-dimension samples deposited in ps regime at $\sim$1 J/cm^2. The optical properties of some samples were investigated by ellipsometry and transmission measurements, which returned refractive index and optical band gap values in line with the data available in the literature. However, even for the best samples, high values of the cut-off wavelength were observed, which could be an indication of important defect density in the films. The refractive index values progressively decreased when reducing the deposition laser pulse duration (from ns to ps to fs) and this effect could not be related to changes in the chemical composition (some contradictory results from the literature are also

discussed in this frame). Future work on other physical parameters is suggested in order to elucidate the cause of this evolution.

Chapter V presented our work on the laser induced plasma plume characterization by optical methods (fast ICCD imaging and space- and time-resolved emission spectroscopy). The ICCD images revealed different dynamic behavior for the GST and GLS induced plasmas. While the first one presented two structures for the ns and ps temporal regimes and only one for the femtosecond ablation, a single structure was observed for the GLS plume in all three regimes. The optical emission spectroscopy analysis results showed comparable species velocities from one temporal regime to another. The temporal distribution of the electronic density and temperature gave evidence on the complex processes that take place during plasma expansion.

These results permitted us to draw only several conclusions on plasma diagnosis and thin film deposition but there are still a lot of questions that need to be answered regarding stoichiometry preservation, droplet elimination, increased optical band gap and optical parameter contrast from amorphous to crystalline structure etc. Femtosecond ablation presents a clear advantage when relating to film uniformity and deposition rate but as observed in our study, the samples present a lower structure ordering. Only for the thickest fs-deposited samples the Raman spectra recorded at high excitation laser powers resembled the one of the crystalline bulk material. Moreover the vibrational spectroscopy analysis recorded with low laser powers suggested Te segregation. Future work should include a more detailed study on the chemical transformation that take place during plasma expansion and thin film deposition, as the variations in chemical composition can determine a different structural arrangement and optical response. As observed in Chapter III, the EDS measurements obtained when analyzing a deposition done on a large area revealed concentration variation of the implied elements (Ge and Te) from the center to the lateral ends of the sample. A similar plasma plume analysis as the one done in our study, but on a longitudinal direction (optical emission spectroscopy of plasma strips parallel to the expansion direction) could be useful in determining the optimum deposition region in which we obtain a uniform film. Moreover, cross-section TEM images can give important information on the growth mechanisms, can confirm the existence of amorphous and crystalline regions and could also explain the dependence of Raman spectra on the thickness of the samples deposited in our study. This type of analysis evidenced the amorphised outer layer of the RF sputtered thin films deposited by [De Bastiani et al. 2010].

A systematic study related on plasma expansion and thin film growth where the only varied experimental parameter would be the laser fluence represents an interesting approach when analyzing the influence of the possible re-sputtering phenomena at the thin film surface on the chemical properties of the samples. Moreover, almost all the samples presented in this thesis were deposited at low pressures (10^{-5}-10^{-6} Torr), however the study of the influence of this parameter variation can point out interesting properties of the deposited samples. Dieker et al. [2005] reported that the RF-sputtered $Ge_2Sb_2Te_5$ thin films presented decreased crystallization temperatures as the Ar pressure during the deposition was increased from 0.2 to 5 Pa.

Future work could also include the study of electrical (resistivity), thermal (annealing) and mechanical (adhesion) behavior of the deposited films. Such measurements permitted other research groups to determine the phase transition temperature and to acknowledge the advantage of using chalcogenide materials in phase change memories [Song et al. 2008, Liu et al. 2005, Ling et al. 2006]. Also, the resistivity dependence of temperature can confirm the more crystalline nature of the ns deposited samples as compared to the ones deposited by fs and ps-PLD. However this difference in long range order can be compensated by using in-situ heating of the substrate and subsequently on the growing film. Moreover, future work could include a dopant concentration influence on the structural, electric and optic properties of Ge-Sb-Te based samples. Ling et al. [2006] reported an increase in optical band gap of GST thin films with the increase of Si and N dopant concentration. Song et al. [2008] study suggested that Ag-doped GST films represent a better alternative for active medium capable of improving the PRAM operation with an ultrafast amorphous-to-crystallization speed. Finally, it would be interesting to investigate the photo-induced effects (photo-darkening, photo-bleaching etc.) on the deposited thin films (as already done by other authors, e.g. [Nemec et al. 2009b, 2010]) by using the various wavelength and pulse duration lasers available in the laboratory. All these investigations could bring some answers to the numerous questions opened by the present study. Moreover, closer comparison with other deposition methods (e.g. PLD *vs* RF-magnetron sputtering, as in [Nazabal et al. 2011]) should be envisaged.

Bibliography

[Aggarwal and Sanghera 2002]: I.D. Aggarwal, J.S. Sanghera, *J. Optoelectron. Adv.Mater.* **4**, 665 (2002).

[Ailavajhala et al. 2012]: M. Ailavajhala, M. Mitkova, D.P. Butt, *Phys. Status Solidi C* **9**, 2415 (2012).

[Allmen et al. 1995]: M. von Allmen, A. Blatter, Laser-Beam Interactions with Materials, Springer-Verlag, Berlin, (1995).

[Amoruso 1999]: S. Amoruso, *Appl. Phys. A* **69**, 323 (1999).

[Amoruso et al. 1999]: S. Amoruso, R. Bruzzese, N. Spinelli, R. Velotta, *J. Phys. B:At. Mol. Opt. Phys.* **32** R131 (1999).

[Amoruso et al. 2010]: S. Amoruso, C. Aruta, R. Bruzzese, D. Maccariello, L. Maritato, F. Miletto Granozio, P. Orgiani, U. Scotti di Uccio, X. Wang, *J. Appl. Phys.* **108**, 043302 (2010).

[Andersen et al. 1981]: H.H. Andersen, H.L. Bay, in: R. Behrisch, Ed., *Sputtering by Particle Bombardment I*, Springer, Berlin Heidelberg (1981), p. 145.

[Andriesh et al. 2002]: A.M. Andriesh, M.S. Iovu, S.D. Shutov, *J. Optoelectron. Adv.Mater.* **4**, 631 (2002).

[Andrikopoulos et al. 2006]: K.S. Andrikopoulos, S.N. Yannopoulos, G.A Voyiatzis, A.V Kolobov, M. Ribes, J. Tominaga, *J.Phys.: Condens. Matter* **18**, 965 (2006).

[Andrikopoulos et al. 2007]: K.S. Andrikopoulos, S.N. Yannopoulos, A.V. Kolobov, P. Fons, J. Tominaga, *J. Phys.Chem.Solids* **68**, 1074 (2007).

[Anisimov et al. 1996]: S.I. Anisimov, B.S. Luk'yanchuk, A. Luches, *Appl. Surf. Sci.* **96-98**, 24 (1996).

[Anisimov et al. 1999]: S.I. Anisimov, N.A. Inogamov, A.M. Oparin, B. Rethfeld, T. Yabe, M. Ogawa, V.E. Fortov, *Appl. Phys. A* **69**, 617 (1999).

[Anne et al. 2009]: M. L. Anne, J. Keirsse, V. Nazabal, K. Hyodo, S. Inoue, C. Boussard-Pledel, H. Lhermite, J. Charrier, K. Yanakata, O. Loréal, J. Le Person, F. Colas, C. Compère, B. Bureau, *Sensors* **9**, 7398 (2009).

[Arnold et al. 1998]: N. Arnold, B. Luk'yanchuk, N. Bityurin, *Appl. Surf. Sci*. **127–129**, 184 (1998).

[Aruta et al. 2012]: C. Aruta, S. Amoruso, G. Ausanio, R. Bruzzese, E. Di Gennaro, M. Lanzano, F. Miletto Granozio, M. Riaz, A. Sambri, U. Scotti di Uccio, X. Wang, *Appl. Phys. Lett.* **101**, 031602 (2012).

[Asal and Rutt 1997]: R. Asal, H.N. Rutt, *Opt. Mater.* **8**, 259 (1997).

[Asal et al. 1997]: R. Asal, P.E. Rivers, H.N. Rutt, *J. Phys.: Condens. Matter* **9**, 6217 (1997).

[Aspnes et al. 1979]: D.E. Aspnes, J.B. Theeten, F. Hottier, *Phys.Rev.B* **20**, 3292 (1979).

[Balazs et al. 1991]: L. Balazs, R. Gijbels, A. Vertes, *Anal. Chem.* **63**, 314 (1991).

[Balooch et al. 1990]: M. Balooch, R.J. Tench, W.J. Siekhaus, M.J. Allen, A.L. Connor, D.R. Olander, *Appl. Phys. Lett.* **57**, 1540 (1990).

[Barnes et al. 2003]: J.P. Barnes, A.K. Petford-Long, R. Serna, A. Suarez-Garcia, *J. Appl. Phys.* **93,** 6396 (2003).

[Barnier and Lucazeau 1976]: S. Barnier, G. Lucazeau, *J. Chim. Phys.* **73**, 580 (1976).

[Bäuerle 2000]: D. Bäuerle, Ed., *"Laser Processing and Chemistry"*, 3rd ed., Springer, Berlin Heidelberg (2000).

[Behrisch and Eckstein 2007]: R. Behrisch, W. Eckstein, Eds., *Sputtering by Particle Bombardment*, Springer, Berlin Heidelberg (2007).

[Bexell 2003]: U.L.F. Bexell, *Surface Characterisation Using ToF-SIMS , AES and XPS of Silane Films and Organic Coatings Deposited on Metal Substrates*, PhD thesis, Uppsala University (2003).

[Bityurin et al. 1998]: N. Bityurin, N. Arnold, B. Luk'yanchuk, D. Bäuerle, *Appl. Surf. Sci.* **127–129**, 164 (1998).

[Biunno et al. 1989]: N. Biunno, J. Narayan, S.K. Hofmeister, A.R. Srinatsa, R.K. Singh, *Appl. Phys. Lett*. **54**, 1519 (1989).

[Boardman et al. 1996]: A.D. Boardman, B. Cresswell, J. Anderson, *Appl. Surf. Sci.* **96–98**, 55 (1996).

[Bogaerts et al. 2003]: A. Bogaerts, Z. Chen, R. Gijbels, A. Vertes, *Spectroc. Acta B* **58**, 1867 (2003).

[Bruggeman 1935]: D.A.G.Bruggeman, *Ann. Phys. N.Y.* **24**, 636 (1935).

[Brundle et al. 1992]: C.R. Brundle, C.A. Evans, S. Wilson, *Encyclopedia of materials characterization*, Butxetworch-Heinemann (1992).

[Bulgakov and Bulgakova 1995]: A.V. Bulgakov, N.M. Bulgakova, *J. Phys. D: Appl. Phys.* **28**, 1710 (1995).

[Bulgakova et al. 2000]: N.M. Bulgakova, A.V. Bulgakov, O.F. Bobrenok, *Phys. Rev. E* **62**, 5624 (2000).

[Canulescu et al. 2009]: S. Canulescu, E.L. Papadopoulou, D. Anglos, T. Lippert, C.W. Schneider, A. Wokaun, *J. Appl. Phys.* **105**, 063107 (2009).

[Canulescu et al. 2011]: S. Canulescu, E. Papadopoulou, D. Anglos, T. Lippert, M.J. Montenegro, S. Georgiou, M. Döbeli, A. Wokaun, *Appl. Phys. A* **105**, 167 (2011).

[Cha et al. 2012]: D.H. Cha, H.J. Kim, Y. Hwang, J.C. Jeong, J.H. Kim, *Appl. Opt.* **51,** 5649 (2012).

[Chang et al. 1990]: C.C. Chang, X.D. Wu, R. Ramesh, X.X. Xi, T.S. Ravi, T. Venkatesan, D.M. Hwang, R.E. Muenchausen, S. Foltyn, N.S. Nogar, *Appl. Phys. Lett.* **57**, 1814 (1990).

[Chen 1994]: L.C. Chen, in: D.B. Chrisey, G.K. Hubler, Eds., *Pulsed Laser Deposition of Thin Films*, Wiley, New York (1994), p. 167.

[Chen et al. 2002]: K. Chen, J. Chen, H. Yang, *Physica C* **376**, 1078 (2002).

[Chen et al. 2006]: Zhaoyang Chen, Davide Bleiner, and Annemie Bogaerts, *J. Appl. Phys.* **99**, 063304 (2006); http://dx.doi.org/10.1063/1.2182078.

[Cho et al. 2006]: E. Cho, S. Yoon, H.R. Yoon, W. Jo, *J. Korean Phys. Soc.* **48**, 1616 (2006).

[Chrisey and Hubler 1994]: D.B Chrisey, G.K. Hubler Eds, in: *Pulsed laser deposition of thin films*, J. Wiley, New York, (1994).

[Chrisey et al. 2003]: D.B. Chrisey, A. Piqué, R.A. McGill, J.S. Horwitz, B.R. Ringeisen, D.M. Bubb, P.K. Wu, *Chem. Rev.* **103**, 553 (2003).

[Cimpoesu et al. 2010a]: R.H. Cimpoesu, G.O. Pompilian, C. Baciu, N. Cimpoesu, C. Nejneru, M. Agop, S. Gurlui, C. Focsa, *Optoelectron. Adv. Materials-Rapid Communications* **4**, 2148 (2010).

[Cimpoesu et al. 2010b]: N. Cimpoeşu, S. Stanciu, M. Meyer, I. Ionita, R. Cimpoesu, *J. Optoelectron. Adv. Mater.* **12**, 386 (2010).

[Cremers and Radziemski 2006]: D.A. Cremers, L.J. Radziemski, Handbook of Laser-Induced Breakdown Spectroscopy, John Wiley & Sons, p 34 (2006).

211

[Cremers et al. 2000]: D. A. Cremers, A. K. Knight, in R.A. Meyers Ed. *In Encyclopedia of Analytical Chemistry*, John Wiley and Sons, Chichester, UK (2000), p. 9595.

[Cristoforetti et al. 2010]: G. Cristoforetti , A. De Giacomo, M. Dell'Aglio, S. Legnaioli, E. Tognoni, V. Palleschi, N. Omenetto, *Spectrochim. Acta Part B* **65,** 86 (2010).

[Curry et al. 2005]: R.J. Curry, A.K. Mairaj, C.C. Huang, R.W. Eason, C. Grivas, D.H. Hewak, J.V. Badding, *J. Am. Ceram. Soc.* **88**, 2451 (2005).

[D. O'Mahony et al. 2007]: D. O'Mahony, J. Lunney, T. Dumont, S. Canulescu, T. Lippert, A. Wokaun, *Appl. Surf. Sci*. **254**, 811 (2007).

[Darby et al. 2008a]: M.S.B. Darby, R.E. Simpson, T.C. May-Smith, D.W. Hewak, R.W. Eason, *J. Non-Cryst. Solids* **354**, 4582 (2008).

[Darby et al. 2008b]: M.S.B. Darby, T.C. May-Smith, R.W. Eason, T. Donnelly, J.G. Lunney, K.D. Rogers, *Appl. Surf. Sci*. **254**, 3364 (2008).

[Dascalu et al. 2013]: G. Dascalu, G.O. Pompilian, B. Chazallon, V. Nica, O.F. Caltun, S. Gurlui, C. Focsa, *Appl. Phys. A* **110**, 915 (2013).

[De Bastiani et al. 2008]: R. De Bastiani, A.M. Piro, M.G. Grimaldi, E. Rimini, G.A. Baratta, G. Strazzulla, *Appl. Phys. Lett.* **92**, 241925 (2008).

[De Bastiani et al. 2010]: R. De Bastiani, E. Carria, S. Gibilisco, A. Mio, C. Bongiorno, F. Piccinelli, M. Bettinelli, A.R. Pennisi, M.G. Grimaldi, E. Rimini, *J. Appl. Phys*. **107**, 113521 (2010).

[Dieker and Wuttig 2005]: H. Dieker, M. Wuttig, *Thin Solid Films* **478**, 248 (2005).

[Doggett and Lunney 2009]: B. Doggett, J.G. Lunney, *J. Appl. Phys*. **105**, 033306 (2009).

[Dreisewerd et al. 2003]: K. Dreisewerd, S. Berkenkamp, A. Leisner, A. Rohlfing, C. Menzel, *Int. J. Mass. Spectrom.* **226**, 189 (2004).

[Eason 2007]: R. Eason, Ed., *Pulsed Laser Deposition of Thin Films: Applications-Led Growth of Functional Materials*, Wiley, Hoboken (2007).

[Eckstein et al. 1984]: W. Eckstein, H. Veerbek, in: R.A. Langley, Ed., *Data Compendium for Plasma–Surface Interactions*, International Atomic Energy Agency, Vienna (1984), p.12.

[Elam 2002]: J.W. Elam, M.D. Groner, S.M. George, *Rev. Sci. Instrum.* **73**, 2981 (2002).

[Eliezer et al. 1989]: S. Eliezer, H. Hora, *Phys. Reports* **172**, 339 (1989).

[Elliot 1986]: S.R. Elliot, *J. Non-Cryst. Solids* **81**, 71 (1986).

[Fähler et al. 1998]: S. Fähler, K. Sturm, H.U. Krebs, *Appl. Phys. Lett*. **72**, 1829 (1998).

[Fähler et al. 1999]: S. Fähler, K. Sturm, H.U. Krebs, *Appl. Phys. Lett*. **75,** 3766 (1999).

[Fähler et al. 2000]: S. Fähler, S. Kahl, M. Weisheit, K. Sturm, H.U. Krebs, *Appl. Surf. Sci*. **154–155**, 419 (2000).

[Feng et al. 2007]: J. Feng, Y. Zhang, B.W. Qiao, Y.F. Lai, Y.Y. Lin, B.C. Cai, T.A. Tang, B. Chen, *Appl. Phys. A* **87**, 57 (2007).

[Ferlauto et al. 2002]: S. Ferlauto, G.M. Ferreira , J.M. Pearce, C.R. Wronski, R.W. Collins, X. Deng, G. Ganguly, *J. Appl. Phys*. **92**, 2424 (2002).

[Flahaut et al. 1983]: J. Flahaut, M. Guittard, A.M. Loireau-Lozac'h, *Glass Tech*. **24**, 149 (1983).

[Focsa et al. 2008]: C.Focsa, M. Ziskind, C. Ursu, S. Gurlui, D. Pagnon, S.Pellerin, N.Pellerin, M. Dudeck, *J. Optoelectron. Adv. Mater*. **10**, 2380 (2008).

[Focsa et al. 2009]: C. Focsa, P. Nemec, M. Ziskind, C. Ursu , S. Gurlui, V. Nazabal, *Appl. Surf. Sci*. **255 (10)**, 5307 (2009).

[Fogarassy et al. 1990]: E. Fogarassy, C. Fuchs, A. Slaoui, J.P. Stoquert, *Appl. Phys. Lett*. **57**, 664 (1990).

[Franta et al. 2008]: D. Franta, M. Hrdlicka, D. Necas, M. Frumar, I. Ohlídal, M. Pavlišta, *Phys. Status Solidi C* **5**, 1324 (2008).

[Frantz et al. 2006a]: J.A. Frantz, J.S. Sanghera, L.B. Shaw, G. Villalobos, I.D. Aggarwal, D.W. Hewak, *Mater. Lett*. **60**, 1350 (2006).

[Frantz et al. 2006b]: J. A. Frantz, L.B. Shaw, J.S. Sanghera, I.D. Aggarwal, *Opt. Express* **14**, 1797 (2006).

[Frerichs 1953]: R. Frerichs, *J. Opt. Soc. Am*. **43**, 1153 (1953).

[Friedrich et al. 2000]: I.Friedrich, V. Weidenhof, W. Njoroge, P. Franz, M. Wutting, *J. Appl. Phys*. **87**, 4130 (2000).

[Frumar et al. 2006]: M. Frumar, B. Frumarov, P. Nemec, T. Wagner, J. Jedelsky, M. Hrdlicka, *J. Non-Cryst.Solids* **352**, 544 (2006).

[Galca et al. 2011]: A.C. Galca, V. Stancu, M.A. Husanu, C. Dragoi, N.G. Gheorghe, L. Trupina, M. Enculescu, E. Vasile, *Appl. Surf. Sci* **257**, 5938 (2011).

[Ganjoo and Golovchak 2008]: A. Ganjoo, R. Golovchak, *J. Optoelectron. Adv. Mater.* **10**, 1328 (2008).

[Garrelie et al. 1999]: F. Garrelie, C. Champeaux, A. Catherinot, *Appl. Phys. A* **69**, 45 (1999).

[Georgiou and Koubenakis 2003]:S. Georgiou, A. Koubenakis, *Chem. Rev.* **103**, 349 (2003).

[Gill et al. 1995]: D.S. Gill, R.W. Eason, C. Zaldo, H.N. Rutt, N.A Vainos, *J. Non-Cryst. Solids* **191**, 321 (1995).

[Gilles et al. 2006]: R. Gilles, D. Mukherji, M. Hoelzel, P. Strunz, D.M. Toebbens, B. Barbier, *Acta Mate.* **54,** 1307 (2006).

[Goldstein et al. 2003]: J. Goldstein, D.E. Newbury, D.E. Joy, C.E. Lyman, P.Echiln, E. Llfshin, L. Sawyer, J.R. Michael, *Scanning Electron Microscopy and X-ray Microanalysis*, Springer (2003).

[Gonzalo et al. 1999]: J. Gonzalo, J.M. Ballesteros, C.N. Afonso, *Appl. Surf. Sci.* **138-139**, 52 (1999).

[Gonzalo et al. 2007]: J. Gonzalo, J. Siegel, A. Perea, D. Puerto, V. Resta, M. Galvan-Sosa, C.N. Afonso, *Phys.Rev. B* **76,** 035435 (2007).

[Gonzalo et al. 2007]: J. Gonzalo, J. Siegel, A. Perea, D. Puerto, V. Resta, M. Galvan-Sosa, C.N. Afonso, *Phys.Rev. B* **76,** 035435 (2007).

[Gorbunov et al. 1996]: A.A. Gorbunov, W. Pompe, A. Sewing, S.V. Gaponov, A.D. Akhsakhalyan, I.G. Zabrodin, L.A. Kas'kov, E.B. Klyenkov, A.P. Morozov, N.N. Salaschenko, R. Dietsch, H. Mai, S. Vollmar, *Appl. Surf. Sci.* **96-98**, 649 (1996).

[Grehl 2003]: T. Grehl, *Improvements in TOF-SIMS Instrumentation for Analytical Application and Fundamental Research*, PhD thesis, University of Münster (2003).

[Griem 1964]: H. R. Griem, Plasma Spectroscopy (McGraw-Hill, New York, 1964).

[Gurlui et al. 2006a]: S. Gurlui, M. Sanduloviciu, M. Strat, G. Strat, C. Mihesan, M. Ziskind, C. Focsa, *J. Optoelectron. Adv.Mater.* **8**, 148 (2006)

[Gurlui et al. 2006b]: S.Gurlui, M. Sanduovici, C. Mihesan, M. Ziskind, C. Focsa. AIP. *Conf. Proc.* **812**, 279 (2006)

[Gurlui et al. 2008]: S. Gurlui, M. Agop, P. Nica, M. Ziskind, C. Focsa, *Phys. Rev. E* **78**, 026405 (2008).

[Gutwirth et al. 2009]: J. Gutwirth, T. Wagner, P. Bezdicka, M. Hrdlicka, M. Vlcek, M. Frumar, *J. Non-Cryst. Solids* **355**, 1935 (2009).

[Gyorgy et al. 2002]: E. Gyorgy, I.N. Mihailescu, M. Kompitsas, A. Giannoudakos, *Appl. Surf. Sci.* **195**, 270 (2002).

[Hahn and Omenetto 2010]: D.W. Hahn, N. Omenetto, *Appl. Spectrosc.* **64**, 335A (2010).

[Hansen et al. 1998]: T.N. Hansen, J. Schou, J.G. Lunney, *Appl. Phys. Lett.* **72,** 1829 (1998).

[Harilal 2001]: S.S. Harilal, *Appl. Surf. Sci.* **172**, 103 (2001).

[Harilal et al. 2006]: S.S. Harilal, B. O'Shay, Y. Tao, M.S. Tillack, *J. Appl. Phys.* **99**, 083303 (2006).

[Hendron et al. 1997]: J.M. Hendron, C.M.O. Mahony, T. Morrow, W.G. Graham, *J. Appl. Phys.* **81**, 2131 (1997).

[Hewak et al. 1994]: D.W. Hewak, J.A. Medeiros Neto, B. Samson, R.S. Brown, K.P. Jedrzejewski, J. Wang, E. Taylor, R.I. Laming, G. Wylangowski, D.N. Payne, *IEEE Photon. Technol. Lett.* **6**, 609 (1994).

[Hewak et al. 2010]: D.W. Hewak, D. Brady, R.J. Curry, G. Elliott, C.C. Huang, M. Hughes, K. Knight, A. Mairaj, M.N. Petrovitch, R.E. Simpson, C. Sproat, *Chalcogenide glasses for photonics device applications*, in: G.S. Murugan, Ed., *Photonic Glasses and Glass Ceramics*, Research Signpost, Kerala, India (2010) p.29.

[Hilton 2010]: A.R. Hilton, *Chalcogenide Glasses for Infrared Optics*, McGraw-Hill Companies, Inc. (2010).

[Horwitz and Sprague 1994]: J.S. Horwitz, J.A. Sprague, in : D.B. Chrisey, G.K. Hubler, Eds., *Pulsed Laser Deposition of Thin Films*, John Wiley & Sons, Australia (1994), p.229.

[Hu et al. 2011]: D.Z. Hu, F.M. Pan, X.M. Lu, J.S. Zhu, *Phys. Status Solidi A* **208**, 2749 (2011).

[Itina et al. 2003]: T.E. Itina, J. Hermann, Ph. Delaporte, M. Sentis, *Appl. Surf. Sci.* **208–209**, 27 (2003).

[Jang et al. 2010]: M.H. Jang, S.J. Park, S.J. Park, M.H. Cho, E.Z. Kurmaev, L.D. Finkelstein, G.S. Chang, *Appl. Phys. Lett.* **97**, 152113 (2010).

[Jeong et al. 1999]: T.H. Jeong, M.R. Kim, H. Seo, S.J. Kim, S.Y. Kim, *J.Appl. Phys.* **86**, 774 (1999).

[Jordan et al. 1995]: R. Jordan, D. Cole, J.G. Lunney, K. Mackay, D. Givord, *Appl. Surf. Sci.* **86**, 24 (1995).

[Jordan et al. 1997]: R.J. Jordan, D. Cole, J.G. Lunney, *Appl. Surf. Sci.* **110**, 403 (1997).

[Kang et al. 1995]: I. Kang, T.D. Krauss, F.W. Wise, B.G. Aitken, N.F. Borelli, *J. Opt. Soc. Am. B* **12**, 2053 (1995).

[Karas et al. 1985]: M. Karas, D. Bachmann, F. Hillenkamp, *Anal. Chem.* **57 (14)**, 2935 (1985).

[Karas et al. 1987]: M. Karas, D. Bachmann, U. Bahr, F. Hillenkamp, *Int. J. Mass. Spectrom.*

Ion. Proc. **78**, 53 (1987).

[Kato et al. 2005]: N. Kato, I. Konomi, Y. Seno, T. Motohiro, *Appl. Surf. Sci.* **244**, 281 (2005).

[Keszler and Nemes 2004]: A.M. Keszler, L. Nemes, *J. Mol. Struct. 695, 211* (2004).

[Kidoh et al. 1991]: H. Kidoh, T. Ogawa, A. Morimoto, T. Shimizu, *Appl. Phys. Lett.* **58**, 2910 (1991).

[Klini et al. 2005]: A. Klini, A. Manousaki, D. Anglos, C. Fotakis, *J. Appl. Phys.* **98**, 123301 (2005).

[Kolobov and Tominaga 2012]: A.V. Kolobov, J. Tominaga, Eds., *Chalcogenides: Metastability and Phase Change Phenomena*, Springer-Verlag Berlin Heidelberg, **164** (2012); doi: 10.1007/978-3-642-28705-3.

[Kolobov et al. 2005]: A.V. Kolobov, P. Fons, J. Tominaga, A.I. Frenkel, A.L. Ankudinov, S.N. Yannopoulos, K.S. Andrikopoulos, T. Uruga, *Jpn. J. Appl. Phys.* **44**, 3345 (2005).

[Kolobov et al. 2006]: A.V. Kolobov, P. Fons, J. Tominaga, T. Uruga, *J. Non-Cryst. Solids* **352**, 1612 (2006).

[Kölpin et al. 2009]: H. Kölpin, D. Music, G. Laptyeva, R. Ghadimi, F. Merget, S. Richter, R. Mykhaylonka, J. Mayer, J.M. Schneider, *J. Phys. Condens. Matter* **21**, 435501 (2009).

[Kondoh et al.1993]: K. Kondoh, M. Suwa, K. Morita, *Nucl. Instr.Meth.Phys. Res. B* **78**, 68 (1993).

[Kosolapov et al. 2011]: A.F. Kosolapov, A.D. Pryamikov, A.S. Biriukov, V.S. Shiryaev, M.S. Astapovich, G.E. Snopatin, V.G. Plotnichenko, M.F. Churbanov, E.M. Dianov, *Opt. Express* **19**, 25723 (2011).

[Kozyukhin et al. 2011]: S.A. Kozyukhin, A.A. Sherchenkov, V.M. Novotortsev, S.P. Timoshenkov, *Nanotechnologies in Russia* **6**, 227 (2011).

[Krishnaswamy et al. 1989]: J. Krishnaswamy, A. Rengan, J. Narayan, *Appl. Phys. Lett.* **54**, 2455 (1989).

[Krusin-Elbaum et al. 2007]: L. Krusin-Elbaum, C. Cabral, K.N. Chen, M. Copel, D.W. Abraham, K.B. Reuter, S.M. Rossnagel, J. Bruley, V.R. Deline, *Appl. Phys. Lett.* **90**, 141902 (2007).

[Kumar et al. 2012]: S. Kumar, D. Singh, S. Sandhu, R. Thangaraj, *Phys. Status Solidi A* **209**, 2014 (2012).

[Kurucz and Bell 1995]: R.L. Kurucz, B. Bell, Atomic Line Data, Kurucz CD-ROM No. 23, Smithsonian Astrophysical Observatory, Cambridge, MA, 1995 http://www.cfa.harvard.edu/ amp/ampdata/kurucz23/sekur.html

[Kwok et al. 1991]: H.S. Kwok, H.S. Kim, S.Witananchchi, E. Petrou, J.P. Zheng, S. Patel, E. Narumi, D.T. Shaw, *Appl. Phys. Lett.* **59** 3643 (1991).

[Larkin 2011]: P. Larkin, *Infrared and Raman Spectroscopy Principles And Spectral Interpretation*, Elsevier Inc. (2011).

[Le Drogoff et al. 2001]:B. Le Drogoff , J. Margot, M. Chaker, M. Sabsabi, O. Barthélemy, T.W. Johnston, S. Laville, F. Vidal, Y. von Kaenel *Spectrochim. Acta Part B* **56**, 987 (2001).

[Lee and Bishop 2009]: B. Lee, S.G. Bishop, in: S. Raoux, M. Wuttig, Eds., *Phase Change Materials*, Springer Science+Business Media, USA (2009), p.175.

[Lee et al. 2005]: B.S. Lee, J.R. Abelson, S.G. Bishop, D.H. Kang, B. Cheong, K.B. Kim, *J. Appl. Phys.* **97**, 093509 (2005).

[Lee et al. 2007]: J. Lee, S. Choi, C. Lee, Y. Kang, D. Kim, *Appl. Surf. Sci.* **253**, 3969 (2007).

[Ling et al. 2006]: Y. Ling, Y. Lin, B. Qiao, Y. Lai, J. Feng, T. Tang, B. Cai, B. Chen, *Jpn. J. Appl.Phys.* **45**, L349 (2006).

[Liu et al. 1997]: X. Liu, D. Du, G. Mourou, *IEEE J. Quantum. Elect.* **33**, 1706 (1997); doi: 10.1109/3.631270.

[Liu et al. 2005]: B. Liu, Z. Song, T. Zhang, J. Xia, S. Feng, B. Chen, *Thin Solid Films* **478**, 49 (2005).

[Lochte et al. 1968]: W. Lochte – Holtgreven, Plasma diagnostics, North – Holland Publishing Company, Amsterdam (1968).

[Loireau-Lozac'h et al. 1974]: A.M. Lozac'h, S. Banner, M. Guittard, P. Besancon, J. Flahut, *Ann. Chim.* **9**, 127 (1974).

[Loireau-Lozac'h et al. 1976]: A.M. Loireau-Lozac'h, M. Guittard, J. Flahaut, *Mat. Res. Bull.* **11**, 1489 (1976).

[Loireau-Lozac'h et al. 1977]: A.M. Loireau-Lozac'h, M. Guittard, J. Flahut, *Mat. Res. Bull.* **12**, 881 (1977).

[Lowndes 1998]: D.H.Lowndes, in: J.C. Miller, R.F Haglund Eds., Experimental Methods in the Physical Sciences, vol 30, Academics Press, New York (1998), p.457.

[Lu et al. 2012]: H. Lu, E. Thelander, J.W. Gerlach, D. Hirsch, U. Decker, B. Rauschenbach, *Appl. Phys. Lett.* **101**, 031905 (2012).

[Lucazeau and Leroy 1978]: G. Lucazeau, J. Leroy, *Spectroc. Acta* A**34**, 29 (1978).

[Lucazeau et al. 1978]: G. Lucazeau, S. Barnier, A.M. Lozac'h, *Spectroc. Acta* A **34**, 21 (1978).

[Lunney and Jordan 1998]: J.G. Lunney, R. Jordan, *Appl. Surf. Sci*. **127–129**, 941 (1998).

[Mairaj et al. 2004]: A.K. Mairaj, R.J. Curry, D.W. Hewak, *Electron. Lett.* **40**, 421 (2004).

[Mairaj et al. 2005]: A.K. Mairaj, R.J. Curry, D.W. Hewak, *Appl. Phys. Lett.* **86**, 094102 (2005).

[May-Smith 2005]: T.C. May-Smith, *Pulsed Laser Deposition of Thick Multilayer Garnet Crystal Films for Waveguide Laser Devices*, PhD thesis, University of Southampton, UK (2005).

[McWhirter 1965]: R.W.P.McWhirter, in: R.H. Huddlestone, S.L. Leonard Eds., *Plasma Diagnostic Techniques*.Ch. 5, Academic Press, New York, vol 21 (1965), p. 201.

[Mehta 2006]: N. Mehta, *J.Sci.Ind. Res.* **65**, 777 (2006).

[Mihesan et al. 2005]: C. Mihesan, S. Gurlui, M. Ziskind, B. Chazallon, G. Martinelli, H. Zeghlache, M. Guignard, V. Nazabal, F. Smektala, C. Focsa, *Appl. Surf. Sci*. **248**, 224 (2005).

[Miller and Haglund 1998]: J.C. Miller, R.F. Haglund, Eds, *Experimental Methods in the Physical Science*, Academic Press **30,** New York (1998).

[Miziolek et al. 2006]: A.W. Miziolek, V. Palleschi, I. Schechter, Eds., *"Laser-Induced Breakdown Spectroscopy (LIBS). Fundamentals and Applications"*, Cambridge University Press (2006).

[Mora 2003]: P. Mora, *Phys. Rev. Lett.* **90**, 185002 (2003).

[Morales-Sánchez et al. 2005]: E. Morales-Sánchez, E.F. Prokhorov, J. González-Hernández, A. Mendoza-Galván, *Thin Solid Films* **471**, 243 (2005).

[Mori et al. 1997]: A. Mori, Y. Ohishi, T. Kanamori, S. Sudo, *Appl. Phys. Lett*. **70**, 1230 (1997).

[Mostako and Khare 2012]: A.T.T. Mostako, A. Khare, *Appl. Nanosci.* **2**, 189 (2012).

[Murakami et al. 2005]: M. Murakami, Y.G. Kang, K. Nishihara, H. Nishimura, *Phys. Plasmas* **12**, 062706 (2005).

[Musgrave et al. 2011]: J.D. Musgraves, N. Carlie, J. Hu, L. Petit, A. Agarwal, L.C. Kimerling, K. A. Richardson, *Acta Mater.* **59**, 5032 (2011).

[Nakata et al. 1994]: Y. Nakata, W. K. A. Kumuduni, T. Okada, M. Maeda, *Appl. Phys. Lett.* **64**, 2599 (1994).

[Nazabal et al. 2011]: V. Nazabal, F. Charpentier, J.-L. Adam, P. Nemec, H. Lhermite, M.-L. Brandily-Anne, J. Charrier, J.-P. Guin, A. Moréac, *Int. J. Appl. Ceram. Technol.* **8**, 990 (2011).

[Němec and Frumar 2003]: P. Němec, M. Frumar, *J. Optoelectron. Adv. Mater.* **5**, 1047 (2003).

[Němec et al. 2000]: P. Němec, M. Frumar, B. Frumarová, M. Jelínek, J. Lančok, J. Jedelský, *Opt. Mater.* **15**, 191 (2000).

[Němec et al. 2009a]: P. Němec, A. Moreac, V. Nazabal, M. Pavlišta, J. Přikryl, M. Frumar, *J. Appl.Phys.* **106**, 103509 (2009).

[Němec et al. 2009b]: P. Němec, V. Nazabal, M. Pavlišta, A. Moreac, M. Frumar, M. Vlček, *Mater. Chem. Phys.* **117**, 23 (2009).

[Němec et al. 2010]: P. Němec, S. Zhang, V. Nazabal, K. Fedus, G. Boudebs, A. Moreac, M. Cathelinaud, X.-H. Zhang, *Opt. Express* **18**, 22944 (2010).

[Němec et al. 2011a]: P. Němec, J. Přikryl, V. Nazabal, M. Frumar, *J. Appl. Phys.* **109**, 073520 (2011).

[Němec et al. 2011b]: P. Nemec, V. Nazabal, A. Moreac, J. Gutwirth, L. Benes, M. Frumar, *Mater. Chem. Phys.* **136** 935 (2012).

[Němec et al. 2012]: P. Němec, V. Nazabal, A. Moreac, J. Gutwirth, L. Beneš, M. Frumar, *Mater. Chem. Phys*. **136**, 935 (2012).

[Neogi et al. 1999]: A. Neogi, V. Narayanan, R.K. Thareja, *Phys. Lett.* A **258**, 135 (1999).

[Nica et al. 2009]: P. Nica, P. Vizureanu, M. Agop, S. Gurlui, C. Focsa, N. Forna, P. Ioannou, Z. Borsos, *Jpn. J. Appl. Phys.* **48**, 066001 (2009).

[Nica et al. 2010]: P. Nica, M. Agop, S. Gurlui, C. Focsa, *Eur. Phys. Lett.* **89**, 65001 (2010).

[Nica et al. 2012]: P.E Nica, M. Agop, S. Gurlui, C. Bejinariu, C. Focsa, *Jpn. J. Appl. Phys.* **51**, 106102 (2012).

[Nino et al. 2001]: J.C. Nino, M.T. Lanagan, C.A. Randall, *J. Mater. Res*. **16**, 1460 (2001).

[NIST ASD]: NIST Atomic Spectra Database: http://physics.nist.gov/cgi-bin/AtData/main_asd

[O'Mahony et al. 2007]: D. O'Mahony, J. Lunney, T. Dumont, S. Canulescu, T. Lippert, A. Wokaun, *Appl. Surf. Sci*. **254**, 811 (2007).

[Oates et al. 2011]: T.W.H. Oates, H. Wormeester, H. Arwin, *Prog. Surf. Sci.* **86,** 328 (2011).

[Ohring 1992]: M. Ohring, *The Materials Science of Thin Films*, Academic Press, San Diego (1992).

[Okada et al. 1992]: T. Okada, Y. Nakayama, W. K. A. Kumuduni, M. Maeda, *Appl. Phys. Lett.* **61**, 2368 (1992); doi: 10.1063/1.108246.

[Orava et al. 2008]: J. Orava, T. Wágner, J. Šik, J. Přikryl, M. Frumar*, J. Appl. Phys.* **104**, 043523 (2008).

[Ovshinsky 1968]: S.R. Ovshinsky, *Phys. Rev. Lett*. **21**, 1450 (1968).

[Owen et al. 1985]: A.E. Owen, A.P. Firth, P.J.S. Ewen, *Phil. Mag. B* **52**, 347 (1985).

[Pangavhane et al. 2010]: S.D. Pangavhane, P. Nemec, T. Wagner, J. Janca, J. Havel, *Rapid. Commun. Mass Spectrom.* **24**, 2000 (2010).

[Pechen et al. 1995]: E.V. Pechen, A.V. Varlashkin, S.I. Krasnosvobodtsev, B. Brunner, K.F. Renk, *Appl. Phys. Lett.* **66**, 2292 (1995).

[Pelusi et al. 2009]: M. Pelusi, F. Luan, T.D. Vo, M.R.E. Lamont, S.J. Madden, D.A. Bulla, D. Choi, B. Luther-Davies, B.J. Eggleton, *Nat. Photon.* **3**, 139 (2009).

[Perrière et al. 2002]: J. Perrière, E. Millon, W. Seiler, C. Boulmer-Leborgne, V. Craciun, O. Albert, J.C. Loulergue, J. Etchepare, *J. Appl. Phys.* **91**, 690 (2002).

[Peterlongo et al. 1994]: A. Peterlongo, A. Miotello, R. Kelly, *Phys. Rev. E* **50**, 4716 (1994).

[Phipps 2007]: C. Phipps, Ed., *Laser Ablation and its Applications* , Springer Series in Optical Sciences 129, Springer, Berlin (2007).

[Pollard et al. 2012]: M.E. Pollard, K.J. Knight, G.J. Parker, D.W. Hewak, M.D.B. Charlton, in: S. Jiang, M.F.J. Digonnet, J.C. Dries, Eds., *Optical Components and Materials IX.Photonics West,* Bellingham, US (2012).

[Pompilian et al. 2013]: O.G.Pompilian, S. Gurlui, P. Nemec, V. Nazabal, M.Ziskind, C. Focsa, *Appl. Surf. Sci.* **278**, 352 (2013).

[Popescu et al. 2011]: A.A. Popescu, D. Savastru, S. Miclos, V. Braic, M. Popescu, A. Manea, A. Kiss, *Dig. J. Nanomater. Bios*. **6**, 341 (2011).

[Prokhorov et al. 2007]: E. Prokhorov, J. Gonzalez-Hernandez, M.A. Hernandez-Landaverde, B. Chao, E. Morales-Sanchez, *J. Phys. Chem. Solids* **68**, 883 (2007).

[Qiao et al. 2006]: B. Qiao, J. Feng, Y. Lai, Y. Ling, Y. Lin, T. Tang, B. Cai, B. Chen, *Appl. Surf. Sci.* **252**, 8404 (2006).

[Radziemski 2002]: L.J. Radziemski, *Spectrochim. Acta, Part B* **57**,1109 (2002).

[Ramachandran and Bishop 1999]: S. Ramachandran, S.G. Bishop, *Appl. Phys. Lett.* **74**, 13 (1999).

[Reif 2010]: J. Reif, in: A. Miotello, P. M. Ossi, Eds., *Laser-Surface Interactions for New Materials Production*, Springer, Berlin Heidelberg (2010), p.19.

[Robinson et al. 2003]: T.G. Robinson, R.G. DeCorby, J.N. McMullin, C.J. Haugen, S.O. Kasap, D. Tonchev, *Opt. Lett.* **28**, 459 (2003).

[Rode at al. 2002]: A.V. Rode, A. Zakery, M. Samoc, R.B. Charters, E.G. Gamaly, B. Luther-Davies, *Appl. Surf. Sci.* **197–198**, 481(2002).

[Rosen et al. 1982]: D.I. Rosen, J. Mitteldorf, G. Kothandaraman, A.N. Pirri, E.R. Pugh, *J. Appl. Phys*. **53**, 3190 (1982).

[Rusak et al. 2002]: D.A. Rusak, B.C. Castle, B.W. Smith, J.D. Winefordner, Critical Reviews in *Anal. Chem.* **27**, 257 (1997).

[Saenger 1994]: K.L. Saenger, in D.B. Chrisey, G.K. Hubler Eds, Pulsed Laser Deposition of Thin Filmd, Wiley, New York, (1994), p.199.

[Santos et al.1998]: P.V Santos, M.T. De Araujo, A.S. Gouveia-Neto, J.A. Medeiros Neto, A.S.B. Sombra, *Appl. Phys. Lett.* **73**, 578 (1998).

[Schou 2006]: J. Schou, in Y. Puleau Ed. , *Materials surface processing by directed energy technique, Elsevier, Oxford (2006), p. 35.*

[Schou 2009]: J. Schou, *Appl. Surf. Sci.* **255**, 5191 (2009).

[Schweizer et al. 1996]: T. Schweizer, D.W. Hewak, D.N. Payne, T. Jensen, G. Huber. *Electron. Lett.* **32**, 666 (1996).

[Schweizer et al. 1997a]: T. Schweizer, D.J. Brady, D.W. Hewak, D.N. Payne, *Electron. Lett.* **33**, 414 (1997).

[Schweizer et al. 1997b]: T. Schweizer, D.J. Brady, D.W. Hewak, *Opt. Express* **1**, 102 (1997).

[Schweizer 1998]: T. Schweizer, PhD Thesis, *Rare-Earth-Doped Gallium Lanthanum Sulphide Glasses for Mid-Infrared Fibre Lasers*, University of Southampton and Hamburg Universität, 1998.

[Schweizer et al. 1999a]: T. Schweizer, B. Samson, J. Hector, W. Brocklesby, D. Hewak, D. Payne, *Infrared Phys.Techn.* **40**, 329 (1999).

[Schweizer et al. 1999b]: T. Schweizer, B. Samson, J. Hector, W. Brocklesby, D. Hewak, D. Payne, *J. Opt. Soc. Am. B* **16**, 308 (1999).

[Schweizer et al. 2001]: T. Schweizer, F. Goutaland, E. Martins, D.W. Hewak, W.S. Brocklesby, *J. Opt. Soc. Am. B* **18**, 1436 (2001).

[Seddon et al. 2010]: A.B. Seddon, Z. Tang, D. Furniss, S. Sujecki, T.M. Benson, *Opt. Express* **18**, 26704 (2010).

[Shin et al. 2005]: M.J. Shin, S.M. Kim, D.J Choi, K.N. Lee, S.K. Hong, Y.J. Parl, *J. Mater. Sci.* **40**, 1543 (2005).

[Sibold and Urbassek 1993]: D. Sibold, H.M. Urbassek, *J. Appl. Phys.* **73**, 8544 (1993).

[Siegert et al. 1999]: M. Siegert, W. Zander, J. Lisoni, J. Schubert, Ch. Buchal, *Appl. Phys. A* **69**, S779 (1999).

[Singh 2010]: A.K. Singh, in: M.R.B. Andreeta, Ed. *Crystallization - Science and Technology*, InTech (2010), p. 29.

[Singh and Kumar 1998]: R.K. Singh, D. Kumar, *Mater. Sci.Eng.* **22**, 113 (1998).

[Singh et al. 1989]: R.K. Singh, J. Narayan, A.K. Singh, *Appl. Phys. Lett.* **54**, 2271 (1989).

[Song et al. 2008]: K.H. Song, S.W. Kim, J.H. Seo, H.Y. Lee, *J. Appl. Phys.* **104**, 103516 (2008).

[Sosso et al. 2009]: G.C. Sosso, S. Caravati, M. Bernasconi, *J. Phys.:Condens. Matter* **21**, 095410 (2009).

[Stapleton et al. 2005]: M.W. Stapleton, A.P. McKiernan, J.P. Mosnier, *J. Appl. Phys.* **97**, 064904 (2005).

[Straub et al. 2010]: F. Straub, T. Wirth, A. Hertwig, V.D. Hodoroaba, W.E.S. Unger, T. Böllinghaus, *Surf. Interface Anal.* **42,** 739 (2010).

[Strickland and Mourou 1985]: D. Strickland, G. Mourou, *Opt. Commun.* **56**, 219 (1985).

[Suarez-Garcia et al. 2003]: A. Suarez-Garcia, J.P. Barnes, R. Serna, A.K. Petford-Long, C.N. Afonso, D. Hole, *Mater. Res. Soc. Symp. Proc.* **780**, Y1.2.1 (2003).

[Sugioka et al. 2010]: K. Sugioka, M. Meunier, A. Piqué, Eds., *Laser Precision Microfabrication* , Springer Series in Materials Science 135, Springer, Berlin, 2010.

[Sun et al. 2008]: H.J. Sun, L.S. Hou, Y.Q. Wu, F.X. Zhai, *Chin. Phys. Lett.* **25**, 2915 (2008).

[Swanepoel 1983]: R. Swanepoel, *J. Phys. E: Sci. Instrum.* **16**, 1214 (1983).

[Tanaka and Shimakawa 2011]: K. Tanaka, K. Shimakawa, *Amorphous Chalcogenide Semiconductors and Related Materials*, Springer Science+Business Media, LLC (2011).

[Tanaka et al. 1998]: M. Tanaka, Y. Fujisawa, T. Nakajima, Y. Tasaka, K. Ota, S. Usami, *J. Appl. Phys.* **83**, 3379 (1998).

[Tauc 1974]: J. Tauc, Ed.: *Amorphous and liquid semiconductors*, Plenum, New-York, (1974).

[Todorov et al. 2012]: R. Todorov, J. Tasseva, T. Babeva, in: A. Massaro, Ed., *Photonic Crystals – Innovative Systems, Lasers and Waveguides*, InTech, Croatia (2012), p.143.

[Toftmann et al. 2000]: B. Toftmann, J. Schou, T.N. Hansen, J.G. Lunney, *Phys. Rev. Lett*. **84**, 3998 (2000).

[Tosto 2002]: S. Tosto, *J. Phys. D: Appl. Phys*. **35**, 770 (2002).

[Ursu and Nica 2013]: C. Ursu, P.E. Nica, J. Optoelectron. *Adv. Mater*. **15**, 42 (2013).

[Ursu et al. 2009]: C. Ursu, S.Gurlui, C. Focsa, G. Popa, *Nucl. Instrum. Meth. B* **267**, 446 (2009).

[Ursu et al. 2010] : C. Ursu, O.G. Pompilian, S. Gurlui, P. Nica, M. Agop, M. Dudeck, C. Focsa, *Appl. Phys. A* **101**, 153 (2010).

[Van de Riet et al. 1993]: E. Van de Riet, J.C.S. Kools, J. Dieleman, *J. Appl. Phys*. **73**, 8290 (1993).

[Vaughan 1999]: D. Vaughan (Ed.) in *Energy-Dispersive X-ray Microanalysis An Introduction*, NORAN Instruments (1999).

[Venables 1994]: J.A. Venables, *Surf. Sci*. **299-300**, 798 (1994).

[Vertes et al. 1993]: A. Vertes, R. Gijbels, F. Adam, *Chemical Analysis Series*, vol 124, J. Wiley, New York, (1993).

[Vickerman and Briggs 2001]: J.C. Vickerman, D. Briggs Eds., in *ToF-SIMS — Surface Analysis by Mass Spectrometry,* IM Publications and Surface Spectra (2001).

[Vinod et al. 2012a]: E.M. Vinod, A.K. Singh, R. Ganesan, K.S. Sangunni, *J. Alloys Compd.* **537**, 127 (2012).

[Vinod et al. 2012b]: E.M. Vinod, R.Naik, R. Ganesan, K.S. Sangunni, *J. Non-Cryst. Solids* **358**, 2927 (2012).

[Vlček et al.2003]: M. Vlček, S. Schroeter, J. Čech, T. Wágner, T. Glaser, *J. Non-Cryst. Solids* **326–327**, 515 (2003).

[Voevodin and Donley 1996]: A.A. Voevodin, M.S. Donley, *Surf. Coat. Technol*. **82**, 199 (1996).

[von Allmen and Blatter 1995]: M. von Allmen, A. Blatter, *Laser-Beam Interactions with Materials*, Springer-Verlag, Berlin, (1995).

[Wágner 2007]: T. Wágner, in: *Symposium Program -E*PCOS2007,* Zermatt, Switzerland (2007), p. 1.

[Warrender and Azziz 2007]: J.M. Warrender, M.J. Azziz, *Phys. Rev. B* **75**, 085433 (2007).

[Watanabe et al. 1995a]: Y. Watanabe, M. Tanamura, Y. Matsumoto, Y. Seki, *J. Appl. Phys.* **78**, 2029 (1995).

[Watanabe et al. 1995b]: Y. Watanabe, Y. Seo, M. Tanamura, H. Asami, Y. Matsumoto, *J. Appl. Phys.* **78**, 5126 (1995).

[Willmott 2004]: P.R. Willmott, *Progress Surf. Sci*. **76**, 163 (2004).

[Willmott et al. 2002]: P.R. Willmott, H. Spillmann, J.R. Huber, *J. Mater. Chem.* **12**, 397 (2002).

[Witanachchi et al. 1988]: S. Witanachchi, H.S. Kwok, X.W. Wang, D.T. Shaw, *Appl. Phys. Lett.* **53**, 234 (1988).

[Xu et al. 2008]: M. Xu, S.J Wei, S. Wu, F. Pei, J. Li, S.Y. Wangy, L.Y. Chen, *J. Korean Phys. Soc*. **53**, 2265 (2008).

[Yamada 2012]: N. Yamada, *Phys. Status Solidi B* **249**, 1837 (2012).

[Yamada et al. 1987]: N. Yamada, E. Ohno, N. Akahira, K. Nishiuchi, K. Nagata, M. Takao, *Jpn. J. Appl. Phys.* **26**, 61 (1987).

[Yamada et al. 1998]: N. Yamada, M. Otaba, K. Kawahara, N. Miyagawa, H. Ohta, N. Akahira, T. Matsunaga, *Jpn. J. Appl. Phys.* **37**, 2104 (1998).

[Yang et al. 2010]: Z. Yang, M.K. Fah, K.A. Reynolds, J.D. Sexton, M.R. Riley, M.L. Anne, B.Bureau, P. Lucas, *Opt.Express* **18**, 26754 (2010).

[Yeates and Kennedy 2011]: P. Yeates, E.T. Kennedy, *J. Appl. Phys.* **110**, 063303 (2011); doi: 10.1063/1.3638697.

[Yoo et al. 2009]: W.J. Yoo, J.K. Seo, D.H. Cho, K.W. Jang, J.Y. Heo, S.C. Chung, B. Lee, B.G. Park, J.H. Moon, S.Kim, *IEEE Symposium on Industrial Electronics & Applications,* 617 (2009).

[Yoon et al. 2005]: H.R. Yoon, W. Jo, E.H. Lee, J.H. Lee, M. Kim, K.Y. Lee, Y. Khang, *J. Non-Cryst. Solids* **351**, 3430 (2005).

[Yoon et al. 2006]: H.R. Yoon, W. Jo, E. Cho, S. Yoon, M. Kim, *J. Non-Cryst. Solids* **352**, 3757 (2006).

[Youden et al. 1993]: K.E. Youden, T. Grevatt, R.W. Eason, H.N. Rutt, R.S. Deol, G. Wylangowski, *Appl. Phys. Lett.* **63**, 1601 (1993).

[Zakery and Elliott 2007]: A. Zakery, S. R. Elliott, *Optical Nonlinearities in Chalcogenide Glasses and Their Applications*, Springer-Verlang, Berlin Heidelberg (2007), p.1.

[Zhang and Lucas 2003]: X. Zhang, J. Lucas, *J. Optoelectron. Adv. Mater.* **5**, 1327 (2003).

[Zhang et al. 2003]: X.H. Zhang, Y. Guimond, Y. Bellec, *J. Non-Cryst. Solids* **326–327**, 519 (2003).

Chalcogenides are among the most promising materials for applications in various fields, like data storage and transmission, integrated optics, bio- and chemical-sensing, or medicine. This is due to their outstanding properties, in terms of wide infrared transparency, photo-induced effects, high rare-earth solubility or high contrast in electrical and optical parameters upon phase transformation. For many of these applications, processing of chalcogenides in form of thin films with required chemical composition and appropriate physical properties is necessary. Pulsed Laser Deposition (PLD) is one of the most efficient and flexible methods for the preparation of such multicomponent layers.

In this thesis we performed a systematic study on the influence of various PLD parameters, like laser wavelength, pulse duration and fluence, background pressure and target-substrate distance, on the properties of deposited thin films. Two families of chalcogenide compounds were explored: $(GeTe)_x(Sb_2Te_3)_{1-x}$ (with x = 0, 1/3, 1/2, 2/3, 1) and GaLaS (pure or doped with Er and Pr rare earths). Additionally, a time- and space-resolved optical emission spectroscopy study was performed in order to characterize the dynamics and energetics of the laser ablation plasma plume. The properties of the thin films were investigated by specific methods, as optical and electronic microscopy, profilometry, X-ray diffraction, Raman spectroscopy, ellipsometry etc.

The main results indicate better properties for samples deposited at lower wavelength, short pulse duration and moderate fluence. They open the way for the optimization of the PLD process for chalcogenide thin film growth in a controlled manner.

Keywords: thin films, chalcogenides, pulsed laser deposition, structural characterisation methods, optical properties of materials, laser ablation plasma, optical emission spectroscopy

Les chalcogénures sont des matériaux très prometteurs pour des applications dans divers domaines, comme l'enregistrement et la transmission des données, l'optique intégrée, les capteurs ou la médecine. Ceci est dû à leurs propriétés exceptionnelles, en termes de transparence dans l'infrarouge, effets photo-induits, grande solubilité pour les terres rares, ou contraste élevé des paramètres électriques et optiques lors d'un changement de phase. Pour beaucoup de ces applications, les chalcogénures doivent se présenter sous forme de couches minces. Une méthode efficace et flexible pour obtenir de telles couches est le dépôt par ablation laser (PLD).

Dans cette thèse nous avons entrepris une étude systématique sur l'influence de divers paramètres, comme la longueur d'onde, la durée de l'impulsion ou la fluence du laser, la pression de dépôt et la distance cible-substrat, sur les propriétés des couches minces déposées. Deux familles de composés ont été étudiées: $(GeTe)_x(Sb_2Te_3)_{1-x}$ (avec x = 0, 1/3, 1/2, 2/3, 1) et GaLaS (pur ou dopé avec des terres rares – Er et Pr). Une étude en spectroscopie optique d'émission a été également effectuée afin d'explorer la dynamique et l'énergétique du plasma créé par ablation laser. Les propriétés des couches minces ont été caractérisées par microscopie optique et électronique, profilométrie, diffraction de rayons X, spectroscopie Raman, ellipsométrie etc.

Les principaux résultats indiquent de meilleures propriétés pour les couches déposées à faible longueur d'onde, courte durée d'impulsion et fluence modérée. Ils ouvrent la voie vers l'optimisation du processus PLD pour la croissance de couches minces de chalcogénures de manière contrôlée.

Mots clés: couches minces, chalcogénures, dépôt par laser pulsé, méthodes de caractérisation structurale, propriétés optiques des matériaux, plasma produit par ablation laser, spectroscopie optique d'émission